Title
A mixed 3d cable element for the nonlinear static and dynamic analysis of cable structures

Author
Crusells Girona, Miquel

Publication Date
2017

Peer reviewed|Thesis/dissertation

A mixed 3d cable element for the nonlinear static and dynamic analysis of cable structures

by

Miquel Crusells Girona

A dissertation submitted in partial satisfaction of the

requirements for the degree of

Doctor of Philosophy

in

Engineering - Civil and Environmental Engineering

in the

Graduate Division

of the

University of California, Berkeley

Committee in charge:

Professor Filip C. Filippou, Co-chair
Professor Robert L. Taylor, Co-chair
Professor Khalid M. Mosalam
Professor Panayiotis Papadopoulos

Fall 2017

A mixed 3d cable element for the nonlinear static and dynamic analysis of cable structures

Miquel Crusells Girona

Abstract

A mixed 3d cable element for the nonlinear
static and dynamic analysis of cable structures

by

Miquel Crusells Girona

Doctor of Philosophy in Engineering - Civil and Environmental Engineering

University of California, Berkeley

Professor Filip C. Filippou, Co-chair

Professor Robert L. Taylor, Co-chair

This dissertation presents the formulation and validation of a new 3d mixed cable element that is based on a two-field variational formulation and is suitable for the nonlinear static and dynamic analysis of cable structures.

The new cable element is derived in general curvilinear coordinates under finite deformations, and identifies conjugate strain and stress measures for the nonlinear catenary problem. The formulation uses the weak form of the strain-displacement relation and the principle of virtual work to propose two numerical implementations of the element, one with a continuous axial force distribution and one with a discontinuous one.

This dissertation also proposes a new filtered energy-momentum conserving algorithm for obtaining the dynamic response of cable structures in time. This new algorithm exactly conserves the Hamiltonian structure of the two-field mixed catenary problem for any nonlinear elastic complementary energy, and provides a consistent time integration in the case of inelastic material response. A postprocessing Savitzky-Golay filter is included to address the high-frequency contributions that appear in cables with a large sag-to-span ratio, without jeopardizing the desired conserving properties.

The new element and the consistent time integration scheme are first validated under nonlinear elastic material response with several benchmark problems from the literature. In these examples, the mixed cable element obtains very accurate results for coarse meshes, and displays especially accurate axial force distributions compared to other models. For cables with a small sag-to-span ratio, the energy-conserving scheme and the Newmark method yield nearly identical results, while in the case of cables with a large sag-to-span ratio, for which the Newmark time integrator diverges, the new scheme gives accurate results and exactly conserves the total energy of the system.

The proposed formulations are also validated under viscoelastic material response. In the case of small viscoelastic strains, the new element behaves robustly and gives excellent results. A new finite viscoelastic material model is formulated for large viscoelastic strains,

and results show that it reduces to the infinitesimal model when small deformations are considered. Simple benchmark problems involving the free vibration and the earthquake response of simply-supported cables demonstrate that small relaxation times can reproduce the internal physical mechanisms that dissipate the high-frequency waves in the axial force field, while long relaxation times account for the decay of the dynamic response.

The study concludes with the structural analysis of three-dimensional cable nets using the proposed 3d mixed cable elements. First, numerical joints are introduced to accommodate the discontinuities in the axial force field that appear in physical cable joints. These complex structures show excellent results for displacements and axial forces. For available experimental results, the proposed formulations give the smallest relative error compared to other models in the literature.

To Anna, Anselm, Maria Teresa and Mireia.

Contents

List of Figures

List of Tables

Acknowledgments

First and foremost, I would like to express my gratitude to my advisors, Prof. Filip C. Filippou and Prof. Robert L. Taylor, for their outstanding guidance during the course of my doctoral degree. They have continuously challenged me with new goals and new problems, and their encouragement and patience has motivated me since the very beginning.

I would also like to thank Prof. Khalid M. Mosalam and Prof. Panayiotis Papadopoulos for being part of my dissertation committee and of my qualifying examination, as well as Prof. Jon Wilkening for representing my math minor in the latter examination. I am also thankful to Prof. Anil K. Chopra for being my academic advisor during the first years of my Berkeley education.

My research has also benefited from the knowledge of Prof. James Casey, Prof. Francisco Armero and Prof. Sanjay Govindjee from UC Berkeley, as well as of Prof. Ángel C. Aparicio from the Universitat Politècnica de Catalunya.

I would also like to thank La Caixa Foundation for the fellowship that allowed me to come to the United States, and the Department of Civil and Environmental Engineering and the Department of Mathematics for giving me the opportunity of being an instructor in this outstanding university.

I am also thankful to all my friends, including those who have supported me from overseas and those who I have met during my stay in Berkeley. They have made me feel 'home away from home' and have turned my American adventure into a memorable experience in all possible aspects.

My deepest gratitude goes to my family. They have made me who I am today, and have supported me regardless of any outcome or achievement. Without their inconditional love and support, I would have never succeeded. I dedicate all my accomplishments to them.

Chapter 1
Introduction

1.1 Motivation

Structural engineering used to rely on the empirical knowledge and mastery of its practitioners until the late XIX century. However, scientific developments during the XX century have resulted in sophisticated mathematical tools for understanding and designing structures that are reliable, safe and aesthetic. The thorough evaluation of limit states under extreme loads such as earthquakes, or the determination of the ultimate capacity of structures are mandatory steps in today's performance-based design guidelines, and hence precise nonlinear structural analyses are expected in the professional practice of structural engineers.

(a) Seri Wawasan bridge, Malaysia (b) BC Place Stadium, Canada

Figure 1.1: Cable structures.

Among all structural typologies, cable structures have been widely used in engineering applications because they offer the advantages of high ultimate strength, flexibility, light weight and prestressing capabilities, among others. Cable-stayed bridges like the Seri

Wawasan bridge in Fig. 1.1(a) or prestressed roofs such as the dome of the BC Place Stadium in Fig. 1.1(b) have become iconic examples of the XXI-century civil engineering practice.

Since the behavior of flexible cables under large displacements is highly nonlinear, significant effort has been invested into developing accurate, robust and computationally efficient models for them. These models have evolved from the initial truss elements, developed in the early 1960s, to the recent elastic elements satisfying the catenary equation.

The simplest approach involves the representation of the cable as a series of straight truss elements, usually based on linear displacement interpolation functions in the context of infinitesimal-deformation theory. The geometric nonlinearity is then accounted for with the corotational formulation, involving the transformation of the node kinematic variables under large displacements. These elements suffer from the excessive mesh refinement required to accurately capture the deformed shape and the axial force distribution and may exhibit snap-through instabilities at states with nearly-singular stiffness. To address these limitations, catenary elements have been proposed. These elements formulate the global balance of linear momentum assuming one-dimensional infinitesimal linear elasticity (Hooke's law) and obtain the deformed shape of the cable by explicit integration. Some authors have also proposed a finite-difference version of this catenary formulation by discretizing the global balance of linear momentum into n segments.

While catenary formulations give more accurate results than truss elements for the same mesh discretization, they also have shortcomings that limit their range of application. Current catenary elements do not support extension to finite deformations and nonlinear material behavior, and thus do not distinguish between the 2nd Piola-Kirchhoff and the Cauchy representations of the axial force. In the dynamic case, catenary elements cannot accommodate a consistent mass matrix and hence very fine meshes are required to obtain accurate results. The assumption of infinitesimal deformations in both element types results in the inaccurate balance of linear momentum in the deformed configuration, for which the distributed loads do not evolve consistently.

For the nonlinear dynamic response of elastic cable structures, an additional challenge arises in the development of accurate and consistent time integration algorithms. While classical time integrators such as the Newmark method and the HHT-α method have been widely used in the dynamic analysis of cable structures, it is well-documented that they do not preserve the Hamiltonian structure of nonlinear elastodynamics. While this limitation does not affect the accuracy of the results for cables with a small sag-to-span ratio, it significantly affects the response of those with a large sag-to-span ratio, and may even provoke the divergence of the numerical solution. For this reason, energy-momentum conserving algorithms, which provide a consistent time integration of the governing equations, have been proposed for single-field elastodynamic problems. The limitations of classical time integration schemes also pose restrictions on the dynamic analysis of cable structures with rate-dependent inelastic material models. In this case, rheological models under small deformations are typically assumed, and thus inaccurate results are obtained for cables with a large sag-to-span ratio.

1.2 Objectives and scope

To address the above-mentioned limitations of truss and catenary elements, this study proposes a new formulation for a family of cable finite elements with the following objectives:

- Use finite-deformation theory to describe the geometric nonlinearity.
- Solve the balance of linear momentum consistently.
- Accommodate nonlinear elastic and inelastic material response.
- Accommodate jumps in the axial force distribution to simulate cable joints.
- Develop a robust and versatile finite element implementation to allow its deployment in a general purpose finite element analysis framework.

The developments focus on a two-field mixed variational formulation that satisfies the equilibrium equation and the strain-displacement relation in the weak sense, and offer two numerical implementations that correspond to a cable finite element with a continuous axial force distribution and another one with a discontinuous axial force distribution.

Considering the new cable formulation, this dissertation studies the dynamic analysis of cable structures with the following objectives:

- Determine the accuracy and range of application of existing time integration schemes when the proposed mixed cable elements are used.
- Formulate a new energy-momentum conserving algorithm that preserves the Hamiltonian structure of the mixed two-field catenary problem for any nonlinear elastic complementary energy under nonlinear geometry.
- Assess the high-frequency contributions that appear in the dynamic response of cables, and propose a filtering process to physically address them.
- Deploy the new time integration scheme in dissipative systems using existing damping and rheological models for cables with small deformations.
- Formulate a new finite viscoelastic material model that gives accurate results for cables undergoing large deformations.

To conclude the study, this dissertation analyzes three-dimensional cable structures with the proposed formulations and compares the results with other models in the literature and with available experimental results.

1.3 Dissertation outline

This dissertation is organized in seven chapters that correspond to three global parts: the formulation of the mixed cable element, its validation under different material models, and the analysis of three-dimensional cable structures.

The discussion begins in Chapter 2 with the preliminary concepts that are required for the developments of the dissertation, and continues with a brief summary of existing formulations for cables, which are later used in the assessment of the new cable finite element. Chapter 3 presents the derivation of the new cable element for a general material model and gives its implementation for the Newmark and the HHT-α methods. The new energy-momentum conserving algorithm in complementary space is presented in the same chapter, and its desired conserving properties are proved. A Savitzky-Golay filter is proposed to address the high-frequency contributions that may appear in the axial force time history. Chapter 4 evaluates the response of the proposed mixed cable element and the energy-momentum conserving algorithm under nonlinear elastic material behavior, and compares the results with those given by existing formulations. Chapter 5 begins with the assessment of the proposed formulations under incrementally-infinitesimal viscoelastic material models, and proceeds to derive a new finite viscoelastic material model for cables under large deformations. Chapter 6 uses the new cable finite element and time integration scheme for the static and dynamic analysis of three-dimensional cable structures, and compares the results with experiments, if available, and other models in the literature. Finally, Chapter 7 provides a summary of the dissertation and offers conclusions and directions for further study.

Chapter 2
Preliminaries and literature review

This chapter presents the mathematical and engineering preliminaries that are necessary for the developments in this dissertation, together with a brief description of the most relevant cable models from the literature.

The discussion begins with the mathematics of curvilinear coordinates and differential geometry, and gives special emphasis on how to operate with tensors in these bases. Curvilinear coordinates are then used to formulate the governing equations of solid mechanics. The literature review presents a summary of the most relevant cable finite elements: truss elements and catenary elements. Geometrically-exact rods are also included at the end of the discussion for their relevance in the formulation developed in this dissertation.

2.1 Preliminaries

The preliminary concepts in the following sections are grouped into two categories: the mathematical tools, which include differential geometry and tensor analysis, and the engineering equations of solid mechanics under curved geometries, which include the formulation of kinematics and the principle of virtual work.

2.1.1 Differential geometry and tensor analysis

Consider the three-dimensional Euclidean space $\mathbb{R}^3$ with the Cartesian coordinate system $\{\mathbf{e}_i\}_{i=1}^3$ defining an orthogonal grid of coordinate lines (x^1, x^2, x^3). At each point $\mathbf{x} \in \mathbb{R}^3$, define a new set of curvilinear coordinate lines $(\theta^1, \theta^2, \theta^3)$ associated with the curvilinear coordinate system $\{\mathbf{g}_i\}_{i=1}^3$, as shown in Fig. 2.1.

The vectors of the new basis $\{\mathbf{g}_i\}_{i=1}^3$ are defined by

$$\mathbf{g}_i = \frac{\partial \mathbf{x}}{\partial \theta^i} = \frac{\partial (x^j \mathbf{e}_j)}{\partial \theta^i} = \frac{\partial x^j}{\partial \theta^i} \mathbf{e}_j \tag{2.1}$$

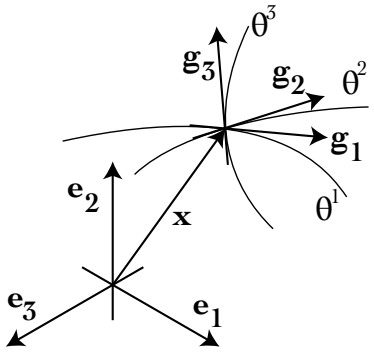

Figure 2.1: Cartesian and curvilinear coordinate systems at a point $\mathbf{x} \in \mathbb{R}^3$.

where the Einstein summation convention is assumed. Equation 2.1 defines a change of basis provided that the frames $\{\mathbf{e}_i\}_{i=1}^3$ and $\{\mathbf{g}_i\}_{i=1}^3$ have the same orientation and that the inverse $\partial\theta^i/\partial x^j$ exists, which is guaranteed by the condition

$$\det\left(\frac{\partial x^j}{\partial \theta^i}\right) \neq 0 \tag{2.2}$$

The differential of length ds at any point $\mathbf{x} \in \mathbb{R}^3$ is given by

$$ds^2 = d\mathbf{x} \cdot d\mathbf{x} = d\theta^i \mathbf{g}_i \cdot d\theta^j \mathbf{g}_j = g_{ij} d\theta^i d\theta^j \tag{2.3}$$

where g_{ij} is the metric tensor associated with the curvilinear coordinate system $\{\mathbf{g}_i\}_{i=1}^3$. It is relevant to observe that, for the Cartesian coordinate system $\{\mathbf{e}_i\}_{i=1}^3$, $ds^2 = \delta_{ij} dx^i dx^j$ with δ_{ij} the Kronecker delta, giving the well-known expression for distances

$$ds^2 = (dx^1)^2 + (dx^2)^2 + (dx^3)^2 \tag{2.4}$$

Equation 2.4 is no longer valid in general curvilinear coordinates. Spaces[1] for which Eq. 2.3 holds, and therefore a metric exists locally, are called *Riemannian spaces*.

The differential of area da at any point $\mathbf{x} \in \mathbb{R}^3$ is given by the cross product between two differential vectors $d\mathbf{x}$ and $d\mathbf{y}$

$$\mathbf{n} da = d\mathbf{x} \times d\mathbf{y} = \mathbf{g}_i \times \mathbf{g}_j \, d\theta^i d\theta^j \tag{2.5}$$

where $\mathbf{n}$ is the unit normal vector to the surface defined by $d\mathbf{x}$ and $d\mathbf{y}$. The differential of volume dv at any point $\mathbf{x} \in \mathbb{R}^3$ is given by the box product

$$dv = d\theta^1 d\theta^2 d\theta^3 \mathbf{g}_1 \cdot (\mathbf{g}_2 \times \mathbf{g}_3) = \sqrt{\det(g_{ij})}\, d\theta^1 d\theta^2 d\theta^3 \tag{2.6}$$

[1]Mathematically speaking, a *Riemannian space* requires the structure of a differentiable manifold, the details of which are outside the scope of this chapter. The interested reader is referred to Ref. [7].

A vector that is represented in the basis $\{\mathbf{g}_i\}_{i=1}^3$ is said to have *contravariant components* $\{\theta^i\}_{i=1}^3$. The *dual basis* or *reciprocal basis* $\{\mathbf{g}^i\}_{i=1}^3$, with *covariant components* $\{\theta_i\}_{i=1}^3$, satisfies

$$\mathbf{g}_i \cdot \mathbf{g}^j = \delta_i^j \tag{2.7}$$

Therefore, it follows that the dual basis of the Cartesian frame $\{\mathbf{e}_i\}_{i=1}^3$ is itself. As a result, a vector $\mathbf{v} \in \mathbb{R}^3$, or tensor of order 1, can be represented in both contravariant and covariant coordinates in the form

$$\mathbf{v} = v^i \mathbf{g}_i = v_i \mathbf{g}^i \tag{2.8}$$

with $v_i = \mathbf{v} \cdot \mathbf{g}_i$ and $v^i = \mathbf{v} \cdot \mathbf{g}^i$. The relation between the two coordinates is given by

$$\begin{aligned} v_j &= \mathbf{v} \cdot \mathbf{g}_j = v^i \mathbf{g}_i \cdot \mathbf{g}_j = g_{ij} v^i \\ v^j &= \mathbf{v} \cdot \mathbf{g}^j = v_i \mathbf{g}^i \cdot \mathbf{g}^j = g^{ij} v_i \end{aligned} \tag{2.9}$$

where g^{ij} is the dual metric tensor. The special case of orthogonal curvilinear coordinates is relevant for the formulations proposed in subsequent chapters. In this case, the metric tensor g_{ij} is diagonal because $\mathbf{g}_i \cdot \mathbf{g}_j = 0$ for $i \neq j$, and

$$v_i = g_{ii} v^i \quad ; \quad v^i = g^{ii} v_i \quad \text{for} \quad i \in \{1, 2, 3\} \tag{2.10}$$

with no summation implied. As a result, the metric tensor and its dual tensor for orthogonal curvilinear coordinates have the form

$$g^{ii} = g_{ii}^{-1} \quad \text{for} \quad i \in \{1, 2, 3\} \quad \text{and} \quad g^{ij} = g_{ij} = 0 \quad \text{for} \quad i \neq j \tag{2.11}$$

A tensor $\mathbf{T}$ of order 2 has four possible representations in contravariant and covariant components,

$$\mathbf{T} = T^{ij} \mathbf{g}_i \otimes \mathbf{g}_j = T_{ij} \mathbf{g}^i \otimes \mathbf{g}^j = T_i^{\cdot j} \mathbf{g}^i \otimes \mathbf{g}_j = T_{\cdot j}^i \mathbf{g}_i \otimes \mathbf{g}^j \tag{2.12}$$

where $\otimes$ represents the outer product in $\mathbb{R}^3$. The components are obtained by the usual projections, for instance,

$$T_{ij} = \mathbf{g}_i \cdot \mathbf{T} \mathbf{g}_j \quad \text{or} \quad T_i^{\cdot j} = \mathbf{g}_i \cdot \mathbf{T} \mathbf{g}^j \tag{2.13}$$

These projections can be used to note that the 2nd order identity tensor $\mathbf{I}$ has the following representations in curvilinear coordinates

$$\mathbf{I} = g_{ij} \mathbf{g}^i \otimes \mathbf{g}^j = g^{ij} \mathbf{g}_i \otimes \mathbf{g}_j = \delta_j^i \mathbf{g}_i \otimes \mathbf{g}^j = \delta_i^j \mathbf{g}^i \otimes \mathbf{g}_j = \mathbf{g}_i \otimes \mathbf{g}^i = \mathbf{g}^i \otimes \mathbf{g}_i \tag{2.14}$$

The transpose of a 2nd order tensor $\mathbf{T}$, represented by $\mathbf{T}^t$, is defined by

$$\mathbf{T}\mathbf{a} \cdot \mathbf{b} = \mathbf{a} \cdot \mathbf{T}^t \mathbf{b} \quad \forall \mathbf{a}, \mathbf{b} \in \mathbb{R}^3 \tag{2.15}$$

In the contravariant components $\mathbf{T} = T^{ij} \mathbf{g}_i \otimes \mathbf{g}_j$, Eq. 2.15 implies that

$$(T^{ij} \mathbf{g}_i \otimes \mathbf{g}_j)(a_k \mathbf{g}^k)(b_l \mathbf{g}^l) = T^{ij} a_j b_i = (a_k \mathbf{g}^k) \cdot \mathbf{T}^t (b_l \mathbf{g}^l) \implies \mathbf{T}^t = T^{ij} \mathbf{g}_j \otimes \mathbf{g}_i \tag{2.16}$$

The inverse of a 2nd order tensor $\mathbf{T}$, represented by $\mathbf{T}^{-1}$, is defined by

$$\mathbf{T}\mathbf{T}^{-1} = \mathbf{I} \tag{2.17}$$

In the contravariant components $\mathbf{T} = T^{ij}\mathbf{g}_i \otimes \mathbf{g}_j$, Eq. 2.17 implies that

$$(T^{ij}\mathbf{g}_i \otimes \mathbf{g}_j)\mathbf{T}^{-1} = \delta^j_i \mathbf{g}_i \otimes \mathbf{g}_j \implies \mathbf{T}^{-1} = T_{ij}\mathbf{g}^j \otimes \mathbf{g}^i \tag{2.18}$$

The extension to 4th order tensors comes naturally from the previous discussion. In particular, the 4th order identity tensor $\mathbb{I}$, for which $\mathbb{I}\mathbf{T} = \mathbf{T}$, has the representation

$$\mathbb{I} = \delta^k_i \delta^l_j \mathbf{g}^i \otimes \mathbf{g}^j \otimes \mathbf{g}_k \otimes \mathbf{g}_l = \mathbf{g}^i \otimes \mathbf{g}^j \otimes \mathbf{g}_i \otimes \mathbf{g}_j \tag{2.19}$$

2.1.2 Solid mechanics in curved geometries

The following preliminaries regarding solid mechanics in curved geometries are structured into three sections: finite kinematics in curvilinear coordinates, Lie dragging and balance laws.

2.1.2.1 Finite kinematics in curvilinear coordinates

Let a body $\mathcal{B}$ undergo a motion $\boldsymbol{\chi}_t$ from a reference configuration $\mathcal{P}_0$ to a current configuration $\mathcal{P}_t$ at time $t \in \mathcal{I}$, as shown in Fig. 2.2, and denote the reference and current positions vectors by $\mathbf{X}$ and $\mathbf{x} = \boldsymbol{\chi}_t(\mathbf{X})$, respectively. Let upper case letters denote variables in the reference configuration and lower case letters, variables in the current configuration. In the global Cartesian coordinates systems $\{\mathbf{E}_i\}_{i=1}^3$ and $\{\mathbf{e}_i\}_{i=1}^3$ for the reference and current configurations, respectively, the components of the position vectors are given by

$$\mathbf{X} = X^i\mathbf{E}_i = X_i\mathbf{E}_i \quad \text{and} \quad \mathbf{x} = x^i\mathbf{e}_i = x_i\mathbf{e}_i \tag{2.20}$$

For simplicity, let the basis in the reference configuration coincide with the basis in the current configuration, $\{\mathbf{E}_i\}_{i=1}^3 \equiv \{\mathbf{e}_i\}_{i=1}^3$.

A set of curvilinear coordinates $\{\theta^i\}_{i=1}^3$ with basis vectors $\{\mathbf{G}_i\}_{i=1}^3$ can be defined in the reference configuration by

$$\mathbf{G}_i = \frac{\partial \mathbf{X}}{\partial \theta^i} = \frac{\partial X^k}{\partial \theta^i}\mathbf{E}_k \tag{2.21}$$

These reference basis vectors $\{\mathbf{G}_i\}_{i=1}^3$ are convected by the motion $\boldsymbol{\chi}_t$ to the current basis vectors $\{\mathbf{g}_i\}_{i=1}^3$

$$\mathbf{g}_i = \boldsymbol{\chi}_t(\mathbf{G}_i) = \boldsymbol{\chi}_t\left(\frac{\partial \mathbf{X}}{\partial \theta^i}\right) = \frac{\partial \mathbf{x}}{\partial \theta^i} = \frac{\partial x^k}{\partial \theta^i}\mathbf{e}_k \tag{2.22}$$

The deformation gradient $\mathbf{F}$ of the motion $\boldsymbol{\chi}_t$ in the Cartesian coordinate system is given by

$$\mathbf{F} = \frac{\partial \mathbf{x}}{\partial \mathbf{X}} = \frac{\partial x^i}{\partial X^j}\mathbf{e}_i \otimes \mathbf{E}^j \tag{2.23}$$

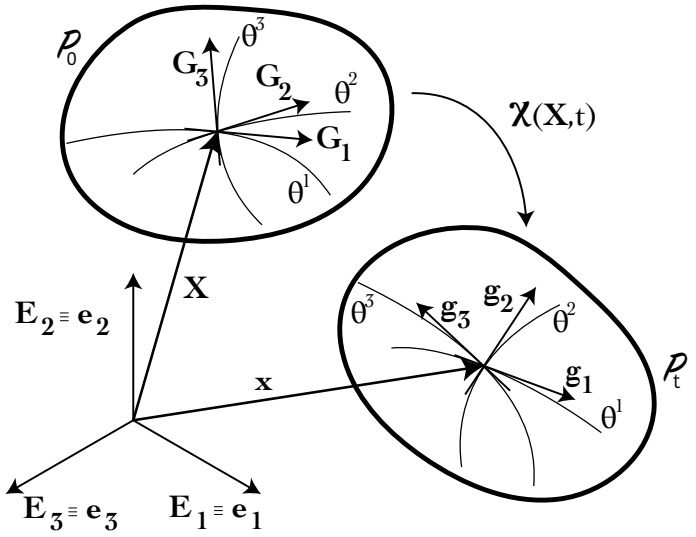

Figure 2.2: Motion $\mathbf{x} = \boldsymbol{\chi}(\mathbf{X}, t)$ of the body $\mathcal{B}$.

Therefore,

$$\mathbf{F}\mathbf{G}_i = \left(\frac{\partial x^k}{\partial X^l}\mathbf{e}_k \otimes \mathbf{E}^l\right)\frac{\partial X_j}{\partial \theta^i}\mathbf{E}_j = \frac{\partial x^k}{\partial X^j}\frac{\partial X^j}{\partial \theta^i}\mathbf{e}_k = \mathbf{g}_i \tag{2.24}$$

and the deformation gradient $\mathbf{F}$ in curvilinear coordinates has the form

$$\mathbf{F} = \mathbf{F}\mathbf{I} = \mathbf{F}\left(\mathbf{G}_i \otimes \mathbf{G}^i\right) = \mathbf{g}_i \otimes \mathbf{G}^i \tag{2.25}$$

The left Cauchy-Green tensor $\mathbf{b}$ and the right Cauchy-Green tensor $\mathbf{C}$ have the form

$$\begin{aligned} \mathbf{b} &= \mathbf{F}\mathbf{F}^t = \left(\mathbf{g}_i \otimes \mathbf{G}^i\right)\left(\mathbf{G}^j \otimes \mathbf{g}_j\right) = G^{ij}\mathbf{g}_i \otimes \mathbf{g}_j \\ \mathbf{C} &= \mathbf{F}^t\mathbf{F} = \left(\mathbf{G}^i \otimes \mathbf{g}_i\right)\left(\mathbf{g}_j \otimes \mathbf{G}^j\right) = g_{ij}\mathbf{G}^i \otimes \mathbf{G}^j \end{aligned} \tag{2.26}$$

while the Green-Lagrange strain tensor $\mathbf{E}$ is expressed by

$$\mathbf{E} = \frac{1}{2}\left(\mathbf{C} - \mathbf{I}\right) = \frac{1}{2}\left(g_{ij} - G_{ij}\right)\mathbf{G}^i \otimes \mathbf{G}^j \tag{2.27}$$

The differential of length ds in the current configuration is given by

$$ds^2 = d\mathbf{x} \cdot d\mathbf{x} = \mathbf{F}d\mathbf{X} \cdot \mathbf{F}d\mathbf{X} = d\mathbf{X} \cdot \mathbf{C}d\mathbf{X} = g_{ij}d\theta^i d\theta^j \tag{2.28}$$

while the differential of volume dv in the current configuration is given by

$$\begin{aligned} dv &= \mathbf{g}_1 \cdot (\mathbf{g}_2 \times \mathbf{g}_3)d\theta^1 d\theta^2 d\theta^3 = \mathbf{F}\mathbf{G}_1 \cdot (\mathbf{F}\mathbf{G}_2 \times \mathbf{F}\mathbf{G}_3)d\theta^1 d\theta^2 d\theta^3 \\ &= \underbrace{(\det \mathbf{F})}_{J}\underbrace{\sqrt{\det(G_{ij})}d\theta^1 d\theta^2 d\theta^3}_{dV} = JdV \end{aligned} \tag{2.29}$$

where $J = \det \mathbf{F}$ is the determinant of the deformation gradient. The differential of area da in the current configuration follows from

$$dv = d\mathbf{a} \cdot d\mathbf{l} = \mathbf{n}da \cdot \mathbf{F}d\mathbf{L} = JdV = Jd\mathbf{A} \cdot d\mathbf{L} \implies \mathbf{n}da = J\mathbf{F}^{-t}\mathbf{N}dA \tag{2.30}$$

where $\mathbf{n}$ and $\mathbf{N}$ are the unit normal vectors to the surfaces in the current and reference configurations respectively, and $d\mathbf{l}$ and $d\mathbf{L}$ are arbitrary differential vectors.

The displacement vector $\mathbf{u}$ is defined by

$$\mathbf{u} = \mathbf{x} - \mathbf{X} \tag{2.31}$$

As a result, the reference gradient $\mathbf{H}$ of the displacement field follows from the derivative

$$\frac{\partial \mathbf{u}}{\partial \theta^i} = \frac{\partial \mathbf{x}}{\partial \theta^i} - \frac{\partial \mathbf{X}}{\partial \theta^i} = \mathbf{g}_i - \mathbf{G}_i = (\mathbf{F} - \mathbf{I})\,\mathbf{G}_i = \mathbf{H}\mathbf{G}_i \tag{2.32}$$

in the form

$$\mathbf{H} = \mathbf{H}\mathbf{I} = \mathbf{H}\left(\mathbf{G}_i \otimes \mathbf{G}^i\right) = \frac{\partial \mathbf{u}}{\partial \theta^i} \otimes \mathbf{G}^i \tag{2.33}$$

The relation between the reference displacement gradient and the Green-Lagrange strain is

$$\mathbf{E} = \frac{1}{2}\left(\mathbf{H} + \mathbf{H}^t + \mathbf{H}^t\mathbf{H}\right) = \frac{1}{2}\left(\frac{\partial \mathbf{u}}{\partial \theta^i} \otimes \mathbf{G}^i + \mathbf{G}^i \otimes \frac{\partial \mathbf{u}}{\partial \theta^i} + \left(\frac{\partial \mathbf{u}}{\partial \theta^i} \cdot \frac{\partial \mathbf{u}}{\partial \theta^j}\right)\mathbf{G}^i \otimes \mathbf{G}^j\right) \tag{2.34}$$

Equation 2.34 is also known as the compatibility equation or the strain-displacement relation.

2.1.2.2 Lie dragging

With the aim of taking derivatives and formulating objective rate equations, tensors are often *pulled back* from the current configuration to the reference configuration or *pushed forward* from the reference configuration to the current configuration. These operations are referred to as *Lie dragging*.

A 2nd order tensor $\mathbf{a}$ living in the current configuration can be pulled back $\boldsymbol{\chi}_*$ from the current configuration to the reference configuration with

$$\boldsymbol{\chi}_*(\mathbf{a}) = \mathbf{F}^{-1}\mathbf{a}\mathbf{F}^{-t} = \mathbf{F}^{-1}(a^{ij}\mathbf{g}_i \otimes \mathbf{g}_j)\mathbf{F}^{-t} = a^{ij}\mathbf{G}_i \otimes \mathbf{G}_j \tag{2.35}$$

while a 2nd order tensor $\mathbf{B}$ living in the reference configuration can be pushed forward $\boldsymbol{\chi}^*$ from the reference configuration to the current configuration with

$$\boldsymbol{\chi}^*(\mathbf{B}) = \mathbf{F}\mathbf{B}\mathbf{F}^t = \mathbf{F}(B^{ij}\mathbf{G}_i \otimes \mathbf{G}_j)\mathbf{F}^t = B^{ij}\mathbf{g}_i \otimes \mathbf{g}_j \tag{2.36}$$

In the process of Lie dragging, the components of the tensors do not change, and only the basis vectors are dragged.

The time derivative of a tensor $\mathbf{a}$ living in the current configuration is given by

$$\dot{\mathbf{a}} = \frac{d\mathbf{a}}{dt} = \frac{d(a^{ij}\mathbf{g}_i \otimes \mathbf{g}_j)}{dt} = \dot{a}^{ij}\mathbf{g}_i \otimes \mathbf{g}_j + a^{ij}\dot{\mathbf{g}}_i \otimes \mathbf{g}_j + a^{ij}\mathbf{g}_i \otimes \dot{\mathbf{g}}_j \tag{2.37}$$

noting that

$$\dot{a}^{ij}\mathbf{g}_i \otimes \mathbf{g}_j = \boldsymbol{\chi}^* \left(\frac{d}{dt}\boldsymbol{\chi}_*(\mathbf{a}) \right) \tag{2.38}$$

This term is called the *Lie derivative* $\mathcal{L}_v\mathbf{a}$ of the tensor $\mathbf{a}$,

$$\mathcal{L}_v\mathbf{a} = \boldsymbol{\chi}^* \left(\frac{d}{dt}\boldsymbol{\chi}_*(\mathbf{a}) \right) \tag{2.39}$$

and is therefore objective under superimposed rigid body motions. For this reason, objective rate equations for finite plasticity and finite viscoelasticity are often written in terms of the Lie derivative instead of in terms of the total time derivative.

2.1.2.3 Balance laws

Balance laws need to be established for finding solutions to the mechanical problem. Under Cauchy's tetrahedron argument [34], there exists a stress tensor $\boldsymbol{\sigma}$ living in the current configuration, called the Cauchy stress tensor, such that

$$\mathbf{t} = \lim_{\Delta a \to 0} \frac{\Delta \mathbf{f}}{\Delta a} = \boldsymbol{\sigma}\mathbf{n} \tag{2.40}$$

where $\Delta\mathbf{f}$ is the current total force acting on the current area Δa and $\mathbf{t}$ is the traction vector acting on the plane with normal vector $\mathbf{n}$. Defining the linear momentum $\mathbf{L}$ with

$$\mathbf{L} = \int_{\mathcal{P}_t} \rho\mathbf{v}\, dv \tag{2.41}$$

the balance of linear momentum gives

$$\dot{\mathbf{L}} = \frac{d}{dt}\int_{\mathcal{P}_t} \rho\mathbf{v}\, dv = \int_{\mathcal{P}_t} \rho\mathbf{b}\, dv + \int_{\partial\mathcal{P}_t} \mathbf{t}\, da \tag{2.42}$$

where ρ is the density in the current configuration, $\mathbf{v}$ is the velocity field, $\mathbf{b}$ are the body forces per unit mass and $\partial\mathcal{P}_t$ is the boundary of the current configuration $\mathcal{P}_t$. Using the divergence and localization theorems, and applying boundary conditions, gives the strong form of the mechanical boundary value problem

$$\begin{cases} \operatorname{div}\boldsymbol{\sigma} + \rho\mathbf{b} = \rho\mathbf{a} \ \text{ in } \ \mathcal{P}_t \times \mathcal{I} \\ \mathbf{u} = \bar{\mathbf{u}} \ \text{ on } \ \Gamma_u \times \mathcal{I} \\ \boldsymbol{\sigma}\mathbf{n} = \bar{\mathbf{t}} \ \text{ on } \ \Gamma_t \times \mathcal{I} \\ \mathbf{u} = \mathbf{u}_0 \ ; \ \mathbf{v} = \mathbf{v}_0 \ \text{ in } \ \mathcal{P}_t \times \{t = 0\} \end{cases} \tag{2.43}$$

where $\mathbf{a}$ is the acceleration field, $\operatorname{div}(\cdot)$ is the divergence operator in the current configuration, Γ_u is the boundary of the current configuration where displacements are imposed, Γ_t is the boundary of the current configuration where tractions are imposed, $\bar{\mathbf{u}}$ and $\bar{\mathbf{t}}$ are imposed displacements and tractions, respectively, and $\mathbf{u}_0$ and $\mathbf{v}_0$ are initial displacements and velocities, respectively.

Different stress measures are used to obtain alternative but equivalent expressions for the balance of linear momentum in Eq. 2.43. The first Piola-Kirchhoff (1st PK) stress tensor $\mathbf{P}$ is obtained by pulling back the current differential area da to the reference configuration in the form

$$\mathbf{t}da = \boldsymbol{\sigma}\mathbf{n}\,da = \underbrace{\boldsymbol{\sigma}J\mathbf{F}^{-t}}_{\mathbf{P}}\mathbf{N}\,dA = \mathbf{P}\mathbf{N}\,dA = \mathbf{T}\,dA \tag{2.44}$$

As a result, the 1st PK stress tensor $\mathbf{P}$ gives the current force per unit reference area. Including the first Piola-Kirchhoff stress tensor $\mathbf{P}$ into the balance of linear momentum results in

$$\begin{cases} \operatorname{Div}\mathbf{P} + \rho_0\mathbf{b} = \rho_0\mathbf{a} \ \text{ in } \ \mathcal{P}_0 \times \mathcal{I} \\ \mathbf{u} = \bar{\mathbf{u}} \ \text{ on } \ \Gamma_U \times \mathcal{I} \\ \mathbf{P}\mathbf{N} = \bar{\mathbf{T}} \ \text{ on } \ \Gamma_T \times \mathcal{I} \\ \mathbf{u} = \mathbf{u}_0 \ ; \ \mathbf{v} = \mathbf{v}_0 \ \text{ in } \ \mathcal{P}_0 \times \{t = 0\} \end{cases} \tag{2.45}$$

where ρ_0 is the reference density and $\operatorname{Div}(\cdot)$ is the divergence operator in the reference configuration. In this case, Γ_U and Γ_T are the boundaries of the reference configuration where displacements and tractions, respectively, are imposed.

The second Piola-Kirchhoff (2nd PK) stress tensor $\mathbf{S}$ pulls back the first index of the first Piola-Kirchhoff stress tensor to the reference configuration, and thus represents the reference force per unit reference area

$$\mathbf{S} = \mathbf{F}^{-1}\mathbf{P} = J\mathbf{F}^{-1}\boldsymbol{\sigma}\mathbf{F}^{-t} = \boldsymbol{\chi}_*(J\boldsymbol{\sigma}) \tag{2.46}$$

In this relation, one identifies the Kirchhoff stress $\boldsymbol{\tau} = J\boldsymbol{\sigma}$ as the push-forward of the 2nd PK stress tensor $\mathbf{S}$ to the current configuration

$$\boldsymbol{\tau} = \boldsymbol{\chi}^*(\mathbf{S}) \tag{2.47}$$

Equations 2.46 and 2.47 give the relations between the contravariant components of the 2nd PK, Cauchy and Kirchhoff stress tensors in the form

$$S^{ij} = J\sigma^{ij} = \tau^{ij} \tag{2.48}$$

For any test function $\boldsymbol{\eta} \in \mathcal{V}$, where $\mathcal{V}$ is the space of test functions,

$$\mathcal{V} = \{\boldsymbol{\eta} : \mathcal{P}_0 \to \mathbb{R}^3 \mid \boldsymbol{\eta} = \mathbf{0} \text{ on } \Gamma_u\} \tag{2.49}$$

it holds that

$$\int_{\mathcal{P}_0} \boldsymbol{\eta} \cdot (\operatorname{Div}\mathbf{P} - \rho_0\mathbf{b} - \rho_0\mathbf{a})\,dV + \int_{\Gamma_T} \boldsymbol{\eta} \cdot (\mathbf{P}\mathbf{N} - \bar{\mathbf{T}})\,dA = 0 \tag{2.50}$$

Applying the divergence theorem to Eq. 2.50 gives the *Principle of Virtual Work* in finite deformations

$$\int_{\mathcal{P}_0} \mathbf{P} \cdot \mathrm{Grad}\, \boldsymbol{\eta}\, dV + \int_{\mathcal{P}_0} \boldsymbol{\eta} \cdot \rho_0 \mathbf{a}\, dV = \int_{\mathcal{P}_0} \boldsymbol{\eta} \cdot \rho_0 \mathbf{b}\, dV + \int_{\Gamma_T} \boldsymbol{\eta} \cdot \bar{\mathbf{T}}\, dA \tag{2.51}$$

where $\mathrm{Grad}\,(\cdot)$ is the gradient operator with respect to the reference configuration. The term $\int_{\mathcal{P}_0} \mathbf{P} \cdot \mathrm{Grad}\, \boldsymbol{\eta}\, dV$ on the left-hand side of Eq. 2.51 is known as the *stress divergence term* and can be written in terms of the 2nd PK stress tensor,

$$\int_{\mathcal{P}_0} \mathbf{FS} \cdot \mathrm{Grad}\, \boldsymbol{\eta}\, dV = \int_{\mathcal{P}_0} \mathbf{S} \cdot \underbrace{\mathrm{sym}(\mathbf{F}^t \mathrm{Grad}\, \boldsymbol{\eta})}_{\mathbf{E}(\boldsymbol{\eta})}\, dV = \int_{\mathcal{P}_0} \mathbf{S} \cdot \mathbf{E}(\boldsymbol{\eta})\, dV \tag{2.52}$$

where $\mathrm{sym}\,(\mathbf{A})$ is the symmetric part of the tensor $\mathbf{A}$. As a result, the principle of virtual work is written in terms of the 2nd PK stress by

$$\int_{\mathcal{P}_0} \mathbf{S} \cdot \mathbf{E}(\boldsymbol{\eta})\, dV + \int_{\mathcal{P}_0} \boldsymbol{\eta} \cdot \rho_0 \mathbf{a}\, dV = \int_{\mathcal{P}_0} \boldsymbol{\eta} \cdot \rho_0 \mathbf{b}\, dV + \int_{\Gamma_T} \boldsymbol{\eta} \cdot \bar{\mathbf{T}}\, dA \tag{2.53}$$

Equation 2.53 for prismatic bodies under a uniaxial state of stress reduces to

$$\int_{\mathcal{P}_0} N E_{11}(\boldsymbol{\eta})\, dS + \int_{\mathcal{P}_0} \boldsymbol{\eta} \cdot m_0 \mathbf{a}\, dS = \int_{\mathcal{P}_0} \boldsymbol{\eta} \cdot \mathbf{W}\, dS + [\boldsymbol{\eta} \cdot \bar{\mathbf{T}}]_{\Gamma_T} \tag{2.54}$$

where $N = S^{11} A$ is the axial force, $m_0 = \rho_0 A$ is the mass per unit reference length and $\mathbf{W} = \rho_0 A \mathbf{b}$ are the body forces per unit reference length.

2.2 Literature review

The following sections present a literature review of relevant formulations for cables and emphasize their advantages and disadvantages. The review begins with a simple corotational truss element that has been widely used in engineering practice since the 1970s [17, 36, 56]. Afterwards, a brief summary is given for the recent catenary elements that are formulated according to the catenary equation [1, 2, 3, 27, 48, 52, 57]. The review ends with a brief description of geometrically-exact rods and their range of application in cable problems [39, 42, 46].

2.2.1 Corotational truss elements

From the mechanical standpoint, truss elements are defined as straight elements with a cross section that is orthogonal to their axis. Several formulations exist for truss elements, either under small or large deformations, or considering the corotation of their local frame to lump large displacements to the nodes [17, 36, 56]. The model that is presented in this

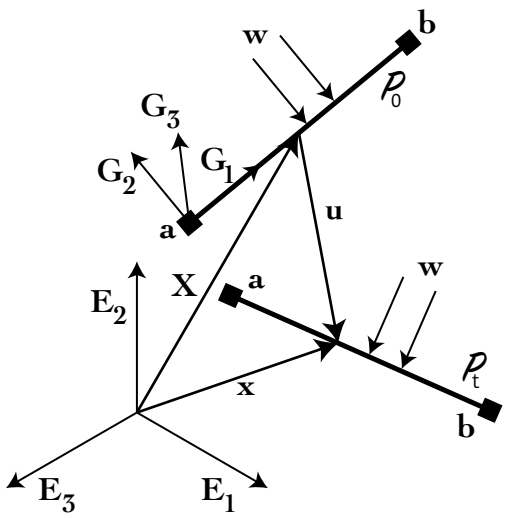

Figure 2.3: Geometric setup for the truss element.

section, and that is used as a comparison in subsequent chapters, uses small deformations and a corotational transformation of the local frame [17].

Figure 2.3 shows the geometric setup for the truss element deforming from a reference configuration $\mathcal{P}_0$ to a current configuration $\mathcal{P}_t$ at time t. In the reference local coordinate system $\{\mathbf{G}_i\}_{i=1}^3$, $\bar{\mathbf{X}}$ and $\bar{\mathbf{x}}$ correspond to the reference and the current position vectors, respectively, with the local displacement field $\bar{\mathbf{u}}$ given by

$$\bar{\mathbf{u}} = \bar{\mathbf{x}} - \bar{\mathbf{X}} \tag{2.55}$$

The local displacements at nodes a and b, $\bar{\mathbf{u}}_a$ and $\bar{\mathbf{u}}_b$, are

$$\bar{\mathbf{u}}_a = \bar{\mathbf{x}}_a - \bar{\mathbf{X}}_a = \bar{u}_1\mathbf{E}_1 + \bar{u}_2\mathbf{E}_2 + \bar{u}_3\mathbf{E}_3 \quad \text{and} \quad \bar{\mathbf{u}}_b = \bar{\mathbf{x}}_b - \bar{\mathbf{X}}_b = \bar{u}_4\mathbf{E}_1 + \bar{u}_5\mathbf{E}_2 + \bar{u}_6\mathbf{E}_3 \tag{2.56}$$

so that the local displacements array $\bar{\mathbf{u}}$ for the truss element has the form

$$\bar{\mathbf{u}}^t = (\bar{\mathbf{u}}_a^t, \bar{\mathbf{u}}_b^t) = (\bar{u}_1, \bar{u}_2, \bar{u}_3, \bar{u}_4, \bar{u}_5, \bar{u}_6) \tag{2.57}$$

Defining the local displacement increment $\Delta\bar{\mathbf{u}}$ with

$$\Delta\bar{\mathbf{u}} = \bar{\mathbf{u}}_b - \bar{\mathbf{u}}_a = \Delta\bar{u}_1\mathbf{E}_1 + \Delta\bar{u}_2\mathbf{E}_2 + \Delta\bar{u}_3\mathbf{E}_3 \tag{2.58}$$

the current length L_n of the element is given by

$$L_n = \sqrt{(L + \Delta\bar{u}_1)^2 + (\Delta\bar{u}_2)^2 + (\Delta\bar{u}_3)^2} \tag{2.59}$$

where L is its reference length. Consequently, the axial deformation v of the truss element under the assumption of small displacements is

$$v = L_n - L = \sqrt{(L + \Delta\bar{u}_1)^2 + (\Delta\bar{u}_2)^2 + (\Delta\bar{u}_3)^2} - L \approx L\left(1 + \frac{\Delta\bar{u}_1}{L}\right) - L = \Delta\bar{u}_1 \quad (2.60)$$

The global displacements at nodes a and b, $\mathbf{u}_a$ and $\mathbf{u}_b$, in the global Cartesian coordinate system $\{\mathbf{E}_i\}_{i=1}^3$ are expressed as a function of the local displacements $\bar{\mathbf{u}}_a$ and $\bar{\mathbf{u}}_b$ by

$$\mathbf{u}_a = \mathbf{Q}\bar{\mathbf{u}}_a \quad \text{and} \quad \mathbf{u}_b = \mathbf{Q}\bar{\mathbf{u}}_b \quad (2.61)$$

where $\mathbf{Q} \in SO(3)$ is the rotation matrix from the local to the global coordinate system, and $SO(3)$ refers to the special orthogonal group in three dimensions. Defining the global element vector $\Delta\mathbf{X}$ in the reference configuration and the global displacement increment $\Delta\mathbf{u}$ in the form

$$\begin{aligned} \Delta\mathbf{X} &= \mathbf{X}_b - \mathbf{X}_a = \Delta X_1\mathbf{E}_1 + \Delta X_2\mathbf{E}_2 + \Delta X_3\mathbf{E}_3 \\ \Delta\mathbf{u} &= \mathbf{u}_b - \mathbf{u}_a = \Delta u_1\mathbf{E}_1 + \Delta u_2\mathbf{E}_2 + \Delta u_3\mathbf{E}_3 \end{aligned} \quad (2.62)$$

the direction cosines $\mathbf{i}$ of the element axis in the deformed configuration are given by

$$\mathbf{i} = \frac{\Delta\mathbf{X} + \Delta\mathbf{u}}{L_n} \quad (2.63)$$

and therefore

$$\begin{aligned} v &\approx \Delta\bar{u}_1 = \bar{u}_4 - \bar{u}_1 = \Delta\mathbf{u}\cdot\mathbf{i} \\ &= \frac{\Delta X_1 + \Delta u_1}{L_n}(u_4 - u_1) + \frac{\Delta X_2 + \Delta u_2}{L_n}(u_5 - u_2) + \frac{\Delta X_3 + \Delta u_3}{L_n}(u_6 - u_3) \end{aligned} \quad (2.64)$$

The equilibrium equation is established in the current configuration $\mathcal{P}_t$ by direct application of the discrete principle of virtual work

$$\begin{aligned} \delta\mathbf{u}^t(\mathbf{p} - \mathbf{p}_0) = (\delta v)n + \delta\mathbf{u}^t\mathbf{m}\mathbf{a} = \delta\mathbf{u}^t\underbrace{\left(\frac{\partial v}{\partial\mathbf{u}}\right)^t}_{\mathbf{a}_g^t} n + \delta\mathbf{u}^t\mathbf{m}\mathbf{a} \\ \Longrightarrow \quad \mathbf{p} - \mathbf{p}_0 = \mathbf{a}_g^t n + \mathbf{m}\mathbf{a} \end{aligned} \quad (2.65)$$

where $\delta\mathbf{u}$ and δv are arbitrary virtual displacements and deformations, respectively, $\mathbf{p}$ are the applied nodal forces, $\mathbf{p}_0$ are the resisting forces corresponding to the element distributed load $\mathbf{w}$, n is the axial force in the element, $\mathbf{m}$ is the mass matrix and $\mathbf{a}$ is the acceleration field. The equilibrium equation gives the explicit form

$$\begin{Bmatrix} p_1 \\ p_2 \\ p_3 \\ p_4 \\ p_5 \\ p_6 \end{Bmatrix} - \frac{1}{2}\begin{Bmatrix} -\mathbf{w}\cdot\mathbf{E}_1 \\ -\mathbf{w}\cdot\mathbf{E}_2 \\ -\mathbf{w}\cdot\mathbf{E}_3 \\ \mathbf{w}\cdot\mathbf{E}_1 \\ \mathbf{w}\cdot\mathbf{E}_2 \\ \mathbf{w}\cdot\mathbf{E}_3 \end{Bmatrix} = \begin{bmatrix} -\Delta X_1 - \Delta u_1 \\ -\Delta X_2 - \Delta u_2 \\ -\Delta X_3 - \Delta u_3 \\ \Delta X_1 + \Delta u_1 \\ \Delta X_2 + \Delta u_2 \\ \Delta X_3 + \Delta u_3 \end{bmatrix} \frac{n}{L_n} + \mathbf{m}\begin{Bmatrix} a_1 \\ a_2 \\ a_3 \\ a_4 \\ a_5 \\ a_6 \end{Bmatrix} \quad (2.66)$$

As a result, this formulation does not distinguish between reference and current stress measures and the axial force n corresponds to the infinitesimal axial force that results from the approximation

$$n = \sigma^{11} A \approx P^{11} A \approx S^{11} A \tag{2.67}$$

where σ^{11}, P^{11} and S^{11} are the axial components of the Cauchy, 1st PK and 2nd PK stress tensors, respectively, as defined in the previous section.

Under the assumption that the external loads do not depend on the displacements, the static tangent stiffness $\mathbf{k}$ for the truss element is given by

$$\mathbf{k} = \underbrace{\mathbf{a}_g^t \frac{\partial n}{\partial v} \mathbf{a}_g}_{\mathbf{k}_m} + \underbrace{\frac{\partial \mathbf{a}_g}{\partial \mathbf{u}} n}_{\mathbf{k}_g} \tag{2.68}$$

where $\mathbf{k}_m$ is the material stiffness of the element and $\mathbf{k}_g$ is its geometric stiffness. The material stiffness $\mathbf{k}_m$ that results from the linear elastic constitutive relation

$$n = \frac{EA}{L_n} v \tag{2.69}$$

has the form

$$\mathbf{k}_m = \frac{EA}{L_n} \begin{bmatrix} \mathbf{T} & -\mathbf{T} \\ -\mathbf{T} & \mathbf{T} \end{bmatrix} \tag{2.70}$$

where $\mathbf{T}$ is the array with components

$$T_{ij} = \left(\frac{\Delta X_i + \Delta u_i}{L_n} \right) \left(\frac{\Delta X_j + \Delta u_j}{L_n} \right) \quad \text{for} \quad i, j \in \{1, 2, 3\} \tag{2.71}$$

The geometric stiffness $\mathbf{k}_g$ has the form

$$\mathbf{k}_g = \frac{n}{L_n} \begin{bmatrix} \mathbf{I}_3 & -\mathbf{I}_3 \\ -\mathbf{I}_3 & \mathbf{I}_3 \end{bmatrix} \tag{2.72}$$

with $\mathbf{I}_3$ being the 3x3 identity tensor.

Truss elements suffer from the excessive mesh refinement required to accurately capture the deformed shape and the axial force distribution, especially because of the constant axial force assumption. Also, because these elements are not specifically formulated as cables, they may exhibit a snap-through instability at states of nearly singular stiffness.

2.2.2 Catenary elements

To address the limitations of simple truss elements, catenary elements were first proposed in the early 2000s [1, 2, 3, 27, 48, 52, 57]. From a mechanical point of view, these elements are defined as curved elements with a cross section that is orthogonal to their axis. Figure

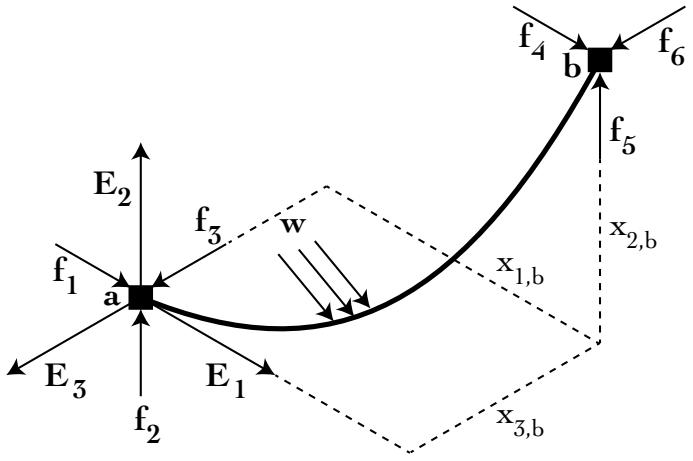

Figure 2.4: Geometric setup for the catenary element.

2.4 shows the deformed shape of the catenary element that is suspended from nodes a and b with current coordinates $\mathbf{x}_a = \mathbf{0}$ and $\mathbf{x}_b = x_{i,b}\mathbf{E}_i$.

Denoting by S and s the unstretched and deformed arc-length coordinates of the cable, respectively, the strain ε of the element is given by the infinitesimal approximation

$$\varepsilon = \frac{d(s-S)}{dS} = \frac{ds}{dS} - 1 \tag{2.73}$$

Consequently, the current position vector $\mathbf{x}_b$ of node b can be obtained by the explicit integration

$$\mathbf{x}_b = \int_0^{l_0} d\mathbf{x} = \int_0^{l_0} \frac{d\mathbf{x}}{ds}\frac{ds}{dS}\, dS = \int_0^{l_0} \frac{d\mathbf{x}}{ds}(\varepsilon + 1)\, dS \tag{2.74}$$

where l_0 is the unstretched length of the cable.

The equilibrium equation in the current configuration requires that each component of the axial force vector $\mathbf{n}$ be in equilibrium with the external forces

$$n\frac{d\mathbf{x}}{ds} = -(\mathbf{w}S + \mathbf{f}) \tag{2.75}$$

where n is the magnitude of the axial force vector $\mathbf{n}$, $d\mathbf{x}/ds$ are the direction cosines of the axial force vector $\mathbf{n}$ in the current configuration, $\mathbf{w}$ is the distributed load on the cable and $\mathbf{f}$ are the end forces at node a according to Fig. 2.4. As a result, the magnitude n of the axial force is given by

$$n = \|\mathbf{n}\| = \sqrt{\sum_{i=1}^{3}(w_i S + f_i)^2} \tag{2.76}$$

where w_i and f_i are the components of the vectors $\mathbf{w}$ and $\mathbf{f}$, respectively.

The continuous implementation of the catenary element substitutes Eqs. 2.75 and 2.76 into Eq. 2.74 to give

$$\mathbf{x}_b = -\int_0^{l_0} \frac{\mathbf{w}S + \mathbf{f}}{\sqrt{\sum_{i=1}^{3}(w_i S + f_i)^2}}(\varepsilon + 1)\, dS \tag{2.77}$$

The explicit integral in Eq. 2.77 requires a constitutive relation of the form $\varepsilon = \varepsilon(n)$. Assuming infinitesimal linear elasticity in one dimension (Hooke's law), the strain ε is related to the axial force n with

$$n = EA\varepsilon \tag{2.78}$$

where E is the Young modulus and A, the cross section of the cable. Introducing this constitutive relation into Eq. 2.77 gives

$$\mathbf{x}_b = -\int_0^{l_0} \frac{\mathbf{w}S + \mathbf{f}}{\sqrt{\sum_{i=1}^{3}(w_i S + f_i)^2}} \left(\frac{\sqrt{\sum_{i=1}^{3}(w_i S + f_i)^2}}{EA} + 1 \right) dS \tag{2.79}$$

The integral in Eq. 2.79 is then solved to give an explicit expression for the current position vector $\mathbf{x}_b$ at node b as a function of the unknown end forces $\mathbf{f}$, $\mathbf{x}_b = \mathbf{x}_b(\mathbf{f})$. This represents a nonlinear system of equations that can be solved to obtain the unknowns $\mathbf{f}$. The differential relation

$$d\mathbf{x}_b = \frac{\partial \mathbf{x}_b}{\partial \mathbf{f}} d\mathbf{f} \tag{2.80}$$

gives the flexibility matrix $\partial \mathbf{x}_b / \partial \mathbf{f}$ of the element.

The discrete catenary element deploys a finite-difference stencil in Eq. 2.75 to subdivide the element into n subelements with equal unstretched length l_s and $n+1$ nodes in the form

$$n_i \frac{\Delta \mathbf{x}_i}{l_i} = -\left(i l_s \mathbf{w} + \mathbf{f} + \sum_{\substack{j=2 \\ j \le i}}^{i} \mathbf{p}_j \right) \quad \text{for} \quad i = 1, ..., n \tag{2.81}$$

where $\Delta \mathbf{x}_i = x_{i+1} - x_i$, l_i is the deformed length of subelement i and $\mathbf{p}_j$ are the applied loads at the internal node j. As a result, the position vector $\mathbf{x}_i$ of the i-th node of the element is given by the Riemann sum

$$\mathbf{x}_i = \sum_{j=1}^{i-1} \Delta \mathbf{x}_j = \sum_{j=1}^{i-1} \frac{\Delta \mathbf{x}_j}{l_j} \frac{l_j}{l_s} l_s \quad \text{for} \quad i = 2, ..., n+1 \tag{2.82}$$

with the boundary condition $\mathbf{x}_a \equiv \mathbf{x}_1 = \mathbf{0}$. Approximating the strain ε_i in subelement i by the relation l_i / l_s and using Hooke's law gives the constitutive relations

$$\varepsilon_i = \frac{ds}{dS} - 1 \approx \frac{l_i}{l_s} - 1 = \frac{n_i}{EA_i} \quad \text{for} \quad i = 1, ..., n \tag{2.83}$$

Introducing these constitutive equations into Eq. 2.82 gives

$$\mathbf{x}_i = -\sum_{j=1}^{i-1}\left(jl_s\mathbf{w} + \mathbf{f} + \sum_{\substack{k=2\\k\leq j}}^{j}\mathbf{p}_k\right)\left(\frac{1}{EA_j}+\frac{1}{n_j}\right)l_s \quad \text{for} \quad i=2,...,n+1 \tag{2.84}$$

Equation 2.84 is the discrete counterpart to Eq. 2.79, and forms a system of n nonlinear equations that can be solved to give the position vectors of all nodes and the end forces $\mathbf{f}$. The assembled differential relation in Eq. 2.80 also gives the flexibility matrix $\partial\mathbf{x}/\partial\mathbf{f}$ of the discrete catenary element.

The dynamic analysis of catenary elements is formulated *ad hoc* by obtaining the stiffness matrix $\mathbf{k}$ as the inverse of the flexibility matrix $\partial\mathbf{x}/\partial\mathbf{f}$, and including it in the dynamic equation [52]

$$\mathbf{ma} + \mathbf{ku} = \mathbf{F} \tag{2.85}$$

where $\mathbf{m}$ is the mass matrix for the element, $\mathbf{a}$ is the acceleration field, $\mathbf{u}$ is the displacement field with respect to the equilibrium state and $\mathbf{F}$ are the external forces.

While catenary elements give more accurate results than truss elements for the same mesh discretization, they also have shortcomings that limit their range of application. First, current catenary elements do not support the extension to finite deformations and nonlinear material behavior. Second, these elements assume infinitesimal deformations and integrate the global balance of linear momentum explicitly or with finite differences without distinguishing between the 2nd PK and Cauchy representations of the axial force. Third, this explicit integration does not accommodate a consistent mass for dynamic analysis, limiting such approaches to the use of a lumped mass with the consequence that a large number of elements is required for accuracy [52]. Finally, because of the assumption of infinitesimal deformations, the distributed loads do not evolve consistently with the cable elongation, resulting in the inaccurate balance of linear momentum in the deformed configuration. To address this problem, *associated catenary elements* impose restrictions of the form $wL = \tilde{w}l$ with w and L the load and length in the reference configuration, and $\tilde{w}$ and l the load and length in the current configuration, respectively [3].

2.2.3 Geometrically-exact rods

Geometrically-exact rods are the natural extension of classical beam theories to finite deformations and finite rotations, and are hence not explicitly formulated as cables [39, 42, 46]. Their formulation, however, provides significant insight on how to incorporate finite-deformation theory into catenary elements and constitutes, together with the formulations in the preceding sections, the starting point for this dissertation.

Figure 2.5 shows the deformation of a rod from a reference configuration $\mathcal{P}_0$ to a current configuration $\mathcal{P}_t$ at time t, with reference position vector $\mathbf{X}$ and current position vector $\mathbf{x}$. The rod in the reference configuration is defined by an axis $\mathbf{R}_0$ and a succession of cross

sections with orthogonal frames $\{\mathbf{G}_i\}_{i=1}^3$, while the rod in the current configuration is defined by an axis $\mathbf{r}$ and a succession of cross sections with frames $\{\mathbf{g}_i\}_{i=1}^3$.

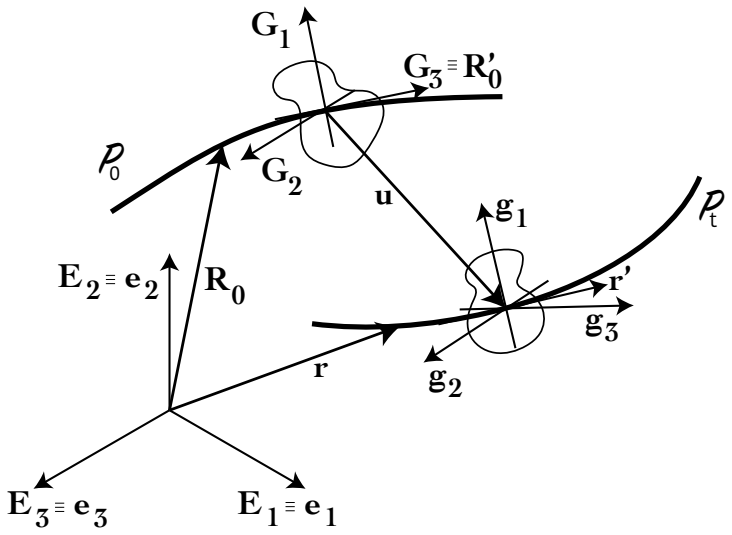

Figure 2.5: Geometric setup for the geometrically-exact rod.

The coordinate systems along the axis of the rod in the reference and current configurations can be obtained from the global Cartesian coordinate system $\{\mathbf{E}_i\}_{i=1}^3$ by means of the rotation matrices $\mathbf{\Lambda}_0(S) \in SO(3)$ in the reference configuration and $\mathbf{\Lambda}(S) \in SO(3)$ in the current configuration,

$$\mathbf{G}_i = \mathbf{\Lambda}_0 \mathbf{E}_i \quad ; \quad \mathbf{g}_i = \mathbf{\Lambda} \mathbf{E}_i \quad \text{for} \quad i \in \{1, 2, 3\} \tag{2.86}$$

Denoting by S the reference arc-length coordinate, the reference position vector $\mathbf{X}$ is given by

$$\mathbf{X} = \varphi_0(\xi^1, \xi^2, S) = \mathbf{R}_0(S) + \sum_{i=1}^{2} \xi^i \mathbf{G}_i(S) \tag{2.87}$$

where $(\cdot)'$ refers to the derivative with respect to the arc-length coordinate S and (ξ^1, ξ^2) are the section coordinates. For the reference configuration, $\mathbf{G}_3 = \mathbf{R}_0'$. The current position vector $\mathbf{x}$ is given by

$$\mathbf{x} = \varphi(\xi^1, \xi^2, S) = \mathbf{r}(S) + \sum_{i=1}^{2} \xi^i \mathbf{g}_i(S) \tag{2.88}$$

noting that $\mathbf{r}' \neq \mathbf{g}_3$ in general because $\mathbf{g}_3$ is not necessarily tangent to the current axis.

The strain measures are defined by the pull-backs

$$\begin{aligned} \mathbf{\Gamma} &= \mathbf{\Lambda}^t \mathbf{r}' - \mathbf{E}_3 \\ \mathbf{\Omega} &= \mathbf{\Lambda}^t \mathbf{\Lambda}' - \mathbf{\Lambda}^t \mathbf{\Lambda}_0' \end{aligned} \tag{2.89}$$

where $\mathbf{\Gamma}$ is the vector measuring the change in the angles between the tangent vectors and the frame of the section (Γ_1, Γ_2) and the axial strain (Γ_3), while $\mathbf{\Omega}$ is the skew-symmetric tensor, whose vector representation is $\boldsymbol{\omega}$, and measures the curvatures (ω_1, ω_2) and the rate of twist (ω_3).

The principle of virtual work is therefore written in the form

$$\int_0^L \mathbf{N} \cdot \delta\mathbf{\Gamma}\, dS + \int_0^L \mathbf{M} \cdot \delta\boldsymbol{\omega}\, dS = \int_0^L \bar{\mathbf{n}} \cdot \delta\mathbf{r}\, dS + \int_0^L \bar{\mathbf{m}} \cdot \delta\boldsymbol{\theta}\, dS \tag{2.90}$$

where $\mathbf{N}$ is the reference axial force, $\mathbf{M}$ is the reference bending moment in vector form, $\bar{\mathbf{n}}$ is the applied distributed axial force, $\bar{\mathbf{m}}$ is the applied distributed moment and $\delta\boldsymbol{\theta}$ is the rotation of the section in vector form. The difficulty of this model is now apparent, as it requires the variations $\delta\mathbf{\Gamma}$ and $\delta\boldsymbol{\omega}$ in terms of the variations $\delta\mathbf{r}$ and $\delta\boldsymbol{\theta}$ with $\mathbf{\Omega}$ not contained in a linear space but in the manifold $SO(3)$. Using the tangent space to the manifold $SO(3)$ gives the explicit form of the principle of virtual work [42]

$$\int_0^L \mathbf{n} \cdot (-\delta\boldsymbol{\theta} \times \mathbf{r}' + \delta\mathbf{r}')\, dS + \int_0^L \mathbf{m} \cdot \delta\boldsymbol{\theta}'\, dS = \int_0^L \bar{\mathbf{n}} \cdot \delta\mathbf{r}\, dS + \int_0^L \bar{\mathbf{m}} \cdot \delta\boldsymbol{\theta}\, dS \tag{2.91}$$

with the pushed-forward stress resultants $\mathbf{n} = \mathbf{\Lambda N}$ and $\mathbf{M} = \mathbf{\Lambda M}$. The objective constitutive relation is given in terms of the reference stress resultants $\mathbf{\Pi} = (\mathbf{N}, \mathbf{M})$ and the reference strain measures $\mathbf{\Psi} = (\mathbf{\Gamma}, \boldsymbol{\omega})$ for the energy function $\mathcal{U}$ in the form

$$\mathbf{\Pi} = \frac{\partial \mathcal{U}}{\partial \mathbf{\Psi}} \tag{2.92}$$

The solution to Eq. 2.91 under the constitutive relations in Eq. 2.92 is obtained by discretizing the domain into finite elements with interpolation functions for the displacement field $\mathbf{u}$ and for the rotation field $\boldsymbol{\theta}$. The tangent stiffness of the element is given by the Fréchet derivative of the stress divergence term on the left-hand side of Eq. 2.91 [46]. The inertia forces for the dynamic analysis can be readily added with the terms $\mathbf{Ma}$ and $\mathbf{J}_\rho\boldsymbol{\alpha}$, where $\mathbf{M}$ and $\mathbf{J}_\rho$ are the mass and the mass moment of inertia matrices, and $\mathbf{a}$ and $\boldsymbol{\alpha}$ are the tangent and the angular acceleration fields.

Geometrically-exact rods cannot be directly used to model cables because the consistent tangent becomes singular in the limit $EI \to 0$. A common trick to numerically overcome this limitation consists of considering a small but non-zero bending stiffness EI in the model. This numerical trick, however, entails three relevant disadvantages. First and most importantly, the small but nonzero bending stiffness EI may result in an ill-conditioned consistent tangent when combined with other material properties with large values, and therefore may give rise to significant errors in the results. Second, the fictitious stiffness EI may generate a significant rotation of the cable cross section, which is not physical for stranded cables even under large deformations. Third, the model is computationally expensive because it requires the storage of rotation degrees of freedom, even in the elastic case, for updating the large rotations.

Chapter 3
Element formulation

This chapter presents the formulation and implementation of a two-field cable element that is based on a mixed variational formulation in curvilinear coordinates and finite deformations. For generality purposes, no assumptions are made at this stage about the constitutive relation of the cable, and subsequent chapters implement different material models to assess this formulation for different applications.

The discussion begins with the assumptions of the model and the geometric preliminaries required to mathematically describe the kinematics of the cable. Afterwards, the equilibrium equation and the principle of virtual work are derived to formulate the weak form of the catenary problem. The governing equations are discretized in space with the finite element method, and integrated in time with different time-stepping algorithms, which include the well-known Newmark [37] and HHT-α [24] methods and a new energy-momentum conserving algorithm in complementary space [13]. Finally, a filtering process based on a Savitzky-Golay filter [41] is used to remove high-frequency contributions in the dynamic response.

3.1 Overview and assumptions

In view of the shortcomings for existing elements in Section 2.2, a new cable element based on finite-deformation theory is proposed [14]. The formulation assumes the cable to be infinitely flexible, and thus does not account for any bending stiffness or deformation of the cross section. This new element formulation considers nonlinear stress measures in the form of axial forces and conjugate strain measures to obtain the strain-displacement relation and the equilibrium equation in the deformed configuration.

The element kinematics relate the Green-Lagrange strain tensor to the displacement field in order to establish compatibility in finite deformations. Conjugate stress measures are derived by transforming the 2nd Piola-Kirchhoff (2nd PK) and Cauchy stress tensors into axial forces, and used to formulate the equilibrium equation and the principle of virtual

work. The continuity requirements of the governing equations allow two different numerical implementations: one with a continuous axial force field and one with a discontinuous axial force field.

The cable element is first integrated in time with the Newmark method [37] and the HHT-α method [24]. Since these do not preserve the Hamiltonian structure of nonlinear elastodynamics [6, 44, 45], a new energy-momentum conserving algorithm in complementary energy space is derived for the problem at hand [13]. Finally, the use of a Savitzky-Golay filter [41] is proposed to dissipate any high-frequency oscillations in the dynamic response [15, 47].

3.2 Geometric preliminaries

The proposed element represents the cable as a one-dimensional manifold $\mathcal{C}$ that is embedded in the three-dimensional Euclidean space $\mathbb{R}^3$. Fig. 3.1 shows the geometric setup for this idealized cable $\mathcal{C}$ with reference Cartesian coordinate system $\{\mathbf{E}_A\}_{A=1}^3$.

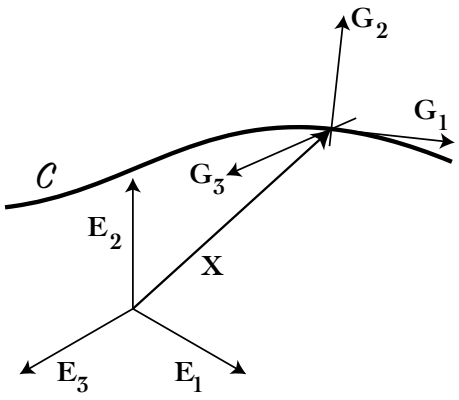

Figure 3.1: Geometric setup for the cable $\mathcal{C}$.

A local orthogonal frame $\{\mathbf{G}_i\}_{i=1}^3$ associated with coordinates $\{\xi^i\}_{i=1}^3$ is defined at any material point $P \in \mathcal{C}$ in the form

$$\mathbf{G}_1 = \frac{d\mathbf{X}}{d\xi^1} \;\; ; \;\; \mathbf{G}_1 \cdot \mathbf{G}_2 = 0 \;\; ; \;\; \|\mathbf{G}_2\| = 1 \;\; ; \;\; \mathbf{G}_3 = \frac{\mathbf{G}_1 \times \mathbf{G}_2}{\|\mathbf{G}_1 \times \mathbf{G}_2\|} \tag{3.1}$$

where ξ^1 is the selected parameter for describing the curve. Note that the frame $\{\mathbf{G}_i\}_{i=1}^3$ is orthogonal but, in general, not orthonormal. Indeed, the metric tensor G_{ij} for the frame $\{\mathbf{G}_i\}_{i=1}^3$ has the structure

$$[G_{ij}] = [\mathbf{G}_i \cdot \mathbf{G}_j] = \begin{bmatrix} \|\mathbf{G}_1\|^2 & 0 & 0 \\ 0 & 1 & 0 \\ 0 & 0 & 1 \end{bmatrix} \tag{3.2}$$

The differential vector $d\mathbf{X}$ along the curve $\mathcal{C}$ is given by

$$d\mathbf{X} = \frac{d\mathbf{X}}{d\xi^1} d\xi^1 = \mathbf{G}_1 d\xi^1 \tag{3.3}$$

while the arc-length differential dS along the curve has the form

$$dS = \sqrt{d\mathbf{X} \cdot d\mathbf{X}} = \|\mathbf{G}_1\| d\xi^1 = \sqrt{G_{11}} d\xi^1 \tag{3.4}$$

The dual frame $\{\mathbf{G}^i\}_{i=1}^3$ is defined with respect to the frame $\{\mathbf{G}_i\}_{i=1}^3$ with the dual metric tensor G^{ij}

$$\mathbf{G}^i = G^{ij} \mathbf{G}_j \tag{3.5}$$

Since the curvilinear coordinates $\{\xi^i\}_{i=1}^3$ are orthogonal, Eq. 2.11 gives the relation

$$\mathbf{G}^i = G^{ii} \mathbf{G}_i = G_{ii}^{-1} \mathbf{G}_i \quad \text{for} \quad i \in \{1, 2, 3\} \tag{3.6}$$

with no summation implied, and $G_{ij} = G^{ij} = 0$ for $i \neq j$.

3.3 Finite-deformation kinematics

With the preceding definitions, let the cable $\mathcal{C}$ undergo the motion $\boldsymbol{\chi}(\mathbf{X}, t) : \mathbb{R}^3 \times \mathcal{I} \to \mathbb{R}^3$ in Fig. 3.2, from a reference configuration $\mathcal{P}_0$ to the current configuration $\mathcal{P}_t$ at time t, where $\mathbf{x} = \boldsymbol{\chi}(\mathbf{X}, t)$ and $\mathbf{X}$ represent the current and reference position vectors, respectively. Upper case letters denote the variables in the reference configuration and lower case letters, the variables in the current configuration. The motion $\boldsymbol{\chi}(\mathbf{X}(\xi^1), t)$ is therefore uniquely described by the curvilinear coordinate ξ^1 at any time t.

In the global Cartesian coordinate system, $\mathbf{X} = X_A \mathbf{E}_A$ defines the reference coordinates, whereas $\mathbf{x} = x_i \mathbf{e}_i$ defines the current coordinates. Note that, in Cartesian coordinates, $\mathbf{E}_A = \mathbf{E}^A$ and $\mathbf{e}_i = \mathbf{e}^i$. Let the basis vectors for the reference and the current configuration coincide for simplicity, $\{\mathbf{E}_A\}_{A=1}^3 \equiv \{\mathbf{e}_i\}_{i=1}^3$.

Under the motion $\boldsymbol{\chi}(\mathbf{X}, t)$, the reference orthogonal frame $\{\mathbf{G}_i\}_{i=1}^3$ is convected to the current orthogonal frame $\{\mathbf{g}_i\}_{i=1}^3$. Consequently, the deformation gradient $\mathbf{F}$ and the right Cauchy-Green tensor $\mathbf{C}$ have the form

$$\mathbf{F} = \frac{\partial \mathbf{x}}{\partial \mathbf{X}} = \mathbf{g}_i \otimes \mathbf{G}^i \quad ; \quad \mathbf{C} = \mathbf{F}^t \mathbf{F} = g_{ij}\, \mathbf{G}^i \otimes \mathbf{G}^j \tag{3.7}$$

with $\mathbf{F}\mathbf{G}_1 = \mathbf{g}_1$ and $\mathbf{G}_1 = \mathbf{F}^{-1}\mathbf{g}_1$.

The Green-Lagrange strain tensor $\mathbf{E}$ in curvilinear coordinates has the form

$$\mathbf{E} = \frac{1}{2}(g_{ij} - G_{ij})\, \mathbf{G}^i \otimes \mathbf{G}^j \tag{3.8}$$

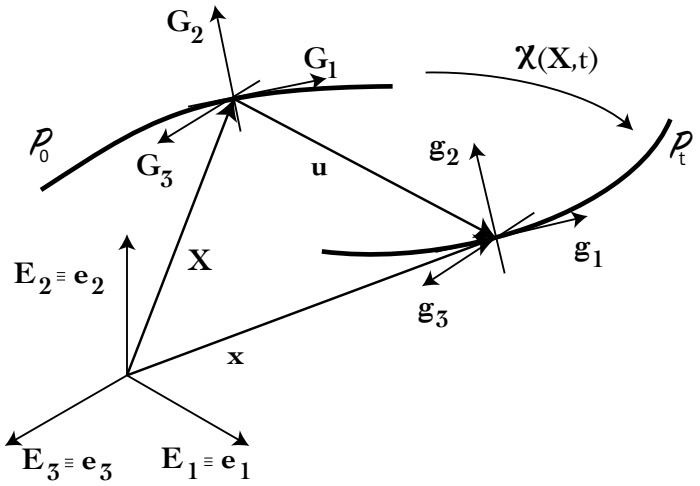

Figure 3.2: Motion $\mathbf{x} = \boldsymbol{\chi}(\mathbf{X}, t)$ of the cable $\mathcal{C}$.

Hence, the only nonzero strain of the problem arises in the $\mathbf{G}_1$ direction. It is

$$\mathrm{E}_{11} = \frac{1}{2}(\|\mathbf{g}_1\|^2 - \|\mathbf{G}_1\|^2) \tag{3.9}$$

The relevant stretch λ in the $\mathbf{G}_1$ direction, which is equal to the determinant J of the deformation gradient $\mathbf{F}$, is

$$\lambda^2 = \left(\frac{ds}{dS}\right)^2 = \frac{d\mathbf{x} \cdot d\mathbf{x}}{d\mathbf{X} \cdot d\mathbf{X}} = \frac{g_{11}}{G_{11}} = \left(\frac{\|\mathbf{g}_1\|}{\|\mathbf{G}_1\|}\right)^2 \tag{3.10}$$

Consequently,

$$\mathrm{E}_{11} = \frac{1}{2}(\lambda^2 - 1)\|\mathbf{G}_1\|^2 \tag{3.11}$$

The displacement field $\mathbf{u}$ at time t depends only on the reference curvilinear coordinate ξ^1 of the material point $P \in \mathcal{C}$

$$\mathbf{u}(\mathbf{X}(\xi^1), t) = \mathbf{x}(\mathbf{X}(\xi^1), t) - \mathbf{X}(\xi^1) = u_A(\xi^1, t)\mathbf{E}_A \tag{3.12}$$

For the referential displacement gradient $\mathbf{H}$ in curvilinear coordinates, one observes that the only nonzero derivative with respect to the coordinates $\{\xi^i\}_{i=1}^3$ is

$$\frac{d\mathbf{u}}{d\xi^1} = \frac{d\mathbf{x}}{d\xi^1} - \frac{d\mathbf{X}}{d\xi^1} = \mathbf{g}_1 - \mathbf{G}_1 \tag{3.13}$$

As a result,

$$\mathbf{H} = \frac{d\mathbf{u}}{d\xi^1} \otimes \mathbf{G}^1 \tag{3.14}$$

so that the relationship between the Green-Lagrange strain tensor $\mathbf{E}$ and the displacement field $\mathbf{u}$, namely the strain-displacement relation, is

$$\mathbf{E} = \frac{1}{2}\left(\frac{d\mathbf{u}}{d\xi^1}\otimes\mathbf{G}^1 + \mathbf{G}^1\otimes\frac{d\mathbf{u}}{d\xi^1} + \left|\frac{d\mathbf{u}}{d\xi^1}\right|^2 \mathbf{G}^1\otimes\mathbf{G}^1\right) \tag{3.15}$$

where $|\cdot|$ represents the L^2-norm of the vector. Introducing the notation $(\cdot)'$ for the derivative with respect to the curvilinear coordinate ξ^1, the only nonzero component of $\mathbf{E}$ can be expressed as

$$\mathrm{E}_{11} = \mathbf{u}'\cdot\mathbf{G}_1 + \frac{1}{2}|\mathbf{u}'|^2 = \mathbf{u}'\cdot\left(\mathbf{G}_1 + \frac{1}{2}\mathbf{u}'\right) = \frac{1}{2}\mathbf{u}'\cdot(\mathbf{G}_1+\mathbf{g}_1) \tag{3.16}$$

It is important to observe that the above Green-Lagrange strain tensor is, in general, not physical. Indeed, the constitutive equation cannot be directly expressed as a function of E_{11} since the metric tensor G_{ij} is not the identity operator, i.e. $G_{11} = \|\mathbf{G}_1\|^2 \neq 1$ in general. However, one can generate an orthonormal basis by normalizing the vectors $\{\mathbf{G}_i\}_{i=1}^3$ into the vectors $\{\hat{\mathbf{G}}_A\}_{A=1}^3$,

$$\hat{\mathbf{G}}_A = \frac{\mathbf{G}_i}{\|\mathbf{G}_i\|} \quad \text{with } i = A \in \{1,2,3\} \tag{3.17}$$

Consequently, the components of $\mathbf{E}$ can be transformed into meaningful quantities by invoking the change of basis

$$\mathbf{E} = \mathrm{E}_{ij}\mathbf{G}^i\otimes\mathbf{G}^j = \hat{\mathrm{E}}_{AB}\hat{\mathbf{G}}_A\otimes\hat{\mathbf{G}}_B \tag{3.18}$$

Hence,

$$\hat{\mathrm{E}}_{AB} = \mathrm{E}_{ij}(\hat{\mathbf{G}}_A\cdot\mathbf{G}^i)(\hat{\mathbf{G}}_B\cdot\mathbf{G}^j) \tag{3.19}$$

noting that $\hat{\mathrm{E}}_{11} = G^{11}\mathrm{E}_{11}$, as $\hat{\mathbf{G}}_1\cdot\mathbf{G}^1 = \|\mathbf{G}^1\|$.

3.4 Equilibrium and Principle of Virtual Work

For expressing the equilibrium equation of the cable, let $\mathbf{n}$ denote the axial force in the current configuration, hence a Cauchy representation of the axial force. Observe that the first Piola-Kirchhoff (1st PK) and the Cauchy representations of the axial force coincide for the problem at hand, which does not account for changes in the cross section dimensions.

With reference to the normalized convected vectors $\{\hat{\mathbf{g}}_i\}_{i=1}^3$ according to Eq. 3.17, the physical Cauchy stress tensor $\hat{\boldsymbol{\sigma}}$ is given by

$$\hat{\boldsymbol{\sigma}} = \hat{\sigma}^{ij}\hat{\mathbf{g}}_i\otimes\hat{\mathbf{g}}_j \tag{3.20}$$

Consequently, the Cauchy axial force $\mathbf{n}$ corresponds to

$$\mathbf{n} = A\hat{\sigma}^{11}\hat{\mathbf{g}}_1\otimes\hat{\mathbf{g}}_1\hat{\mathbf{g}}^1 = A\hat{\sigma}^{11}\hat{\mathbf{g}}_1 = A\hat{\sigma}^{11}\sqrt{g^{11}}\mathbf{g}_1 \tag{3.21}$$

with magnitudes $\mathbf{n} = \hat{\mathrm{n}}\hat{\mathbf{g}}_1 = \mathrm{n}\mathbf{g}_1$ in the two bases, where A is the area of the cross section. With the expression for the physical 2nd Piola-Kirchhoff stress tensor $\hat{\mathbf{S}}$ in the form

$$\hat{\mathbf{S}} = \hat{\mathrm{S}}^{ij}\hat{\mathbf{G}}_i \otimes \hat{\mathbf{G}}_j \tag{3.22}$$

the 2nd Piola-Kirchhoff axial force $\mathbf{N}$ becomes

$$\mathbf{N} = A\hat{\mathrm{S}}^{11}\hat{\mathbf{G}}_1 \otimes \hat{\mathbf{G}}_1\hat{\mathbf{G}}^1 = A\hat{\mathrm{S}}^{11}\hat{\mathbf{G}}_1 = A\hat{\mathrm{S}}^{11}\sqrt{G^{11}}\mathbf{G}_1 \tag{3.23}$$

with magnitudes $\mathbf{N} = \hat{\mathrm{N}}\hat{\mathbf{G}}_1 = \mathrm{N}\mathbf{G}_1$ in the two bases.

The 2nd Piola-Kirchhoff stress S^{11} is related to the Cauchy stress σ^{11} with the pull-back transformation in Eq. 2.48

$$\mathrm{S}^{11} = J\sigma^{11} = \lambda\sigma^{11} \tag{3.24}$$

where J is the determinant of the deformation gradient $\mathbf{F}$. The physical components of $\mathbf{S}$ and $\boldsymbol{\sigma}$ are derived similarly to Eq. 3.19 so that

$$\mathbf{N} = AG_{11}\frac{\sqrt{g_{11}}}{\sqrt{G_{11}}}\sigma^{11}\hat{\mathbf{G}}_1 = A\sqrt{G_{11}}\hat{\sigma}^{11}\sqrt{g^{11}}\hat{\mathbf{G}}_1 = \mathrm{n}\sqrt{G_{11}}\hat{\mathbf{G}}_1 \tag{3.25}$$

Hence,

$$\hat{\mathrm{N}} = \mathrm{n}\sqrt{G_{11}} \iff \mathrm{n} = \hat{\mathrm{N}}\sqrt{G^{11}} \iff \hat{\mathrm{n}} = \lambda\hat{\mathrm{N}} \tag{3.26}$$

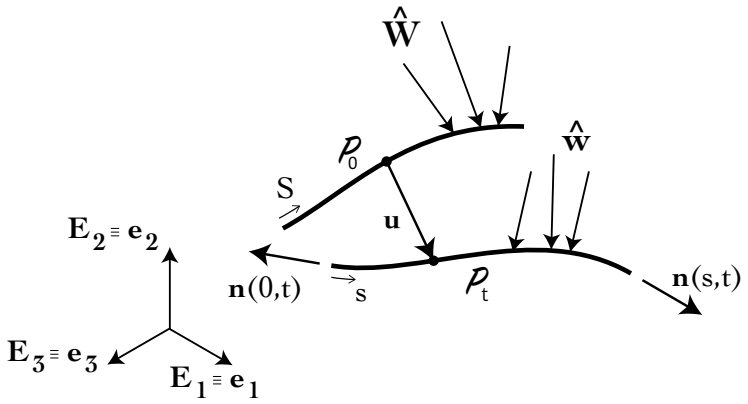

Figure 3.3: Representation of a cable element in equilibrium.

The global equilibrium of the cable $\mathcal{C}$ in the current configuration in Fig. 3.3 requires that each component of $\mathbf{n}$ be in equilibrium with the external loads $\mathbf{w}$ expressed per unit of length in the current configuration [4, Ch.3]

$$\mathbf{n}(s,t) - \mathbf{n}(0,t) + \int_0^s \mathbf{w}(s,t)\,ds = \frac{d}{dt}\int_0^s m(s)\dot{\mathbf{u}}(s,t)\,ds \tag{3.27}$$

where $m(s)$ is the linear density of the cable in the current configuration and $\dot{(\cdot)}$ represents the material time derivative. The local counterpart in the current configuration can be obtained with the Fundamental Theorem of Calculus

$$\int_0^s \left(\frac{d\mathbf{n}}{ds} + \mathbf{w} - m\ddot{\mathbf{u}} \right) ds = \mathbf{0} \tag{3.28}$$

Hence, by the localization theorem,

$$\frac{d\mathbf{n}}{ds} + \mathbf{w} - m\ddot{\mathbf{u}} = \mathbf{0} \tag{3.29}$$

This expression arises directly from enforcing equilibrium for a differential cable segment [34, Ch.3].

The external loads $\mathbf{w}(s,t)$ can be pulled back to the reference configuration with

$$\mathbf{w}(s,t)ds = \hat{\mathbf{W}}(S,t)dS = \mathbf{W}(\xi^1,t)d\xi^1 \tag{3.30}$$

On account of Eq. 3.26, the pulled-back equilibrium equation in the reference configuration becomes

$$\frac{d}{dS}\left(\mathrm{n}\mathbf{g}_1\right) + \hat{\mathbf{W}} - m_0\ddot{\mathbf{u}} = \frac{d}{dS}\left(\hat{\mathrm{N}}\sqrt{G^{11}}\mathbf{g}_1\right) + \hat{\mathbf{W}} - m_0\ddot{\mathbf{u}} = \mathbf{0} \tag{3.31}$$

where $m_0 = \lambda m$ is the reference linear density of the cable.

In summary, if $\hat{\mathrm{N}} = \Psi(\hat{\mathrm{E}}, \kappa)$ is a frame-indifferent constitutive relation [21, Ch.7] between the physical Green-Lagrange strain $\hat{\mathrm{E}}$ and the physical 2nd Piola-Kirchhoff axial force $\hat{\mathrm{N}}$, with κ a set of internal variables for use in the inelastic constitutive models to be discussed in Chapter 5, the pair of fields $(\mathbf{u}, \hat{\mathrm{N}})$ will be the solution of the cable problem, if and only if, they satisfy the following equations

$$\begin{cases} G^{11}\mathbf{u}' \cdot \left(\mathbf{G}_1 + \dfrac{1}{2}\mathbf{u}' \right) - \hat{\mathrm{E}} = 0 & \text{in } \Omega \times \mathcal{I} \\ \dfrac{d}{dS}\left(\sqrt{G^{11}}\hat{\mathrm{N}}\mathbf{g}_1 \right) + \hat{\mathbf{W}} = m_0\ddot{\mathbf{u}} & \text{in } \Omega \times \mathcal{I} \\ \hat{\mathrm{N}} - \Psi(\hat{\mathrm{E}}, \kappa) = 0 & \text{in } \Omega \times \mathcal{I} \\ \mathbf{u} = \bar{\mathbf{u}} & \text{on } \Gamma_u \times \mathcal{I} \\ \sqrt{G^{11}}\hat{\mathrm{N}}\mathbf{g}_1 = \bar{\mathbf{T}} & \text{on } \Gamma_q \times \mathcal{I} \\ \mathbf{u} = \mathbf{u}_0 \ ; \ \ \mathbf{v} = \mathbf{v}_0 \ ; \ \ \hat{\mathrm{N}} = \hat{\mathrm{N}}_0 & \text{in } \Omega \times \{t = 0\} \end{cases} \tag{3.32}$$

for $S \in \Omega = (0, L)$ equivalent to $\xi^1 \in \Omega_\xi = (\xi^1_0, \xi^1_L)$, and $t \in \mathcal{I} = (0, T)$. In these, $\bar{\mathbf{u}}$ and $\bar{\mathbf{T}}$ denote the imposed displacements and boundary forces, respectively. Note that the boundary condition on Γ_q does not represent a prestressing force but a boundary force. In general, this condition is not used in cable problems.

Eq. 3.32 is a nonlinear second-order system of differential equations that can be transformed into first order by introducing the velocity field $\mathbf{v}$ as an unknown, together with the relation $\dot{\mathbf{u}} = \mathbf{v}$ in $\Omega \times \mathcal{I}$.

If the pair $(\mathbf{u}, \hat{\mathrm{N}})$ satisfies Eq. 3.32, then for any variation $\delta\mathbf{u} \in \mathcal{V}$, the space of displacement test functions, and any variation $\delta\hat{\mathrm{N}} \in \mathcal{W}$, the space of test functions for the 2nd Piola-Kirchhoff axial force, it holds that

$$\begin{cases} \displaystyle\int_0^L \delta\hat{\mathrm{N}} \left\{ G^{11}\mathbf{u}' \cdot \left(\mathbf{G}_1 + \frac{1}{2}\mathbf{u}' \right) - \hat{\mathrm{E}} \right\} dS = 0 \\ \displaystyle\int_0^L \delta\mathbf{u} \cdot \left(\frac{d}{dS}\left(\sqrt{G^{11}}\hat{\mathrm{N}}\mathbf{g}_1 \right) + \hat{\mathbf{W}} - m_0\ddot{\mathbf{u}} \right) dS + \left[\delta\mathbf{u} \cdot \left(\bar{\mathbf{t}} - \sqrt{G^{11}}\hat{\mathrm{N}}\mathbf{g}_1 \right) \right]_{\Gamma_q} = 0 \end{cases} \tag{3.33}$$

with the requirements for spaces $\mathcal{V}$ and $\mathcal{W}$ to be discussed in the following.

Eq. 3.33 corresponds to the two-field weak formulation of Eq. 3.32. Its solution produces weakly-compatible solutions of the boundary value problem with the constitutive relation imposed strongly.

Regarding the weak form of the strain-displacement relation, sufficient smoothness requirements for $\mathbf{u}$ are $\mathbf{u} \in \mathcal{C}^0(\Omega)$ with $\delta\hat{\mathrm{N}} \in L^2(\Omega)$, so that u_i' has finite jumps at the points with discontinuous derivative and is, therefore, square-integrable.

Regarding the weak form of the equilibrium equation, one can integrate by parts to reduce the order of the highest derivative of the displacement field $\mathbf{u}$, thus obtaining the *Principle of Virtual Work* (PVW) for the cable problem

$$\int_0^L \delta\mathbf{u}' \cdot G^{11}\hat{\mathrm{N}}\mathbf{g}_1 \, dS + \int_0^L \delta\mathbf{u} \cdot m_0\ddot{\mathbf{u}} \, dS = \left[\delta\mathbf{u} \cdot \bar{\mathbf{t}} \right]_{\Gamma_q} + \int_0^L \delta\mathbf{u} \cdot \hat{\mathbf{W}} \, dS \tag{3.34}$$

or, equivalently, integrating over the curvilinear coordinate

$$\int_{\xi_0^1}^{\xi_L^1} \delta\mathbf{u}' \cdot \sqrt{G^{11}}\hat{\mathrm{N}}\mathbf{g}_1 \, d\xi^1 + \int_{\xi_0^1}^{\xi_L^1} \delta\mathbf{u} \cdot m_0\ddot{\mathbf{u}}\sqrt{G_{11}} d\xi^1 = \left[\delta\mathbf{u} \cdot \bar{\mathbf{t}} \right]_{\Gamma_q} + \int_{\xi_0^1}^{\xi_L^1} \delta\mathbf{u} \cdot \mathbf{W} \, d\xi^1 \tag{3.35}$$

Eq. 3.34 can also be derived from the general principle of virtual work under finite deformations in Eq. 2.54. As a result, the corresponding weak problem to Eq. 3.32 becomes

$$\begin{cases} \displaystyle\int_0^L \delta\hat{\mathrm{N}} \left\{ G^{11}\mathbf{u}' \cdot \left(\mathbf{G}_1 + \frac{1}{2}\mathbf{u}' \right) - \hat{\mathrm{E}} \right\} dS = 0 \\ \displaystyle\int_0^L \delta\mathbf{u}' \cdot G^{11}\hat{\mathrm{N}}\mathbf{g}_1 \, dS + \int_0^L \delta\mathbf{u} \cdot m_0\ddot{\mathbf{u}} \, dS = \left[\delta\mathbf{u} \cdot \bar{\mathbf{t}} \right]_{\Gamma_q} + \int_0^L \delta\mathbf{u} \cdot \hat{\mathbf{W}} \, dS \end{cases} \tag{3.36}$$

The spaces for the trial solutions of the displacements and the axial forces, $\mathcal{S}$ and $\mathcal{N}$, respectively, are

$$\begin{aligned} \mathcal{S} &= \{ \mathbf{u} \in H^1(0, L) \,|\, \mathbf{u} = \bar{\mathbf{u}} \text{ on } \Gamma_u \} \\ \mathcal{N} &= \left\{ \hat{\mathrm{N}} \in H^0(0, L) \,|\, \hat{\mathrm{N}} > 0, \text{ and } \hat{\mathrm{N}} = g^{11}\sqrt{G_{11}}\bar{\mathbf{t}} \cdot \mathbf{g}_1 \text{ on } \Gamma_q \right\} \end{aligned} \tag{3.37}$$

Similarly, the spaces for the test functions of the displacements and the axial forces, $\mathcal{V}$ and $\mathcal{W}$, respectively, are

$$\begin{aligned} \mathcal{V} &= \{\delta\mathbf{u} \in H^1(0,L) \,|\, \delta\mathbf{u} = 0 \text{ on } \Gamma_u\} \\ \mathcal{W} &= \{\delta\hat{\mathrm{N}} \in H^0(0,L) \,|\, \delta\hat{\mathrm{N}} = 0 \text{ on } \Gamma_q\} \end{aligned} \tag{3.38}$$

where $H^k(\Omega)$ represents the Sobolev space for the $k-$th weak derivative in the $L^2(\Omega)$ norm [16, Ch.5].

Note that the absence of derivatives of the axial force field $\hat{\mathrm{N}}$ in Eq. 3.36 implies no continuity requirements for it in Eqs. 3.37 and 3.38. Consequently, it is possible to explore cable finite element implementations with continuous and discontinuous axial force distributions.

The second-order weak problem in Eq. 3.36 can be transformed into first order by considering the velocity field $\mathbf{v}$ as an unknown and adding the weak momentum relation

$$\int_0^L \delta\mathbf{v} \cdot m_0\dot{\mathbf{u}}\, dS = \int_0^L \delta\mathbf{v} \cdot m_0\mathbf{v}\, dS \tag{3.39}$$

where $\mathbf{v} \in \mathcal{T}$, the space of trial solutions for the velocity, and $\delta\mathbf{v} \in \mathcal{Z}$, the space of velocity test functions,

$$\begin{aligned} \mathcal{T} &= \{\mathbf{v} \in H^1(0,L) \,|\, \mathbf{v} = \bar{\mathbf{v}} \text{ in } \Gamma_v \times \mathcal{I}\} \\ \mathcal{Z} &= \{\delta\mathbf{v} \in H^1(0,L) \,|\, \mathbf{v} = 0 \text{ in } \Gamma_v \times \mathcal{I}\} \end{aligned} \tag{3.40}$$

for the boundary Γ_v where velocities are imposed.

3.5 Hamiltonian structure

In the case of the physical Green-Lagrange strain $\hat{\mathrm{E}}$ resulting from a complementary energy function χ, a standard calculation shows that the problem in Eq. 3.36 can be derived from the mixed Hamiltonian function $\mathcal{H}(\mathbf{u}, \hat{\mathrm{N}})$

$$\mathcal{H}(\mathbf{u}, \hat{\mathrm{N}}) = W(\mathbf{u}, \hat{\mathrm{N}}) + K(\dot{\mathbf{u}}) - W_{ext}(\mathbf{u}) \tag{3.41}$$

where $W(\mathbf{u}, \hat{\mathrm{N}})$ is the stored energy, $K(\dot{\mathbf{u}})$ is the kinetic energy and $W_{ext}(\mathbf{u})$ is the work of the external loads in the form

$$\begin{aligned} W(\mathbf{u}, \hat{\mathrm{N}}) &= \int_0^L \left\{ \hat{\mathrm{N}} G^{11}\mathbf{u}' \cdot \left(\mathbf{G}_1 + \frac{1}{2}\mathbf{u}' \right) - \chi(\hat{\mathrm{N}}) \right\} dS \\ K(\dot{\mathbf{u}}) &= \frac{1}{2}\int_0^L \rho_0 \dot{\mathbf{u}} \cdot \dot{\mathbf{u}}\, dS \\ W_{ext}(\mathbf{u}) &= [\mathbf{u} \cdot \bar{\mathbf{T}}]_{\Gamma_q} + \int_0^L \mathbf{u} \cdot \hat{\mathbf{W}}\, dS \end{aligned} \tag{3.42}$$

In Eq. 3.42, the stored energy $W(\mathbf{u}, \hat{\mathrm{N}})$ is given as a function of the complementary energy $\chi(\hat{\mathrm{N}})$, for which the constitutive relation reads as $\hat{\mathrm{E}} = d\chi/d\hat{\mathrm{N}}$.

The material time derivative of the Hamiltonian function in Eq. 3.41 gives the so-called *Hamilton equation*

$$\dot{\mathcal{H}} = 0 \tag{3.43}$$

for time-independent boundary conditions and external forces, i.e. for the case that no energy is input into the system. Under these conditions, the Hamiltonian function $\mathcal{H}(\mathbf{u}, \hat{\mathrm{N}})$ is conserved in time with Eq. 3.43 expressing the conservation of total energy.

With the definition of the linear momentum $\mathbf{p}$ and of the angular momentum $\mathbf{L}$ for the cable by

$$\mathbf{p} = \int_0^L \rho_0 \dot{\mathbf{u}}\, dS \quad ; \quad \mathbf{L} = \int_0^L \mathbf{x} \times \rho_0 \dot{\mathbf{u}}\, dS \tag{3.44}$$

it follows that

$$\begin{aligned} \dot{\mathbf{p}} &= [\bar{\mathbf{T}}]_{\Gamma_q} + \int_0^L \hat{\mathbf{W}}\, dS \\ \dot{\mathbf{L}} &= [\mathbf{x} \times \bar{\mathbf{T}}]_{\Gamma_q} + \int_0^L \mathbf{x} \times \hat{\mathbf{W}}\, dS \end{aligned} \tag{3.45}$$

Eqs. 3.43 and 3.45 constitute the Hamiltonian structure of the catenary problem as long as the complementary energy function $\chi(\hat{\mathrm{N}})$ exists.

3.6 Discretization and implementation

The following sections discuss the discretization and implementation of the proposed mixed cable element in time and space. To this end, the different terms in the weak statement of the governing equations are identified.

$$\left\{ \begin{array}{ll} \underbrace{\displaystyle\int_0^L \delta\hat{\mathrm{N}} \left\{ G^{11}\mathbf{u}' \cdot \left(\mathbf{G}_1 + \frac{1}{2}\mathbf{u}' \right) - \hat{\mathrm{E}} \right\} dS}_{\mathbf{r}_1} & = 0 \\ \underbrace{\displaystyle\int_0^L \delta\mathbf{u}' \cdot G^{11}\hat{\mathrm{N}}\mathbf{g}_1\, dS}_{\mathbf{r}_2} + \underbrace{\displaystyle\int_0^L \delta\mathbf{u} \cdot m_0 \ddot{\mathbf{u}}\, dS}_{\mathbf{f}_i} & = \underbrace{[\delta\mathbf{u} \cdot \bar{\mathbf{t}}]_{\Gamma_q} + \displaystyle\int_0^L \delta\mathbf{u} \cdot \hat{\mathbf{W}}\, dS}_{\mathbf{f}_{ext}} \end{array} \right. \tag{3.46}$$

$\mathbf{r}^t = (\mathbf{r}_1, \mathbf{r}_2)$ is the *expanded* stress-divergence term of the proposed cable element, where one identifies the usual stress divergence term $\mathbf{r}_2$ of the principle of virtual work. Also, $\mathbf{f}_i$ and $\mathbf{f}_{ext}$ define the inertia forces and the external forces, respectively. As a result, the weak statement of the catenary problem can be written in compact form as

$$\underbrace{\begin{bmatrix} \mathbf{r}_1(t) \\ \mathbf{r}_2(t) \end{bmatrix}}_{\mathbf{r}(t)} + \begin{bmatrix} \mathbf{0} \\ \mathbf{f}_i(t) \end{bmatrix} = \begin{bmatrix} \mathbf{0} \\ \mathbf{f}_{ext}(t) \end{bmatrix} \tag{3.47}$$

As usual in the context of finite elements, the time domain $\mathcal{I}$ is subdivided into a finite-difference stencil $t_0, t_1, t_2, ..., t_{n-1}, t_n, t_{n+1}, ..., T$ in which the governing equations need to be satisfied. In general, advancing from time step t_n to time step t_{n+1} requires that the governing equations be satisfied at some intermediate time $t_{n+\alpha}$ defined by

$$t_{n+\alpha} = (1-\alpha)t_n + \alpha t_{n+1} \tag{3.48}$$

with $0 < \alpha \leq 1$, so that the governing equations are evaluated in the form

$$\underbrace{\begin{bmatrix} \mathbf{r}_{1,n+\alpha} \\ \mathbf{r}_{2,n+\alpha} \end{bmatrix}}_{\mathbf{r}_{n+\alpha}} + \begin{bmatrix} \mathbf{0} \\ \mathbf{f}_{i,n+\alpha} \end{bmatrix} = \begin{bmatrix} \mathbf{0} \\ \mathbf{f}_{ext,n+\alpha} \end{bmatrix} \tag{3.49}$$

with the notation $\mathbf{a}_{n+\alpha} = \mathbf{a}(t_{n+\alpha})$ for the time-dependent variable $\mathbf{a}(t)$.

3.6.1 Spatial discretization

The discretization in space of the governing equations in Eq. 3.49 requires interpolations for the 2nd PK axial force field $\hat{\mathrm{N}}(\xi^1, t)$, the displacement field $\mathbf{u}(\xi^1, t)$, the velocity field $\mathbf{v}(\xi^1, t)$ and the acceleration field $\mathbf{a}(\xi^1, t)$. In general, different interpolation functions are possible for these independent fields in a mixed finite element formulation [58, Ch.2].

For the 2nd Piola-Kirchhoff axial force field $\hat{\mathrm{N}}(\xi^1, t_n)$, consider a k-th order Galerkin approximation of the form

$$\hat{\mathrm{N}}(\xi^1, t_n) = \sum_{i=1}^{k+1} \varphi_i(\xi^1)\hat{\mathrm{N}}_{i,n} \quad \text{and} \quad \delta\hat{\mathrm{N}}(\xi^1) = \sum_{i=1}^{k+1} \varphi_i(\xi^1)\delta\hat{\mathrm{N}}_i \tag{3.50}$$

with a vector representation in the form

$$\hat{\mathrm{N}}_n = \underbrace{\begin{Bmatrix} \varphi_1 & \varphi_2 & \cdots & \varphi_{k+1} \end{Bmatrix}}_{\boldsymbol{\varphi}^t} \underbrace{\begin{Bmatrix} \hat{\mathrm{N}}_{1,n} \\ \hat{\mathrm{N}}_{2,n} \\ \vdots \\ \hat{\mathrm{N}}_{k+1,n} \end{Bmatrix}}_{\hat{\mathbf{N}}_n} = \boldsymbol{\varphi}^t \hat{\mathbf{N}}_n = \hat{\mathbf{N}}_n^t \boldsymbol{\varphi} \tag{3.51}$$

where $\boldsymbol{\varphi}$ and $\hat{\mathbf{N}}_n$ are $(k+1) \times 1$ arrays.

For the displacement field $\mathbf{u}(\xi^1, t_n)$, consider an l-th order Galerkin approximation of the form

$$\mathbf{u}(\xi^1, t_n) = \sum_{i=1}^{l+1} \phi_i(\xi^1)\mathbf{u}_{i,n} \quad \text{and} \quad \delta\mathbf{u}(\xi^1) = \sum_{i=1}^{l+1} \phi_i(\xi^1)\delta\mathbf{u}_i \tag{3.52}$$

with a vector representation in three dimensions in the form

$$\mathbf{u}_n = \underbrace{\begin{bmatrix} \phi_1 & 0 & 0 & \cdots & \phi_{l+1} & 0 & 0 \\ 0 & \phi_1 & 0 & \cdots & 0 & \phi_{l+1} & 0 \\ 0 & 0 & \phi_1 & \cdots & 0 & 0 & \phi_{l+1} \end{bmatrix}}_{\boldsymbol{\phi}^t} \underbrace{\begin{Bmatrix} u^1_{1,n} \\ u^2_{1,n} \\ u^3_{1,n} \\ \vdots \\ u^1_{l+1,n} \\ u^2_{l+1,n} \\ u^3_{l+1,n} \end{Bmatrix}}_{\hat{\mathbf{u}}_n} = \begin{bmatrix} \boldsymbol{\phi}^t_1 \\ \boldsymbol{\phi}^t_2 \\ \boldsymbol{\phi}^t_3 \end{bmatrix} \hat{\mathbf{u}}_n = \boldsymbol{\phi}^t \hat{\mathbf{u}}_n \tag{3.53}$$

In this case, $\boldsymbol{\phi}$ is a $d(l+1) \times d$ array, while $\hat{\mathbf{u}}_n$ is a $d(l+1) \times 1$ array, with d the dimension of the problem. Using the same shape functions for the reference configuration, $\mathbf{X} = \boldsymbol{\phi}^t \hat{\mathbf{X}}$, the current configuration $\mathbf{x}_n$ at time t_n results from

$$\mathbf{x}_n = \mathbf{X} + \mathbf{u}_n = \boldsymbol{\phi}^t(\hat{\mathbf{X}} + \hat{\mathbf{u}}_n) = \boldsymbol{\phi}^t \hat{\mathbf{x}}_n \tag{3.54}$$

For simplicity, the same l-th order Galerkin approximation is considered for the velocity field $\mathbf{v}(\xi^1, t_n)$ and for the acceleration field $\mathbf{a}(\xi^1, t_n)$, so that

$$\mathbf{v}_n = \begin{bmatrix} \boldsymbol{\phi}^t_1 \\ \boldsymbol{\phi}^t_2 \\ \boldsymbol{\phi}^t_3 \end{bmatrix} \hat{\mathbf{v}}_n = \boldsymbol{\phi}^t \hat{\mathbf{v}}_n \quad \text{and} \quad \mathbf{a}_n = \begin{bmatrix} \boldsymbol{\phi}^t_1 \\ \boldsymbol{\phi}^t_2 \\ \boldsymbol{\phi}^t_3 \end{bmatrix} \hat{\mathbf{a}}_n = \boldsymbol{\phi}^t \hat{\mathbf{a}}_n \tag{3.55}$$

Observing that the interpolations in Eqs. 3.51, 3.53 and 3.55 lump the time dependency of the variables at the nodal values, the 2nd PK axial force field $\hat{\mathrm{N}}_{n+\alpha}$, the displacement field $\mathbf{u}_{n+\alpha}$, the velocity field $\mathbf{v}_{n+\alpha}$ and the acceleration field $\mathbf{a}_{n+\alpha}$ at the configuration $t_{n+\alpha}$ become

$$\begin{aligned} \hat{\mathrm{N}}_{n+\alpha} &= (1-\alpha)\hat{\mathrm{N}}_n + \alpha \hat{\mathrm{N}}_{n+1} \\ \mathbf{u}_{n+\alpha} &= (1-\alpha)\mathbf{u}_n + \alpha \mathbf{u}_{n+1} \\ \mathbf{v}_{n+\alpha} &= (1-\alpha)\mathbf{v}_n + \alpha \mathbf{v}_{n+1} \\ \mathbf{a}_{n+\alpha} &= (1-\alpha)\mathbf{a}_n + \alpha \mathbf{a}_{n+1} \end{aligned} \tag{3.56}$$

3.6.1.1 Stress-divergence term

Introducing the interpolations in Eqs. 3.51 and 3.53 into the stress-divergence term $\mathbf{r}_{n+\alpha}$ in Eq. 3.49 gives the spatial discretization

$$\mathbf{r}_{n+\alpha} = \begin{bmatrix} \delta\hat{\mathbf{N}}^t \mathbf{R}_{1,n+\alpha} \\ \delta\hat{\mathbf{u}}^t \mathbf{R}_{2,n+\alpha} \end{bmatrix} \tag{3.57}$$

where $\delta\hat{\mathbf{N}}^t$ and $\delta\hat{\mathbf{u}}^t$ are arbitrary nodal values for the variations $\delta\hat{\mathrm{N}}$ and $\delta\mathbf{u}$, respectively. As a result, the discretized stress-divergence term $\mathbf{R}_{n+\alpha}$, or simply stress-divergence term, is

given for arbitrary nodal values of the variations by

$$\mathbf{R}_{n+\alpha} = \left[\begin{array}{c} \mathbf{R}_{1,n+\alpha} \\ \mathbf{R}_{2,n+\alpha} \end{array} \right] \tag{3.58}$$

The absence of a derivative of the axial force $\hat{\mathrm{N}}$ in the expanded stress-divergence term $\mathbf{R}_{n+\alpha}$, as corroborated by Eq. 3.46, permits a continuous and a discontinuous representation of the axial force for the cable, as discussed in the following.

3.6.1.1.1 Mixed cable element with continuous axial force

In the case of a continuous axial force distribution, the stress-divergence term $\mathbf{R}_{n+\alpha}$ at the configuration $t_{n+\alpha}$ has components

$$\begin{aligned} \mathbf{R}_{1,n+\alpha} &= \int_{\Omega_e} \boldsymbol{\varphi} \left(\left[G^{11} \hat{\mathbf{u}}^t \boldsymbol{\phi}' \left(\mathbf{G}_1 + \frac{1}{2} (\boldsymbol{\phi}')^t \hat{\mathbf{u}} \right) \right]_{n+\alpha} - \hat{\mathrm{E}}_{n+\alpha} \right) dS \\ \mathbf{R}_{2,n+\alpha} &= \int_{\Omega_e} G^{11} \boldsymbol{\varphi}^t \hat{\mathbf{N}}_{n+\alpha} \, \boldsymbol{\phi}' \hat{\mathbf{g}}_{n+\alpha} \, dS \end{aligned} \tag{3.59}$$

where $\hat{\mathbf{g}}_{n+\alpha} = \mathbf{G}_1 + (\boldsymbol{\phi}')^t \hat{\mathbf{u}}_{n+\alpha}$ is the numerical counterpart to $\mathbf{g}_{1,n+\alpha}$ and the Green-Lagrange strain $\hat{\mathrm{E}}_{n+\alpha}$ is interpolated by $\hat{\mathrm{E}}_{n+\alpha} = (1-\alpha)\hat{\mathrm{E}}_n + \alpha \hat{\mathrm{E}}_{n+1}$, as will become evident in Section 3.6.2.

The consistent linearization of the stress-divergence term $\mathbf{R}_{n+\alpha}$ at the point $\bar{\mathbf{V}}_{n+1} = (\hat{\mathbf{u}}_{n+1}, \hat{\mathbf{N}}_{n+1})$ for the m-th iterate establishes

$$\mathcal{L}\mathbf{R}_{n+\alpha} = \mathbf{R}|_{\bar{\mathbf{V}}^{(m)}_{n+\alpha}} + \underbrace{\left. \frac{\partial \mathbf{R}_{n+\alpha}}{\partial \hat{\mathbf{V}}_{n+1}} \right|_{\bar{\mathbf{V}}^{(m)}_{n+\alpha}} (\hat{\mathbf{V}}^{(m+1)}_{n+1} - \bar{\mathbf{V}}^{(m)}_{n+1})}_{\mathrm{D}\mathbf{R}_{n+\alpha}(\bar{\mathbf{V}}^{(m)}_{n+\alpha}, \Delta \mathbf{V}_{n+1})} \tag{3.60}$$

where $\bar{\mathbf{V}}^{(m)}_{n+\alpha} = (1-\alpha)\bar{\mathbf{V}}_n + \alpha \bar{\mathbf{V}}^{(m)}_{n+1}$. The Fréchet derivative at $\bar{\mathbf{V}}^{(m)}_{n+\alpha}$, $\partial \mathbf{R}_{n+\alpha} / \partial \hat{\mathbf{V}}_{n+1}|_{\bar{\mathbf{V}}^{(m)}_{n+\alpha}}$, represents the static stiffness $\mathbf{K}_s$ of the element in the form of a $d(l+1)+k+1 \times d(l+1)+k+1$ array

$$\mathbf{K}_s = \left. \frac{\partial \mathbf{R}_{n+\alpha}}{\partial \hat{\mathbf{V}}_{n+1}} \right|_{\bar{\mathbf{V}}^{(m)}_{n+\alpha}} = \left[\begin{array}{cc} \mathbf{K_{NN}} & \mathbf{K_{Nu}} \\ \mathbf{K_{uN}} & \mathbf{K_{uu}} \end{array} \right] = \left[\begin{array}{cc} \dfrac{\partial \mathbf{R}_1}{\partial \hat{\mathbf{N}}_{n+1}} & \dfrac{\partial \mathbf{R}_1}{\partial \hat{\mathbf{u}}_{n+1}} \\ \dfrac{\partial \mathbf{R}_2}{\partial \hat{\mathbf{N}}_{n+1}} & \dfrac{\partial \mathbf{R}_2}{\partial \hat{\mathbf{u}}_{n+1}} \end{array} \right] \tag{3.61}$$

with components

$$\begin{aligned}
\mathbf{K_{NN}} &= \frac{\partial \mathbf{R}_1}{\partial \hat{\mathbf{N}}_{n+1}} = -\int_{\Omega_e} \boldsymbol{\varphi} \frac{\partial \hat{\mathrm{E}}_{n+\alpha}}{\partial \hat{\mathbf{N}}_{n+1}}\, dS = -\int_{\Omega_e} \boldsymbol{\varphi} \frac{\partial \hat{\mathrm{E}}_{n+\alpha}}{\partial \hat{\mathrm{N}}_{n+1}} \boldsymbol{\varphi}^t\, dS \\
\mathbf{K_{Nu}} &= \frac{\partial \mathbf{R}_1}{\partial \hat{\mathbf{u}}_{n+1}} = \alpha \int_{\Omega_e} G^{11} \boldsymbol{\varphi} \hat{\mathbf{g}}^t_{n+1} (\boldsymbol{\phi}')^t dS \\
\mathbf{K_{uN}} &= \frac{\partial \mathbf{R}_2}{\partial \hat{\mathbf{N}}_{n+1}} = \alpha \int_{\Omega_e} G^{11} \boldsymbol{\phi}' \hat{\mathbf{g}}_{n+\alpha} \boldsymbol{\varphi}^t\, dS \\
\mathbf{K_{uu}} &= \frac{\partial \mathbf{R}_2}{\partial \hat{\mathbf{u}}_{n+1}} = \alpha \int_{\Omega_e} G^{11} \boldsymbol{\varphi}^t \hat{\mathbf{N}}_{n+\alpha} \boldsymbol{\phi}' (\boldsymbol{\phi}')^t dS
\end{aligned} \tag{3.62}$$

$\mathbf{K_{NN}}$ and $\mathbf{K_{uu}}$ are symmetric. However, only if $\alpha = 1$, $\mathbf{K_{Nu}} = \mathbf{K}^t_{\mathbf{uN}}$, resulting in a symmetric stiffness $\mathbf{K}_s$.

3.6.1.1.2 Mixed cable element with discontinuous axial force

In the case of a discontinuous axial force distribution, the axial forces are treated as internal degrees of freedom rather than as global, and are consequently condensed out at the element level before assembly of the element response. This results in two independent axial force values at the node shared by two adjacent elements, when noting that Eq. 3.46 does not involve derivatives of $\hat{\mathrm{N}}$, so that $\hat{\mathrm{N}} \in H^0(\Omega)$. This permits a discontinuity in the axial force distribution.

The stress-divergence term $\mathbf{R}_{n+\alpha}$ of the element with a discontinuous axial force distribution is interpreted as $\mathbf{R}_{n+\alpha}(\hat{\mathbf{N}}_{n+1}(\hat{\mathbf{u}}_{n+1}), \hat{\mathbf{u}}_{n+1})$ with the axial force values $\hat{\mathbf{N}}_{n+1}$ determined in each element. The stress-divergence term for the global solution strategy is then $\mathbf{R}_{n+\alpha} \equiv \mathbf{R}_{2,n+\alpha}$ and has the form

$$\mathbf{R}_{n+\alpha} = \int_{\Omega_e} G^{11} \boldsymbol{\varphi}^t \hat{\mathbf{N}}_{n+\alpha}\, \boldsymbol{\phi}' \hat{\mathbf{g}}_{n+\alpha}\, dS \tag{3.63}$$

The strain-displacement relation is enforced within each element in the form

$$\int_{\Omega_e} \boldsymbol{\varphi} \hat{\mathrm{E}}_{n+\alpha} dS = \int_{\Omega_e} \boldsymbol{\varphi} \left[G^{11} \hat{\mathbf{u}}^t \boldsymbol{\phi}' \left(\mathbf{G}_1 + \frac{1}{2} (\boldsymbol{\phi}')^t \hat{\mathbf{u}} \right) \right]_{n+\alpha} dS \tag{3.64}$$

which gives a set of equations that can be solved iteratively for the unknown axial forces $\hat{\mathbf{N}}_{n+1}$. If the constitutive relation $\hat{\mathrm{E}}(\hat{\mathbf{N}})$ is linear in $\hat{\mathbf{N}}$, the determination of the axial forces is rather straightforward from the linear system in Eq. 3.64.

The consistent linearization of the stress-divergence term $\mathbf{R}_{n+\alpha}$ at the point $\bar{\mathbf{u}}_{n+1}$ for the m-th iterate gives

$$\mathcal{L}\mathbf{R}_{n+\alpha} = \mathbf{R}|_{\bar{\mathbf{u}}^{(m)}_{n+\alpha}} + \underbrace{\left.\frac{\partial \mathbf{R}_{n+\alpha}}{\partial \hat{\mathbf{u}}_{n+1}}\right|_{\bar{\mathbf{u}}^{(m)}_{n+\alpha}} (\hat{\mathbf{u}}^{(m+1)}_{n+1} - \bar{\mathbf{u}}^{(m)}_{n+1})}_{\mathrm{D}\mathbf{R}_{n+\alpha}(\bar{\mathbf{u}}^{(m)}_{n+\alpha}, \Delta \mathbf{u}_{n+1})} \tag{3.65}$$

where the Fréchet derivative at $\bar{\mathbf{u}}_{n+\alpha}^{(m)}$, $\partial \mathbf{R}_{n+\alpha}/\partial \hat{\mathbf{u}}_{n+1}|_{\bar{\mathbf{u}}_{n+\alpha}^{(m)}}$, represents the condensed static stiffness $\mathbf{K}_{sc}$ of the element in the form of a $d(l+1) \times d(l+1)$ array, and can be derived for a particular iterate from static condensation

$$\mathbf{K_{NN}}\Delta\mathbf{N}_{n+1} + \mathbf{K_{Nu}}\Delta\mathbf{u}_{n+1} = 0 \quad \Rightarrow \quad \Delta\mathbf{N}_{n+1} = -\mathbf{K_{NN}^{-1}}\mathbf{K_{Nu}}\Delta\mathbf{u}_{n+1} \tag{3.66}$$

Consequently,

$$\mathrm{D}\mathbf{R}_{n+\alpha}(\bar{\mathbf{u}}_{n+\alpha}^{(m)}, \Delta\mathbf{u}_{n+1}) = \underbrace{(\mathbf{K_{uu}} - \mathbf{K_{uN}}\mathbf{K_{NN}^{-1}}\mathbf{K_{Nu}})}_{\mathbf{K}_{sc}}\Delta\mathbf{u}_{n+1} \tag{3.67}$$

with the stiffness contributions $\mathbf{K_{NN}}$, $\mathbf{K_{uu}}$ and $\mathbf{K_{Nu}}$ in Eq. 3.62. Analogously to the element with a continuous axial force distribution, the condensed stiffness $\mathbf{K}_{sc}$ for the element with discontinuous axial force distribution is symmetric provided that $\alpha = 1$ and, as a result, it is symmetric for static analysis.

3.6.1.1.3 Stability considerations

The mixed formulation of the nonlinear catenary problem with the displacements $\hat{\mathbf{u}}$ and the 2nd Piola-Kirchhoff axial forces $\hat{\mathbf{N}}$ as unknown independent fields results in the system of equations

$$\underbrace{\begin{bmatrix} \mathbf{K_{NN}} & \mathbf{K_{Nu}} \\ \mathbf{K_{Nu}^t} & \mathbf{K_{uu}} \end{bmatrix}}_{\mathbf{K}(\bar{\mathbf{V}})} \underbrace{\begin{bmatrix} \Delta\hat{\mathbf{N}} \\ \Delta\hat{\mathbf{u}} \end{bmatrix}}_{\Delta\hat{\mathbf{V}}} = \underbrace{\begin{bmatrix} \mathbf{F}_1 \\ \mathbf{F}_2 \end{bmatrix}}_{\mathbf{b}} \tag{3.68}$$

for the static case, where $\mathbf{K}(\bar{\mathbf{V}}) \equiv \mathbf{K}(\bar{\mathbf{u}}, \bar{\mathbf{N}})$ is symmetric. This problem corresponds to the compressible Stokes problem [25, Sec.4.3] and a mathematical discussion of the numerical stability for it is presented in Ref. [8].

Noting that

$$\mathbf{K_{NN}}\Delta\hat{\mathbf{N}} + \mathbf{K_{Nu}}\Delta\hat{\mathbf{u}} = \mathbf{F}_1 \;\; ; \;\; \mathbf{K_{Nu}^t}\Delta\hat{\mathbf{N}} + \mathbf{K_{uu}}\Delta\hat{\mathbf{u}} = \mathbf{F}_2 \tag{3.69}$$

gives

$$\Delta\hat{\mathbf{u}} = \mathbf{K_{uu}^{-1}}(\mathbf{F}_2 - \mathbf{K_{Nu}^t}\Delta\hat{\mathbf{N}}) \tag{3.70}$$

and consequently

$$\underbrace{(\mathbf{K_{NN}} - \mathbf{K_{Nu}}\mathbf{K_{uu}^{-1}}\mathbf{K_{Nu}^t})}_{\boldsymbol{\Xi}}\Delta\hat{\mathbf{N}} = \mathbf{F}_1 - \mathbf{K_{Nu}}\mathbf{K_{uu}^{-1}}\mathbf{F}_2 \tag{3.71}$$

If a mode $\hat{\mathbf{N}}$ exists such that $\boldsymbol{\Xi}\Delta\hat{\mathbf{N}} = \mathbf{0}$, the solution will not be unique and instabilities will arise in the form of spurious modes for the axial forces. To avoid this, it is required that

$$\ker \boldsymbol{\Xi} = \mathbf{0} \tag{3.72}$$

The same considerations hold for the condensed stiffness matrix $\mathbf{K}_{sc}$ in Eq. 3.67, leading to the requirement that

$$\ker \mathbf{K}_{sc} = \mathbf{0} \tag{3.73}$$

While these conditions are satisfied for elastic materials, because of the existence of a one-to-one correspondence between stress and strain, they may not be satisfied for general inelastic materials. Further computational details for inelastic materials are available in Refs. [43] and [58].

3.6.1.2 Inertia forces

The spatial discretization of the inertia forces leads to

$$\mathbf{f}_{i,n+\alpha} = \delta\hat{\mathbf{u}}^t \mathbf{F}_{i,n+\alpha} = \delta\hat{\mathbf{u}}^t \underbrace{\int_0^L m_0 \boldsymbol{\phi}\boldsymbol{\phi}^t \, dS}_{\mathbf{M}} \, \hat{\mathbf{a}}_{n+\alpha} \tag{3.74}$$

where one identifies the mass matrix $\mathbf{M}$ of the element with

$$\mathbf{M} = \int_0^L m_0 \boldsymbol{\phi}\boldsymbol{\phi}^t \, dS \tag{3.75}$$

As a result, the discretized inertia forces $\mathbf{F}_{i,n+\alpha}$ for arbitrary nodal values of the variation $\delta\mathbf{u}$ are given by

$$\mathbf{F}_{i,n+\alpha} = \mathbf{M}\mathbf{a}_{n+\alpha} \tag{3.76}$$

If the corresponding first-order system to Eq. 3.46 is considered with the weak momentum relation

$$\underbrace{\int_0^L \delta\mathbf{v} \cdot m_0 \dot{\mathbf{u}}_{n+\alpha} dS}_{\mathbf{f}_{u,n+\alpha}} = \underbrace{\int_0^L \delta\mathbf{v} \cdot m_0 \mathbf{v}_{n+\alpha} dS}_{\mathbf{f}_{v,n+\alpha}} \tag{3.77}$$

the interpolations in Eqs. 3.53 and 3.55 give

$$\delta\mathbf{u}^t \underbrace{\int_0^L m_0 \boldsymbol{\phi}\boldsymbol{\phi}^t \, dS}_{\mathbf{M}} \dot{\hat{\mathbf{u}}}_{n+\alpha} = \delta\mathbf{u}^t \underbrace{\int_0^L m_0 \boldsymbol{\phi}\boldsymbol{\phi}^t \, dS}_{\mathbf{M}} \hat{\mathbf{v}}_{n+\alpha} \tag{3.78}$$

Consequently, the discrete weak momentum relation for arbitrary nodal values of the variations reads as

$$\underbrace{\mathbf{M}\dot{\hat{\mathbf{u}}}_{n+\alpha}}_{\mathbf{F}_{u,n+\alpha}} = \underbrace{\mathbf{M}\hat{\mathbf{v}}_{n+\alpha}}_{\mathbf{F}_{v,n+\alpha}} \tag{3.79}$$

The particular updates for $\dot{\hat{\mathbf{u}}}_{n+\alpha}$, $\hat{\mathbf{v}}_{n+\alpha}$ and $\hat{\mathbf{a}}_{n+\alpha}$ from time step t_n to time step t_{n+1} produce additional inertia contributions to the stiffness $\mathbf{K}$ of the element, as discussed in Section 3.6.2.

3.6.1.3 External forces

The spatial discretization of the external forces gives

$$\mathbf{f}_{ext,n+\alpha} = \delta\mathbf{u}^t\mathbf{F}_{ext,n+\alpha} = \delta\hat{\mathbf{u}}^t\left([\boldsymbol{\phi}\,\bar{\mathbf{t}}_{n+\alpha}]_{\partial\Omega_e} + \int_{\Omega_e}\boldsymbol{\phi}\,\hat{\mathbf{W}}_{n+\alpha}dS\right) \tag{3.80}$$

where one identifies the discretized external forces $\mathbf{F}_{ext,n+\alpha}$ for arbitrary nodal values of the variation $\delta\mathbf{u}$

$$\mathbf{F}_{ext,n+\alpha} = [\boldsymbol{\phi}\,\bar{\mathbf{t}}_{n+\alpha}]_{\partial\Omega_e} + \int_{\Omega_e}\boldsymbol{\phi}\,\hat{\mathbf{W}}_{n+\alpha}dS \tag{3.81}$$

The Fréchet derivative of the external forces $\mathbf{F}_{ext,n+\alpha}$ with respect to the unknown degrees of freedom gives the contribution of the external forces to the stiffness $\mathbf{K}$ of the element. Consequently, if the external forces do not depend on the unknowns, this contribution vanishes. The following sections consider the latter case for simplicity.

3.6.2 Time discretization

The time discretization of the governing equations in Eq. 3.49 provides the algorithm to advance from time step t_n to time step t_{n+1} of the dynamic response. The following sections give the implementation of the proposed mixed cable element with the Newmark method, the HHT-α method and a new energy-momentum conserving algorithm that preserves the Hamiltonian structure of the catenary problem if a complementary energy function χ for the material model exists.

3.6.2.1 Newmark method

For the Newmark method, the discretized governing equations in Eq. 3.49 are satisfied at time t_{n+1} such that

$$\underbrace{\begin{bmatrix}\mathbf{R}_{1,n+1}\\ \mathbf{R}_{2,n+1}\end{bmatrix}}_{\mathbf{R}_{n+1}} + \begin{bmatrix}\mathbf{0}\\ \mathbf{F}_{i,n+1}\end{bmatrix} = \begin{bmatrix}\mathbf{0}\\ \mathbf{F}_{ext,n+1}\end{bmatrix} \tag{3.82}$$

with the displacement and the velocity fields evolving from time step t_n to time step t_{n+1} according to the Newmark discrete time integrator [12, 37]

$$\begin{cases}\hat{\mathbf{u}}_{n+1} = \hat{\mathbf{u}}_n + \hat{\mathbf{v}}_n\Delta t + \dfrac{1}{2}\left((1-2\beta)\hat{\mathbf{a}}_n + 2\beta\hat{\mathbf{a}}_{n+1}\right)\Delta t^2\\ \hat{\mathbf{v}}_{n+1} = \hat{\mathbf{v}}_n + \left((1-\gamma)\hat{\mathbf{a}}_n + \gamma\hat{\mathbf{a}}_{n+1}\right)\Delta t\end{cases} \tag{3.83}$$

for two algorithmic parameters $0 \leq 2\beta, \gamma \leq 1$ and $\Delta t = t_{n+1} - t_n$. Typical values for these parameters are $\beta = 0.25$ and $\gamma = 0.5$, which correspond to the implicit average acceleration method [12]. Depending on the treatment of the axial forces, the following two implementations are possible.

3.6.2.1.1 Mixed cable element with continuous axial force

For the element with a continuous axial force distribution, the algebraic system of equations to be solved, $\mathbf{\Phi} = \mathbf{0}$, results from introducing the time integrator in Eq. 3.83 into the governing equations in Eq. 3.82, and gives the objective function $\mathbf{\Phi}$ in the form

$$\begin{aligned}\mathbf{\Phi} = &\frac{1}{\beta\Delta t^2}\begin{bmatrix}\mathbf{0}\\ \mathbf{M}\hat{\mathbf{u}}_{n+1}\end{bmatrix} + \mathbf{R}_{n+1} - \begin{bmatrix}\mathbf{0}\\ \mathbf{F}_{ext,n+1}\end{bmatrix}\\ &- \frac{1}{\beta\Delta t^2}\begin{bmatrix}\mathbf{0}\\ \mathbf{M}(\hat{\mathbf{u}}_n + \Delta t_n\hat{\mathbf{v}}_n)\end{bmatrix} - \frac{1-2\beta}{2\beta}\begin{bmatrix}\mathbf{0}\\ \mathbf{M}\hat{\mathbf{a}}_n\end{bmatrix}\end{aligned} \tag{3.84}$$

The consistent linearization of the above system of equations at the point $\bar{\mathbf{V}}_{n+1} = (\hat{\mathbf{u}}_{n+1}, \hat{\mathbf{N}}_{n+1})$ for the m-th iterate establishes

$$\mathcal{L}\mathbf{\Phi} = \mathbf{\Phi}|_{\bar{\mathbf{V}}^{(m)}_{n+1}} + \underbrace{\left.\frac{\partial\mathbf{\Phi}}{\partial\hat{\mathbf{V}}_{n+1}}\right|_{\bar{\mathbf{V}}^{(m)}_{n+1}}(\hat{\mathbf{V}}^{(m+1)}_{n+1} - \bar{\mathbf{V}}^{(m)}_{n+1})}_{\mathrm{D}\mathbf{\Phi}(\bar{\mathbf{V}}^{(m)}_{n+1}, \Delta\mathbf{V}_{n+1})} \tag{3.85}$$

where the Fréchet derivative $\partial\mathbf{\Phi}/\partial\hat{\mathbf{V}}_{n+1}|_{\bar{\mathbf{V}}^{(m)}_{n+1}}$ represents the dynamic stiffness $\mathbf{K}$ of the element in the form

$$\mathbf{K} = \left.\frac{\partial\mathbf{\Phi}}{\partial\hat{\mathbf{V}}_{n+1}}\right|_{\bar{\mathbf{V}}^{(m)}_{n+1}} = \mathbf{K}_s + \frac{1}{\beta\Delta t^2}\begin{bmatrix}\mathbf{0} & \mathbf{0}\\ \mathbf{0} & \mathbf{M}\end{bmatrix} \tag{3.86}$$

with the static stiffness matrix $\mathbf{K}_s$ given in Eq. 3.61, and the mass matrix $\mathbf{M}$ given in Eq. 3.75. As a result, the dynamic stiffness matrix $\mathbf{K}$ is symmetric in this case.

3.6.2.1.2 Mixed cable element with discontinuous axial force

For the element with a discontinuous axial force distribution, the algebraic system of equations to be solved, $\mathbf{\Phi} = \mathbf{0}$, results from introducing the time integrator in Eq. 3.83 into the governing equations in Eq. 3.82 and then condensing out the axial force degrees of freedom. This process results into the objective function $\mathbf{\Phi}$

$$\mathbf{\Phi} = \frac{1}{\beta\Delta t^2}\mathbf{M}\hat{\mathbf{u}}_{n+1} + \mathbf{R}_{n+1} - \mathbf{F}_{ext,n+1} - \frac{1}{\beta\Delta t^2}\mathbf{M}(\hat{\mathbf{u}}_n + \Delta t\hat{\mathbf{v}}_n) - \frac{1-2\beta}{2\beta}\mathbf{M}\hat{\mathbf{a}}_n \tag{3.87}$$

The consistent linearization of the former system of equations at the point $\bar{\mathbf{u}}_{n+1}$ for the m-th iterate establishes

$$\mathcal{L}\mathbf{\Phi} = \mathbf{\Phi}|_{\bar{\mathbf{u}}^{(m)}_{n+1}} + \underbrace{\left.\frac{\partial\mathbf{\Phi}}{\partial\hat{\mathbf{u}}_{n+1}}\right|_{\bar{\mathbf{u}}^{(m)}_{n+1}}(\hat{\mathbf{u}}^{(m+1)}_{n+1} - \bar{\mathbf{u}}^{(m)}_{n+1})}_{\mathrm{D}\mathbf{\Phi}(\bar{\mathbf{u}}^{(m)}_{n+1}, \Delta\mathbf{u}_{n+1})} \tag{3.88}$$

where the Fréchet derivative $\partial\mathbf{\Phi}/\partial\hat{\mathbf{u}}_{n+1}|_{\bar{\mathbf{u}}_{n+1}^{(m)}}$ corresponds to the condensed dynamic stiffness $\mathbf{K}$ of the problem in the form

$$\mathbf{K} = \left.\frac{\partial\mathbf{\Phi}}{\partial\hat{\mathbf{u}}_{n+1}}\right|_{\bar{\mathbf{u}}_{n+1}^{(m)}} = \mathbf{K}_{sc} + \frac{1}{\beta\Delta t^2}\mathbf{M} \tag{3.89}$$

with the condensed static stiffness matrix $\mathbf{K}_{sc}$ given in Eq. 3.67, and the mass matrix $\mathbf{M}$ given in Eq. 3.75. As a result, the dynamic stiffness matrix $\mathbf{K}$ is also symmetric in this case.

3.6.2.2 HHT-α method

For the HHT-α method, the displacement and velocity fields evolve from time step t_n to time step t_{n+1} according to the Newmark time integrator in Eq. 3.83, but the stress divergence term $\mathbf{R}_{n+\alpha}$ is interpolated linearly between the two time steps in the form

$$\mathbf{R}_{n+\alpha} = (1-\alpha)\mathbf{R}_n + \alpha\mathbf{R}_{n+1} \tag{3.90}$$

for $0 < \alpha \leq 1$. Consequently, it is readily concluded that the HHT-α method coincides with the Newmark method when $\alpha = 1$. Hilber *et al.* [24] proposed the collapse of the resulting three-parameter (α, β, γ) method into a one-parameter (α) method that is unconditionally stable in the linear case and displays improved numerical dissipation by selecting

$$\beta = \frac{(2-\alpha)^2}{4} \quad \text{and} \quad \gamma = \frac{3}{2} - \alpha \tag{3.91}$$

The discretized governing equations for the HHT-α method become

$$\underbrace{\alpha\begin{bmatrix}\mathbf{R}_{1,n+1}\\ \mathbf{R}_{2,n+1}\end{bmatrix}}_{\alpha\mathbf{R}_{n+1}} + \underbrace{(1-\alpha)\begin{bmatrix}\mathbf{R}_{1,n}\\ \mathbf{R}_{2,n}\end{bmatrix}}_{(1-\alpha)\mathbf{R}_n} + \begin{bmatrix}\mathbf{0}\\ \mathbf{F}_{i,n+1}\end{bmatrix} = \begin{bmatrix}\mathbf{0}\\ \mathbf{F}_{ext,n+1}\end{bmatrix} \tag{3.92}$$

and the different treatments of the axial force degrees of freedom give the following two implementations.

3.6.2.2.1 Mixed cable element with continuous axial force

For the element with a continuous axial force distribution, the algebraic system of equations to be solved, $\mathbf{\Phi} = \mathbf{0}$, results from introducing the time integrator in Eq. 3.83 into the governing equations in Eq. 3.92, and gives the objective function $\mathbf{\Phi}$ in the form

$$\begin{aligned}\mathbf{\Phi} = &\frac{1}{\beta\Delta t^2}\begin{bmatrix}\mathbf{0}\\ \mathbf{M}\hat{\mathbf{u}}_{n+1}\end{bmatrix} + \alpha\mathbf{R}_{n+1} - \begin{bmatrix}\mathbf{0}\\ \mathbf{F}_{ext,n+1}\end{bmatrix} + (1-\alpha)\mathbf{R}_n\\ &- \frac{1}{\beta\Delta t^2}\begin{bmatrix}\mathbf{0}\\ \mathbf{M}(\hat{\mathbf{u}}_n + \Delta t\hat{\mathbf{v}}_n)\end{bmatrix} - \frac{1-2\beta}{2\beta}\begin{bmatrix}\mathbf{0}\\ \mathbf{M}\hat{\mathbf{a}}_n\end{bmatrix}\end{aligned} \tag{3.93}$$

The consistent linearization of Eq. 3.93 at the point $\bar{\mathbf{V}}_{n+1} = (\hat{\mathbf{u}}_{n+1}, \hat{\mathbf{N}}_{n+1})$ follows from Eq. 3.85, and gives the dynamic stiffness matrix $\mathbf{K}$ of the element in the form

$$\mathbf{K} = \left.\frac{\partial \mathbf{\Phi}}{\partial \hat{\mathbf{V}}_{n+1}}\right|_{\bar{\mathbf{V}}^{(m)}_{n+1}} = \alpha \mathbf{K}_s + \frac{1}{\beta \Delta t^2} \begin{bmatrix} \mathbf{0} & \mathbf{0} \\ \mathbf{0} & \mathbf{M} \end{bmatrix} \tag{3.94}$$

with the static stiffness matrix $\mathbf{K}_s$ in Eq. 3.61 at time t_{n+1}, and the mass matrix $\mathbf{M}$ in Eq. 3.75. As a result, the dynamic stiffness matrix $\mathbf{K}$ is symmetric for this case.

3.6.2.2.2 Mixed cable element with discontinuous axial force

For the element with a discontinuous axial force distribution, the algebraic system of equations to be solved, $\mathbf{\Phi} = \mathbf{0}$, results from introducing the time integrator in Eq. 3.83 into the governing equations in Eq. 3.92 and then condensing out the axial force degrees of freedom. This process results into the objective function $\mathbf{\Phi}$

$$\mathbf{\Phi} = \frac{1}{\beta \Delta t^2}\mathbf{M}\hat{\mathbf{u}}_{n+1} + \alpha \mathbf{R}_{n+1} - \mathbf{F}_{ext,n+1} + (1-\alpha)\mathbf{R}_n - \frac{1}{\beta \Delta t^2}\mathbf{M}(\hat{\mathbf{u}}_n + \Delta t \hat{\mathbf{v}}_n) - \frac{1-2\beta}{2\beta}\mathbf{M}\hat{\mathbf{a}}_n \tag{3.95}$$

The consistent linearization of Eq. 3.95 at the point $\bar{\mathbf{u}}_{n+1}$ follows from Eq. 3.88, and gives the condensed dynamic stiffness matrix $\mathbf{K}$ of the element in the form

$$\mathbf{K} = \alpha \mathbf{K}_{sc} + \frac{1}{\beta \Delta t^2}\mathbf{M} \tag{3.96}$$

with the condensed static stiffness matrix $\mathbf{K}_{sc}$ in Eq. 3.67 at time t_{n+1}, and the mass matrix $\mathbf{M}$ in Eq. 3.75. As a result, the dynamic stiffness matrix $\mathbf{K}$ is also symmetric in this case.

3.6.2.3 Energy-momentum conserving algorithm

The integration of the governing equations with the new energy-momentum conserving, or consistent[1], algorithm considers the catenary problem in first-order form at the intermediate

[1]The proposed algorithm is energy-momentum conserving provided that a complementary energy function χ exists for the material model. Otherwise, the algorithm provides a consistent time integration and is therefore said to be energy-momentum consistent.

configuration $t_{n+1/2}$

$$\begin{cases} \displaystyle\int_0^L \delta\mathbf{v}\cdot m_0 \underbrace{\frac{\mathbf{u}_{n+1}-\mathbf{u}_n}{\Delta t}}_{\dot{\mathbf{u}}_{n+1/2}}\, dS = \int_0^L \delta\mathbf{v}\cdot m_0\mathbf{v}_{n+1/2}\, dS \\ \displaystyle\int_0^L \delta\hat{\mathrm{N}}\left\{\left[G^{11}\mathbf{u}'\cdot\left(\mathbf{G}_1+\frac{1}{2}\mathbf{u}'\right)\right]_{n+1/2} - \hat{\mathrm{E}}_{n+1/2}\right\} dS = 0 \\ \displaystyle\int_0^L \delta\mathbf{u}\cdot m_0 \underbrace{\frac{\mathbf{v}_{n+1}-\mathbf{v}_n}{\Delta t}}_{\mathbf{a}_{n+1/2}}\, dS + \int_0^L \delta\mathbf{u}'\cdot G^{11}\hat{\mathrm{N}}_{n+1/2}\mathbf{g}_{1,n+1/2}\, dS \\ \qquad\qquad = \left[\delta\mathbf{u}\cdot\bar{\mathbf{T}}_{n+1/2}\right]_{\Gamma_q} + \displaystyle\int_0^L \delta\mathbf{u}\cdot\hat{\mathbf{W}}_{n+1/2}\, dS \end{cases} \tag{3.97}$$

If a complementary energy function χ exists for the material model, the physical Green-Lagrange strain $\hat{\mathrm{E}}_{n+1/2}$ is obtained incrementally as

$$\hat{\mathrm{E}}_{n+1/2} = \frac{\chi(\hat{\mathrm{N}}_{n+1}) - \chi(\hat{\mathrm{N}}_n)}{\hat{\mathrm{N}}_{n+1} - \hat{\mathrm{N}}_n} \tag{3.98}$$

with the well-defined limit, for $\hat{\mathrm{N}}_{n+1} = \hat{\mathrm{N}}_n$,

$$\hat{\mathrm{E}} = \left.\frac{d\chi}{d\hat{\mathrm{N}}}\right|_{\hat{\mathrm{N}}_{n+1/2}} \tag{3.99}$$

On the other hand, if no complementary energy function χ exists for the material model, the physical Green-Lagrange strain $\hat{\mathrm{E}}_{n+1/2}$ is given by the usual interpolation with $\alpha = 1/2$

$$\hat{\mathrm{E}}_{n+1/2} = \frac{1}{2}\left(\hat{\mathrm{E}}_{n+1} + \hat{\mathrm{E}}_n\right) \tag{3.100}$$

The principle of virtual work in Eq. 3.97(3) is satisfied in the intermediate configuration $t_{n+1/2}$, while the term in square brackets of the strain-displacement relation in Eq. 3.97(2) corresponds to *the strain average, instead of the strain at the intermediate configuration.* While this fact was established by Simo and Tarnow [44] for the single-field formulation and a St. Venant-Kirchhoff elastic material model, no assumption needs to be made in the present scheme about the constitutive relation.

To show that the time integration scheme in Eq. 3.97 preserves the Hamiltonian structure for a complementary energy function χ, it is necessary to show that the discrete Hamilton equation is satisfied for time-independent boundary conditions and external loads in the form

$$\frac{1}{\Delta t}\left(\mathcal{H}_{n+1} - \mathcal{H}_n\right) = 0 \tag{3.101}$$

where $\mathcal{H}_n = \mathcal{H}(\mathbf{u}_n, \hat{\mathrm{N}}_n)$ is the Hamiltonian function of the system at time t_n as defined in Eq. 3.41. Indeed, adding and subtracting the work done by the strain in the compatibility

equation (last term in Eq. 3.102) to the Hamiltonian increment translates the 2nd PK axial force to the configuration $t_{n+1/2}$,

$$\begin{aligned}\mathcal{H}_{n+1} - \mathcal{H}_n = &\int_0^L \left\{ \hat{\mathrm{N}}_{n+1/2} G^{11} (\mathbf{u}')_{n+1} \cdot \left(\mathbf{G}_1 + \frac{1}{2} (\mathbf{u}')_{n+1} \right) - \chi(\hat{\mathrm{N}}_{n+1}) \right\} dS \\ &- \int_0^L \left\{ \hat{\mathrm{N}}_{n+1/2} G^{11} (\mathbf{u}')_{n} \cdot \left(\mathbf{G}_1 + \frac{1}{2} (\mathbf{u}')_{n} \right) - \chi(\hat{\mathrm{N}}_{n}) \right\} dS \\ &+ \frac{1}{2} \int_0^L \rho_0 \left(\mathbf{v}_{n+1} \cdot \mathbf{v}_{n+1} - \mathbf{v}_n \cdot \mathbf{v}_n \right) dS - (W_{ext,n+1} - W_{ext,n}) \\ &+ \int_0^L (\hat{\mathrm{N}}_{n+1} - \hat{\mathrm{N}}_n) \left[G^{11} \mathbf{u}' \cdot \left(\mathbf{G}_1 + \frac{1}{2} \mathbf{u}' \right) \right]_{n+1/2} dS\end{aligned} \tag{3.102}$$

With the variation $\delta\mathbf{u} = \mathbf{v}_{n+1} - \mathbf{v}_n$ in the weak momentum relation in Eq. 3.97(1) and the variation $\delta\mathbf{u} = \mathbf{x}_{n+1} - \mathbf{x}_n$ in the principle of virtual work in Eq. 3.97(3), and after subtracting the first equation from the second, the energy balance is

$$\int_0^L ((\mathbf{u}')_{n+1} - (\mathbf{u}')_n) \cdot G^{11} \hat{\mathrm{N}}_{n+1/2} \mathbf{g}_{1,n+1/2} \, dS + \int_0^L \mathbf{v}_{n+1/2} \cdot \rho_0 (\mathbf{v}_{n+1} - \mathbf{v}_n) \, dS = W_{ext,n+1} - W_{ext,n} \tag{3.103}$$

noting that, in the configuration $t_{n+1/2}$, it holds that

$$\begin{aligned}\mathbf{v}_{n+1/2} \cdot (\mathbf{v}_{n+1} - \mathbf{v}_n) &= \frac{1}{2} \left(\mathbf{v}_{n+1} \cdot \mathbf{v}_{n+1} - \mathbf{v}_n \cdot \mathbf{v}_n \right) \\ \mathbf{g}_{1,n+1/2} \cdot ((\mathbf{u}')_{n+1} - (\mathbf{u}')_n) &= (\mathbf{u}')_{n+1} \cdot \left(\mathbf{G}_1 + \frac{1}{2} (\mathbf{u}')_{n+1} \right) - (\mathbf{u}')_n \cdot \left(\mathbf{G}_1 + \frac{1}{2} (\mathbf{u}')_n \right)\end{aligned} \tag{3.104}$$

Substituting Eqs. 3.103 and 3.104 into Eq. 3.102, the Hamiltonian increment simplifies to

$$\mathcal{H}_{n+1} - \mathcal{H}_n = \int_0^L \left\{ (\hat{\mathrm{N}}_{n+1} - \hat{\mathrm{N}}_n) \left[G^{11} \mathbf{u}' \cdot \left(\mathbf{G}_1 + \frac{1}{2} \mathbf{u}' \right) \right]_{n+1/2} - \left(\chi(\hat{\mathrm{N}}_{n+1}) - \chi(\hat{\mathrm{N}}_n) \right) \right\} dS \tag{3.105}$$

Eq. 3.105 can be interpreted as the compatibility equation in Eq. 3.97(2) with $\delta\hat{\mathrm{N}} = \hat{\mathrm{N}}_{n+1} - \hat{\mathrm{N}}_n$. As a result, the Hamiltonian increment $\mathcal{H}_{n+1} - \mathcal{H}_n$ vanishes provided that

$$\chi(\hat{\mathrm{N}}_{n+1}) - \chi(\hat{\mathrm{N}}_n) = (\hat{\mathrm{N}}_{n+1} - \hat{\mathrm{N}}_n) \hat{\mathrm{E}} \tag{3.106}$$

which is automatically satisfied by the incremental definition of the physical Green-Lagrange strain in Eq. 3.98.

The discrete conservation of linear and angular momentum is proven by inserting the variations $\delta\mathbf{u}_1 = \boldsymbol{\eta}$ and $\delta\mathbf{u}_2 = \boldsymbol{\eta} \times \mathbf{x}^{n+1/2}$ with $\boldsymbol{\eta}$ constant in the principle of virtual work in

Eq. 3.97(3) to give

$$\begin{aligned}\frac{1}{\Delta t}(\mathbf{p}_{n+1}-\mathbf{p}_n) &= [\bar{\mathbf{T}}_{n+1/2}]_{\Gamma_q} + \int_0^L \hat{\mathbf{W}}_{n+1/2}\,dS \\ \frac{1}{\Delta t}(\mathbf{L}_{n+1}-\mathbf{L}_n) &= [\mathbf{x}_{n+1/2}\times\bar{\mathbf{T}}_{n+1/2}]_{\Gamma_q} + \int_0^L \mathbf{x}_{n+1/2}\times\hat{\mathbf{W}}_{n+1/2}\,dS\end{aligned} \tag{3.107}$$

Eqs. 3.101 and 3.107 establish the discrete Hamiltonian structure of the proposed time integration scheme.

If the external loads are time-dependent, the discrete energy conservation follows from Eq. 3.103 in the form

$$W_{n+1}-W_n+K_{n+1}-K_n = [(\mathbf{u}_{n+1}-\mathbf{u}_n)\cdot\bar{\mathbf{T}}_{n+1/2}]_{\Gamma_q} + \int_0^L (\mathbf{u}_{n+1}-\mathbf{u}_n)\cdot\hat{\mathbf{W}}_{n+1/2}\,dS \tag{3.108}$$

Introducing the interpolation functions in Eqs. 3.51, 3.53 and 3.55 into Eq. 3.97 gives the governing equations for the energy-momentum conserving, or consistent, algorithm in the form

$$\underbrace{\begin{bmatrix}\mathbf{R}_{1,n+1/2}\\ \mathbf{R}_{2,n+1/2}\\ \mathbf{0}\end{bmatrix}}_{\mathbf{R}_{n+1/2}} + \begin{bmatrix}\mathbf{0}\\ \mathbf{F}_{i,n+1/2}\\ \mathbf{F}_{u,n+1/2}-\mathbf{F}_{v,n+1/2}\end{bmatrix} = \begin{bmatrix}\mathbf{0}\\ \mathbf{F}_{ext,n+1/2}\\ \mathbf{0}\end{bmatrix} \tag{3.109}$$

The consideration of a continuous or a discontinuous axial force field gives the following two possible implementations.

3.6.2.3.1 Mixed cable element with continuous axial force

In the case of a continuous axial force distribution and considering the state-space degrees of freedom $\hat{\mathbf{u}}_{n+1}$ and $\hat{\mathbf{v}}_{n+1}$, the governing equations in Eq. 3.109 in the algebraic form $\mathbf{\Phi}=\mathbf{0}$ give the objective function $\mathbf{\Phi}$

$$\mathbf{\Phi} = \begin{bmatrix}\mathbf{0} & \mathbf{0}\\ \mathbf{0} & \frac{1}{\Delta t}\mathbf{M}\\ \frac{1}{\Delta t}\mathbf{M} & -\frac{1}{2}\mathbf{M}\end{bmatrix}\begin{bmatrix}\hat{\mathbf{u}}_{n+1}\\ \hat{\mathbf{v}}_{n+1}\end{bmatrix} + \mathbf{R}_{n+1/2} - \begin{bmatrix}\mathbf{0}\\ \mathbf{F}_{ext,n+1/2}\\ \mathbf{0}\end{bmatrix} - \begin{bmatrix}\mathbf{0} & \mathbf{0}\\ \mathbf{0} & \frac{1}{\Delta t}\mathbf{M}\\ \frac{1}{\Delta t}\mathbf{M} & \frac{1}{2}\mathbf{M}\end{bmatrix}\begin{bmatrix}\hat{\mathbf{u}}_{n}\\ \hat{\mathbf{v}}_{n}\end{bmatrix} \tag{3.110}$$

The consistent linearization of the objective function $\mathbf{\Phi}$ at the state-space point $\bar{\mathbf{V}}_{n+1} = (\hat{\mathbf{N}}_{n+1}, \hat{\mathbf{u}}_{n+1}, \hat{\mathbf{v}}_{n+1})$ for the m-th iterate establishes

$$\mathcal{L}\mathbf{\Phi} = \mathbf{\Phi}|_{\bar{\mathbf{V}}^{(m)}_{n+1}} + \underbrace{\left.\frac{\partial\mathbf{\Phi}}{\partial\hat{\mathbf{V}}_{n+1}}\right|_{\bar{\mathbf{V}}^{(m)}_{n+1}}(\hat{\mathbf{V}}^{(m+1)}_{n+1}-\bar{\mathbf{V}}^{(m)}_{n+1})}_{\mathrm{D}\mathbf{\Phi}(\bar{\mathbf{V}}^{(m)}_{n+1},\Delta\mathbf{V}_{n+1})} \tag{3.111}$$

where the Fréchet derivative $\partial\mathbf{\Phi}/\partial\hat{\mathbf{V}}_{n+1}|_{\hat{\mathbf{V}}^{(m)}_{n+1}}$ corresponds to the dynamic stiffness $\mathbf{K}$ of the element in the form

$$\mathbf{K} = \left.\frac{\partial\mathbf{\Phi}}{\partial\hat{\mathbf{V}}_{n+1}}\right|_{\bar{\mathbf{V}}^{(m)}_{n+1}} = \begin{bmatrix} \mathbf{K_{NN}} & \mathbf{K_{Nu}} & \mathbf{0} \\ \mathbf{K_{uN}} & \mathbf{K_{uu}} & \frac{1}{\Delta t}\mathbf{M} \\ \mathbf{0} & \frac{1}{\Delta t}\mathbf{M} & -\frac{1}{2}\mathbf{M} \end{bmatrix} = \left[\begin{array}{cc|c} \multicolumn{2}{c|}{\mathbf{K}_s} & \frac{1}{\Delta t}\mathbf{M} \\ \hline \mathbf{0} & \frac{1}{\Delta t}\mathbf{M} & -\frac{1}{2}\mathbf{M} \end{array}\right] \tag{3.112}$$

with the static stiffness matrix $\mathbf{K}_s$ in Eq. 3.61 at time $t_{n+1/2}$, and the mass matrix $\mathbf{M}$ in Eq. 3.75. Equation 3.112 shows that the dynamic stiffness $\mathbf{K}$ is non-symmetric due to the different configurations at which $\mathbf{K_{Nu}}$ and $\mathbf{K_{uN}}$ are evaluated, a common feature in energy-momentum conserving algorithms.

In this solution strategy, the state-space vector $\bar{\mathbf{V}}_{n+1} = (\hat{\mathbf{N}}_{n+1}, \hat{\mathbf{u}}_{n+1}, \hat{\mathbf{v}}_{n+1})$ is used to treat the velocities as independent degrees of freedom. This treatment relaxes the pointwise relationship between $\dot{\mathbf{u}}$ and $\mathbf{v}$, so that it is satisfied in the weak sense [20, 31]. It is also possible to apply this relationship pointwise, as described in Section 3.6.2.3.3. In this case, the global DOFs comprise only the displacements $\hat{\mathbf{u}}_{n+1}$ and the 2nd PK axial forces $\hat{\mathbf{N}}_{n+1}$.

3.6.2.3.2 Mixed cable element with discontinuous axial force

In the case of a discontinuous axial force distribution and considering the state-space degrees of freedom $\hat{\mathbf{u}}_{n+1}$ and $\hat{\mathbf{v}}_{n+1}$, the governing equations in Eq. 3.109 in the algebraic form $\mathbf{\Phi} = \mathbf{0}$ give the objective function $\mathbf{\Phi}$, after the static condensation of the axial forces,

$$\mathbf{\Phi} = \begin{bmatrix} \mathbf{0} & \frac{1}{\Delta t}\mathbf{M} \\ \frac{1}{\Delta t}\mathbf{M} & -\frac{1}{2}\mathbf{M} \end{bmatrix} \begin{bmatrix} \hat{\mathbf{u}}_{n+1} \\ \hat{\mathbf{v}}_{n+1} \end{bmatrix} + \mathbf{R}_{n+1/2} - \begin{bmatrix} \mathbf{F}_{ext,n+1/2} \\ \mathbf{0} \end{bmatrix} - \begin{bmatrix} \mathbf{0} & \frac{1}{\Delta t}\mathbf{M} \\ \frac{1}{\Delta t}\mathbf{M} & \frac{1}{2}\mathbf{M} \end{bmatrix} \begin{bmatrix} \hat{\mathbf{u}}_{n} \\ \hat{\mathbf{v}}_{n} \end{bmatrix} \tag{3.113}$$

The consistent linearization of the objective function $\mathbf{\Phi}$ at the state-space point $\bar{\mathbf{V}}_{n+1} = (\hat{\mathbf{u}}_{n+1}, \hat{\mathbf{v}}_{n+1})$ for the m-th iterate gives

$$\mathcal{L}\mathbf{\Phi} = \mathbf{\Phi}|_{\bar{\mathbf{V}}^{(m)}_{n+1}} + \underbrace{\left.\frac{\partial\mathbf{\Phi}}{\partial\hat{\mathbf{V}}_{n+1}}\right|_{\bar{\mathbf{V}}^{(m)}_{n+1}} (\hat{\mathbf{V}}_{n+1} - \bar{\mathbf{V}}^{(m)}_{n+1})}_{\mathrm{D}\mathbf{\Phi}(\bar{\mathbf{V}}^{(m)}_{n+1}, \Delta\mathbf{V}_{n+1})} \tag{3.114}$$

where the Fréchet derivative $\partial\mathbf{\Phi}/\partial\hat{\mathbf{V}}_{n+1}|_{\hat{\mathbf{V}}^{(m)}_{n+1}}$ corresponds to the condensed dynamic stiffness $\mathbf{K}$ of the element in the form

$$\mathbf{K} = \left.\frac{\partial\mathbf{\Phi}}{\partial\hat{\mathbf{V}}_{n+1}}\right|_{\bar{\mathbf{V}}^{(m)}_{n+1}} = \begin{bmatrix} \mathbf{K}_{sc} & \frac{1}{\Delta t}\mathbf{M} \\ \frac{1}{\Delta t}\mathbf{M} & -\frac{1}{2}\mathbf{M} \end{bmatrix} \tag{3.115}$$

with the condensed static stiffness matrix $\mathbf{K}_{sc}$ in Eq. 3.67 at time $t_{n+1/2}$, and the mass matrix $\mathbf{M}$ in Eq. 3.75. The dynamic stiffness $\mathbf{K}$ of the element with a discontinuous axial force distribution is also non-symmetric.

The pointwise relationship between $\dot{\mathbf{u}}$ and $\mathbf{v}$ can also be used with a discontinuous axial force field if desired, as discussed in the following section. In this case, the displacements $\hat{\mathbf{u}}_{n+1}$ are the only global DOFs of the problem.

3.6.2.3.3 Pointwise momentum relation

The use of the state-space DOFs $\hat{\mathbf{u}}_{n+1}$ and $\hat{\mathbf{v}}_{n+1}$ may restrict the generality of the algorithm in some applications, especially when combining different element types in the same structural model. In such cases, it may be advantageous to use the pointwise relationship between the displacement $\mathbf{u}$ and the velocity $\mathbf{v}$, either with a continuous or with a discontinuous axial force field.

The strong form of Eq. 3.97(1) is

$$\frac{1}{\Delta t}(\mathbf{u}_{n+1} - \mathbf{u}_n) = \mathbf{v}_{n+1/2} = \frac{1}{2}(\mathbf{v}_{n+1} + \mathbf{v}_n) \tag{3.116}$$

corresponding to the linear approximation of $\mathbf{v}_{n+1}$

$$\mathbf{v}_{n+1} = \frac{2}{\Delta t}(\mathbf{u}_{n+1} - \mathbf{u}_n) - \mathbf{v}_n \tag{3.117}$$

As a result, the discrete form of the principle of virtual work

$$\frac{1}{\Delta t}\mathbf{M}(\hat{\mathbf{v}}_{n+1} - \hat{\mathbf{v}}_n) + \mathbf{R}_{2,n+1/2} = \mathbf{F}_{ext,n+1/2} \tag{3.118}$$

can be rewritten as

$$\frac{2}{\Delta t^2}\mathbf{M}(\hat{\mathbf{u}}_{n+1} - \hat{\mathbf{u}}_n) + \mathbf{R}_{2,n+1/2} = \frac{2}{\Delta t}\mathbf{M}\hat{\mathbf{v}}_n + \mathbf{F}_{ext,n+1/2} \tag{3.119}$$

and the objective function $\mathbf{\Phi}$ for the continuous axial force implementation becomes

$$\mathbf{\Phi} = \frac{2}{\Delta t^2}\begin{bmatrix} \mathbf{0} \\ \mathbf{M}\hat{\mathbf{u}}_{n+1} \end{bmatrix} + \mathbf{R}_{n+1/2} - \begin{bmatrix} \mathbf{0} \\ \mathbf{F}_{ext,n+1/2} \end{bmatrix} - \frac{2}{\Delta t}\begin{bmatrix} \mathbf{0} & \mathbf{0} \\ \frac{1}{\Delta t}\mathbf{M} & \mathbf{M} \end{bmatrix}\begin{bmatrix} \hat{\mathbf{u}}_n \\ \hat{\mathbf{v}}_n \end{bmatrix} \tag{3.120}$$

while the objective function $\mathbf{\Phi}$ for the discontinuous axial force implementation is

$$\mathbf{\Phi} = \frac{2}{\Delta t^2}\mathbf{M}\mathbf{u}_{n+1} + \mathbf{R}_{n+1/2} - \mathbf{F}_{ext,n+1/2} - \frac{2}{\Delta t}\begin{bmatrix} \frac{1}{\Delta t}\mathbf{M} & \mathbf{M} \end{bmatrix}\begin{bmatrix} \hat{\mathbf{u}}_n \\ \hat{\mathbf{v}}_n \end{bmatrix} \tag{3.121}$$

The system of equations $\mathbf{\Phi} = \mathbf{0}$ is then solved by an appropriate iterative algorithm such as Newton's method. The corresponding dynamic stiffness matrices result from the linearization of the objective function $\mathbf{\Phi}$ in the form

$$\mathbf{K} = \mathbf{K}_s + \frac{2}{\Delta t^2}\begin{bmatrix} \mathbf{0} & \mathbf{0} \\ \mathbf{0} & \mathbf{M} \end{bmatrix} \tag{3.122}$$

for the continuous formulation, and in the form

$$\mathbf{K} = \mathbf{K}_{sc} + \frac{2}{\Delta t^2}\mathbf{M} \tag{3.123}$$

for the discontinuous formulation.

3.6.2.4 Filtering the dynamic response

The time discretization of the dynamic response may give rise to undesirable high-frequency oscillations [15, 47]. It is therefore important to eliminate these without compromising any properties of the algorithm used.

The filtering of the dynamic response can be introduced into the time integration scheme with two different methods: a) the governing equations of the filter are added at the element level [32]; or b) a postprocessing of the dynamic response is used. This study adopts the second approach because the first approach may be computationally expensive for large structures and the derivation of the consistent tangent may be difficult for complex filters.

A digital filter operator L of width N acting on a discrete signal f_k is defined in the frequency domain by the discrete convolution

$$L[f_k] = (a * f)_k = \sum_{n=-N}^{N} a_n f_{k-n} \tag{3.124}$$

where the values of a_n define the filter coefficients. Because polynomials are often selected as shape functions in finite elements, a Savitzky-Golay filter [41] is adopted for the smoothing of the dynamic response. The $2m$-order Savitzky-Golay filter of width N uses least squares to fit a polynomial of degree $2m+1$ to $2N+1$ adjacent data. Explicit coefficients a_n for the cases $2m \in \{0, 2, 4\}$ are available in Ref. [10].

The Savitzky-Golay filter has the following relevant properties for the problem at hand:

1. If p_{2m+1} is a polynomial of, at most, degree $2m+1$, the Savitzky-Golay filter of order $2m$, D_{2m}, conserves every polynomial signal of degree up to $2m+1$,

   $$D_{2m}[p_{2m+1}] = p_{2m+1} \tag{3.125}$$

   Among all filters of width N having this property, the Savitzky-Golay filter ensures maximum noise reduction for stationary noise [9].

2. If the n-th moment μ_n of a signal f is defined as

   $$\mu_n(f) = \sum_{k=-\infty}^{\infty} f_k k^n \quad n = 0, 1, ... \tag{3.126}$$

   it can be shown that the moments of the original signal are identical with those of the filtered signal [9],

   $$\mu_n(D_{2m}[f]) = \mu_n(f) \quad n = 0, 1, ... \tag{3.127}$$

   Consequently, the energy of the filtered signal is conserved on average.

The Savitzky-Golay filter can thus be understood as the truncation of the Taylor expansion T_{2m+1} of the signal f to order $2m+1$

$$D_{2m}[f] \approx D_{2m}[T_{2m+1}] = T_{2m+1} \approx f \tag{3.128}$$

This interpretation is used to select the frame length of the filter in terms of the dominant period of the signal as a multiple of its half period or of its full period for simplicity. The order of the filter is selected according to the number of data points in the frame length: it is desirable to capture as many polynomial orders as possible without including the high frequencies with the selection of too high a filter order. An empirical relation of three to four data points to one polynomial coefficient (3-4:1 rule) seems to give excellent results in free vibration, while a more restrictive smoothing rule of 6:1-7:1 may be required for earthquake excitations, as discussed in Section 4.3.

3.7 Form finding problem

At the start of the cable analysis, a shape finding or form finding problem arises because typically the initial length of the cable and the span between supports are specified.

The form finding problem is addressed in several studies to date and an overview of prevailing methods for it is available in Ref. [55]. Most commonly, two methods are used involving the following procedures:

1. Release some degrees of freedom at the fixed supports and impose appropriate support displacements to obtain the desired span, either statically as a boundary condition (*stiffness matrix methods*), or dynamically in a pseudo-time approach (*dynamic equilibrium methods*) [5].

2. Apply a constraint for imposing the known length of the cable and derive the corresponding extension of the stiffness matrix (*geometric stiffness methods*) [22, 23].

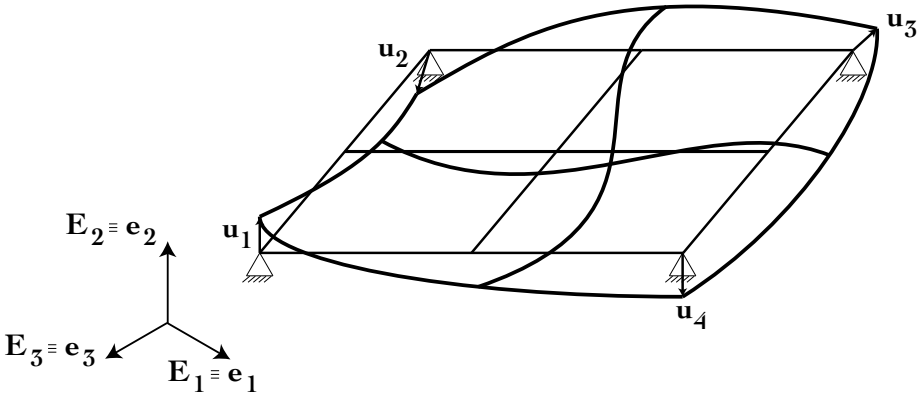

Figure 3.4: Form finding strategy according to Argyris *et al.* [5].

The present study uses the former method by Argyris *et al.* [5] in a static manner, as illustrated in Fig. 3.4 for a simple cable net with a plane reference configuration. This ap-

proach is always possible for cables because they are modeled as one-dimensional manifolds. In general, it may be difficult to establish the displacement field of a flat reference configuration for the desired span. However, because the proposed formulation assumes a general reference configuration, the adopted procedure is also suitable for any non-flat initial shape, thus making it easier to find such a displacement field.

3.8 Concluding remarks

This chapter proposes a new family of cable elements based on finite deformations and a weakly-compatible mixed finite-element approach. To begin with, the kinematics of the catenary problem in general curvilinear coordinates are derived and the kinematic variables are identified. Afterwards, dual test functions for the strong form of the governing equations are considered to obtain the principle of virtual work and the weak form of the stress-displacement relation. The weak statement of the problem at hand gives two possible implementations for the proposed mixed cable element: one with a continuous axial force distribution and one with a discontinuous axial force distribution.

This chapter also presents a new energy-momentum conserving algorithm for the dynamic analysis of cable structures. The developments show that the discrete Hamilton equation and the discrete balance equations of linear and angular momentum are exactly conserved for this algorithm, as opposed to classical integration schemes such as the Newmark method or the HHT-α method.

Chapter 4
Nonlinear elastic material models

This chapter presents the validation of the proposed 3d cable element and of the new energy-momentum conserving algorithm under nonlinear elastic material response. This assessment compares the results of the proposed formulation with those of reference elements and time integration schemes for a few simple structural models.

The discussion begins with a brief summary of the relevant nonlinear elastic material models for cables, and continues with the analysis of several benchmark problems that assess the static and dynamic response with the formulations. These benchmark problems correspond to examples from the literature [1, 3, 11, 26, 52, 54], and include distributed and concentrated loads, in-plane and out-of-plane free vibration and earthquake response.

4.1 Nonlinear elastic material models

The proposed formulation for nonlinear static and dynamic analysis of cables supports any constitutive relation of the form $\hat{\mathrm{N}} - \Psi(\hat{\mathrm{E}}, \kappa) = 0$, as stated in Eq. 3.32. In the context of elastic material behavior, two models are relevant for cables [19, Ch.2]: a St. Venant-Kirchhoff elastic material as an extension of linear elasticity to finite deformations and a compressible neo-Hookean material. A brief description of these material models is provided below and additional information can be found in Ref. [58].

4.1.1 St. Venant-Kirchhoff elasticity

For a St. Venant-Kirchhoff elastic material, the stored energy $\mathcal{U}$ per unit reference length can be expressed in terms of the stretch λ as

$$\mathcal{U}(\lambda) = \frac{E}{8}\left(\lambda^2 - 1\right)^2 \tag{4.1}$$

where E represents the Young modulus under finite deformation.

The 2nd Piola-Kirchhoff stress $\hat{\mathrm{S}}$ in the physical basis becomes

$$\hat{\mathrm{S}} = \frac{d\mathcal{U}}{d\hat{\mathrm{E}}} = \frac{\partial \mathcal{U}}{\partial \lambda}\frac{\partial \lambda}{\partial \hat{\mathrm{E}}} = \frac{E}{2}(\lambda^2 - 1) = E\,\hat{\mathrm{E}} \tag{4.2}$$

and the constitutive relation between the 2nd Piola-Kirchhoff axial force $\hat{\mathrm{N}}$ and the Green-Lagrange strain $\hat{\mathrm{E}}$ can be written as

$$\hat{\mathrm{N}} - \hat{\mathrm{N}}_0 = (EA)\hat{\mathrm{E}} \tag{4.3}$$

where A is the cross-sectional area and $\hat{\mathrm{N}}_0$, the prestressing force. Figure 4.1 compares the stress-strain relation of the St. Venant-Kirchhoff material model (SV) to the compressible neo-Hookean model (NH).

If the cross-sectional stiffness is independent of the axial force,

$$\frac{\partial \hat{\mathrm{E}}}{\partial \hat{\mathbf{N}}} = \frac{\partial \hat{\mathrm{E}}}{\partial \hat{\mathrm{N}}}\frac{\partial \hat{\mathrm{N}}}{\partial \hat{\mathbf{N}}} = \frac{\boldsymbol{\varphi}^t}{EA} \tag{4.4}$$

For St. Venant-Kirchhoff elastic materials, $\hat{\mathrm{n}} - \hat{\mathrm{n}}_0 = \lambda(\hat{\mathrm{N}} - \hat{\mathrm{N}}_0) \to +\infty$ as $\lambda \to +\infty$. Nevertheless, it is important to note that these elastic materials may misbehave because $\hat{\mathrm{N}} - \hat{\mathrm{N}}_0$ is finite for $\lambda = 0$ (Eqs. 4.2 and 4.3). Also, the model is single-valued in tension, as desired.

The complementary energy χ per unit reference length is expressed in terms of the 2nd PK axial force $\hat{\mathrm{N}}$ as

$$\chi(\hat{\mathrm{N}}) = (\hat{\mathrm{N}} - \hat{\mathrm{N}}_0)\hat{\mathrm{E}} - \mathcal{U} = \frac{1}{2EA}(\hat{\mathrm{N}} - \hat{\mathrm{N}}_0)^2 \tag{4.5}$$

4.1.2 Compressible neo-Hookean elasticity

In a compressible neo-Hookean material model, the stored energy $\mathcal{U}$ per unit reference length is related to the stretch λ as

$$\mathcal{U}(\lambda) = E\left(\frac{1}{4}(\lambda^2 - 1) - \frac{1}{2}\ln\lambda\right) \tag{4.6}$$

In this case, the 2nd Piola-Kirchhoff stress $\hat{\mathrm{S}}$ in the physical basis becomes

$$\hat{\mathrm{S}} = \frac{d\mathcal{U}}{d\hat{\mathrm{E}}} = \frac{\partial \mathcal{U}}{\partial \lambda}\frac{\partial \lambda}{\partial \hat{\mathrm{E}}} = \frac{E}{2}\left(1 - \frac{1}{\lambda^2}\right) \tag{4.7}$$

and the constitutive relation for the 2nd Piola-Kirchhoff axial force $\hat{\mathrm{N}}$ can be expressed in terms of the stretch λ by

$$\hat{\mathrm{N}} - \hat{\mathrm{N}}_0 = \frac{EA}{2}\left(1 - \frac{1}{\lambda^2}\right) \tag{4.8}$$

Figure 4.1 compares the stress-strain relation of the compressible neo-Hookean material model (NH) to the St. Venant-Kirchhoff material model (SV).

For compressible neo-Hookean elastic materials, $\hat{\mathrm{n}} - \hat{\mathrm{n}}_0 = \lambda(\hat{\mathrm{N}} - \hat{\mathrm{N}}_0) \to +\infty$ as $\lambda \to +\infty$ and $\hat{\mathrm{N}} - \hat{\mathrm{N}}_0 \to -\infty$ as $\lambda \to 0$, as desired. Moreover, if the cross-sectional stiffness is independent of the axial force,

$$\frac{\partial \hat{\mathrm{E}}}{\partial \hat{\mathbf{N}}} = \frac{\partial \hat{\mathrm{E}}}{\partial \lambda}\frac{\partial \lambda}{\partial \hat{\mathrm{N}}}\frac{\partial \hat{\mathrm{N}}}{\partial \hat{\mathbf{N}}} = \frac{\lambda^4}{EA}\boldsymbol{\varphi}^t \tag{4.9}$$

As is the case for the St. Venant-Kirchhoff elastic model, the compressible neo-Hookean elastic model is single-valued in tension.

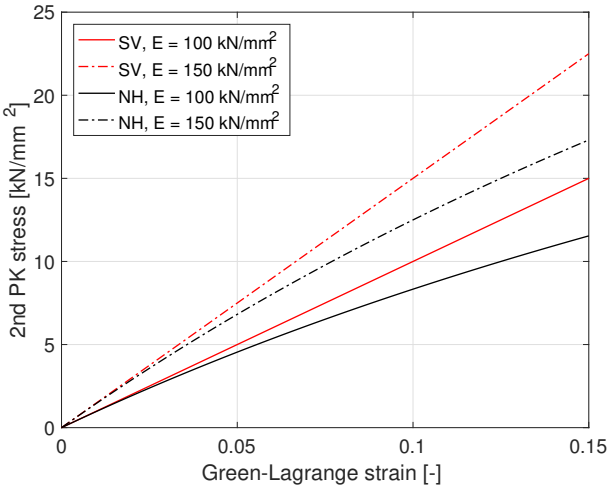

Figure 4.1: Stress - strain relation for the two elastic material models.

The complementary energy χ per unit reference length in terms of the axial force $\hat{\mathrm{N}}$ is given implicitly as a function of $\lambda = \lambda(\hat{\mathrm{N}})$ by

$$\chi(\hat{\mathrm{N}}) = (\hat{\mathrm{N}} - \hat{\mathrm{N}}_0)\hat{\mathrm{E}} - \mathcal{U} = \frac{EA}{2}\left(\ln\lambda - \frac{\lambda^2 - 1}{2\lambda^2}\right) \tag{4.10}$$

with

$$\lambda^2 = \frac{EA}{EA - 2(\hat{\mathrm{N}} - \hat{\mathrm{N}}_0)} \tag{4.11}$$

4.2 Static analysis

For the static analysis, the proposed formulation is implemented in two cable finite elements, one with a continuous axial force distribution and another with a discontinuous one.

These elements are deployed in the general purpose finite element program FEAP [51] and in the Matlab toolbox FEDEASLab [18] for conducting the following numerical studies. The elements use a linear approximation for the axial forces ($k = 1$) and a quadratic approximation for the displacements ($l = 2$). Fig. 4.2 depicts the Lagrange polynomials for the interpolation functions of the element that results, for the continuous formulation, in eight degrees of freedom (DOFs) in 2d, six displacement DOFs (◯) and two axial force DOFs (•); and in eleven DOFs in 3d, nine displacement DOFs (◯) and two axial force DOFs (•). The discontinuous formulation condenses out the axial force degrees of freedom at the element level and thus the corresponding DOFs do not appear in the global solution.

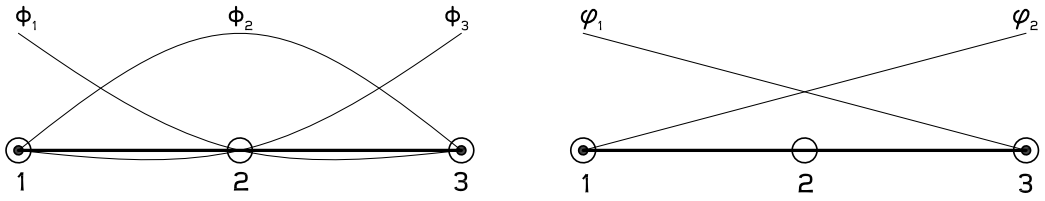

Figure 4.2: Interpolation functions for displacements (left) and axial forces (right).

In the following, the proposed elements are used to investigate several examples from the literature. For the element with a continuous axial force distribution, an initial guess for the axial forces and for the displacements is required, while, for the element with a discontinuous axial force distribution, only an initial guess for the displacements is required, as will be discussed for each example.

4.2.1 Example 1: Cable under self-weight

The simplest model for study consists of a horizontal elastic cable under its own weight. Fig. 4.3 and Table 4.1 list the geometric and material properties of the cable that was previously studied in Ahmad Abad *et al.* [1], Andreu *et al.* [3], Thai and Kim [52] and Tibert [54]. A St. Venant-Kirchhoff material model and a neo-Hookean material model are considered for the cable. Following Argyris *et al.* [5], the deformed shape is obtained by assuming a straight horizontal reference configuration and imposing a support displacement of $\Delta\mathbf{u} = (0, -7.93)$ m at the right support, as shown in Fig. 4.4.

Using a mesh of equal-size elements, Fig. 4.5 shows the maximum cable sag at midspan, as a function of the number of elements for both elastic material models. The continuous and the discontinuous formulations are compared to the corotational elastic truss element discussed in Section 2.2.1. An initial shape following a hyperbolic-cosine function is assumed for the vertical displacements as the starting guess of the Newton-Raphson iterative solution and a constant axial force of 15 kN is assumed for the continuous formulation. Note that

Property	Value
Cross-sectional area	548.4 mm^2
Elastic modulus	131.0 kN/mm^2
Cable self-weight	46.12 N/m
Cable length	312.73 m

Table 4.1: Geometric and material properties for Example 1.

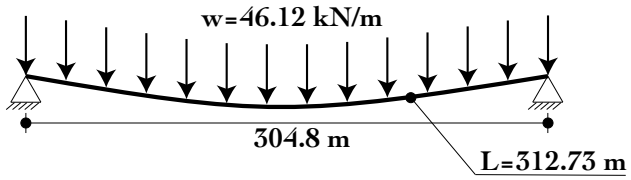

Figure 4.3: Structural model for Example 1.

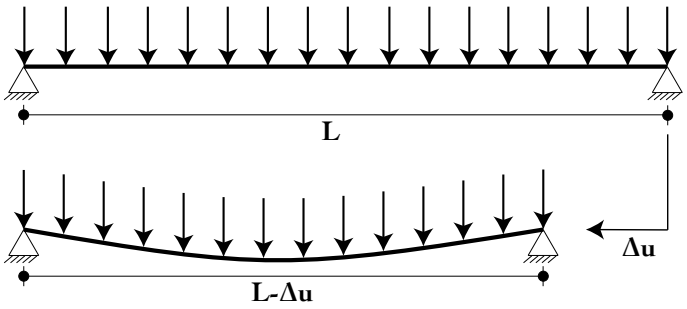

Figure 4.4: Form finding strategy for Example 1 according to Argyris *et al.* [5].

the solution for the corotational truss element oscillates because of the absence of a node at midspan for an odd number of elements.

For a mesh of equal-size elements, the continuous and discontinuous formulations give identical results in Fig. 4.5. It is evident that the accuracy of the proposed elements is excellent even with a rather coarse mesh, in contrast to the corotational truss element which requires ten or more elements for the cable. Both catenary elements give a midspan displacement of $y_{sv} = -30.5336$ m for a mesh of ten elements with the St. Venant-Kirchhoff elastic material. The midspan displacement of both catenary elements for the same mesh is practically the same for the neo-Hookean elastic material at $y_{nh} = -30.5337$ m. In contrast, the midspan displacement for a mesh of ten corotational linear elastic truss elements is $y_t = -30.5404$ m.

Fig. 4.6(a) shows the 2nd Piola-Kirchhoff axial force distribution along the cable for a

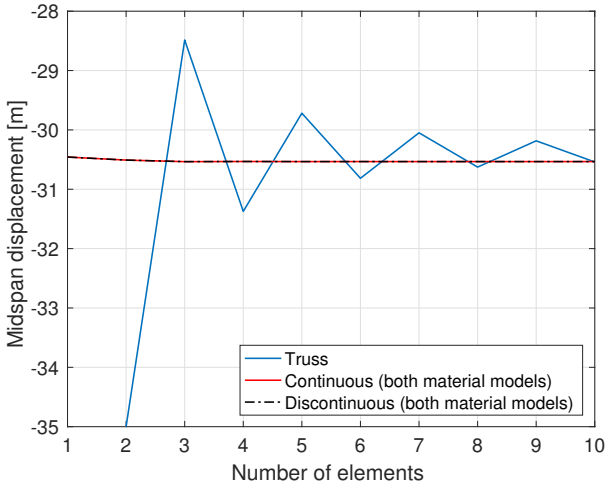

Figure 4.5: Maximum sag at midspan for both materials models and formulations, and for corotational linear elastic truss elements.

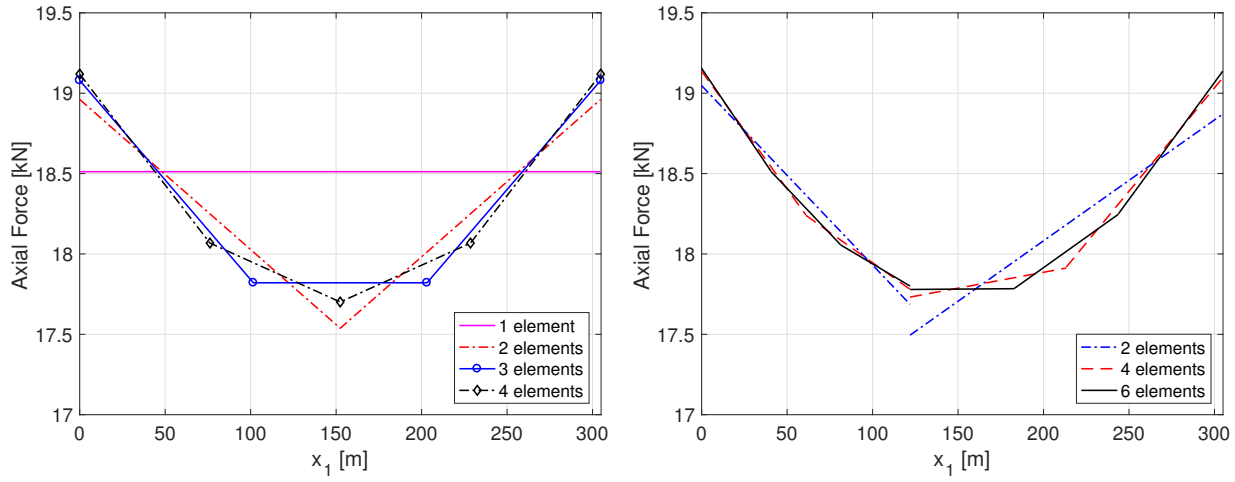

(a) Mesh with equal-size elements (b) Mesh with unequal-size elements

Figure 4.6: 2nd PK axial force distribution; (a) both formulations and material models; (b) discontinuous formulation with both material models.

mesh of equal-size elements and both material models and formulations. As is the case with Fig. 4.5, the discontinuous and the continuous cable elements and both material models give identical results. For a mesh with unequal-size elements that is generated by placing a node at 2/5 of the cable span and subdividing each portion into equal-size elements, an inter-element discontinuity arises in Fig. 4.6(b) at the common node of elements with unequal

size. The jump in the axial force value at the node located at 2/5 of the cable span reduces quickly with increasing number of elements and is very small for a mesh with six elements in Fig. 4.6(b).

While the response of the cable under self-weight in Figs. 4.5 and 4.6 is practically identical for the St. Venant-Kirchhoff and neo-Hookean elastic materials, it is possible to detect a response difference by increasing the distributed load value $W = \|\hat{\mathbf{W}}\|$. Fig. 4.7 shows the midspan sag and the 2nd PK axial force vs. the distributed load and stretch, respectively, with a mesh of four equal-size elements and projecting the stretch linearly from the Gauss points to the midspan node. As expected for small deformations, the relation between the midspan sag and the distributed load in Fig. 4.7(a) is initially linear and practically identical for the two material models, as is also the relation between the 2nd PK axial force and the stretch in Fig. 4.7(b). With an increasing value of W, the St. Venant-Kirchhoff elastic material model gives smaller midspan sags and larger 2nd PK axial forces.

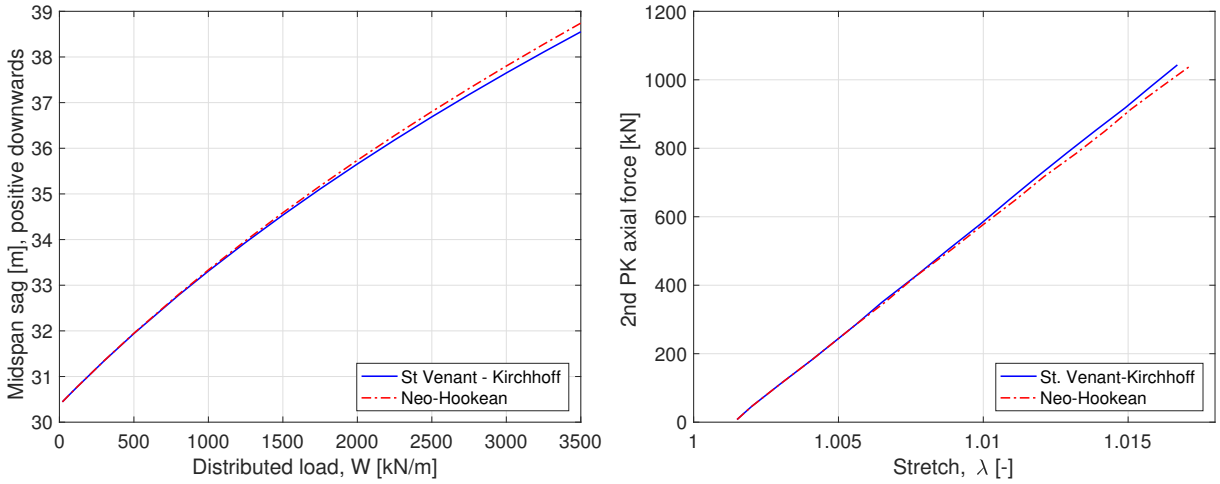

(a) Midspan sag vs. distributed load (b) 2nd PK axial force vs. stretch

Figure 4.7: Cable response at midspan for St. Venant-Kirchhoff and neo-Hookean material models.

4.2.2 Example 2: Cable under point load

The second example deals with the same structural model as Example 1 under an additional concentrated load that is applied off-center, as shown in Fig. 4.8. This problem was subject of previous studies in Ahmad Abad *et al.* [1], Andreu *et al.* [3], Thai and Kim [52] and Tibert [54], so that the results of different models can be readily compared. Figure 4.8 and Table 4.1 summarize the geometry of the model and its material properties. The cable is also assessed with St. Venant-Kirchhoff and neo-Hookean material models.

The initial cable length between sections 1 and 2 in Fig. 4.8 is 125.88 m, while the initial cable length between sections 2 and 3 is 186.85 m. The applied concentrated force is 35.586

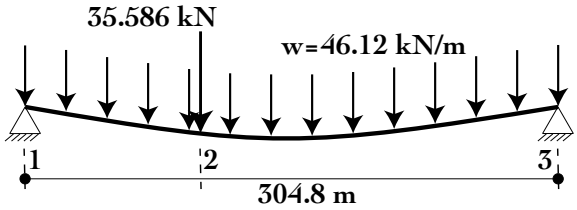

Figure 4.8: Structural model for Example 2.

kN. The form finding problem is solved again with a horizontal reference configuration and a displacement $\Delta\mathbf{u} = (0, -7.93)$ m at the right support. The support displacement and the point load are applied simultaneously.

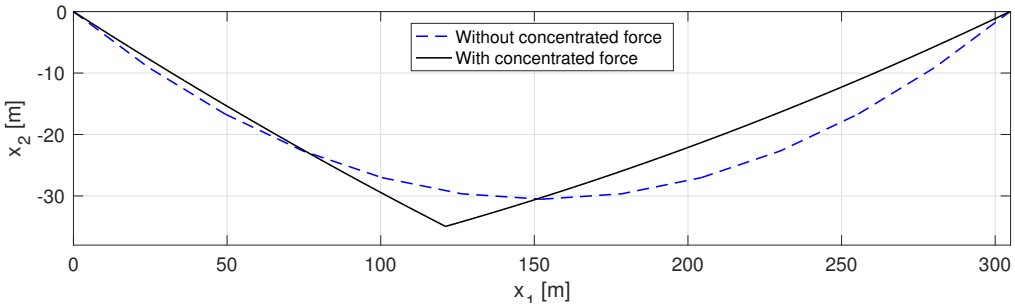

Figure 4.9: Deformed shape for Example 2.

Fig. 4.9 shows the deformed shape of the structure. Fig. 4.10 compares the sag and lateral drift of the cable at the point of the concentrated load application for the continuous and the discontinuous axial force distribution. The translation values are measured relative to the catenary shape from Example 1 and are practically the same for both elastic material models. Fig. 4.11 shows the 2nd Piola-Kirchhoff axial force distribution for the continuous and the discontinuous formulations. The advantage of the discontinuous axial force formulation is evident in Fig. 4.11(b): its ability to capture the jump in the axial force at the point of the concentrated load application results in the significantly better accuracy of the sag and lateral drift for coarse finite element meshes. In contrast, the continuous axial force formulation gives rise to the characteristic Gibbs phenomenon at the point of the concentrated load application as is evident from the axial force oscillation in Fig. 4.11(a).

It takes a very fine finite element mesh to capture accurately the change in the axial force at the point of load application and to produce an accurate result for the translations at this point with the continuous formulation. In fact, it takes more than a hundred elements with the continuous formulation for the lateral drift to converge to the exact result in Fig. 4.10(b), while even two elements with the discontinuous formulation produce a value very close to

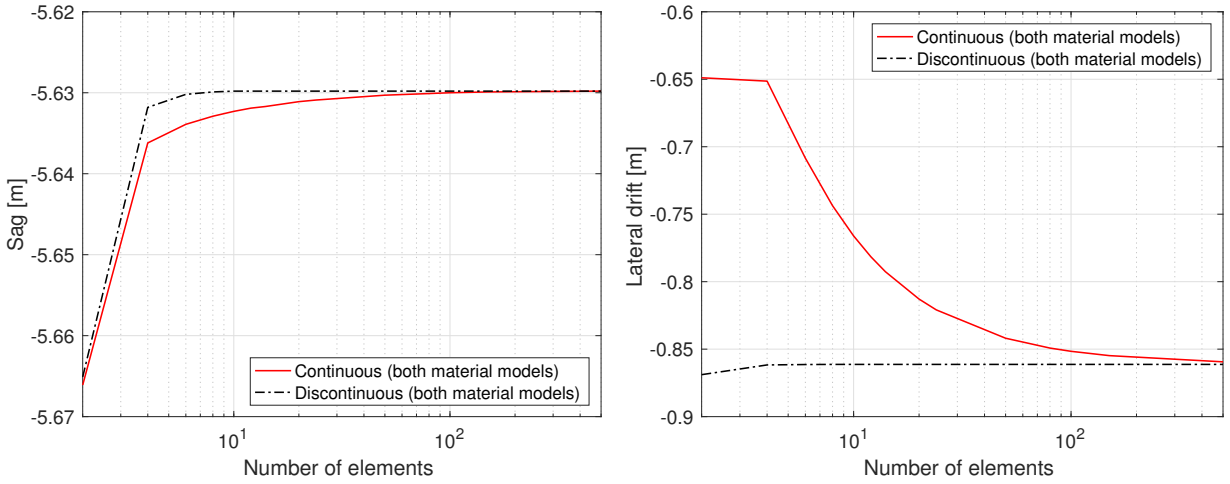

(a) Sag (b) Lateral drift

Figure 4.10: Translations at the point of the concentrated load application relative to the deformed shape of the catenary for Example 2.

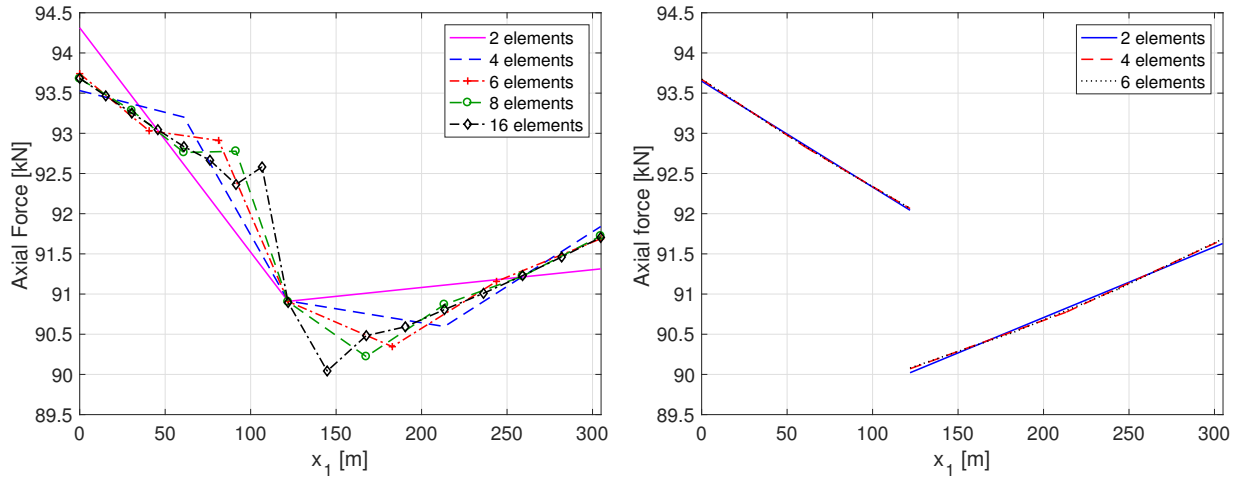

(a) Continuous axial force (b) Discontinuous axial force

Figure 4.11: 2nd Piola-Kirchhoff axial force distribution for Example 2.

the exact solution. No noticeable differences arise between the two elastic material models in Figs. 4.10 and 4.11. It is possible to eliminate the shortcoming of the continuous axial force formulation by placing two nodes at the same spatial point and linking only the cable displacements of adjacent elements, thus, in effect, allowing for a discontinuous axial force distribution with two independent axial force degrees of freedom. With this procedure and the same mesh discretization, both implementations of the element give the same results for

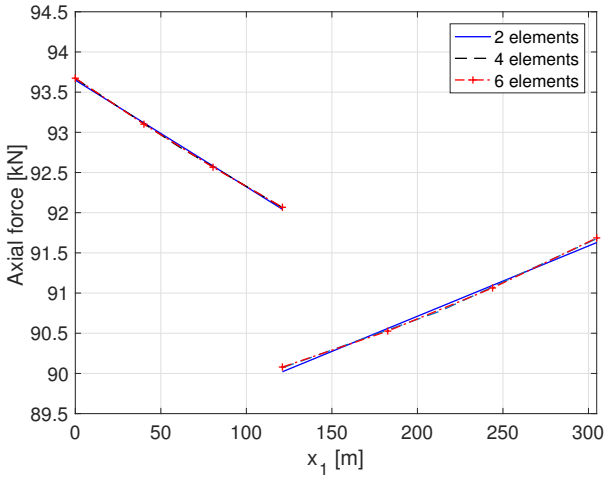

Figure 4.12: 2nd Piola-Kirchhoff axial force for the continuous implementation and two different nodes at the point of the concentrated load application.

Reference	**Element type**	**Vertical disp. (m)**	**Horizontal displ. (m)**
Michalos and Birnstiel [36]	Truss	-5.472	-0.845
O'Brien and Francis [38]	Elastic catenary	-5.627	-0.860
Jayaraman and Knudson [28]	Truss	-5.471	-0.845
Jayaraman and Knudson [28]	Elastic catenary	-5.626	-0.859
Tibert [54]	Elastic catenary	-5.626	-0.859
Andreu *et al.* [3]	Elastic catenary	-5.626	-0.860
Yang and Tsay [57]	Elastic catenary	-5.625	-0.859
Thai and Kim [52]	Elastic catenary	-5.626	-0.859
Ahmad Abad *et al.* [1]	Discrete elastic catenary	-5.592	-0.855
Ahmad Abad *et al.* [1]	Elastic catenary	-5.626	-0.859
Ahmad Abad *et al.* [1]	Discrete elastic catenary with point loads	-5.830	-0.873
Present work (continuous, nonlinear elasticity)	Discrete elastic catenary, finite deformations	-5.630	-0.861
Present work (discontinuous, nonlinear elasticity)	Discrete elastic catenary, finite deformations	-5.630	-0.861

Table 4.2: Results for the cable model of Example 2 from different studies.

the displacements and the 2nd PK axial forces, as shown in Fig. 4.12 for the latter.

Table 4.2 compares the converged translation values of the present study with the results of several models in earlier studies. The agreement is excellent, even though the assumption

of infinitesimal deformations in earlier studies appears to slightly underestimate the translation values. Another cause for the slight discrepancy is the lack of distinction between axial force representations in earlier studies and the assumption of a constant axial force along the cable in some.

4.2.3 Example 3: Continuation and stability points

The third example investigates the stability of a cable supported by a pulley that was previously studied in Bruno and Leonardi [11], Impollonia *et al.* [26] and Such *et al.* [48]. This cable is studied first in a 2d arrangement and is then extended to 3d by placing the pulley support out-of-plane.

4.2.3.1 Two-dimensional arrangement

Figure 4.13 shows the structural model in two dimensions, consisting of an inclined cable anchored at both ends and supported by an intermediate roller. Table 4.3 summarizes the geometric and material properties of the structural model. The St. Venant-Kirchhoff elastic material model is used in this case.

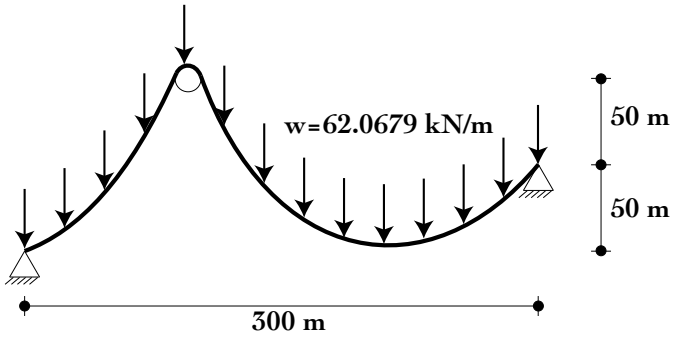

Figure 4.13: Structural model for Example 3.

Property	Value
Cross-sectional area	805 mm^2
Elastic modulus	16.0 kN/mm^2
Cable self-weight	62.0679 N/m
Cable length	500 m

Table 4.3: Geometry and material properties for Example 3.

The objective of this example is the determination of the equilibrium configurations of the cable under the assumption that the pulley is free to move horizontally and that the pulley

radius is negligible. For the nonlinear analysis, the cable is subdivided in two segments, one for each span, with the curvilinear coordinate ξ^1 of the roller as problem unknown. The curvilinear coordinate ξ^1 refers to the arc-length in the reference configuration with origin at the left support, and is used to locate the roller node and subsequently construct the finite element mesh. The analysis starts from a horizontal reference configuration and imposes a displacement of $\Delta\mathbf{u} = (-200, 50)$ m at the right support and a displacement of $\Delta u_2 = 100$ m at the intermediate roller. Moreover, the condition is imposed that the Cauchy axial force have zero jump at the roller support, as friction is neglected. As a result, the problem is solved by iterating over the curvilinear coordinate ξ^1 so that the jump in the Cauchy axial force at the roller becomes zero.

Table 4.4 summarizes the results for the equilibrium configurations of the 2d cable by different authors with ξ_i^1 referring to the curvilinear coordinate of the pulley and N_i, to the axial force. Because studies in Bruno and Leonardi [11], Impollonia *et al.* [26] and Such *et al.* [48] do not account for finite deformations, the corresponding values in Table 4.4 correspond to infinitesimal deformations. For the results of the present study, the axial force corresponds to the 2nd Piola-Kirchhoff axial force and the curvilinear coordinate, to the reference configuration. While the values of the present study agree very well with those of previous studies, it is worth noting the variation of the axial force that the current formulation captures, as indicated by the range of axial force values for the cable in Table 4.4. In contrast, previous models overestimate the axial force by reporting a value corresponding to the maximum of the current formulation.

	Bruno and Leonardi [11]	**Such *et al.*** [48]	**Impollonia *et al.*** [26]	**Present work (continuous)**	**Present work (discontinuous)**
ξ_1^1 (m)	111.07	110.96	110.83	110.83	110.83
N_1 (kN)	15.499	14.531	14.531	4.709 - 14.514	4.709 - 14.515
ξ_2^1 (m)	-	-	221.52	221.53	221.51
N_2 (kN)	-	-	10.631	2.726 - 10.622	2.726 - 10.622
ξ_3^1 (m)	446.37	446.92	447.30	447.30	447.29
N_3 (kN)	17.952	17.966	17.982	5.222 - 17.960	5.222 - 17.957

Table 4.4: Results for the 2d cable model of Example 3 from different studies.

Three equilibrium states result from the analysis, as Fig. 4.14(a) shows: two stable configurations, denoted with 1 and 3, and one unstable configuration, denoted with 2, as reflected by the change of direction for the horizontal component of the reaction at the pulley in Fig. 4.15, where a zero horizontal reaction implies an equilibrium configuration. The stable configurations 1 and 3 are not symmetric because the cable is inclined. The x_1 coordinates of the pulley for these equilibrium states in Fig. 4.14(a) are $x_1^1 = 47.253/47.253$ m, $x_1^2 = 136.540/136.533$ m and $x_1^3 = 283.155/283.144$ m for the continuous and the discontinuous formulations, respectively. Fig. 4.14(b) shows the 2nd Piola-Kirchhoff axial force distribution

for the three equilibrium states. Both formulations produce very similar results, as is also confirmed by the values in Table 4.4, because the axial force is continuous at the pulley in the absence of friction.

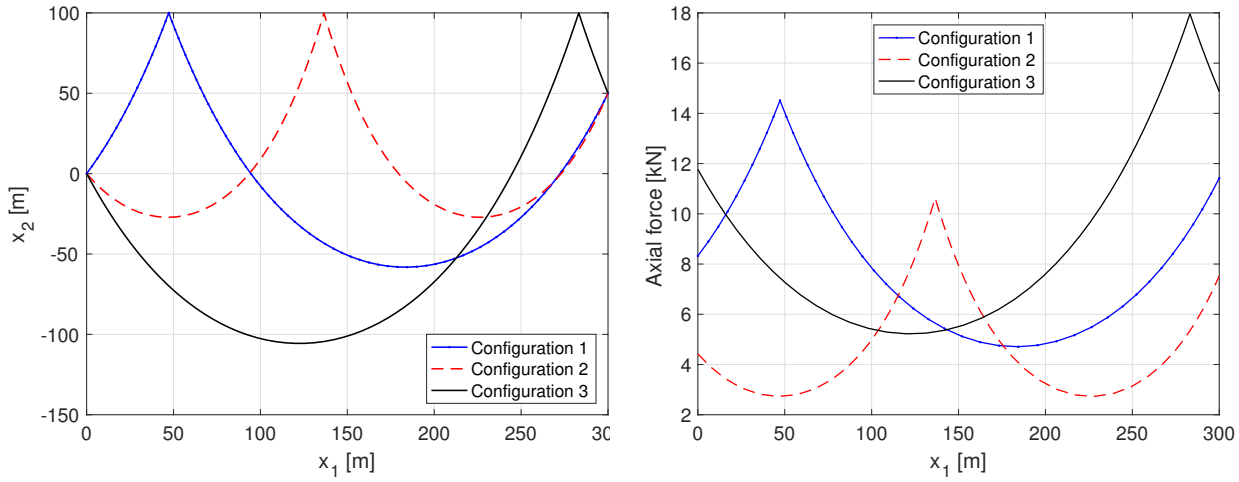

(a) Deformed shape (b) 2nd PK axial force

Figure 4.14: Deformed shape of equilibrium states (2d) and 2nd PK axial force distribution for 45 equal-size elements and Example 3.

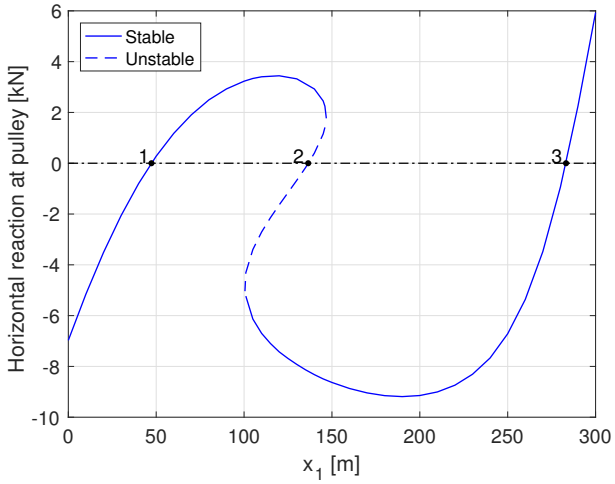

Figure 4.15: Horizontal reaction at pulley support (2d) vs. horizontal position x_1 for Example 3.

4.2.3.2 Three-dimensional arrangement

A three-dimensional arrangement of the cable is considered by placing the roller support out-of-plane. Following the form finding procedure by Argyris *et al.* [5], the analysis starts from a straight reference configuration and imposes a displacement $\Delta\mathbf{u} = (-200, 0, 50)$ m at the right support and a pair of displacements $\Delta u_2 = 50$ m and $\Delta u_3 = 100$ m at the intermediate roller. The problem is then solved with the same procedure as for the 2d case.

Table 4.5 summarizes the results for the 3d equilibrium configurations of the cable and compares them to the study by Impollonia *et al.* [26], with ξ_i^1 referring to the reference curvilinear coordinate of the pulley and N_i, to the 2nd PK axial force. Because the study by Impollonia *et al.* does not account for finite deformations, its results in Table 4.5 correspond to infinitesimal deformations. As for the 2d case, it is worth noting the variation of the axial force that the current formulation captures, which is indicated by the range of axial force values in Table 4.5. In contrast, the model by Impollonia *et al.* overestimates the axial force by reporting a value corresponding to the maximum of the current formulation.

	Impollonia *et al.* [26]	**Present work (continuous)**	**Present work (discontinuous)**
ξ_1^1 (m)	126.12	126.26	126.25
N_1 (kN)	14.12	4.79-14.08	4.79-14.08
ξ_2^1 (m)	219.98	219.46	219.47
N_2 (kN)	10.79	3.04-10.78	3.04-10.78
ξ_3^1 (m)	424.76	424.69	424.70
N_3 (kN)	17.42	5.40-17.36	5.40-17.34

Table 4.5: Results for the 3d cable model of Example 3 from different studies.

Three equilibrium states result from the analysis, as Fig. 4.16 shows: two stable configurations depicted with solid lines (C_1 and C_3) and one unstable configuration, depicted with a dashed line (C_2), as also reflected by the change in direction of the horizontal component of the reaction at the pulley in Fig. 4.17, where a zero horizontal reaction implies an equilibrium configuration. The x_1 positions of the pulley for these equilibrium states in Fig. 4.16 are $x_1^1 = 56.54/56.53$ m, $x_1^2 = 134.00/134.01$ m and $x_1^3 = 274.31/274.31$ m for the continuous and for the discontinuous formulations, respectively.

4.3 Dynamic analysis

For the dynamic analysis, the Newmark method, the HHT-α method and the new energy-momentum conserving algorithm are implemented in the Matlab toolbox FEDEASLab [18] for the following numerical studies. The corresponding elements use linear interpolation functions for the axial forces ($k = 1$) and quadratic interpolation functions for the displacements, velocities and accelerations ($l = 2$), as depicted in Fig. 4.2.

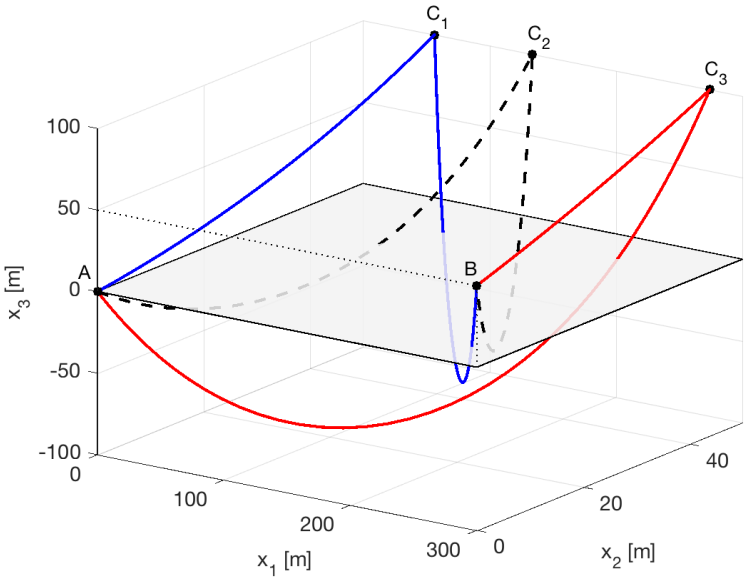

Figure 4.16: Deformed shape (30 elements) of the 3d equilibrium states for Example 3.

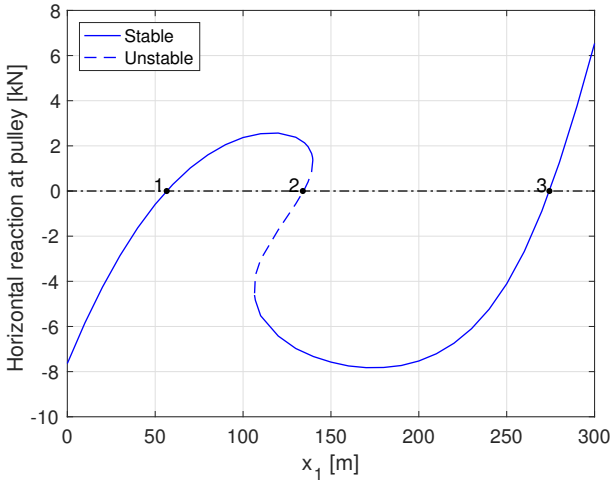

Figure 4.17: Horizontal reaction at pulley support (3d) vs. horizontal position x_1 for Example 3.

The implementation of the proposed cable elements with the Newmark and the HHT-α methods does not use state-space variables, and thus the number of DOFs is the same as for the static case in Section 4.2. In contrast, for the energy-momentum conserving algorithm, the two-dimensional element with continuous axial force distribution in state-

space results in fourteen DOFs, six displacement and six velocity DOFs, and two axial force DOFs, while the three-dimensional element results in twenty DOFs, nine displacement and nine velocity DOFs, and two axial force DOFs. The element with the discontinuous axial force distribution in state-space condenses out the axial force DOFs reducing the total number of DOFs accordingly. This number of DOFs can be further reduced with the use of a pointwise momentum relation, as discussed in Section 3.6.2.3.3.

Before starting the dynamic analysis, the form finding problem is solved statically at $t = 0$ following the procedure by Argyris *et al.* [5] in Section 3.7. This procedure is performed in the same way as in Section 4.2 by imposing appropriate support displacements for the desired span.

The Newmark method, the HHT-α method and the energy-momentum conserving algorithm are used to investigate the large-amplitude, in-plane and out-of-plane free vibration of three cables with small, large and very large sag-to-span ratios, as well as their 2d and 3d dynamic response under an earthquake support excitation. In the absence of concentrated loads, no discontinuities arise in the axial force field, so that the continuous and the discontinuous implementations of the proposed element give the same results for the following symmetric examples.

4.3.1 Linearized natural modes of vibration

The following assessment examples consider three cables with different sag-to-span ratios that were investigated by Srinil *et al.* [47]. These cables, denoted with C1, C2 and C3, are simply supported and span 850 m in all cases. Table 4.6 summarizes their geometric and material properties.

Property	**C1**	**C2**	**C3**
Cross-sectional area	0.1159 m^2		
Elastic modulus	17.94 GPa		
Density	8337.9 kg/m^3		
Unstretched cable length	840.48 m	870.51 m	926.65 m

Table 4.6: Geometric and material properties of cables C1, C2 and C3.

First, the equilibrium configurations are found at $t = 0$ using the static form finding procedure in Section 3.7. Figure 4.18 presents, for each cable and with a St. Venant-Kirchhoff material model, the convergence analysis of the midspan sag, the 2nd PK end tension and the total energy when the proposed cable elements and the corotational truss elements in Section 2.2.1 are used. The relative error in Fig. 4.18 is given in terms of the results for a mesh with 256 elements. It is evident that, for all sag-to-span ratios, the accuracy of the proposed cable elements is excellent compared to the corototational truss elements in terms of convergence rate and level of accuracy. The end tension in Fig. 4.18 shows the lowest accuracy in all cases, but is two orders of magnitude higher for the proposed elements than

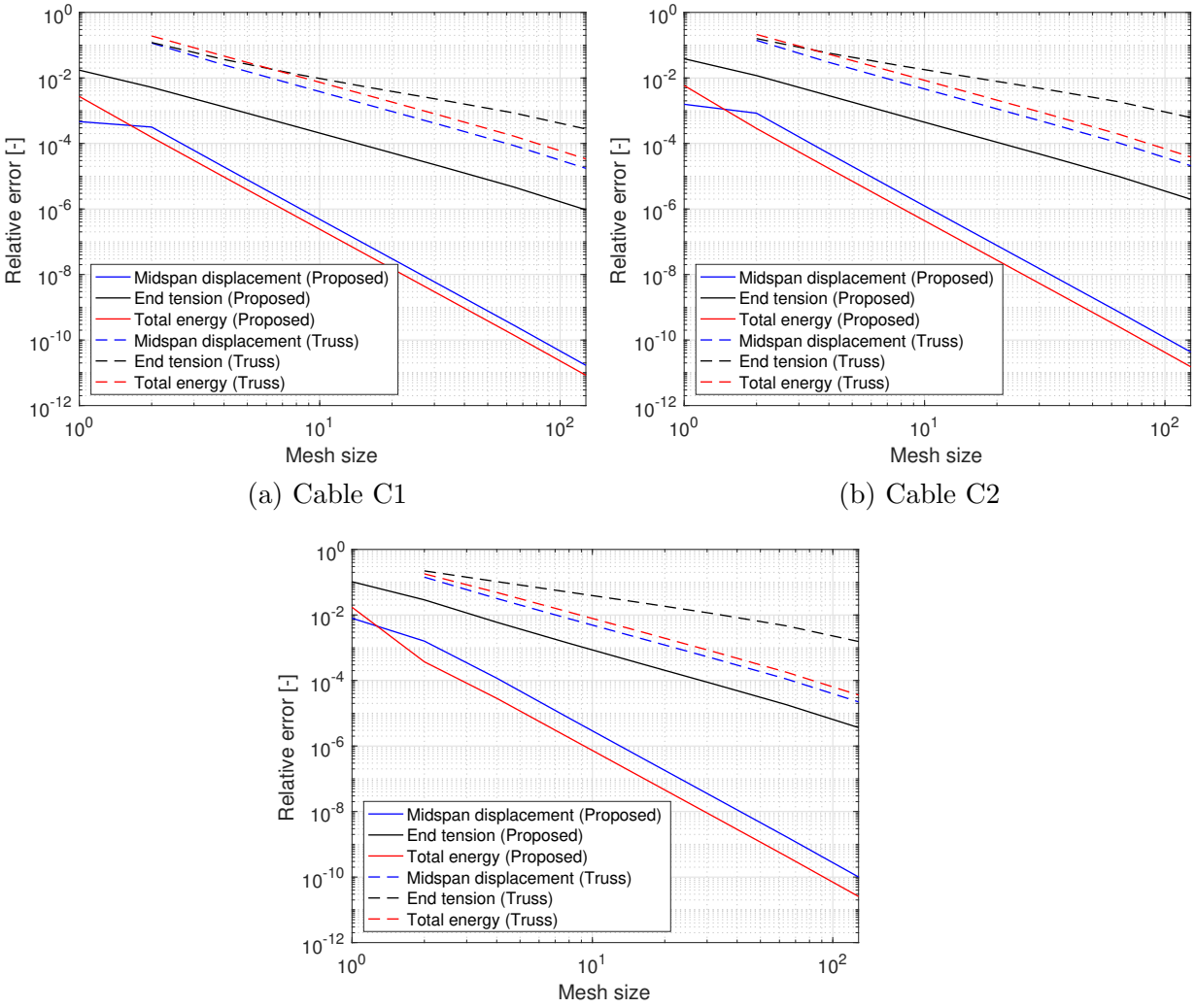

(a) Cable C1

(b) Cable C2

(c) Cable C3

Figure 4.18: Convergence analysis of the equilibrium configurations for cables C1, C2 and C3.

for the reference ones, which represents a significant contribution of the proposed model. According to these results, cables C1 to C3 are discretized with a mesh of 10 elements for the following dynamic examples, in contrast to the much finer mesh of 50 elements by Srinil *et al.* [47].

The linearized first two in-plane ("I") and out-of-plane ("O") natural modes of vibration about the equilibrium configuration are obtained from the solution of the standard linear eigenvalue problem

$$\det[\mathbf{K}_{st} - \omega^2 \mathbf{M}] = 0 \tag{4.12}$$

where ω is the angular frequency and $\mathbf{K}_{st}$ is the static stiffness matrix at the equilibrium

configuration. Table 4.7 reports the results for a St. Venant-Kirchhoff elastic material (SV) and a neo-Hookean elastic material (NH), where "S" and "A" refer to the symmetric and antisymmetric mode, respectively, and the end tension is reported as 2nd PK axial force. These results are compared with the results by Srinil *et al.* [47], who assumed infinitesimal linear elasticity (LE) for the material. The results lead to the conclusion that all material models give very similar results for the three cables.

	C1			**C2**			**C3**		
	SV	NH	LE	SV	NH	LE	SV	NH	LE
Sag [m]	56.4	56.6	56.6	89.5	89.6	89.6	164.1	164.1	164.1
Sag-to-span [-]	1/15	1/15	1/15	1/9.5	1/9.5	1/9.5	1/5	1/5	1/5
End tension [kN]	15559	15506	15642	10444	10437	10500	6965	6965	7000
Freq. (1st S-I) [Hz]	0.146	0.145	0.145	0.158	0.158	0.158	0.119	0.119	0.119
Freq. (1st A-I) [Hz]	0.145	0.144	0.145	0.112	0.112	0.112	0.076	0.076	0.076
Freq. (1st S-O) [Hz]	0.074	0.074	0.074	0.059	0.059	0.058	0.043	0.043	0.043
Freq. (1st A-O) [Hz]	0.147	0.147	0.147	0.117	0.116	0.115	0.085	0.085	0.085

Table 4.7: Results for equilibrium of cables C1 to C3 and natural frequencies of vibration.

Figures 4.19 and 4.20 show the normalized eigenvectors for the first symmetric and the first antisymmetric modes in the plane of the cable about the equilibrium configuration. It is observed that, when the sag-to-span ratio increases, the single vertical extremum of the symmetric mode divides into three because of the effect of larger antisymmetric horizontal displacements. In contrast, the vertical displacements of the antisymmetric mode are almost insensitive to the increase of the sag-to-span ratio.

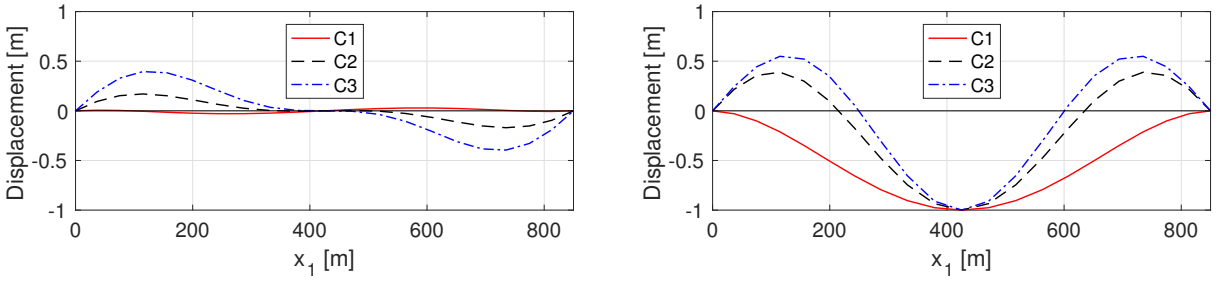

(a) Horizontal component (b) Vertical component

Figure 4.19: Normalized in-plane eigenvector for first symmetric mode (cables C1, C2, C3).

Figure 4.21 shows the normalized eigenvectors for the first symmetric and the first antisymmetric modes in the plane orthogonal to the cable about the equilibrium configuration. In this case, the horizontal and the vertical components of these eigenvectors are zero, and only the out-of-plane component is depicted. From Fig. 4.21, it is observed that the increase of the sag-to-span ratio has a reduced impact on the first symmetric and on the first antisymmetric out-of-plane modes.

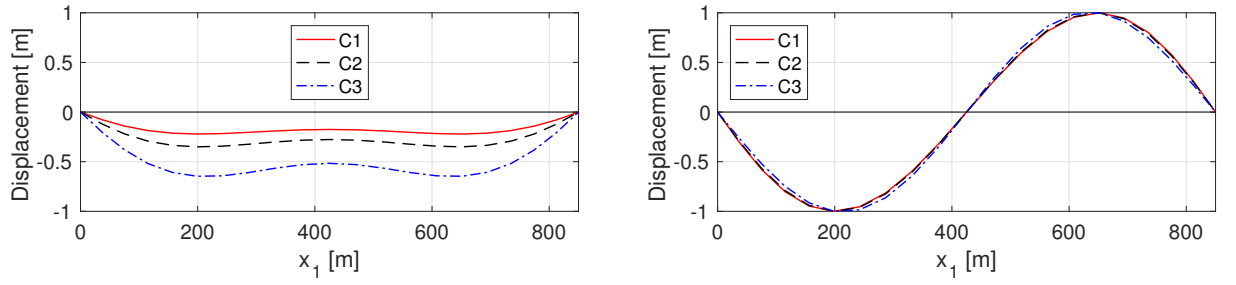

(a) Horizontal component (b) Vertical component

Figure 4.20: Normalized in-plane eigenvector for first antisymmetric mode (cables C1, C2, C3).

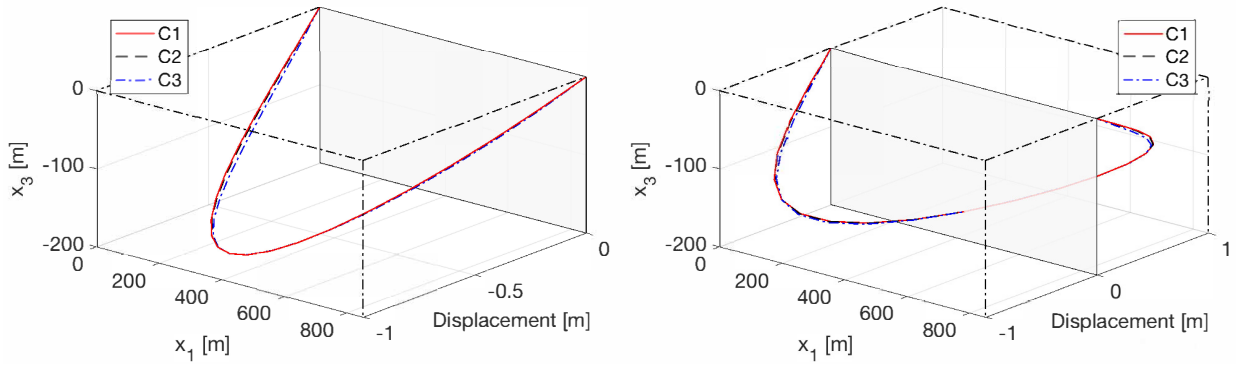

(a) First symmetric mode (b) First antisymmetric mode

Figure 4.21: Normalized out-of-plane eigenvector for first symmetric and antisymmetric modes (cables C1, C2, C3).

4.3.2 Example 5: Free vibration for small sag-to-span ratio

The fifth example studies the large-amplitude in-plane and out-of-plane free vibration of cable C1, with a small sag-to-span ratio. The structural model consists of a simply-supported cable with the geometric and material properties in Tables 4.6 and 4.7. A St. Venant-Kirchhoff elastic material model and a neo-Hookean elastic material model are used in this example, but no significant differences are observed in the dynamic response because the cable stretch remains relatively small. The cable is discretized with a mesh of ten elements, in contrast to the fifty elements used by Srinil *et al.* [47].

The large-amplitude free vibration is evaluated for an initial displacement field $\mathbf{u}_0$ of the form

$$\mathbf{u}_0 = \alpha_s \mathbf{u}_{s1} + \alpha_a \mathbf{u}_{a1} \tag{4.13}$$

where $\mathbf{u}_{s1}$ is the normalized first symmetric mode and $\mathbf{u}_{a1}$ is the normalized first antisymmetric mode, either in the cable plane or in the plane orthogonal to it, with α_s and α_a the corresponding amplification factors. An initial velocity $\mathbf{v}_0 = \mathbf{0}$ is assumed, and the necessary

initial d'Alembert acceleration $\mathbf{a}_0$ is computed so that the initial state is in dynamic equilibrium. The dynamic response of the cable is obtained with the implicit Newmark method with parameters $\beta = 0.25$ and $\gamma = 0.5$, the HHT-α method with $\alpha = 0.75$ and the new energy-momentum conserving algorithm. The time step is set so that the dominant period of each simulation contains about a hundred steps.

4.3.2.1 In-plane free vibration for small sag-to-span ratio

First, the large-amplitude free vibration in the plane of the cable is studied with a time step of $\Delta t = 0.05$ sec. Figure 4.22 presents the normalized results of the Newmark method under a symmetric initial displacement field with amplification factors $\alpha_s = 15$ and $\alpha_a = 0$. As expected, the cable response for this small sag-to-span ratio is essentially periodic with linear oscillations for the displacement time history. In contrast, the axial force time history shows a periodic response that contains a high-frequency component representing the axial wave produced by the sudden release of the imposed displacements, as observed by Srinil *et al.* [47]. Figure 4.25 gives the spectral decomposition of the axial force time history at midspan and at the supports, for which two main frequencies appear, 0.14 Hz (7.00 sec) and 3.20 Hz (0.31 sec), corresponding to the two periods observed in Fig. 4.22(a). The Newmark method conserves the total energy of the cable in Fig. 4.22(b) at its initial value of 3.64×10^4 kJ.

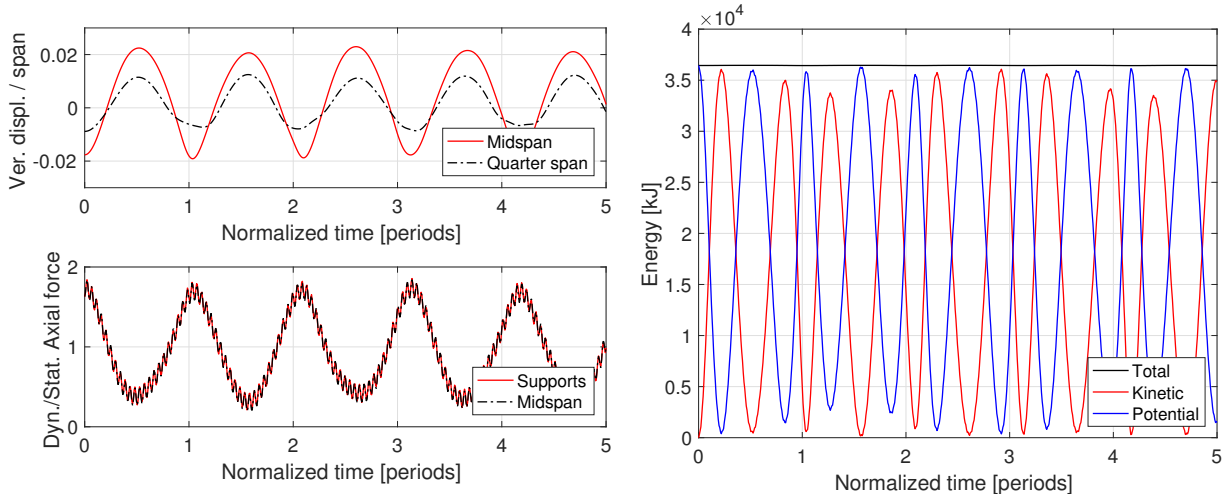

(a) Normalized displacements and axial forces (b) Energy evolution

Figure 4.22: Results for in-plane free vibration with the Newmark method, $\beta = 0.25$ and $\gamma = 0.5$ (Example 5).

The same study, under the symmetric initial displacement field with $\alpha_s = 15$ and $\alpha_a = 0$, is performed with the HHT-α method in Fig. 4.23. The dynamic response of the cable in Fig. 4.23(a) is again essentially periodic with linear oscillations for the displacements

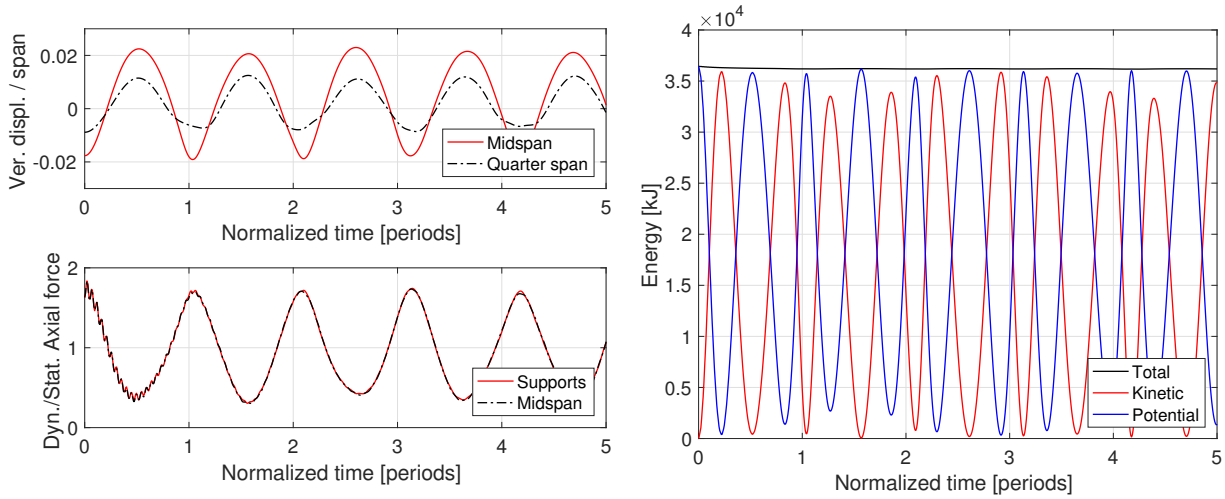

(a) Normalized displacements and axial forces (b) Energy evolution

Figure 4.23: Results for in-plane free vibration with the HHT-α method, $\alpha = 0.75$ (Example 5).

at midspan and at quarter span. In this case, the numerical dissipation of the algorithm produces the decay of the high-frequency component in the axial force history, with an almost imperceptible initial decay in the total energy in Fig. 4.23(b). Figure 4.25 gives the spectral decomposition of the axial force history at midspan and at the supports, for which only the low frequency at 0.14 Hz (7.00 sec) is relevant.

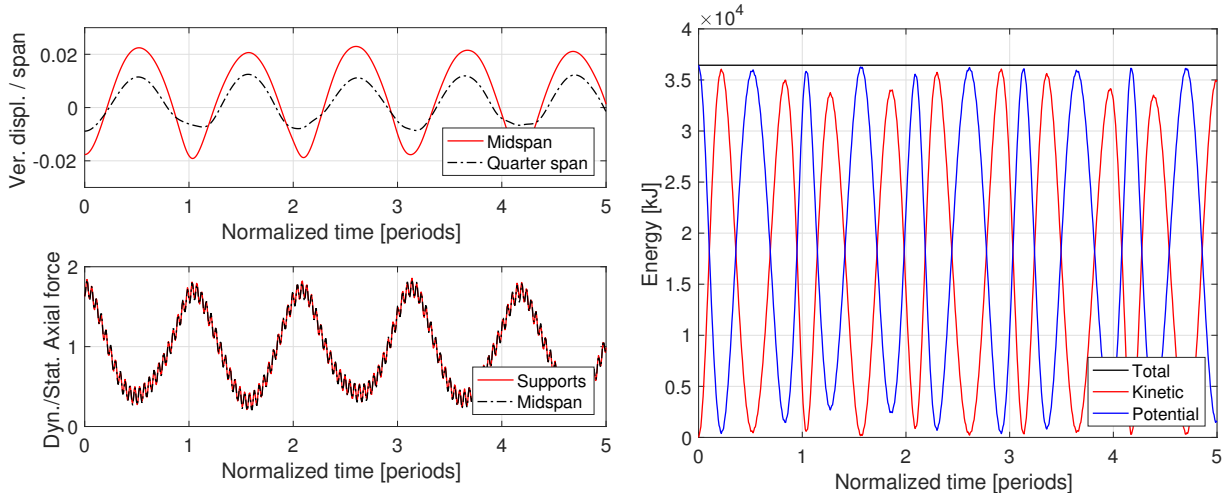

(a) Normalized displacements and axial forces (b) Energy evolution

Figure 4.24: Results for in-plane free vibration with the energy-momentum conserving algorithm (Example 5).

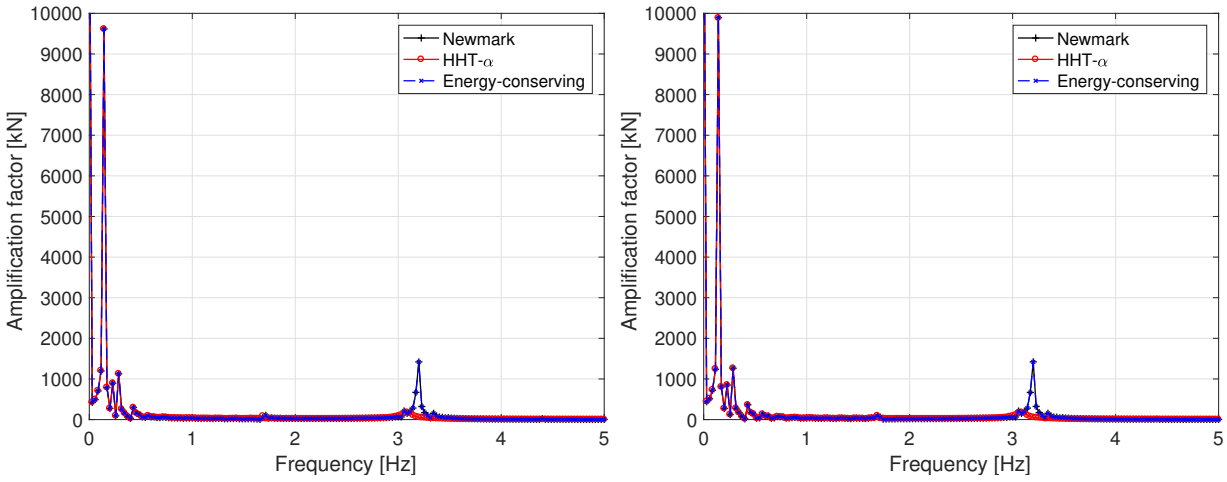

(a) Midspan (b) Supports

Figure 4.25: Spectral decomposition for axial force history and in-plane vibration (Example 5).

The same analysis with magnification factors $\alpha_s = 15$ and $\alpha_a = 0$ is performed with the energy-momentum conserving algorithm in Fig. 4.24. In this case, the displacement and the axial force time histories in Fig. 4.24(a) are identical to those of the Newmark method in Fig. 4.22(a). The total energy is exactly conserved in Fig. 4.24(b) at the initial value of 3.64×10^4 kJ, as is the case for the Newmark solution. Figure 4.25 shows the spectral decomposition of the axial force time history at midspan and at the supports, with the same two dominant frequencies as for the Newmark method at 0.14 Hz (7.00 sec) and 3.20 (0.31 sec).

4.3.2.2 Out-of-plane free vibration for small sag-to-span ratio

The large-amplitude free vibration of cable C1 in the plane orthogonal to the cable is also studied with the same time integration schemes and a time step of $\Delta t = 0.1$ sec. Figure 4.26 shows the normalized results of the Newmark method for a combined out-of-plane initial displacement field with amplification factors $\alpha_s = 15$ and $\alpha_a = 15$. The results show that the out-of-plane (OOP) displacement history at midspan is periodic with constant maximums, while the quarter-span OOP displacement history shows 3d coupling with the periodic translation of a double peak. The 2nd PK axial force history in Fig. 4.26(a) includes high-frequency contributions due to the sudden release of the imposed initial displacements [47], and its spectral decomposition at midspan and at the supports is presented in Fig. 4.30. It is observed that the axial force time history at the supports reproduces the same frequencies of the midspan axial force time history, but adds a few new frequencies that amplify the noise in Fig. 4.26(a). The Newmark method conserves the total energy for this cable with a slight oscillation in Fig. 4.26(b) at a mean value of 8.40×10^4 kJ.

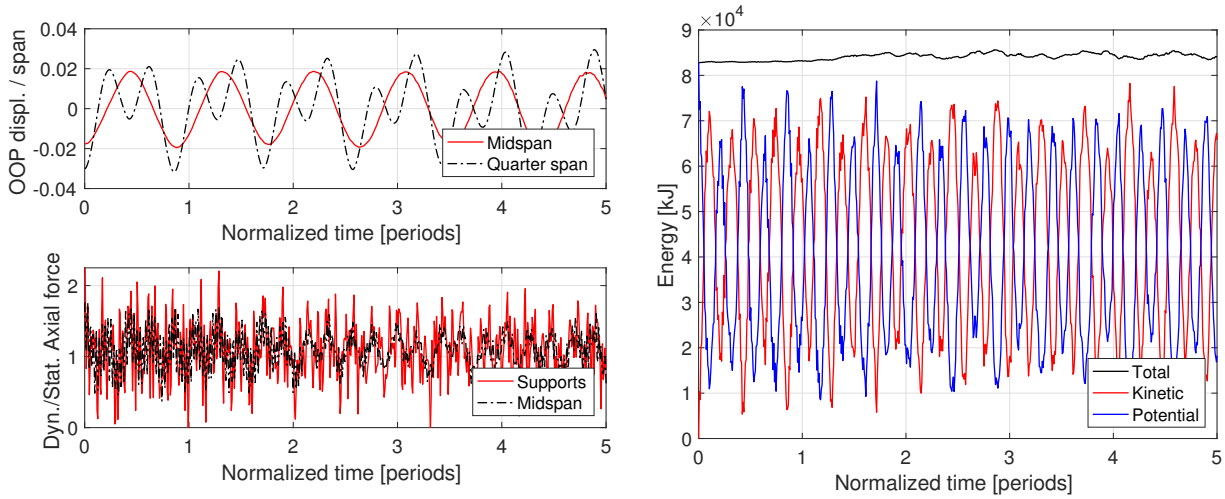

(a) Normalized displacements and axial forces (b) Energy evolution

Figure 4.26: Results for out-of-plane free vibration with the Newmark method, $\beta = 0.25$ and $\gamma = 0.5$ (Example 5).

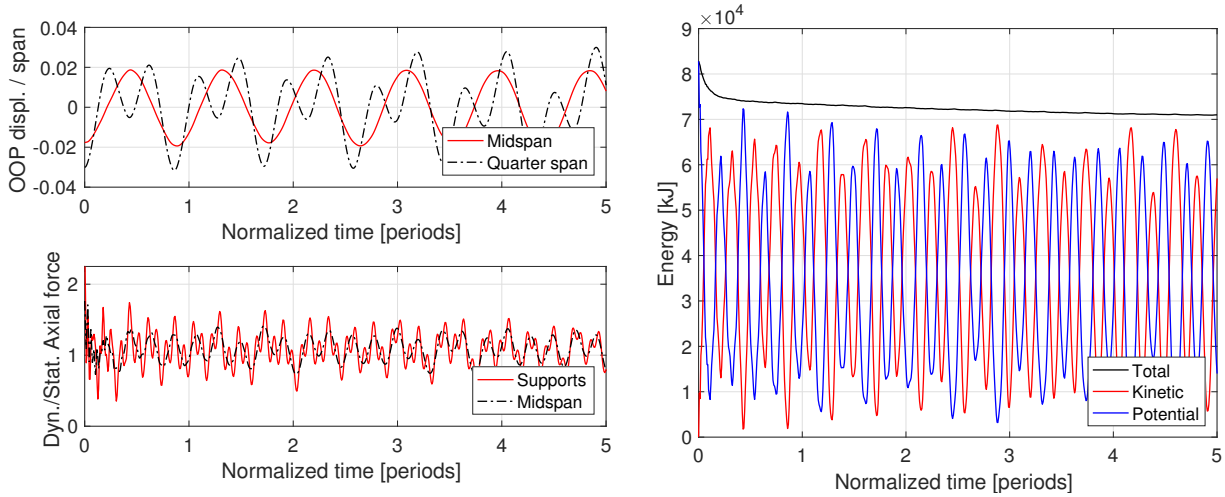

(a) Normalized displacements and axial forces (b) Energy evolution

Figure 4.27: Results for out-of-plane free vibration with HHT-α method, $\alpha = 0.75$ (Example 5).

The same study, with out-of-plane amplification factors $\alpha_s = 15$ and $\alpha_a = 15$, is performed with the HHT-α method in Fig. 4.27. The dynamic response of the cable in Fig. 4.27(a) shows very similar midspan and quarter span OOP displacements compared with the Newmark method, but includes numerical dissipation that dampens out the high frequencies in the axial force time history. This energy dissipation is reflected in the total energy evolution in Fig. 4.27(b) with a sudden initial drop, and in the spectral decomposition

in Fig. 4.30, which removes the high frequencies observed in the Newmark solution.

Finally, the same case with out-of-plane amplification factors $\alpha_s = 15$ and $\alpha_a = 15$ is studied with the energy-momentum conserving algorithm in Fig. 4.28. The results show that the dynamic response for the OOP displacements and for the 2nd PK axial forces in Fig. 4.28(a) is very similar to the one obtained with the Newmark method in Fig. 4.26(a), but the total energy is exactly conserved in this case at the initial value of 8.28×10^4 kJ in Fig. 4.28(b). The spectral decomposition of the axial force time history in Fig. 4.30 shows that the relevant high frequencies of the signal are identical to those for the Newmark solution but have a larger amplitude in this case.

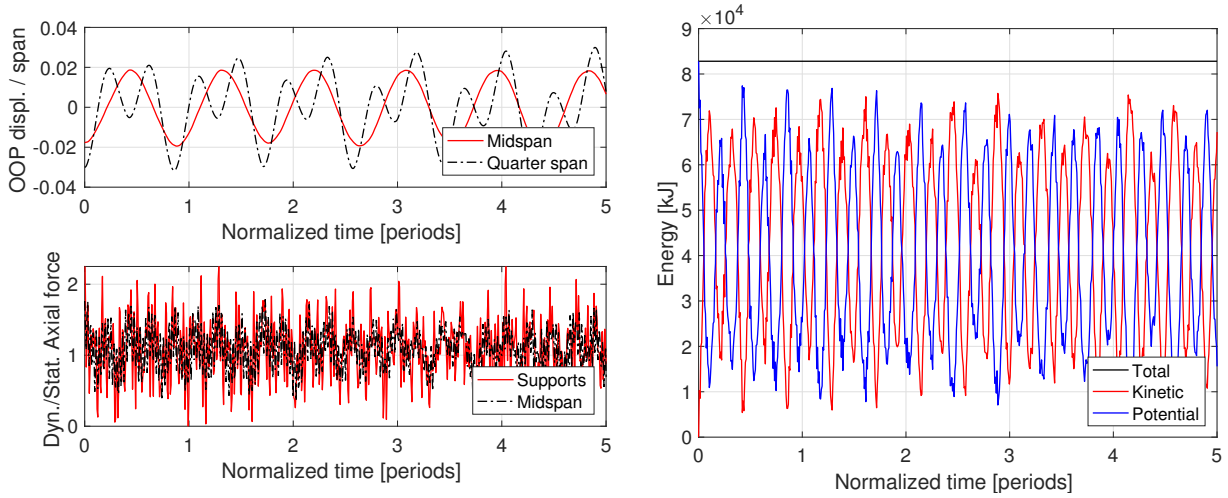

(a) Normalized displacements and axial forces

(b) Energy evolution

Figure 4.28: Results for out-of-plane free vibration with the energy-momentum conserving algorithm (Example 5).

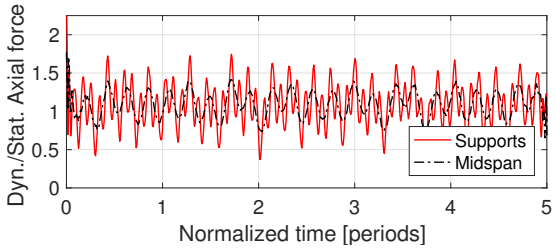

Figure 4.29: Filtered out-of-plane axial force history for energy-momentum conserving scheme (Example 5).

The high-frequency contributions in the 2nd PK axial force history for the Newmark method and the energy-momentum conserving algorithm can be removed with a Savitzky-Golay filter with a one-period frame length, following the guidelines of Section 3.6.2.4. For

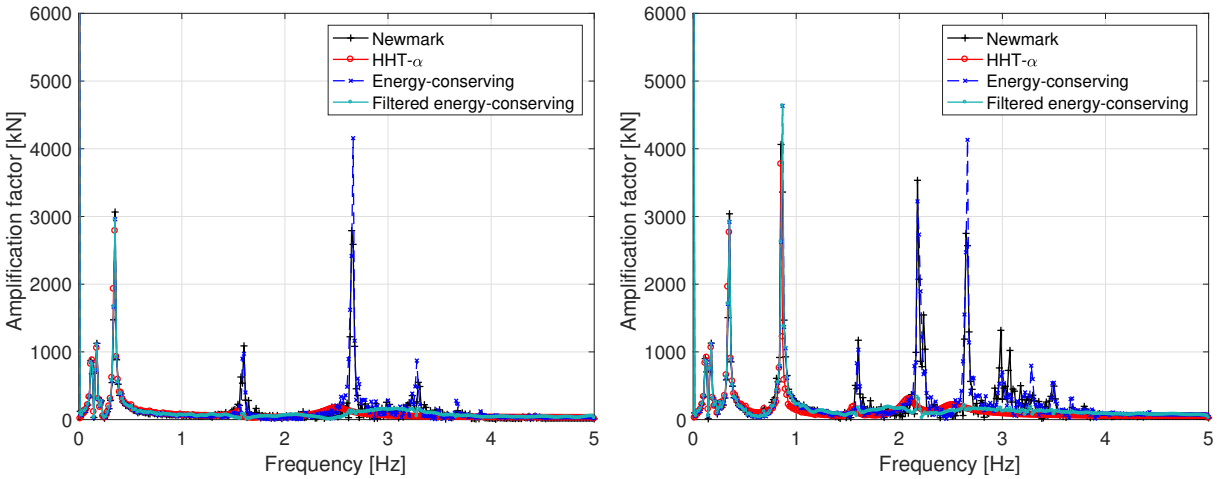

(a) Midspan (b) Supports

Figure 4.30: Spectral decomposition for axial force time history and out-of-plane vibration (Example 5).

this example, the period of the symmetric mode contains about 135 time steps, so that a filter of order 45 is selected. Figure 4.29 shows the resulting axial force history that gives a total energy of 8.03×10^4 kJ, representing a 3% reduction with respect to the non-filtered solution, and thus showing an energy decrease significantly smaller than that of the HHT-α method. The spectral decomposition of the filtered axial forces at midspan and at the supports in Fig. 4.30 shows the drop in the amplification factor of the high frequencies when the filter is applied, while keeping the low frequencies unchanged.

4.3.3 Example 6: Free vibration for large sag-to-span ratio

The sixth example evaluates the large-amplitude in-plane and out-of-plane free vibration of cable C2, with a large sag-to-span ratio. The structural model consists of a simply-supported cable with the geometric and material properties in Tables 4.6 and 4.7. A St. Venant-Kirchhoff and a neo-Hookean elastic material model are used in this example, but no significant differences arise between the two because the cable stretch remains relatively small. The cable is discretized with a mesh of ten elements, in contrast to the fifty elements used by Srinil *et al.* [47].

The large-amplitude free vibration is evaluated for an initial displacement field $\mathbf{u}_0$ of the form

$$\mathbf{u}_0 = \alpha_s \mathbf{u}_{s1} + \alpha_a \mathbf{u}_{a1} \tag{4.14}$$

where $\mathbf{u}_{s1}$ is the normalized first symmetric mode and $\mathbf{u}_{a1}$ is the normalized first antisymmetric mode, either in the cable plane or in the plane orthogonal to it, with α_s and α_a the corresponding amplification factors. An initial velocity $\mathbf{v}_0 = \mathbf{0}$ is assumed, and the necessary

initial d'Alembert acceleration $\mathbf{a}_0$ is computed so that the initial state is in dynamic equilibrium. The implicit Newmark method with parameters $\beta = 0.25$ and $\gamma = 0.5$, the HHT-α method with $\alpha = 0.75$ and the new energy-momentum conserving algorithm are used to obtain the dynamic response of the cable. The time step is set so that the dominant period of each simulation contains about a hundred steps.

4.3.3.1 In-plane free vibration for large sag-to-span ratio

First, the large-amplitude free vibration in the plane of the cable is studied with a time step of $\Delta t = 0.05$ sec. Figure 4.31 presents the normalized results of the Newmark method under the symmetric initial displacement field with amplification factors $\alpha_s = 15$ and $\alpha_a = 0$. The cable response in Fig. 4.31(a) is essentially periodic for the displacements at midspan and quarter-span, even though a nonlinear wave is observed because of the large sag-to-span ratio of cable C2. The 2nd PK axial force time history shows significant high-frequency oscillations caused by the sudden release of the imposed displacements. Figure 4.34 shows the spectral decomposition of the axial force history at midspan and at the supports, with a large-amplitude high frequency at 4.34 Hz (0.23 sec). The total energy of the cable in Fig. 4.31(b) is conserved with a slight oscillation at the mean value of 2.49×10^4 kJ.

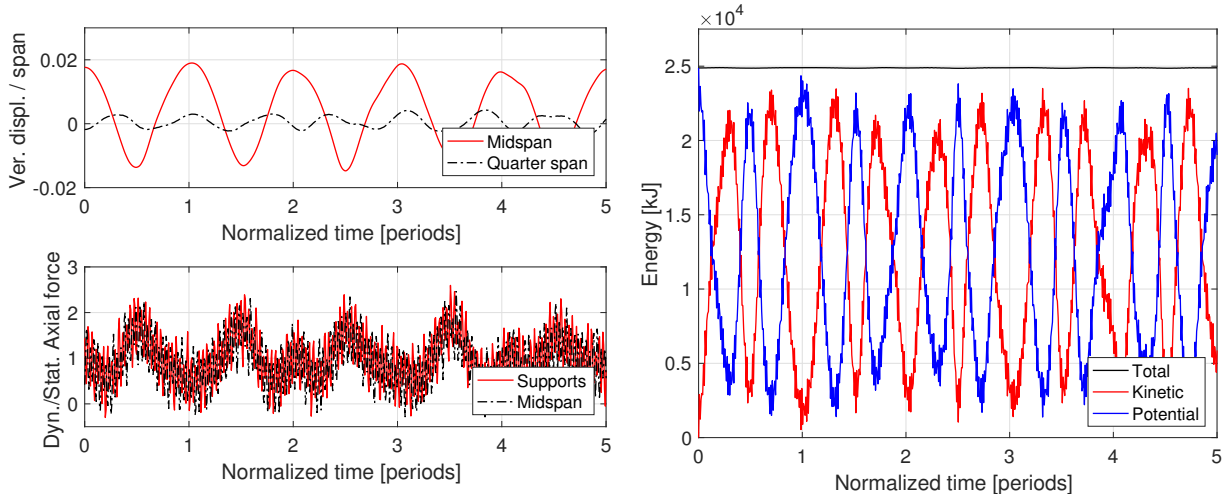

(a) Normalized displacements and axial forces (b) Energy evolution

Figure 4.31: Results for in-plane free vibration with the Newmark method, $\beta = 0.25$ and $\gamma = 0.5$ (Example 6).

Figure 4.32 presents the same analysis, with amplification factors $\alpha_s = 15$ and $\alpha_a = 0$, for the HHT-α method. In this case, the cable response in Fig. 4.32(a) shows very similar results for the displacement time history at midspan and at quarter span compared to the Newmark method, but includes numerical dissipation that reduces the amplitude of the high-frequency contributions to the axial forces. The spectral decomposition of the axial force history at

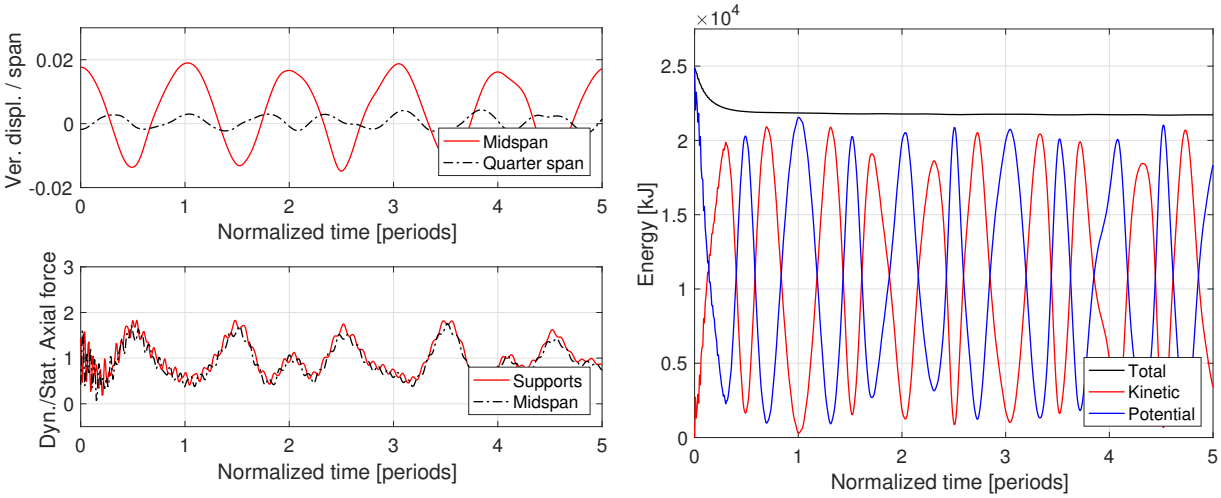

(a) Normalized displacements and axial forces (b) Energy evolution

Figure 4.32: Results for in-plane free vibration with the HHT-α method, $\alpha = 0.75$ (Example 6).

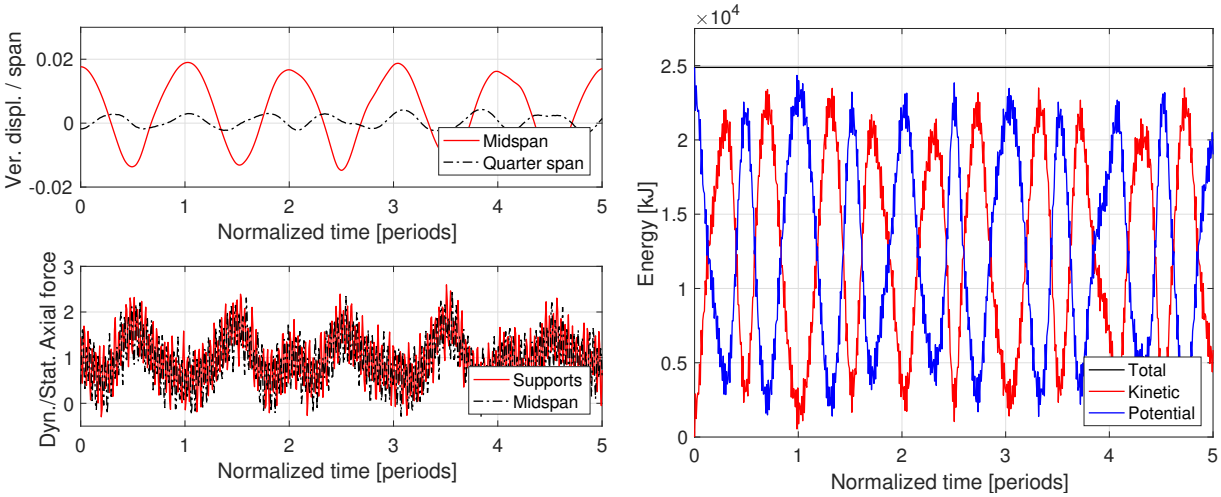

(a) Normalized displacements and axial forces (b) Energy evolution

Figure 4.33: Results for in-plane free vibration with the energy-momentum conserving algorithm (Example 6).

midspan and at the supports in Fig. 4.34 demonstrates the reduction in the amplification factor of the high frequencies, and Fig. 4.32(b) shows the impact of this numerical dissipation on the total energy of the cable, which shows a notable decrease in the early steps of the simulation.

The same analysis, with amplification factors $\alpha_s = 15$ and $\alpha_a = 0$, is performed with the energy-momentum conserving algorithm in Fig. 4.33. The time histories for the normalized

displacements and the 2nd PK axial forces in Fig. 4.33(a) show very similar results to the Newmark method. Significant high-frequency oscillations appear in the axial force time history because of the compression wave produced by the sudden release of the imposed displacements. These oscillations appear in the spectral decomposition in Fig. 4.34 at the same frequencies and with very similar amplitudes as those for the Newmark method. The total energy in Fig. 4.33(b) is exactly conserved at the initial value of 2.49×10^4 kJ.

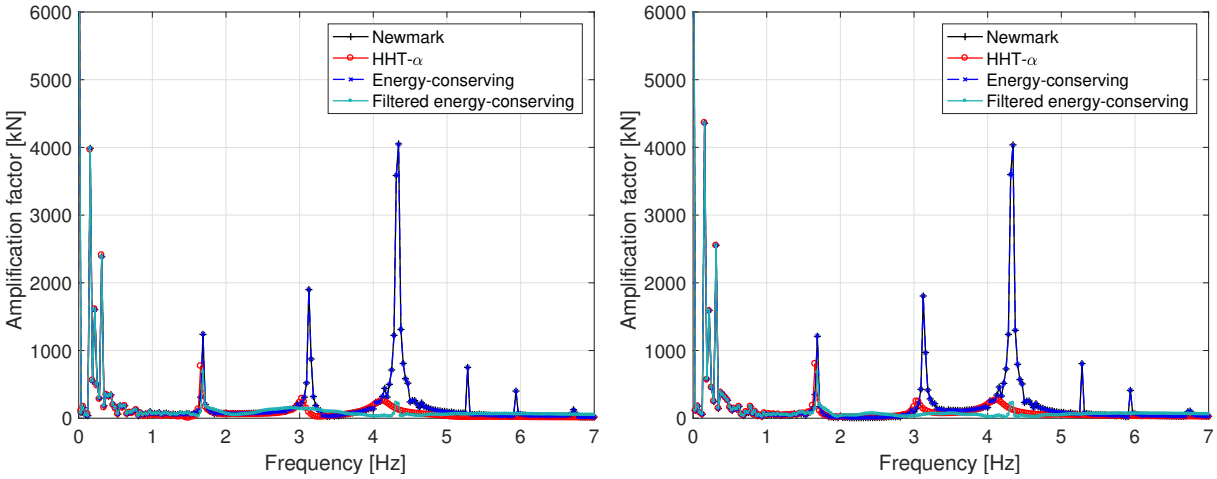

(a) Midspan (b) Supports

Figure 4.34: Spectral decomposition for axial force history and in-plane vibration (Example 6).

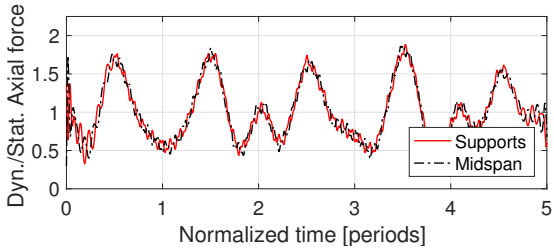

Figure 4.35: Filtered in-plane axial force history for the energy-momentum conserving scheme (Example 6).

A Savitzky-Golay filter with a one-period frame length is used to remove the high frequencies in the axial force time history. In this case, the dominant period of the signal contains about 126 time steps and hence a filter of order 31 is selected according to the guidelines in Section 3.6.2.4. Figure 4.35 shows the axial force history at midspan and at the supports that results from the filtering process, with a 6.4% decrease in total energy to 2.33×10^4 kJ, while their corresponding spectral decomposition is presented in Fig. 4.34, showing a significant amplitude reduction in the frequencies beyond 2 Hz (0.5 sec).

4.3.3.2 Out-of-plane free vibration for large sag-to-span ratio

The large-amplitude free vibration in the plane orthogonal to the cable is studied with the same integration methods and a time step of $\Delta t = 0.2$ sec. Figure 4.36 presents the normalized results of the Newmark method with out-of-plane amplification factors $\alpha_s = 15$ and $\alpha_a = 15$. The out-of-plane (OOP) displacement history in Fig. 4.36(a) shows the expected periodic behavior at midspan and the 3d coupling that results from the translation of a double peak at quarter span. The axial force time history contains significant high-frequency contributions due to the sudden release of the imposed displacements, and its spectral decomposition at midspan and at quarter span is shown in Fig. 4.39. This decomposition demonstrates that a wide range of high frequencies between 1.25 Hz (0.80 sec) and 2.25 Hz (0.44 sec) is present in the signal. The total energy evolution for this case presents some oscillations in Fig. 4.36(b), with a mean value of 5.77×10^4 kJ.

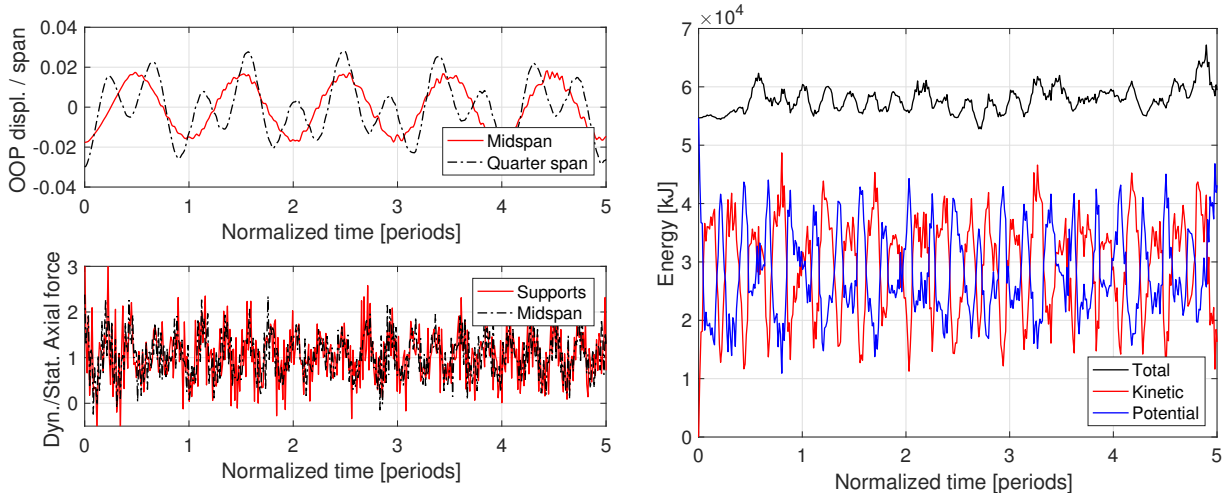

(a) Normalized displacements and axial forces

(b) Energy evolution

Figure 4.36: Results for out-of-plane free vibration with the Newmark method, $\beta = 0.25$ and $\gamma = 0.5$ (Example 6).

The same study, with out-of-plane amplification factors $\alpha_s = 15$ and $\alpha_a = 15$, is conducted with the HHT-α method in Fig. 4.37. The dynamic response of the cable in Fig. 4.37(a) shows a periodic wave for the displacement history at midspan, and captures the 3d coupling represented by the translation of a double peak at quarter span. The numerical dissipation of this integration scheme produces a clear signal for the displacements and the 2nd PK axial forces in Fig. 4.37(a), while the total energy in Fig. 4.37(b) drops significantly in the early stages of the response. Figure 4.39 presents the spectral decomposition of the axial force time history at midspan and at the supports, with the complete removal of the high frequency range present in the Newmark solution.

Figure 4.38 presents the same analysis for out-of-plane amplification factors of $\alpha_s = 15$ and $\alpha_a = 15$ with the proposed energy-momentum conserving algorithm. The results for the

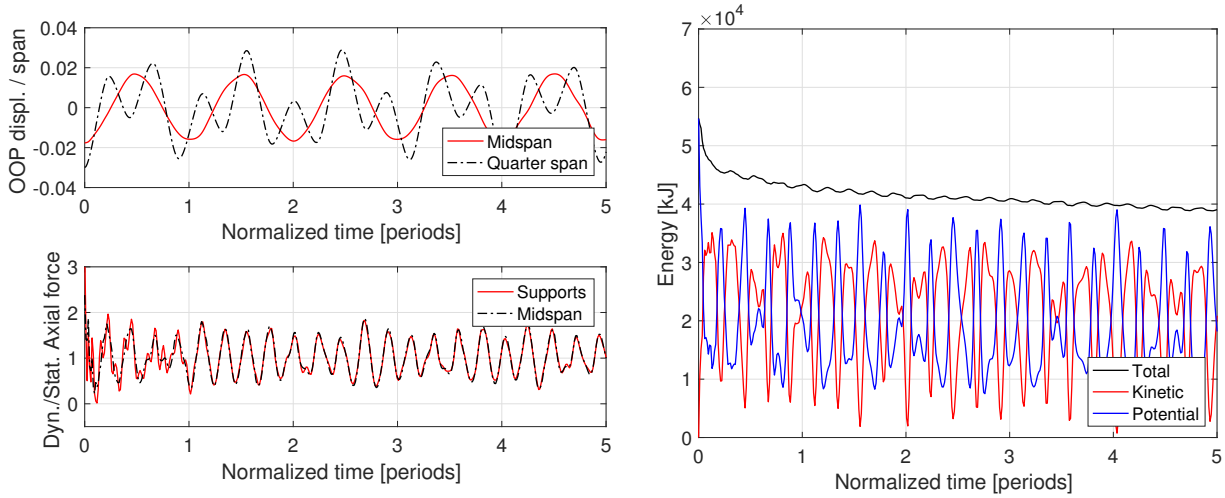

(a) Normalized displacements and axial forces (b) Energy evolution

Figure 4.37: Results for out-of-plane free vibration with HHT-α method, $\alpha = 0.75$ (Example 6).

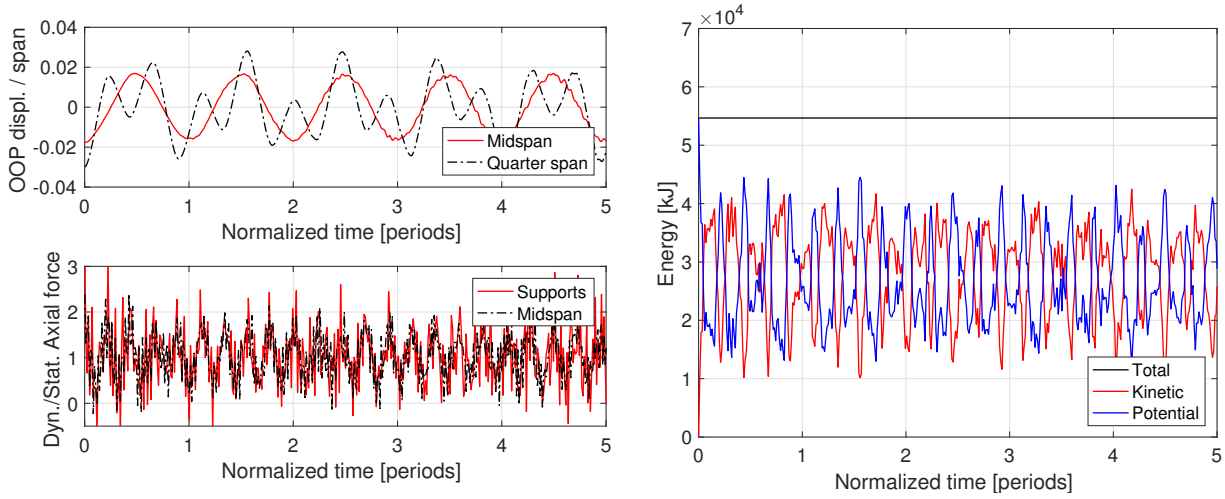

(a) Normalized displacements and axial forces (b) Energy evolution

Figure 4.38: Results for out-of-plane free vibration with the energy-momentum conserving algorithm (Example 6).

normalized out-of-plane (OOP) displacements and the 2nd PK axial force time histories in Fig. 4.38(a) are very similar to those for the Newmark method. The axial force time history shows a compressive wave with significant high-frequency contributions, as demonstrated in the spectral decomposition in Fig. 4.39. However, in contrast to the Newmark method, the total energy of the cable in Fig. 4.38(b) is, in this case, exactly conserved at the initial value of 5.47×10^4 kJ.

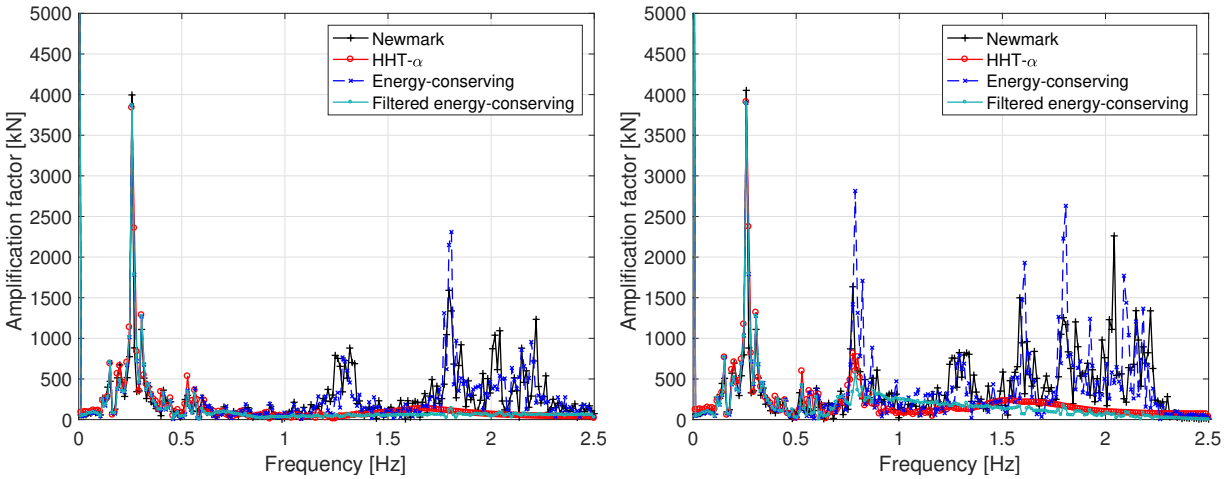

(a) Midspan (b) Supports

Figure 4.39: Spectral decomposition for axial force time history and out-of-plane vibration (Example 6).

The high-frequency oscillations in the axial force time history in Fig. 4.38(a) are addressed in Fig. 4.40 with the use of a Savitzky-Golay filter with a one-period frame length. Because the dominant period of the symmetric mode contains about 85 time steps in this case, a filter of order 28 is selected according to the 1:3 rule in Section 3.6.2.4. The filtering process produces a total energy for the cable of 5.23×10^4 kJ, with a reduction of 4.4% with respect to the non-filtered solution, and thus significantly smaller than the HHT-α method. The spectral decomposition of the filtered axial force history in Fig. 4.39 demonstrates the effective removal of the targeted high frequencies with the proposed filter.

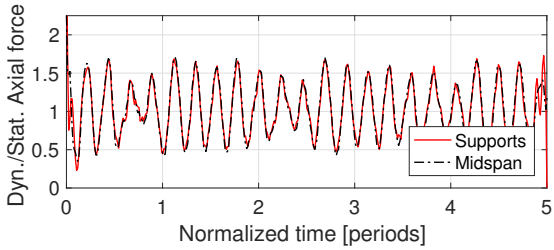

Figure 4.40: Filtered out-of-plane axial force history for the energy-momentum conserving algorithm (Example 6).

4.3.4 Example 7: Free vibration for very large sag-to-span ratio

The seventh example evaluates the large-amplitude in-plane and out-of-plane free vibration of cable C3, with a very large sag-to-span ratio. The structural model consists of a simply-supported cable with the geometric and material properties in Tables 4.6 and 4.7. A St. Venant-Kirchhoff and a neo-Hookean elastic material model are used in this example, but no significant differences appear between the two because the cable stretch remains relatively small. The cable is discretized with a mesh of ten elements, in contrast to the fifty elements used by Srinil *et al.* [47].

The large-amplitude free vibration is evaluated for an initial displacement field $\mathbf{u}_0$ of the form

$$\mathbf{u}_0 = \alpha_s \mathbf{u}_{s1} + \alpha_a \mathbf{u}_{a1} \tag{4.15}$$

where $\mathbf{u}_{s1}$ is the normalized first symmetric mode and $\mathbf{u}_{a1}$ is the normalized first antisymmetric mode, either in the cable plane or in the plane orthogonal to it, with α_s and α_a the corresponding amplification factors. An initial velocity $\mathbf{v}_0 = \mathbf{0}$ is assumed, and the necessary initial d'Alembert acceleration $\mathbf{a}_0$ is computed so that the initial state is in dynamic equilibrium. The implicit Newmark method with parameters $\beta = 0.25$ and $\gamma = 0.5$, the HHT-α method with $\alpha = 0.75$ and the new energy-momentum conserving algorithm are used to obtain the dynamic response of the cable. The time step is set so that the dominant response period encompasses about a hundred steps.

4.3.4.1 In-plane free vibration for very large sag-to-span ratio

First, the large-amplitude free vibration in the plane of the cable is studied with a time step of $\Delta t = 0.1$ sec. Figure 4.41 presents the normalized results for the Newmark method under the symmetric initial displacement field with amplification factors $\alpha_s = 16.5$ and $\alpha_a = 0$. In this case, the very large sag-to-span ratio of cable C3 produces a highly nonlinear wave for the displacement time history at midspan and at quarter span, and a 2nd PK axial force time history with very significant high-frequency contributions and non-physical negative values in Fig. 4.41(a). Figure 4.44 presents the spectral decomposition of the axial force signal at midspan and at the supports, containing a wide range of high frequencies with two dominant amplitudes at 2.61 Hz (0.38 sec) and at 3.19 Hz (0.31 sec). The total energy of the cable oscillates slightly around a mean value of 5.29×10^4 kJ in Fig. 4.41(b).

Figure 4.42 presents the same analysis, under the symmetric initial displacement field with amplification factors $\alpha_s = 16.5$ and $\alpha_a = 0$, for the HHT-α method. In this case, the displacement time history at midspan and at quarter span in Fig. 4.42(a) show significant damping with respect to the Newmark solution. The numerical dissipation of the algorithm, which reduces the total energy almost by a factor of two in Fig. 4.42(b), smoothes out the 2nd PK axial force time history at midspan and at the supports, even though non-physical negative values are still present in the early time steps. The spectral decomposition of these signals in Fig. 4.44 corroborates the energy dissipation with the removal of the frequencies higher than 2 Hz (0.5 sec).

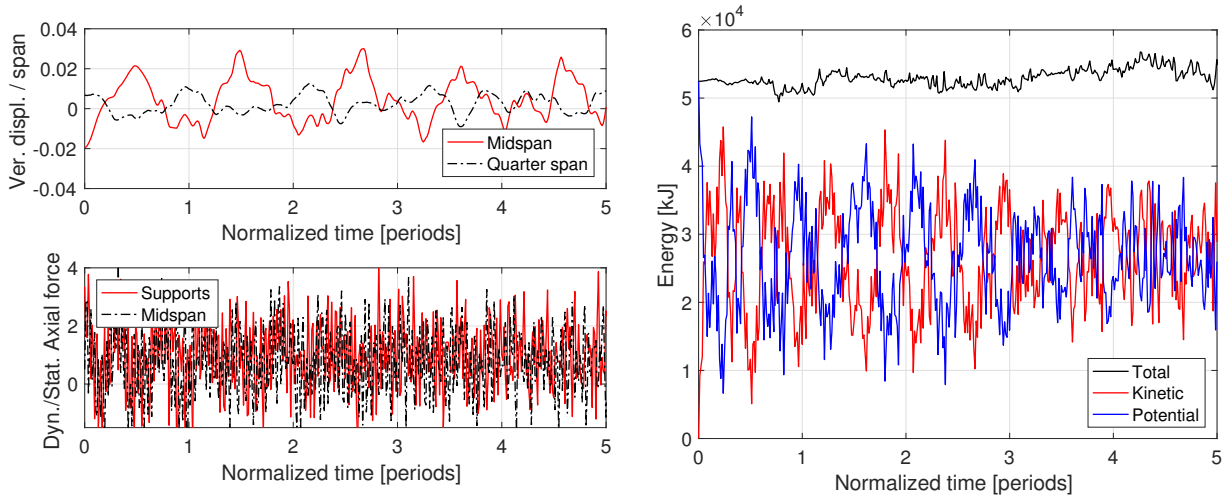

(a) Normalized displacements and axial forces (b) Energy evolution

Figure 4.41: Results for in-plane free vibration with the Newmark method, $\beta = 0.25$ and $\gamma = 0.5$ (Example 7).

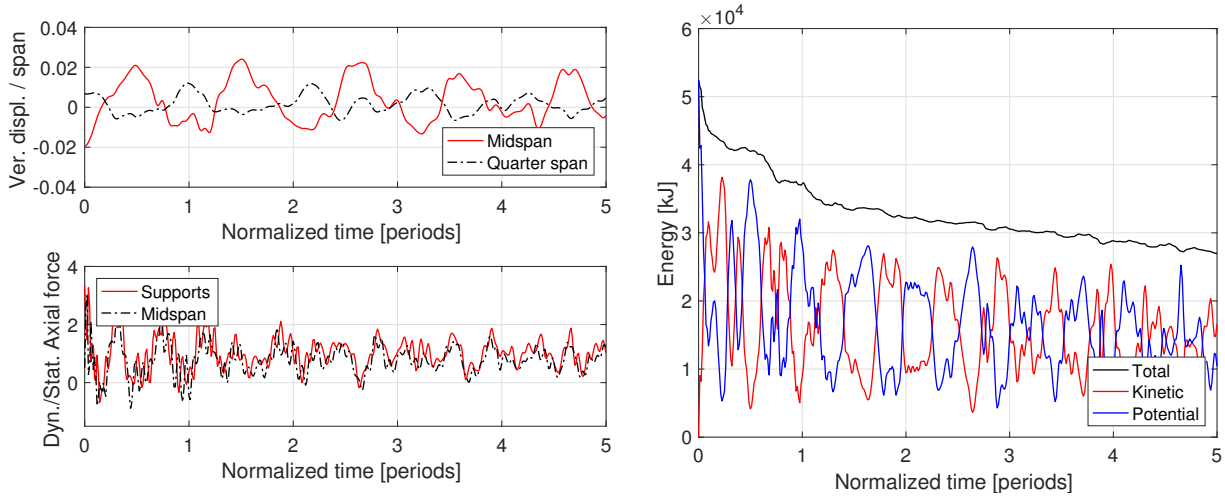

(a) Normalized displacements and axial forces (b) Energy evolution

Figure 4.42: Results for in-plane free vibration with the HHT-α method, $\alpha = 0.75$ (Example 7).

The same analysis with amplification factors of $\alpha_s = 16.5$ and $\alpha_a = 0$ is performed with the energy-momentum conserving algorithm in Fig. 4.43. While the normalized displacements at midspan and at quarter span in Fig. 4.43(a) are very similar to those obtained with the Newmark method in the early time steps of the simulation, a slight decrease in their amplitude is observed in later time steps. The axial force time history at midspan and at the supports, with spectral decompositions in Fig. 4.44, show higher amplitudes than those

of the Newmark solution at the same high frequencies, while the total energy in Fig. 4.43(b) is exactly conserved at the initial value of 5.25×10^4 kJ.

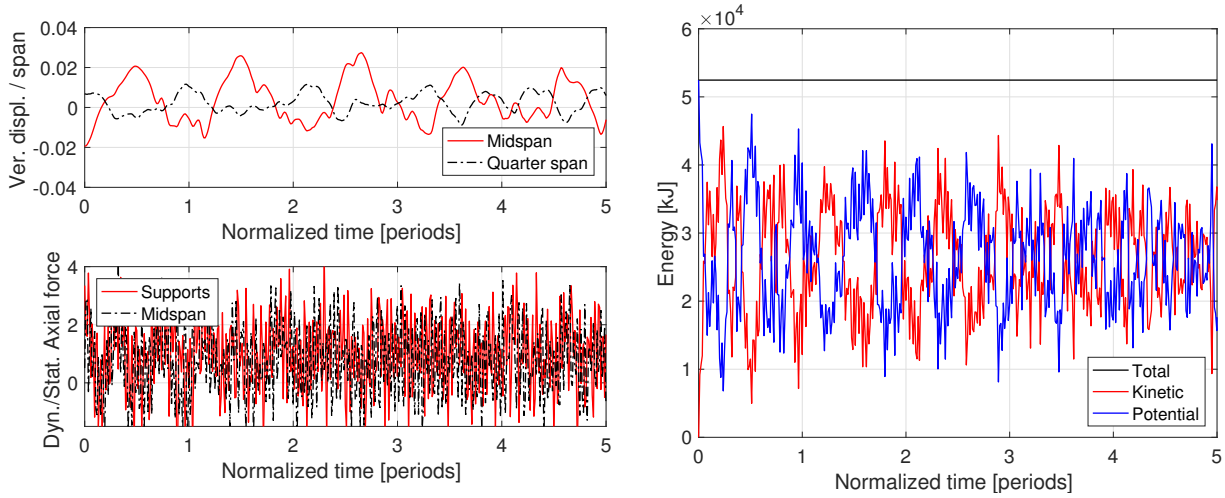

(a) Normalized displacements and axial forces (b) Energy evolution

Figure 4.43: Results for in-plane free vibration with the energy-momentum conserving algorithm (Example 7).

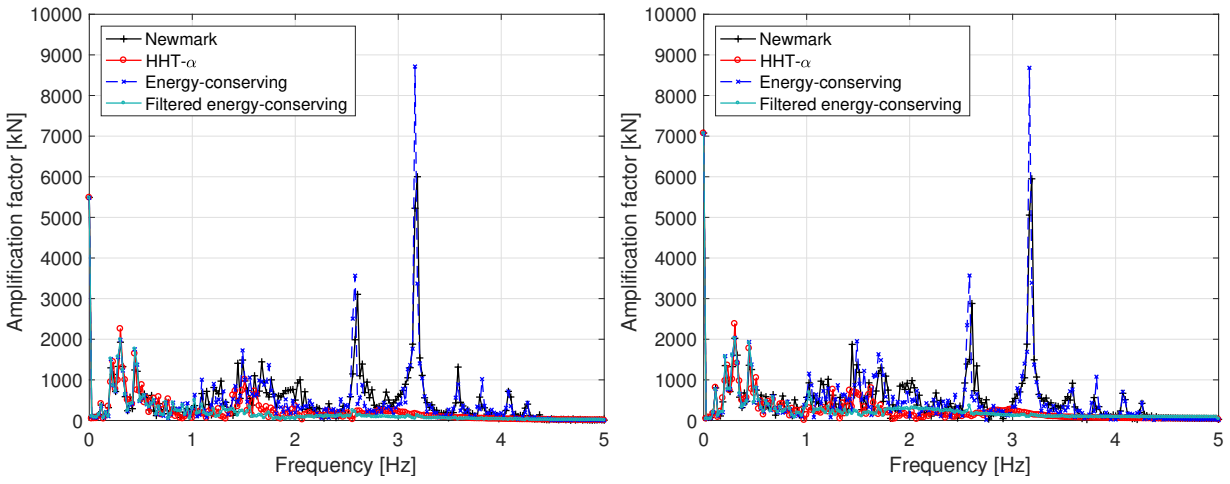

(a) Midspan (b) Supports

Figure 4.44: Spectral decomposition of the axial force history for in-plane vibration (Example 7).

The significant high-frequency contributions that appear in the axial force history in Fig. 4.43(a) are addressed in Fig. 4.45 with the use of a Savitzky-Golay filter. Because the dominant period of this simulation contains about 84 time steps, a filter of order 25 with

a one-period frame length is selected. The resulting total energy after the filtering process reduces to 4.66×10^4 kJ, which represents an 11.2% decrease with respect to the non-filtered solution, and represents a much smaller energy reduction than that of the HHT-α method. The spectral decomposition of the filtered signal in Fig. 4.44 shows the effective removal of the frequencies higher than 1 Hz (1 sec) in the dynamic response.

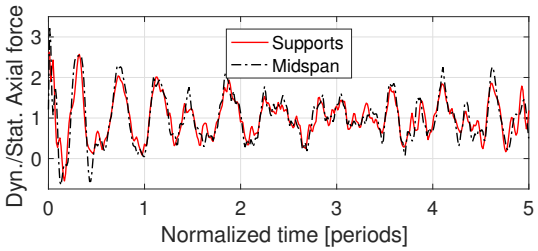

Figure 4.45: Filtered in-plane axial forces for energy-momentum conserving scheme (Example 7).

4.3.4.2 Out-of-plane free vibration for very large sag-to-span ratio

The large-amplitude free vibration in the plane orthogonal to the cable is studied with the same integration schemes with a time step of $\Delta t = 0.25$ sec. Figure 4.46 presents the time histories for the normalized displacements, 2nd PK axial forces and energy for the Newmark method with out-of-plane amplification factors of $\alpha_s = 16.5$ and $\alpha_a = 16.5$. These results demonstrate that the Newmark method is unable to conserve the Hamiltonian structure of the problem under large deformations [6, 44, 45] and thus diverges early in the simulation.

The same study, with out-of-plane amplification factors $\alpha_s = 16.5$ and $\alpha_a = 16.5$, is performed with the HHT-α method in Fig. 4.47. In this case, the numerical dissipation of the algorithm prevents the total energy in Fig. 4.47(b) from diverging, and meaningful displacement and 2nd PK axial force results are obtained. The out-of-plane (OOP) displacement history in Fig. 4.47(a) is periodic with constant maximums at midspan, and the expected 3d coupling appears at quarter span with the periodic translation of a double peak. The 2nd PK axial force history does not include significant high frequency contributions, as is also demonstrated in the spectral decomposition in Fig. 4.49.

Figure 4.48 presents the results for the proposed energy-momentum conserving algorithm with the same out-of-plane amplification factors $\alpha_s = 16.5$ and $\alpha_a = 16.5$. The normalized displacement results in Fig. 4.48(a) display the same periodic behavior and 3d coupling at midspan and quarter span, respectively, as those observed in the HHT-α solution in Fig. 4.47(a). In this case, however, significant high-frequency contributions appear in the 2nd PK axial force time history, with negative values in some time steps. The spectral decomposition of these axial forces in Fig. 4.49 shows significant amplitudes for the frequencies between 1 Hz (1 sec) and 1.8 Hz (0.55 sec), which cause the wild oscillations in the signals. The total energy is exactly conserved in Fig. 4.48(b) at the initial value of 4.82×10^4 kJ.

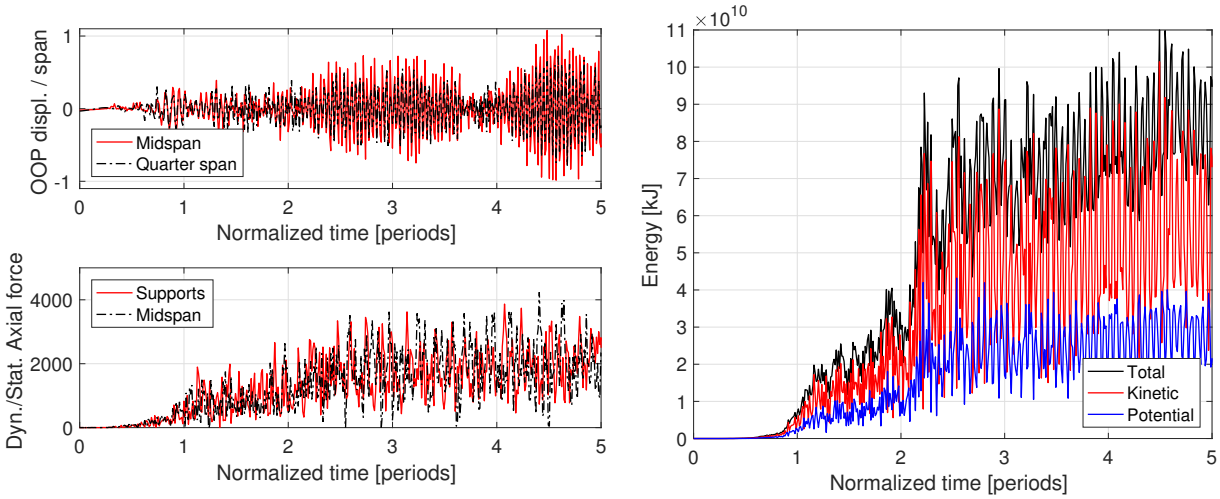

(a) Normalized displacements and axial forces (b) Energy evolution

Figure 4.46: Results for out-of-plane free vibration with the Newmark method, $\beta = 0.25$ and $\gamma = 0.5$ (Example 7).

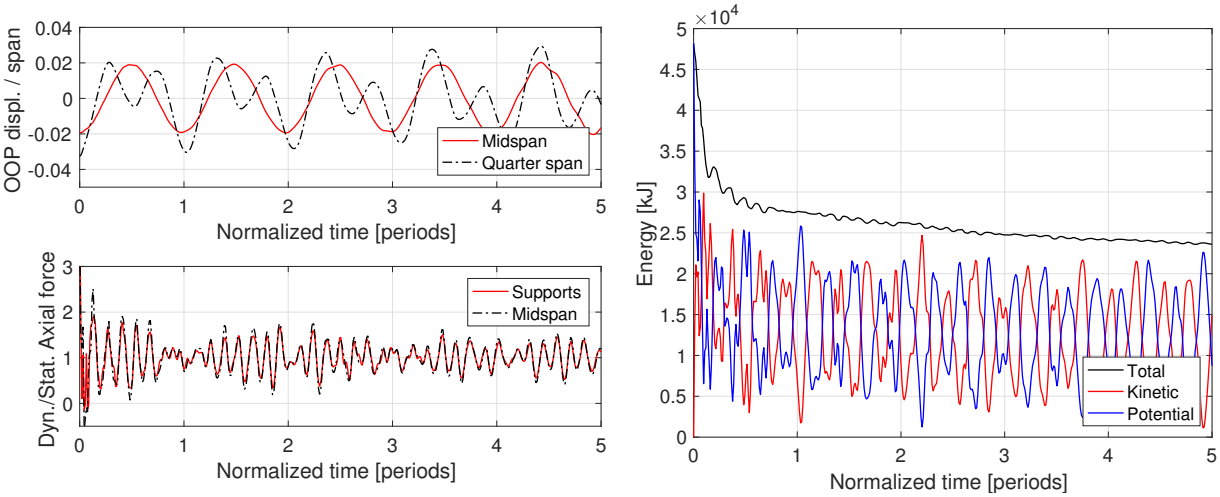

(a) Normalized displacements and axial forces (b) Energy evolution

Figure 4.47: Results for out-of-plane free vibration with HHT-α method, $\alpha = 0.75$ (Example 7).

The high-frequency oscillations in the axial force history with the energy-conserving algorithm are effectively removed in Fig. 4.50 with the use of a Savitzky-Golay filter. The dominant period of the symmetric mode contains about 93 time steps in this case, and hence a filter of order 31 with a one-period frame length is used according to the guidelines in Section 3.6.2.4. The filtering process produces a total energy for the cable of 4.45×10^4 kJ, which represents an energy reduction of 7.7% with respect to the non-filtered solution,

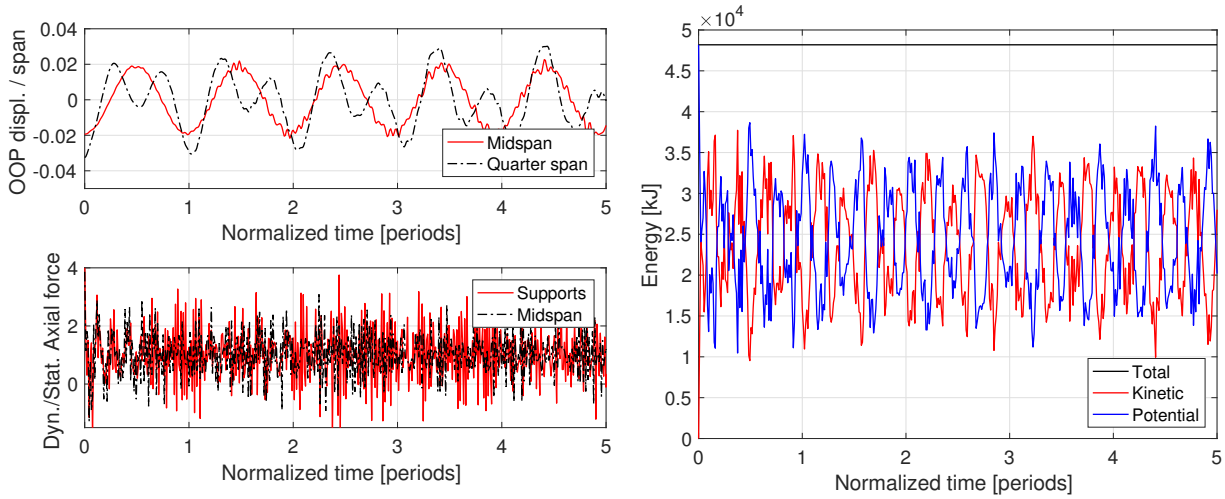

(a) Normalized displacements and axial forces (b) Energy evolution

Figure 4.48: Results for out-of-plane free vibration with the energy-momentum conserving algorithm (Example 7).

and constitutes a significantly smaller energy decrease than that of the HHT-α method. The spectral decomposition of the filtered axial force time history in Fig. 4.39 demonstrates the reduction in the amplification factor of the high frequencies in the range between 1 Hz (1 sec) and 1.8 Hz (0.55 sec) after the filtering process.

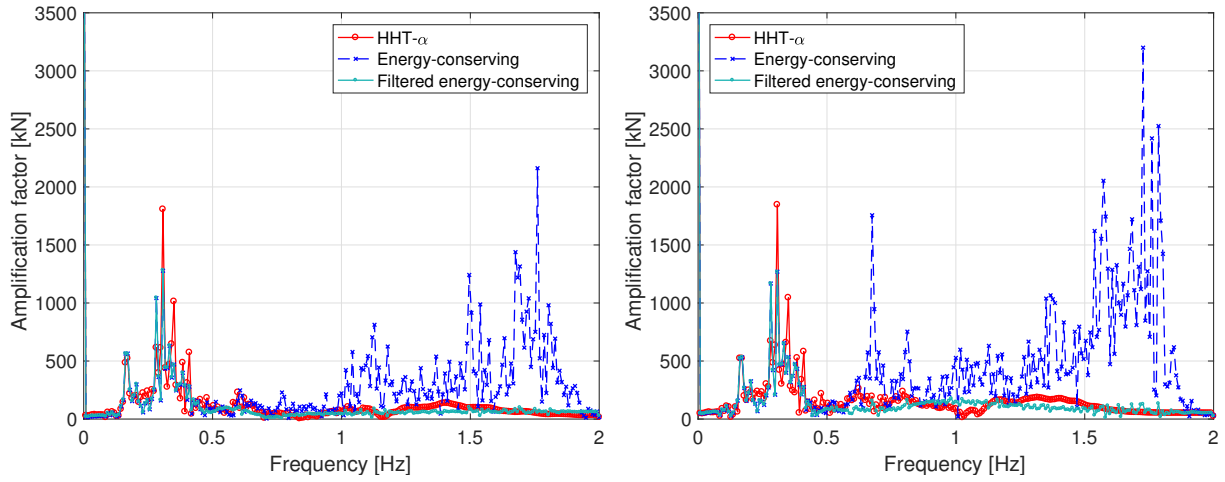

(a) Midspan (b) Supports

Figure 4.49: Spectral decomposition for the axial force time history and out-of-plane vibration (Example 7).

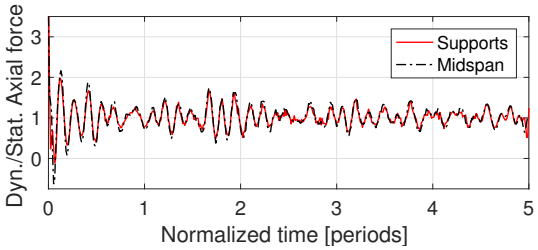

Figure 4.50: Filtered out-of-plane axial force history for energy-momentum conserving algorithm (Example 7).

4.3.5 Example 8: Earthquake response

The last example studies the forced vibration of a simply-supported cable under an earthquake excitation, relevant for applications related to substation equipment stability. Because these applications use cables with a small sag-to-span ratio, the structural model for this example corresponds to cable C1 with a St. Venant-Kirchhoff elastic material model. No damping is considered in this simulation, as inelastic material models are discussed in Chapter 5 of this dissertation. The structural model is subjected to the El Centro ground acceleration magnified 8 times to induce nonlinear cable behavior under large displacements. The ground acceleration $\mathbf{a}_g$ is imposed according to the method in Ref. [12] by defining $\mathbf{u}$, $\mathbf{v}$ and $\dot{\mathbf{v}}$ as values relative to the ground motion and replacing the inertia forces $\mathbf{F}_i$ by

$$\mathbf{F}_i \implies \mathbf{M}\dot{\mathbf{v}} + \mathbf{M}\mathbf{a}_g \tag{4.16}$$

The term $\mathbf{M}\mathbf{a}_g$ is then introduced in the equations as an applied load.

The cable is discretized with a mesh of ten equal-size elements and the dynamic response is obtained with the implicit Newmark method ($\beta = 0.25$ and $\gamma = 0.5$) and with the proposed energy-momentum conserving algorithm. The time step is set to $\Delta t = 0.02$ sec according to the data record of the ground motion in Ref. [12]. In this simulation, the stretch of the cable remains small and, as observed in Example 5, both time integration schemes give almost identical results.

4.3.5.1 Two-dimensional earthquake response

In the first simulation the ground acceleration is imposed in the direction of the cable span so that the dynamic response is two-dimensional. Figure 4.51 presents the time histories for the vertical and horizontal displacements with the two integration schemes. Because the imposed ground acceleration is identical for both supports, the horizontal displacements show a periodic behavior that aligns with the magnitude of the ground motion. In contrast, the vertical displacement history shows the influence of the waves that initiate at the supports and travel along the cable towards the midspan, noting that the quarter span peaks precede the midspan ones.

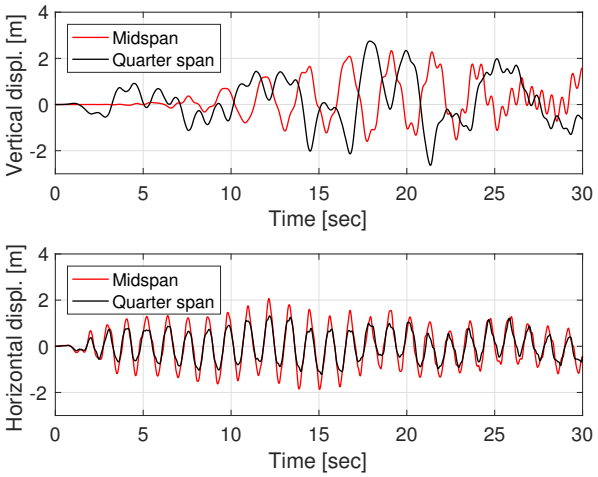

Figure 4.51: Displacements for cable C1 under 2d earthquake excitation (Example 8).

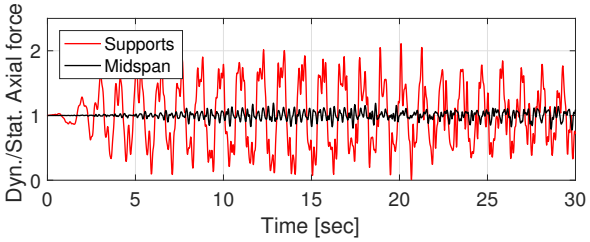

Figure 4.52: Axial force time history for cable C1 under 2d earthquake excitation (Example 8).

The time history for the 2nd PK axial force at midspan and at the supports is presented in Fig. 4.52. The results show that the seismic excitation has a small effect on the midspan axial force history, which is characterized by small-amplitude oscillations around the static value. In contrast, the axial force history at the supports suffers significantly from the dynamic effect produced by the earthquake excitation, and its oscillations reach up to a factor of two with respect to the static value.

4.3.5.2 Three-dimensional earthquake response

A second earthquake simulation is performed by imposing the same horizontal ground acceleration with a 10-degree angle relative to the cable plane, so that the dynamic response of the cable is three-dimensional.

Figure 4.53 shows the time histories for the out-of-plane (OOP), the vertical and the horizontal displacements with the two time integration schemes. Results show that the

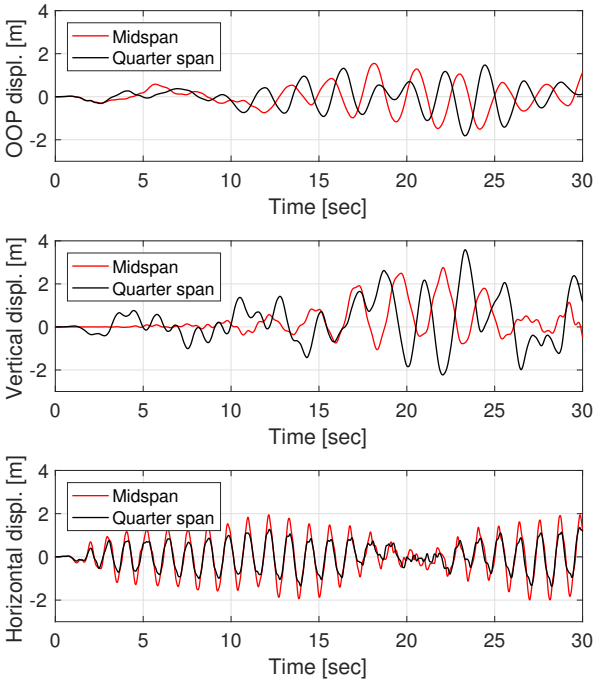

Figure 4.53: Displacements for cable C1 under 3d earthquake excitation (Example 8).

small angle of 10 degrees excites the out-of-plane displacements significantly while keeping the vertical and the horizontal displacements with a similar magnitude compared to the 2d case. A 3d coupling of the response is observed in the horizontal displacement history that transfers energy to the OOP and vertical displacement histories 20 seconds into the simulation. This phenomenon is corroborated by the 2nd PK axial force time history in Fig. 4.54, for which a progressive decrease in the axial force magnitude at the supports takes place during the same time interval. As observed in the 2d case, the 2nd PK axial forces at midspan are only slightly affected by the earthquake excitation, while the corresponding axial forces at the supports increase their magnitude up to a factor of two with respect to the static value.

The results of this three-dimensional earthquake simulation suggest that very small angles in the direction of the imposed ground acceleration excite the out-of-plane behavior of interconnecting cables significantly. As a result, related applications may be affected significantly by geometric defects or spurious out-of-plane displacements.

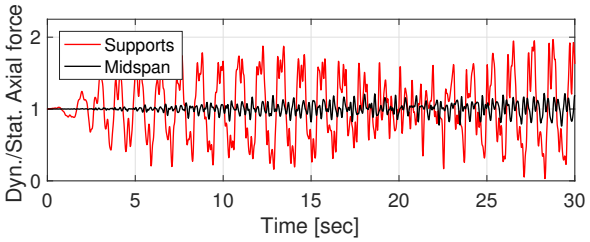

Figure 4.54: Axial force time history for cable C1 under 3d earthquake excitation (Example 8).

4.4 Concluding remarks

The proposed mixed cable element, either with a continuous or a discontinuous axial force implementation, can accommodate different material models. In this chapter, nonlinear elastic materials are discussed with the results confirming that St. Venant-Kirchhoff and neo-Hookean elastic materials behave roboustly in both implementations. The two material models give very similar displacements and axial forces for the same material stiffness EA under small distributed loads, as is expected for small cable strains. Under increasing distributed loads, the results show that the St. Venant-Kirchhoff material model gives smaller midspan sags and larger 2nd PK axial forces than the neo-Hookean material model.

The static examples presented in this chapter show that the continuous and the discontinuous implementations of the proposed mixed cable element give virtually identical results for meshes of equal-size elements in symmetric problems. Moreover, they also show that a small number of elements is required for very accurate results. In contrast, the discontinuous formulation produces discontinuous axial force distributions when used in meshes of unequal-size elements and symmetric problems, with the results converging to the continuous solution as the mesh is refined.

Under concentrated loads, the continuous formulation provides inaccurate results for coarse meshes, especially for horizontal displacements. In contrast, the discontinuous formulation intrinsically accommodates jumps in the axial force at the point of load application, and thus produces very accurate results for coarse meshes. The continuous formulation converges to the exact solution when the mesh is refined, despite the presence of Gibbs oscillations due to the nature of the approximation. This shortcoming of the continuous form can be eliminated by placing two nodes with linked displacements at the point of the concentrated load application. It is confirmed that both implementations of the cable element give the same results in this case.

The proposed cable element is able to identify the equilibrium configurations of 2d and 3d cable arrangements with significant accuracy, and distinguish stable from unstable states. For these equilibrium configurations, the accuracy of the resulting axial force distribution is noteworthy, in contrast to existing catenary elements which overestimate the axial forces

because of their assumption of a constant axial force distribution.

The first symmetric and antisymmetric in-plane and out-of-plane modes of vibration of cables with different sag-to-span ratios can be computed with accuracy for the two nonlinear elastic material models with the proposed formulation. The study of the in-plane and out-of-plane free vibration of these cables shows that, for small sag-to-span ratios, the Newmark method, the HHT-α method and the proposed energy-momentum conserving algorithm give very similar results for displacements and axial forces, even though the HHT-α method introduces a small decay in the total energy. For large sag-to-span ratios, the Newmark method and the energy-momentum conserving algorithm give rise to high-frequency oscillations in the axial forces, with the former not being able to exactly conserve the total energy of the system. In this case, the HHT-α method removes the high frequencies in the axial forces at the cost of a significant energy reduction. For the case of very large sag-to-span ratios and large initial displacement fields, the Newmark method is unable to conserve the Hamiltonian structure of the problem and diverges early in the simulation. The HHT-α method and the energy-momentum conserving algorithm provide meaningful results for the displacements and axial forces in this case, with the latter showing high-frequency oscillations in the axial force field.

The use of a Savitzky-Golay filter effectively removes the high-frequency oscillations in the axial force time history regardless of the cable sag-to-span ratio. Furthermore, it is observed that the energy reduction of this filtering process is significantly smaller than that of the HHT-α method, and thus represents a better approximation for the solution of the conserving system.

When subjected to an earthquake excitation, the proposed mixed cable elements are able to reproduce the waves that form at the supports and travel towards the cable midspan. Moreover, the proposed elements corroborate the high sensitivity of simply-supported cables to 3d offsets in the imposed ground acceleration, and thus reproduce significant out-of-plane displacements for small offset values.

Chapter 5
Viscoelastic material models

Once the excitation stops, the dynamic response of real structures decays with time due to the energy dissipation caused by complex physical internal mechanisms and air resistance. This behavior, which has not yet been considered in previous developments, is incorporated into the proposed mixed cable element.

From a mechanics point of view, there exist three basic approaches to account for energy dissipation under an elastic material response. First, viscous damping forces can be included directly in the equilibrium equation and assembled into a global damping term in the principle of virtual work. Second, rheological models such as the standard linear solid or the generalized Maxwell solid can be used to model the constitutive behavior of the material with incrementally-infinitesimal dissipative strains. And third, viscoelastic models with finite dissipative strains can be considered for the constitutive behavior of the material when large strains occur. These three approaches are implemented in the following sections and are used in some simple structural models to assess the dynamic response of cables.

5.1 Viscous damping forces

The most common model for considering damping in structures consists of including viscous damping forces in the equilibrium equation. This section formulates the governing equations under this assumption and discusses their numerical implementation.

5.1.1 Formulation

Viscous damping forces are distributed loads $\mathbf{d}$ that act along the cable and go against its motion. These forces are proportional to the velocity field $\dot{\mathbf{u}}$ in the form

$$\mathbf{d} = \boldsymbol{\vartheta}(s)\dot{\mathbf{u}} \tag{5.1}$$

where $\boldsymbol{\vartheta}(s)$ is the damping tensor per unit current length. The equilibrium equation in Eq. 3.27 is therefore modified to

$$\mathbf{n}(s,t) - \mathbf{n}(0,t) + \int_0^s \mathbf{w}(s,t)\, ds - \int_0^s \boldsymbol{\vartheta}(s)\dot{\mathbf{u}}\, ds = \frac{d}{dt}\int_0^s m(s)\dot{\mathbf{u}}(s,t)\, ds \tag{5.2}$$

Applying the fundamental theorem of calculus and the localization theorem gives the local form of the equilibrium equation in the reference configuration

$$\frac{d}{dS}\left(\hat{\mathrm{N}}\sqrt{G^{11}}\mathbf{g}_1\right) + \hat{\mathbf{W}} - \boldsymbol{\Upsilon}\dot{\mathbf{u}} - m_0\ddot{\mathbf{u}} = \mathbf{0} \tag{5.3}$$

where $\boldsymbol{\Upsilon}(S)$ represents the damping tensor per unit reference length.

The same procedure as in Section 3.4 gives the modified principle of virtual work

$$\int_0^L \delta\mathbf{u}' \cdot G^{11}\hat{\mathrm{N}}\mathbf{g}_1\, dS + \underbrace{\int_0^L \delta\mathbf{u}\cdot\boldsymbol{\Upsilon}\dot{\mathbf{u}}\, dS}_{\mathbf{f}_d} + \int_0^L \delta\mathbf{u}\cdot\rho_0\ddot{\mathbf{u}}\, dS = \left[\delta\mathbf{u}\cdot\bar{\mathbf{t}}\right]_{\Gamma_q} + \int_0^L \delta\mathbf{u}\cdot\hat{\mathbf{W}}\, dS \tag{5.4}$$

where the new term $\mathbf{f}_d$ represents the virtual work of the damping forces.

The spatial discretization of the damping term $\mathbf{f}_d$ at the configuration $t_{n+\alpha}$ uses the interpolation functions for the displacement and the velocity fields in Eqs. 3.53 and 3.55 to give

$$\mathbf{f}_{d,n+\alpha} = \delta\mathbf{u}^t\mathbf{F}_{d,n+\alpha} = \delta\mathbf{u}^t \underbrace{\int_{\Omega_e} \boldsymbol{\phi}^t\boldsymbol{\Upsilon}\boldsymbol{\phi}\, dS}_{\mathbf{C}}\, \hat{\mathbf{v}}_{n+\alpha} = \delta\mathbf{u}^t\mathbf{C}\hat{\mathbf{v}}_{n+\alpha} \tag{5.5}$$

where one identifies the damping matrix $\mathbf{C}$ with

$$\mathbf{C} = \int_{\Omega_e} \boldsymbol{\phi}^t\boldsymbol{\Upsilon}\boldsymbol{\phi}\, dS \tag{5.6}$$

The following sections give the time discretization of the damping term under the Newmark method, the HHT-α method and the proposed energy-momentum consistent algorithm.

5.1.2 Implementation with Newmark and HHT-α methods

The numerical implementation of the damping term $\mathbf{F}_d$ with the Newmark and the HHT-α methods only affects the principle of virtual work component of the objective function $\boldsymbol{\Phi}$ with the extra term

$$\mathbf{F}_{d,n+1} = \mathbf{C}\mathbf{v}_{n+1} \tag{5.7}$$

Introducing the velocity update from the Newmark time integrator in Eq. 3.83 into Eq. 5.7 gives the extra term $\Delta\boldsymbol{\Phi}_d$ in the objective function

$$\Delta\boldsymbol{\Phi}_d = \frac{\gamma}{\beta}\frac{1}{\Delta t}\mathbf{C}(\hat{\mathbf{u}}_{n+1} - \hat{\mathbf{u}}_n) + \left(1 - \frac{\gamma}{\beta}\right)\mathbf{C}\hat{\mathbf{v}}_n + \Delta t\left(1 - \frac{\gamma}{2\beta}\right)\mathbf{C}\hat{\mathbf{a}}_n \tag{5.8}$$

The additional term in Eq. 5.8 depends on the unknown displacements $\hat{\mathbf{u}}_{n+1}$ and thus adds a contribution $\mathbf{K}_d$ to the dynamic stiffness $\mathbf{K}$ of the element according to

$$\mathbf{K}_d = \frac{\partial \Delta \mathbf{\Phi}_d}{\partial \hat{\mathbf{u}}_{n+1}} = \frac{\gamma}{\beta}\frac{1}{\Delta t}\mathbf{C} \tag{5.9}$$

5.1.3 Implementation with energy-momentum algorithm

The implementation of the damping term $\mathbf{F}_d$ with the proposed energy-momentum consistent algorithm adds the term

$$\mathbf{F}_{d,n+1/2} = \mathbf{C}\hat{\mathbf{v}}_{n+1/2} \tag{5.10}$$

to the principle of virtual work component of the objective function $\mathbf{\Phi}$. The solution to the corresponding governing equations can be obtained with state-space variables or with the pointwise momentum relation, as discussed in the following.

5.1.3.1 State-space solution

The state-space solution of the governing equations considers the velocities $\hat{\mathbf{v}}_{n+1}$ as independent degrees of freedom. If a continuous implementation of the axial force field is assumed, the governing equations give the objective function $\mathbf{\Phi}$

$$\begin{aligned}\mathbf{\Phi} = &\begin{bmatrix} \mathbf{0} & \mathbf{0} \\ \mathbf{0} & \frac{1}{\Delta t}\mathbf{M} + \frac{1}{2}\mathbf{C} \\ \frac{1}{\Delta t}\mathbf{M} & -\frac{1}{2}\mathbf{M} \end{bmatrix} \begin{bmatrix} \hat{\mathbf{u}}_{n+1} \\ \hat{\mathbf{v}}_{n+1} \end{bmatrix} + \mathbf{R}_{n+1/2} \\ &- \begin{bmatrix} \mathbf{0} \\ \mathbf{F}_{ext,n+1/2} \\ \mathbf{0} \end{bmatrix} - \begin{bmatrix} \mathbf{0} & \mathbf{0} \\ \mathbf{0} & \frac{1}{\Delta t}\mathbf{M} - \frac{1}{2}\mathbf{C} \\ \frac{1}{\Delta t}\mathbf{M} & \frac{1}{2}\mathbf{M} \end{bmatrix} \begin{bmatrix} \hat{\mathbf{u}}_n \\ \hat{\mathbf{v}}_n \end{bmatrix}\end{aligned} \tag{5.11}$$

with the corresponding dynamic stiffness matrix $\mathbf{K}$ for the m-th iterate given by differentiation with respect to the state-space variables $\hat{\mathbf{V}}_{n+1} = (\hat{\mathbf{N}}_{n+1}, \hat{\mathbf{u}}_{n+1}, \hat{\mathbf{v}}_{n+1})$

$$\mathbf{K} = \left.\frac{\partial \mathbf{\Phi}}{\partial \hat{\mathbf{V}}_{n+1}}\right|_{\bar{\mathbf{V}}^{(m)}_{n+1}} = \begin{bmatrix} \mathbf{K_{NN}} & \mathbf{K_{Nu}} & \mathbf{0} \\ \mathbf{K_{uN}} & \mathbf{K_{uu}} & \frac{1}{\Delta t}\mathbf{M} + \frac{1}{2}\mathbf{C} \\ \mathbf{0} & \frac{1}{\Delta t}\mathbf{M} & -\frac{1}{2}\mathbf{M} \end{bmatrix} = \left[\begin{array}{cc|c} & & \mathbf{0} \\ & \mathbf{K}_s & \frac{1}{\Delta t}\mathbf{M} + \frac{1}{2}\mathbf{C} \\ \hline \mathbf{0} & \frac{1}{\Delta t}\mathbf{M} & -\frac{1}{2}\mathbf{M} \end{array}\right] \tag{5.12}$$

where $\mathbf{K}_s$ is the static stiffness matrix given in Eq. 3.61 at the configuration $t_{n+1/2}$.

In the case of a discontinuous axial force distribution, the strain-displacement relation is solved at the element level so that the governing equations give the objective function $\mathbf{\Phi}$

$$\begin{aligned}\mathbf{\Phi} = &\begin{bmatrix} \mathbf{0} & \frac{1}{\Delta t}\mathbf{M} + \frac{1}{2}\mathbf{C} \\ \frac{1}{\Delta t}\mathbf{M} & -\frac{1}{2}\mathbf{M} \end{bmatrix} \begin{bmatrix} \hat{\mathbf{u}}_{n+1} \\ \hat{\mathbf{v}}_{n+1} \end{bmatrix} + \mathbf{R}_{n+1/2} \\ &- \begin{bmatrix} \mathbf{F}_{ext,n+1/2} \\ \mathbf{0} \end{bmatrix} - \begin{bmatrix} \mathbf{0} & \frac{1}{\Delta t}\mathbf{M} - \frac{1}{2}\mathbf{C} \\ \frac{1}{\Delta t}\mathbf{M} & \frac{1}{2}\mathbf{M} \end{bmatrix} \begin{bmatrix} \hat{\mathbf{u}}_n \\ \hat{\mathbf{v}}_n \end{bmatrix}\end{aligned} \tag{5.13}$$

with the corresponding dynamic stiffness matrix $\mathbf{K}$ for the m-th iterate obtained from differentiation with respect to the state-space variables $\hat{\mathbf{V}}_{n+1} = (\hat{\mathbf{u}}_{n+1}, \hat{\mathbf{v}}_{n+1})$

$$\mathbf{K} = \left.\frac{\partial \mathbf{\Phi}}{\partial \hat{\mathbf{V}}_{n+1}}\right|_{\bar{\mathbf{V}}_{n+1}^{(m)}} = \begin{bmatrix} \mathbf{K}_{sc} & \frac{1}{\Delta t}\mathbf{M} + \frac{1}{2}\mathbf{C} \\ \frac{1}{\Delta t}\mathbf{M} & -\frac{1}{2}\mathbf{M} \end{bmatrix} \tag{5.14}$$

and the condensed stiffness matrix $\mathbf{K}_{sc}$ in Eq. 3.67 at the configuration $t_{n+1/2}$.

5.1.3.2 Pointwise solution

The solution of the governing equations with the pointwise relation for $\mathbf{v}_{n+1/2}$ in Eq. 3.116 gives the extra term $\Delta\mathbf{\Phi}_d$ to the objective function $\mathbf{\Phi}$

$$\Delta\mathbf{\Phi}_d = \frac{1}{\Delta t}\mathbf{C}(\hat{\mathbf{u}}_{n+1} - \hat{\mathbf{u}}_n) \tag{5.15}$$

so that, for the continuous formulation,

$$\begin{aligned} \mathbf{\Phi} = \frac{1}{\Delta t}\begin{bmatrix} \mathbf{0} \\ \left(\frac{2}{\Delta t}\mathbf{M} + \mathbf{C}\right)\hat{\mathbf{u}}_{n+1} \end{bmatrix} + \mathbf{R}_{n+1/2} \\ - \begin{bmatrix} \mathbf{0} \\ \mathbf{F}_{ext,n+1/2} \end{bmatrix} - \frac{1}{\Delta t}\begin{bmatrix} \mathbf{0} & \mathbf{0} \\ \frac{2}{\Delta t}\mathbf{M} + \mathbf{C} & \mathbf{M} \end{bmatrix}\begin{bmatrix} \hat{\mathbf{u}}_n \\ \hat{\mathbf{v}}_n \end{bmatrix} \end{aligned} \tag{5.16}$$

while, for the discontinuous formulation, it is

$$\mathbf{\Phi} = \left(\frac{2}{\Delta t^2}\mathbf{M} + \frac{1}{\Delta t}\mathbf{C}\right)\mathbf{u}_{n+1} + \mathbf{R}_{n+1/2} - \mathbf{F}_{ext,n+1/2} - \frac{1}{\Delta t}\begin{bmatrix} \frac{2}{\Delta t}\mathbf{M} + \mathbf{C} & \mathbf{M} \end{bmatrix}\begin{bmatrix} \hat{\mathbf{u}}_n \\ \hat{\mathbf{v}}_n \end{bmatrix} \tag{5.17}$$

The corresponding stiffness matrices result from the linearization of the objective functions $\mathbf{\Phi}$ in the form

$$\mathbf{K} = \mathbf{K}_s + \frac{1}{\Delta t}\begin{bmatrix} \mathbf{0} & \mathbf{0} \\ \mathbf{0} & \frac{2}{\Delta t}\mathbf{M} + \mathbf{C} \end{bmatrix} \tag{5.18}$$

for the continuous formulation, and in the form

$$\mathbf{K} = \mathbf{K}_{sc} + \frac{2}{\Delta t^2}\mathbf{M} + \frac{1}{\Delta t}\mathbf{C} \tag{5.19}$$

for the discontinuous formulation.

5.2 Incrementally-infinitesimal viscoelasticity

An alternative approach for including damping in structures consists of accounting for viscous flow at the material level. If strains are small, additive strain rates can be assumed, and one can consider rheological models from infinitesimal deformation theory. The corresponding formulation places a restriction on the magnitude of the strain rates and is therefore said to be *incrementally-infinitesimal in time*. Nevertheless, finite deformations can be considered at a particular time step.

5.2.1 Rheological models

The viscous flow at the material level is idealized in incrementally-infinitesimal formulations by rheological models that use a component known as *dashpot*. A dashpot establishes a relation between the stress and the strain rate in the form

$$\mathrm{S} = \eta \dot{\mathrm{E}} \tag{5.20}$$

where S is the physical[1] 2nd PK stress, η is the viscosity and $\dot{\mathrm{E}}$ is the rate of change of the physical Green-Lagrange strain.

Two rheological models are relevant in the context of viscoelastic cables, the standard linear solid and the generalized Maxwell solid. The following sections give the constitutive relations for these material models and discuss their numerical implementation for the proposed mixed cable element.

5.2.1.1 Standard linear solid

The rheological model for the standard linear solid, shown in Fig. 5.1, is composed of a spring of stiffness k_∞ in parallel with a Maxwell element, which is in turn composed of a spring of stiffness k and a dashpot of viscosity η in series.

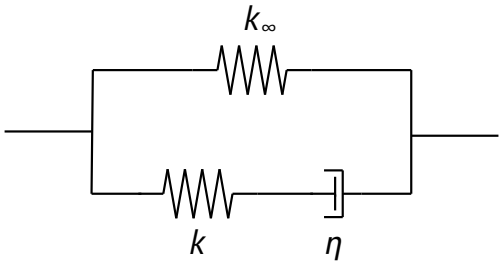

Figure 5.1: Rheological model for the standard linear solid.

The equilibrium and the compatibility equations of this rheological model give the linear relations

$$\begin{cases} \mathrm{S} = \mathrm{S}_\infty + \mathrm{S}_k \\ \dot{\mathrm{E}} \equiv \dot{\mathrm{E}}_\infty = \dot{\mathrm{E}}_1 = \dot{\mathrm{E}}_k + \dot{\mathrm{E}}_\eta \end{cases} \tag{5.21}$$

where the subscripts refer to the components in Fig. 5.1 and $\dot{\mathrm{E}}_1$ is the rate of change of the Green-Lagrange strain for the entire Maxwell element. Assuming St. Venant-Kirchhoff elasticity for the springs and defining the relaxation time τ for the Maxwell element by

$$\tau = \frac{\eta}{k} \tag{5.22}$$

[1]Section 5.2 assumes all stress and strain measures expressed in the physical basis, so that the hat is dropped for simplicity.

a standard calculation shows that the constitutive relation for the standard linear solid is [43]

$$k_0\dot{\mathrm{E}} + \frac{k_\infty}{\tau}\mathrm{E} = \dot{\mathrm{S}} + \frac{\mathrm{S}}{\tau} \tag{5.23}$$

with k_0 being the initial stiffness

$$k_0 = k_\infty + k \tag{5.24}$$

Multiplying Eq. 5.23 by the cross-sectional area A gives the constitutive equation as a function of the 2nd PK axial force N,

$$k_0 A\dot{\mathrm{E}} + \frac{k_\infty A}{\tau}\mathrm{E} = \dot{\mathrm{N}} + \frac{\mathrm{N}}{\tau} \tag{5.25}$$

5.2.1.2 Generalized Maxwell solid

The standard linear solid can be generalized to include m Maxwell elements in parallel with the spring of stiffness k_∞. The resulting model, shown in Fig. 5.2, is known as the generalized Maxwell solid.

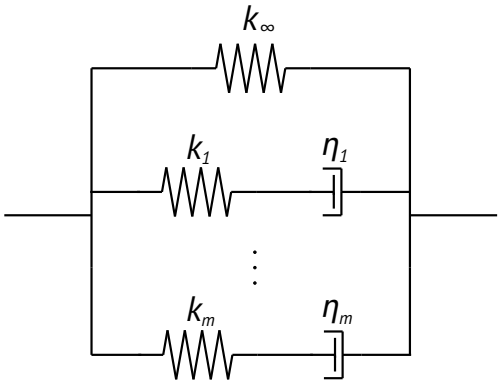

Figure 5.2: Rheological model for the generalized Maxwell solid.

The equilibrium and the compatibility equations for the generalized Maxwell solid follow the linear relations

$$\begin{cases} \mathrm{S} = \mathrm{S}_\infty + \displaystyle\sum_{i=1}^{m} \mathrm{S}_i \\ \dot{\mathrm{E}} \equiv \dot{\mathrm{E}}_\infty = \dot{\mathrm{E}}_1 = \cdots = \dot{\mathrm{E}}_m \\ \dot{\mathrm{E}}_i = \dot{\mathrm{E}}_{k_i} + \dot{\mathrm{E}}_{\eta_i} \quad \text{for} \quad i = 1, ..., m \end{cases} \tag{5.26}$$

where the subscripts refer to the components in Fig. 5.2 and $\dot{\mathrm{E}}_i$ is the rate of change of the Green-Lagrange strain for the i-th Maxwell element. Assuming St. Venant-Kirchhoff

elasticity for the springs, relaxation times τ_i can be defined for each Maxwell element in the form

$$\tau_i = \frac{\eta_i}{k_i} \quad \text{for} \quad i = 1, ..., m \tag{5.27}$$

with an initial stiffness k_0 for the model

$$k_0 = k_\infty + \sum_{i=1}^{m} k_i \tag{5.28}$$

The constitutive equations for the generalized Maxwell solid include rate equations for each Maxwell element and the equilibrium equation for the entire rheological model in the form [43]

$$\begin{cases} \mathrm{S} = \mathrm{S}_\infty + \sum_{i=1}^{m} \mathrm{S}_i \\ k_i \dot{\mathrm{E}} = \dot{\mathrm{S}}_i + \dfrac{\mathrm{S}_i}{\tau_i} \quad \text{for } i = 1, ..., m \end{cases} \tag{5.29}$$

It is straight-forward to show that the combination of the above two equations for $m = 1$ gives the constitutive relation for the standard linear solid in Eq. 5.23. The governing equations for the generalized Maxwell solid can be expressed in terms of the axial forces by multiplying Eq. 5.29 by the cross-sectional area A

$$\begin{cases} \mathrm{N} = \mathrm{N}_\infty + \sum_{i=1}^{m} \mathrm{N}_i = k_\infty A\mathrm{E} + \sum_{i=1}^{m} \mathrm{N}_i \\ k_i A \dot{\mathrm{E}} = \dot{\mathrm{N}}_i + \dfrac{\mathrm{N}_i}{\tau_i} \quad \text{for } i = 1, ..., m \end{cases} \tag{5.30}$$

where N_i is the 2nd PK axial force in the i-th Maxwell element.

5.2.2 Numerical implementation

Two approaches are possible for the numerical implementation of incrementally-infinitesimal viscoelastic models. On the one hand, the exact solution of the differential equation can be used to advance from time step t_n to time step t_{n+1} and, on the other hand, a finite-difference stencil can be deployed to integrate the differential equation numerically between time steps t_n and t_{n+1}. While the first approach is more accurate in theory, the assumption of small strains with small time steps for the current formulation gives very small discrepancies between the two approaches in practice.

5.2.2.1 Exact integration

5.2.2.1.1 Standard linear solid

The exact integration of the constitutive equation for the standard linear solid in Eq. 5.25 uses the integrating factor $\exp((k_\infty t)/(k_0\tau))$ to give

$$A\frac{d}{dt}\left(k_0 \mathrm{E} e^{\frac{k_\infty}{k_0}\frac{t}{\tau}}\right) = A\left(k_0 \dot{\mathrm{E}} e^{\frac{k_\infty}{k_0}\frac{t}{\tau}} + \frac{k_\infty}{\tau}\mathrm{E} e^{\frac{k_\infty}{k_0}\frac{t}{\tau}}\right) = \left(\dot{\mathrm{N}} + \frac{\mathrm{N}}{\tau}\right) e^{\frac{k_\infty}{k_0}\frac{t}{\tau}} \tag{5.31}$$

and thus the strain evolution within the time step (t_n, t_{n+1}) is given as a function of the axial force N by the integral

$$\mathrm{E}(t) e^{\frac{k_\infty}{k_0}\frac{t}{\tau}} = \frac{1}{k_0 A}\int \left(\dot{\mathrm{N}} + \frac{\mathrm{N}}{\tau}\right) e^{\frac{k_\infty}{k_0}\frac{s}{\tau}}\, ds + C \tag{5.32}$$

where C is the constant of integration determined by the initial condition $\mathrm{E}(t_n) = \mathrm{E}_n$.

If a linear evolution for the axial force N is assumed, as corresponds to the usual finite-difference discretization in time,

$$\mathrm{N}(t) = \mathrm{N}_{n+1}\frac{t - t_n}{\Delta t} + \mathrm{N}_n \frac{t_{n+1} - t}{\Delta t} \tag{5.33}$$

the physical Green-Lagrange strain E_{n+1} results from the explicit integration of Eq. 5.32 evaluated at $t = t_{n+1}$ in the form

$$\mathrm{E}_{n+1} = \frac{1}{k_\infty A}\left(\Delta \mathrm{N}\frac{\tau}{\Delta t}\left(1 - \frac{k_0}{k_\infty}\right)\left(1 - e^{-\frac{k_\infty}{k_0}\frac{\Delta t}{\tau}}\right) + \mathrm{N}_{n+1} - \mathrm{N}_n e^{-\frac{k_\infty}{k_0}\frac{\Delta t}{\tau}}\right) + \mathrm{E}_n e^{-\frac{k_\infty}{k_0}\frac{\Delta t}{\tau}} \tag{5.34}$$

with $\Delta \mathrm{N} = \mathrm{N}_{n+1} - \mathrm{N}_n$.

Consequently, the material tangent for the Newmark and the HHT-α methods has the form

$$\frac{d\mathrm{E}_{n+1}}{d\mathrm{N}_{n+1}} = \frac{1}{k_\infty A}\left(\frac{\tau}{\Delta t}\left(1 - \frac{k_0}{k_\infty}\right)\left(1 - e^{-\frac{k_\infty}{k_0}\frac{\Delta t}{\tau}}\right) + 1\right) \tag{5.35}$$

while, for the energy-momentum consistent algorithm, the material tangent is given from the strain average $\mathrm{E}_{n+1/2}$ and follows from the chain rule in the form

$$\frac{d\mathrm{E}_{n+1/2}}{d\mathrm{N}_{n+1}} = \underbrace{\frac{d\mathrm{E}_{n+1/2}}{d\mathrm{E}_{n+1}}}_{1/2}\frac{d\mathrm{E}_{n+1}}{d\mathrm{N}_{n+1}} = \frac{1}{2k_\infty A}\left(\frac{\tau}{\Delta t}\left(1 - \frac{k_0}{k_\infty}\right)\left(1 - e^{-\frac{k_\infty}{k_0}\frac{\Delta t}{\tau}}\right) + 1\right) \tag{5.36}$$

5.2.2.1.2 Generalized Maxwell solid

The exact integration of Eq. 5.30 for the generalized Maxwell solid uses the linear evolution in Eq. 5.33 for the axial forces $\mathrm{N}_i(t)$, and solves the resulting linear differential equations

$$k_i A\dot{\mathrm{E}} = \frac{\mathrm{N}_{i,n+1} - \mathrm{N}_{i,n}}{\Delta t} + \frac{\mathrm{N}_{i,n+1}}{\tau_i}\frac{t - t_n}{\Delta t} + \frac{\mathrm{N}_{i,n}}{\tau}\frac{t_{n+1} - t}{\Delta t} \quad \text{for } i = 1, ..., m \tag{5.37}$$

where $\mathrm{N}_{i,n}$ is the 2nd PK axial force in the i-th Maxwell element at time t_n. Integrating in time and imposing the initial condition $\mathrm{E}(t_n) = \mathrm{E}_n$ gives the expression for $\mathrm{E}(t_{n+1}) = \mathrm{E}_{n+1}$

$$\left\{\begin{array}{l} \dfrac{k_i A}{\Delta t}\mathrm{E}_{n+1} = \dfrac{\mathrm{N}_{i,n+1} - \mathrm{N}_{i,n}}{\Delta t} + \dfrac{\mathrm{N}_{i,n+1} + \mathrm{N}_{i,n}}{2\tau_i} + \dfrac{k_i A}{\Delta t}\mathrm{E}_n \quad \text{for } i = 1, ..., m \\ \mathrm{N}_{n+1} = \mathrm{N}_{\infty,n+1} + \displaystyle\sum_{i=1}^{m} \mathrm{N}_{i,n+1} = k_\infty A \mathrm{E}_{n+1} + \sum_{i=1}^{m} \mathrm{N}_{i,n+1} \end{array}\right. \tag{5.38}$$

or, in compact form,

$$\begin{bmatrix} \frac{k_1 A}{\Delta t} & -\left(\frac{1}{\Delta t_n} + \frac{1}{2\tau_1}\right) & 0 & \cdots & 0 \\ \frac{k_2 A}{\Delta t} & 0 & -\left(\frac{1}{\Delta t} + \frac{1}{2\tau_2}\right) & \cdots & 0 \\ \vdots & \vdots & \vdots & \ddots & \vdots \\ \frac{k_m A}{\Delta t} & 0 & 0 & \cdots & -\left(\frac{1}{\Delta t} + \frac{1}{2\tau_m}\right) \\ k_\infty A & 1 & 1 & \cdots & 1 \end{bmatrix} \begin{bmatrix} \mathrm{E}_{n+1} \\ \mathrm{N}_{1,n+1} \\ \mathrm{N}_{2,n+1} \\ \vdots \\ \mathrm{N}_{m,n+1} \end{bmatrix} = \frac{A}{\Delta t}\begin{bmatrix} k_1 \\ k_2 \\ \vdots \\ k_m \\ 0 \end{bmatrix} \mathrm{E}_n + \begin{bmatrix} \left(\frac{1}{2\tau_1} - \frac{1}{\Delta t}\right)\mathrm{N}_{1,n} \\ \left(\frac{1}{2\tau_2} - \frac{1}{\Delta t}\right)\mathrm{N}_{2,n} \\ \vdots \\ \left(\frac{1}{2\tau_m} - \frac{1}{\Delta t}\right)\mathrm{N}_{m,n} \\ \mathrm{N}_{n+1} \end{bmatrix} \tag{5.39}$$

Equation 5.39 is a linear system of equations that gives the Green-Lagrange strain E_{n+1} and the 2nd PK axial forces $\mathrm{N}_{i,n+1}$ as a function of the total axial force N_{n+1} and the history variables E_n and $\mathrm{N}_{i,n}$.

The material stiffness of the generalized Maxwell solid for the Newmark and the HHT-α methods is obtained by implicit differentiation of the equilibrium equation in Eq. 5.38(2) in the form

$$\frac{d\mathrm{E}_{n+1}}{d\mathrm{N}_{n+1}} = \frac{1}{k_\infty A + \sum_{i=1}^{m} \frac{d\mathrm{N}_{i,n+1}}{d\mathrm{E}_{n+1}}} \tag{5.40}$$

with the derivatives $d\mathrm{N}_{i,n+1}/d\mathrm{N}_{n+1}$ given by the compatibility conditions in Eq. 5.38(1),

$$\frac{d\mathrm{N}_{i,n+1}}{d\mathrm{E}_{n+1}} = \frac{\frac{k_i A}{\Delta t}}{\frac{1}{\Delta t_n} + \frac{1}{2\tau_i}} \quad \text{for } i = 1, ..., m \tag{5.41}$$

The corresponding material stiffness for the proposed energy-momentum consistent algorithm is obtained by the chain rule in the form

$$\frac{d\mathrm{E}_{n+1/2}}{d\mathrm{N}_{n+1}} = \underbrace{\frac{d\mathrm{E}_{n+1/2}}{d\mathrm{E}_{n+1}}}_{1/2} \frac{d\mathrm{E}_{n+1}}{d\mathrm{N}_{n+1}} = \frac{1}{2k_\infty A + 2\sum_{i=1}^{m} \frac{d\mathrm{N}_{i,n+1}}{d\mathrm{E}_{n+1}}} \tag{5.42}$$

with the same contributions $d\mathrm{N}_{i,n+1}/d\mathrm{N}_{n+1}$ as in Eq. 5.41.

5.2.2.2 Numerical integration

5.2.2.2.1 Standard linear solid

The numerical integration of Eq. 5.25 for the standard linear solid uses linear discrete approximations for the time derivatives to give the algebraic counterpart to the differential equation

$$k_0 A \frac{\mathrm{E}_{n+1} - \mathrm{E}_n}{\Delta t} + \frac{k_\infty A}{\tau} \mathrm{E}_{n+1/2} = \frac{\mathrm{N}_{n+1} - \mathrm{N}_n}{\Delta t} + \frac{1}{\tau} \mathrm{N}_{n+1/2} \tag{5.43}$$

Equation 5.43 is linear in E_{n+1} and thus has the explicit solution

$$\mathrm{E}_{n+1} = \frac{1}{A\left(\frac{k_0}{\Delta t} + \frac{k_\infty}{2\tau}\right)} \left(\frac{\mathrm{N}_{n+1} + \mathrm{N}_n}{\Delta t} + \frac{1}{\tau} \mathrm{N}_{n+1/2} + A \left(\frac{k_0}{\Delta t} - \frac{k_\infty}{2\tau} \right) \mathrm{E}_n \right) \tag{5.44}$$

The material tangent for the Newmark and the HHT-α methods is therefore given by

$$\frac{d\mathrm{E}_{n+1}}{d\mathrm{N}_{n+1}} = \frac{\frac{1}{\Delta t} + \frac{1}{2\tau}}{A\left(\frac{k_0}{\Delta t} + \frac{k_\infty}{2\tau}\right)} \tag{5.45}$$

while, for the energy-momentum consistent algorithm, the material tangent follows from chain rule in the form

$$\frac{d\mathrm{E}_{n+1/2}}{d\mathrm{N}_{n+1}} = \underbrace{\frac{d\mathrm{E}_{n+1/2}}{d\mathrm{E}_{n+1}}}_{1/2} \frac{d\mathrm{E}_{n+1}}{d\mathrm{N}_{n+1}} = \frac{\frac{1}{\Delta t} + \frac{1}{2\tau}}{A\left(\frac{2k_0}{\Delta t} + \frac{k_\infty}{\tau}\right)} \tag{5.46}$$

Equations 5.45 and 5.46 correspond to the linearized versions of Eqs. 5.35 and 5.36, respectively.

5.2.2.2.2 Generalized Maxwell solid

The numerical integration of Eq. 5.30 for the generalized Maxwell solid also uses linear discrete approximations for the time derivatives to give

$$\begin{cases} k_i A \dfrac{\mathrm{E}_{n+1} - \mathrm{E}_n}{\Delta t} = \dfrac{\mathrm{N}_{i,n+1} - \mathrm{N}_{i,n}}{\Delta t} + \dfrac{1}{\tau_i} \mathrm{N}_{i,n+1/2} \quad \text{for } i = 1, ..., m \\ \mathrm{N}_{n+1} = \mathrm{N}_{\infty,n+1} + \displaystyle\sum_{i=1}^{m} \mathrm{N}_{i,n+1} = k_\infty A \mathrm{E}_{n+1} + \sum_{i=1}^{m} \mathrm{N}_{i,n+1} \end{cases} \tag{5.47}$$

where $\mathrm{N}_{m,n}$ refers to the 2nd PK axial force in the m-th Maxwell element at the time step t_n. It is readily observed that Eq. 5.47 is identical to Eq. 5.38 because, for given linear axial forces $\mathrm{N}_i(t)$, the exact solution of $\mathrm{E}(t)$ is linear. As a result, the numerical integration of the generalized Maxwell solid is identical to its exact solution for linear axial forces $\mathrm{N}_i(t)$.

5.3 Finite viscoelasticity

The assumption of additive strain rates is abandoned when considering finite deformation theory in the viscoelastic material model. In this case, the viscous strains and their evolution are nonlinear functions of the deformation tensors.

5.3.1 Formulation

Two finite viscoelastic material models, corresponding to the extension of the standard linear solid and the generalized Maxwell element to finite deformations, are formulated in this section. First, the model with one viscoelastic strain, corresponding to the standard linear solid, is formulated. Afterwards, this model is generalized to multiple viscoelastic strains in a generalized Maxwell element manner.

5.3.1.1 Finite viscoelasticity with one viscoelastic strain

In the case of finite viscoelasticity with one viscoelastic strain, the total motion $\boldsymbol{\chi}$ of the cable is decomposed into an elastic part $\boldsymbol{\chi}_e$ and a viscous part $\boldsymbol{\chi}_v$ as shown in Fig. 5.3. Consequently, the total motion $\boldsymbol{\chi}$ of the cable is given by the composition

$$\boldsymbol{\chi} = \boldsymbol{\chi}_e \circ \boldsymbol{\chi}_v \tag{5.48}$$

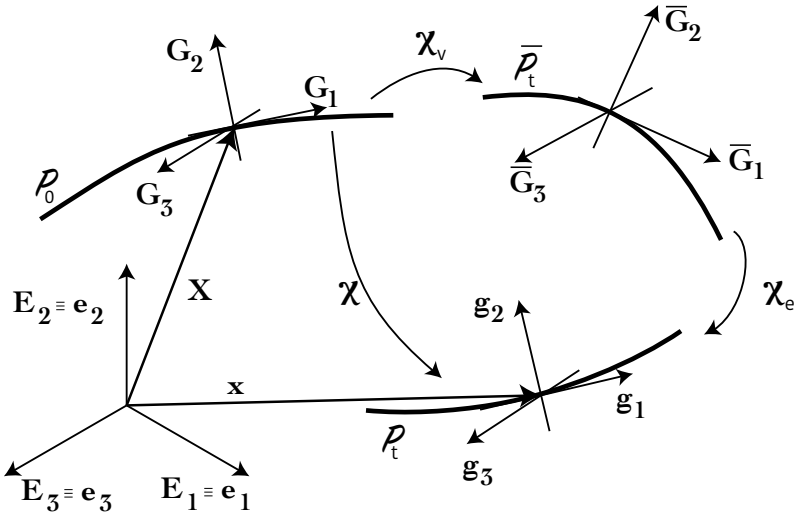

Figure 5.3: Decomposition of the deformation for finite viscoelasticity with one viscoelastic strain.

Under the decomposition in Eq. 5.48, the deformation gradient $\mathbf{F}$ can be expressed in the multiplicative form

$$\mathbf{F} = \mathbf{F}_e\mathbf{F}_v \tag{5.49}$$

and thus a set of basis vectors $\{\bar{\mathbf{G}}_i\}_{i=1}^3$ arises in the intermediate configuration $\bar{\mathcal{P}}_t$ by convecting the reference set $\{\mathbf{G}_i\}_{i=1}^3$ in the form

$$\bar{\mathbf{G}}_i = \mathbf{F}_v\mathbf{G}_i \quad \text{for } i \in \{1,2,3\} \tag{5.50}$$

Also, convecting the basis vectors $\{\bar{\mathbf{G}}_i\}_{i=1}^3$ from the intermediate configuration $\bar{\mathcal{P}}_t$ to the current configuration $\mathcal{P}_t$ gives the current basis vectors $\{\mathbf{g}_i\}_{i=1}^3$,

$$\mathbf{g}_i = \mathbf{F}_e\bar{\mathbf{G}}_i \quad \text{for } i \in \{1,2,3\} \tag{5.51}$$

The deformation gradient $\mathbf{F}$ is therefore expressed in curvilinear coordinates by

$$\mathbf{F} = \underbrace{(\mathbf{g}_i \otimes \bar{\mathbf{G}}^i)}_{\mathbf{F}_e}\underbrace{(\bar{\mathbf{G}}_j \otimes \mathbf{G}^j)}_{\mathbf{F}_v} = \mathbf{g}_i \otimes \mathbf{G}^i \tag{5.52}$$

The 2nd Piola-Kirchhoff stress tensor $\mathbf{S}$ is decomposed accordingly into a *time-infinity* component $\mathbf{S}_\infty$ coming from $\mathbf{F}$ and a viscous component $\mathbf{S}_v$ coming from $\mathbf{F}_e\mathbf{F}_v$ in the form

$$\mathbf{S} = \mathbf{S}_\infty(\mathbf{E}) + \mathbf{S}_v(\mathbf{E}_e) \tag{5.53}$$

where $\mathbf{S}_\infty$ is a function of the total Green-Lagrange strain $\mathbf{S}_\infty = \mathbf{S}_\infty(\mathbf{E})$ and $\mathbf{S}_v$, a function of the elastic Green-Lagrange strain $\mathbf{S}_v = \mathbf{S}_v(\mathbf{E}_e)$. The time-infinity component $\mathbf{S}_\infty$ of the stress is given from an energy function $\mathcal{U}_\infty$ with the usual relation

$$\mathbf{S}_\infty = \frac{\partial \mathcal{U}_\infty}{\partial \mathbf{E}} \tag{5.54}$$

while an objective evolution law for $\mathbf{S}_v(\mathbf{E}_e)$ is required. Following the thermodynamic argument of Reese and Govindjee [40], an appropriate evolution law is given by the quadratic form

$$-\frac{1}{2}(\mathcal{L}_v\mathbf{b}_e)\mathbf{b}_e^{-1} = \mathbb{V}^{-1}\boldsymbol{\tau}_v \tag{5.55}$$

where $\mathcal{L}_v\mathbf{b}_e$ is the Lie derivative of the left Cauchy-Green tensor $\mathbf{b}_e$, $\mathbb{V}^{-1}(\mathbf{b}_e)$ is the fourth-order viscosity tensor and $\boldsymbol{\tau}_v$ is the Kirchhoff stress for the viscous part of the deformation. In curvilinear coordinates, the left Cauchy-Green tensor $\mathbf{b}_e$ has the form

$$\mathbf{b}_e = \bar{G}^{ij}\mathbf{g}_i \otimes \mathbf{g}_j \tag{5.56}$$

while the Kirchhoff stress, coming from the energy function $\mathcal{U}_v$, is the push-forward of the corresponding 2nd PK stress $\mathbf{S}_v = \partial\mathcal{U}_v/\partial\mathbf{E}_e$ of the viscous part,

$$\boldsymbol{\tau}_v = \tau_v^{ij}\mathbf{g}_i \otimes \mathbf{g}_j = \boldsymbol{\chi}^*(\mathbf{S}_v) = \mathbf{F}_e\frac{\partial \mathcal{U}_v}{\partial \mathbf{E}_e}\mathbf{F}_e^t \tag{5.57}$$

Note that the 2nd PK stress $\mathbf{S}_v = \partial \mathcal{U}_v / \partial \mathbf{E}_e$ in Eq. 5.57 resides in the intermediate configuration $\bar{\mathcal{P}}_t$ and has the form in contravariant components

$$\bar{\mathbf{S}}_v = \frac{\partial \mathcal{U}_v}{\partial \mathbf{E}_e} = \bar{S}_v^{ij} \bar{\mathbf{G}}_i \otimes \bar{\mathbf{G}}_j = \hat{\bar{S}}_v^{ij} \hat{\bar{\mathbf{G}}}_i \otimes \hat{\bar{\mathbf{G}}}_j \tag{5.58}$$

for the convected basis $\{\bar{\mathbf{G}}_i\}_{i=1}^3$ and for the physical basis $\{\hat{\bar{\mathbf{G}}}_i\}_{i=1}^3$, respectively. The corresponding 2nd PK stress $\mathbf{S}_v$ in the reference configuration $\mathcal{P}_0$ is given by the pull-back

$$\mathbf{S}_v = \boldsymbol{\chi}_*(\boldsymbol{\tau}_v) = \mathbf{F}^{-1} \boldsymbol{\tau}_v \mathbf{F}^{-t} = \bar{S}_v^{ij} \mathbf{G}_i \otimes \mathbf{G}_j \tag{5.59}$$

The Lie derivative $\mathcal{L}_v \mathbf{b}_e$ in Eq. 5.55 is expressed in curvilinear coordinates by

$$\mathcal{L}_v \mathbf{b}_e = \dot{\bar{G}}^{ij} \mathbf{g}_i \otimes \mathbf{g}_j \tag{5.60}$$

and therefore

$$-\frac{1}{2} (\mathcal{L}_v \mathbf{b}_e) \mathbf{b}_e^{-1} = -\frac{1}{2} (\dot{\bar{G}}^{ij} \mathbf{g}_i \otimes \mathbf{g}_j)(\bar{G}_{kl} \mathbf{g}^k \otimes \mathbf{g}^l) = -\frac{1}{2} \dot{\bar{G}}^{ij} \bar{G}_{jl} \mathbf{g}_i \otimes \mathbf{g}^l \tag{5.61}$$

The relevant 11-contravariant component is given by the projection

$$\hat{\mathbf{g}}^1 \cdot \left(-\frac{1}{2} (\mathcal{L}_v \mathbf{b}_e) \mathbf{b}_e^{-1} \hat{\mathbf{g}}^1 \right) = -\frac{1}{2} \dot{\bar{G}}^{11} \bar{G}_{11} \tag{5.62}$$

and the internal variable for the evolution law becomes the metric coefficient $\bar{G}^{11}$ in the intermediate configuration $\bar{\mathcal{P}}_t$.

The viscosity tensor is assumed volumetric in the form

$$\mathbb{V}^{-1} = \frac{1}{\eta} \mathbb{I} \tag{5.63}$$

where η is the finite-deformation viscosity and $\mathbb{I}$ is the fourth-order identity tensor in Eq. 2.19. The right-hand side in Eq. 5.55 is then given by

$$\mathbb{V}^{-1} \boldsymbol{\tau}_v = \frac{1}{\eta} \boldsymbol{\tau}_v = \frac{1}{\eta} \mathbf{F}_e \frac{\partial \mathcal{U}_v}{\partial \mathbf{E}_e} \mathbf{F}_e^t \tag{5.64}$$

and can be expressed in curvilinear coordinates with

$$\mathbb{V}^{-1} \boldsymbol{\tau}_v = \frac{1}{\eta} (\mathbf{g}_i \otimes \bar{\mathbf{G}}^i)(\bar{S}_v^{jk} \bar{\mathbf{G}}_j \otimes \bar{\mathbf{G}}_k)(\bar{\mathbf{G}}^l \otimes \mathbf{g}_l) = \frac{\bar{S}_v^{ij}}{\eta} \mathbf{g}_i \otimes \mathbf{g}_j \tag{5.65}$$

The relevant 11-contravariant component becomes

$$\hat{\mathbf{g}}^1 \cdot \left(\mathbb{V}^{-1} \boldsymbol{\tau}_v \right) \hat{\mathbf{g}}^1 = \frac{\bar{S}_v^{ij}}{\eta} \|\mathbf{g}_1\|^2 = \frac{\bar{S}_v^{11}}{\eta} g_{11} \tag{5.66}$$

In conclusion, the evolution law for the problem at hand results in

$$-\frac{1}{2}\frac{\dot{\bar{G}}^{11}}{\bar{G}^{11}} = \frac{\bar{S}_v^{11}}{\eta} g_{11} \tag{5.67}$$

where one needs to express $\bar{S}_v^{11} = \bar{S}_v^{11}(\bar{G}^{11})$ recalling that

$$\mathrm{E}_e = \frac{1}{2}\left(g_{11} - \bar{G}_{11}\right) \tag{5.68}$$

The solution of the material model will therefore satisfy the nonlinear system of equations

$$\begin{cases} \mathrm{N} = \mathrm{N}_\infty(\mathrm{E}) + \mathrm{N}_v(\mathrm{E}_e) \\ -\frac{1}{2}\frac{\dot{\bar{G}}^{11}}{\bar{G}^{11}} = \frac{\bar{S}_v^{11}}{\eta} g_{11} \end{cases} \tag{5.69}$$

If St. Venant-Kirchhoff elasticity is assumed for the viscous part of the deformation, it holds that

$$\bar{S}_v^{11} = \bar{G}^{11}\hat{\bar{S}}_v^{11} = \bar{G}^{11} k_e \mathrm{E}_e = \frac{\bar{G}^{11} k_e}{2}\left(g_{11} - \bar{G}_{11}\right) \tag{5.70}$$

where k_e is the elastic modulus of the viscous part. Note that a factor $\bar{G}^{11}$ is necessary because $\bar{S}_v^{11}$ is not defined in the physical basis $\{\hat{\bar{\mathbf{G}}}\}_{i=1}^3$ of the intermediate configuration $\bar{\mathcal{P}}_t$ in Eq. 5.58. The explicit evolution law for this material is therefore

$$-\dot{\bar{G}}^{11} = \frac{(\bar{G}^{11})^2}{\tau} g_{11}\left(g_{11} - \bar{G}_{11}\right) \tag{5.71}$$

where the relaxation time τ is defined as

$$\tau = \frac{\eta}{k_e} \tag{5.72}$$

Moreover, if one assumes a St. Venant-Kirchhoff elastic material with stiffness k_∞ for the time-infinity part of the strain, the total 2nd PK axial force is given by

$$\mathrm{N} = k_\infty A \mathrm{E} + G_{11}\bar{G}^{11} k_e A \mathrm{E}_e = k_\infty A \mathrm{E} + G_{11}\bar{G}^{11}\frac{k_e A}{2}\left(g_{11} - \bar{G}_{11}\right) \tag{5.73}$$

Again, a factor G_{11} is required because the pull-back $\mathbf{S}_v = \boldsymbol{\chi}_*(\boldsymbol{\tau}_v)$ is not expressed in the physical basis $\{\hat{\mathbf{G}}_i\}_{i=1}^3$ of the reference configuration $\mathcal{P}_0$.

5.3.1.2 Generalized finite viscoelasticity

In the case of m viscoelastic strains, the total motion $\boldsymbol{\chi}$ of the cable is decomposed m times into an elastic part $\boldsymbol{\chi}_e^{(i)}$ and a viscous part $\boldsymbol{\chi}_v^{(i)}$ for $i = 1, ..., m$ as shown in Fig. 5.4.

$$\boldsymbol{\chi} = \boldsymbol{\chi}_e^{(1)} \circ \boldsymbol{\chi}_v^{(1)} = \cdots = \boldsymbol{\chi}_e^{(m)} \circ \boldsymbol{\chi}_v^{(m)} \tag{5.74}$$

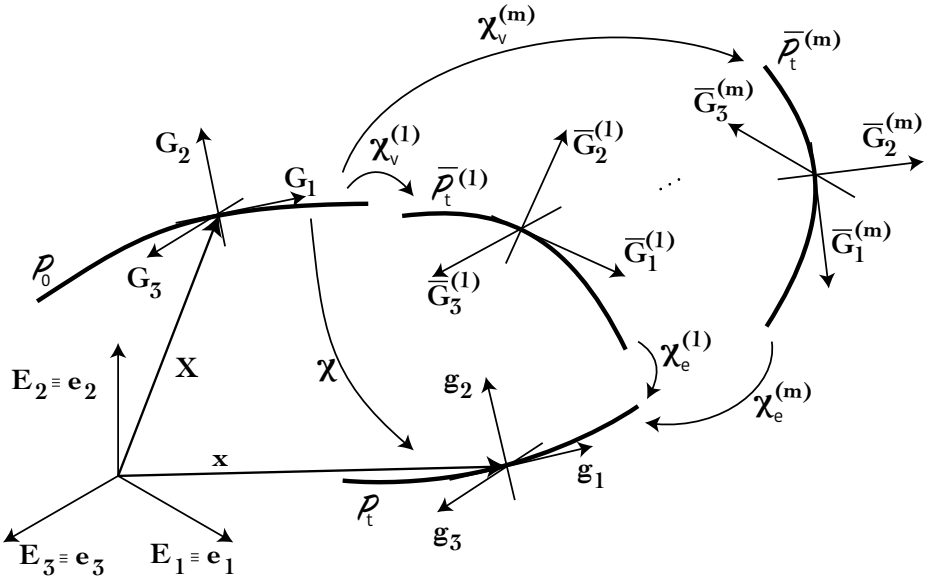

Figure 5.4: Decomposition of the deformation for finite viscoelasticity with m viscoelastic strains.

Since the deformation is the same for all parts of the model, the deformation gradient $\mathbf{F}$ may be decomposed into

$$\mathbf{F} = \mathbf{F}_e^{(1)}\mathbf{F}_v^{(1)} = \cdots = \mathbf{F}_e^{(m)}\mathbf{F}_v^{(m)} \tag{5.75}$$

and the developments in the previous section apply to each viscous part. As a result, the solution of the finite viscoelastic material model with m viscoelastic strains satisfies the nonlinear system of equations

$$\begin{cases} \mathrm{N} = \mathrm{N}_\infty(\mathrm{E}) + \displaystyle\sum_{i=1}^{m} \mathrm{N}_v^{(i)}(\mathrm{E}_e^{(i)}) \\ -\dfrac{1}{2}\dfrac{\dot{\bar{G}}^{11,(i)}}{\bar{G}^{11,(i)}} = \dfrac{\bar{S}_v^{11,(i)}}{\eta} g_{11} \quad \text{for} \quad i = 1, ..., m \end{cases} \tag{5.76}$$

with m internal variables corresponding to the metric coefficients $G^{11,(i)}$ for each intermediate configuration $\bar{\mathcal{P}}_t^{(i)}$.

If St. Venant-Kirchhoff elasticity is assumed for all elastic behaviors of the model, it holds that

$$\begin{cases} \mathrm{N} = k_\infty A\mathrm{E} + \displaystyle\sum_{i=1}^{m} G_{11,(i)}\bar{G}^{11,(i)}\frac{k_e^{(i)}A}{2}\left(g_{11} - \bar{G}_{11}^{(i)}\right) \\ -\dot{\bar{G}}^{11,(i)} = \dfrac{(\bar{G}^{11,(i)})^2}{\tau} g_{11}\left(g_{11} - \bar{G}_{11}^{(i)}\right) \quad \text{for} \quad i = 1, ..., m \end{cases} \tag{5.77}$$

where k_∞ is the stiffness of the time-infinity part and $k_e^{(i)}$ are the stiffnesses of the m viscous parts.

5.3.2 Numerical implementation

The numerical implementation of the two finite viscoelastic material models reduces to discretizing the evolution laws in the time domain. Assuming a St. Venant-Kirchhoff elastic material model for the time-infinity part of the strain and for the viscous part of the strain, the finite-difference discretization of the material model with one viscoelastic strain gives

$$\left\{\begin{array}{l} \mathrm{N}_{n+1} = \underbrace{k_\infty A \mathrm{E}_{n+1}}_{\mathrm{N}_{\infty,n+1}} + \underbrace{\bar{G}^{11}_{n+1} G_{11,n+1} \dfrac{k_e A}{2} \left(g_{11,n+1} - \bar{G}_{11,n+1}\right)}_{\mathrm{N}_{v,n+1}} \\ -\dfrac{\bar{G}^{11}_{n+1} - \bar{G}^{11}_{n}}{\Delta t} = \dfrac{(\bar{G}^{11}_{n+1/2})^2}{\tau} g_{11,n+1/2} \left(g_{11,n+1/2} - \bar{G}_{11,n+1/2}\right) \end{array}\right. \tag{5.78}$$

where the metric coefficients at time $t_{n+1/2}$ refer to the usual interpolations

$$g_{11,n+1/2} = \frac{g_{11,n+1} + g_{11,n}}{2} \quad \text{and} \quad \bar{G}_{11,n+1/2} = \frac{\bar{G}_{11,n+1} + \bar{G}_{11,n}}{2} \tag{5.79}$$

Equation 5.78 is a nonlinear algebraic system of equations in $\bar{G}^{11}_{n+1}$ and E_{n+1} that can be solved by any suitable iterative method.

The tangent of the material model for the Newmark and the HHT-α methods is given by the derivative

$$\frac{d\mathrm{E}_{n+1}}{d\mathrm{N}_{n+1}} = \frac{1}{k_\infty A + \frac{d\mathrm{N}_{v,n+1}}{d\mathrm{E}_{n+1}}} \tag{5.80}$$

where

$$\frac{d\mathrm{N}_{v,n+1}}{d\mathrm{E}_{n+1}} = \frac{d\mathrm{N}_{v,n+1}}{dg_{11,n+1}} \frac{dg_{11,n+1}}{d\mathrm{E}_{n+1}} = 2\frac{d\mathrm{N}_{v,n+1}}{dg_{11,n+1}} = k_e A G_{11,n+1} \left(\bar{G}^{11}_{n+1} + g_{11,n+1} \frac{d\bar{G}^{11}_{n+1}}{dg_{11,n+1}}\right) \tag{5.81}$$

The derivative $d\bar{G}^{11}_{n+1}/dg_{11,n+1}$ can be computed implicitly from Eq. 5.78(2) to give

$$\frac{d\bar{G}^{11}_{n+1}}{dg_{11,n+1}} = \frac{2(\bar{G}^{11}_{n+1/2})^2 g_{11,n+1/2} - \bar{G}^{11}_{n+1/2}}{g_{11,n+1/2}(1 - 2\bar{G}^{11}_{n+1/2} g_{11,n+1/2}) - \frac{2\tau}{\Delta t}} \tag{5.82}$$

The tangent of the material model for the energy-momentum consistent algorithm is obtained by the chain rule after multiplying Eq. 5.80 by a factor of 1/2.

The finite-difference discretization of the model with m viscoelastic strains for St. Venant-Kirchhoff elasticity of all elastic behaviors gives

$$\left\{\begin{array}{l} \mathrm{N}_{n+1} = \underbrace{k_\infty A \mathrm{E}_{n+1}}_{\mathrm{N}_{\infty,n+1}} + \displaystyle\sum_{i=1}^{m} \underbrace{\bar{G}^{11,(i)}_{n+1} G^{(i)}_{11,n+1} \dfrac{k^{(i)}_e A}{2} \left(g_{11,n+1} - \bar{G}^{(i)}_{11,n+1}\right)}_{\mathrm{N}^{(i)}_{v,n+1}} \\ -\dfrac{\bar{G}^{11,(i)}_{n+1} - \bar{G}^{11,(i)}_{n}}{\Delta t} = \dfrac{(\bar{G}^{11,(i)}_{n+1/2})^2}{\tau} g_{11,n+1/2} \left(g_{11,n+1/2} - \bar{G}^{(i)}_{11,n+1/2}\right) \quad \text{for} \;\; i = 1, ..., m \end{array}\right. \tag{5.83}$$

Equation 5.83 is a nonlinear system of equations in $\bar{G}^{11,(i)}$, $i = 1, ..., m$, and E_{n+1} that can be solved by any suitable iterative method.

The tangent of the material model with m viscoelastic strains for the Newmark and the HHT-α methods is given by the derivative

$$\frac{d\mathrm{E}_{n+1}}{d\mathrm{N}_{n+1}} = \frac{1}{k_\infty A + \sum_{i=1}^{m} \frac{d\mathrm{N}_{v,n+1}^{(i)}}{d\mathrm{E}_{n+1}}} \tag{5.84}$$

with the derivatives $d\mathrm{N}_{v,n+1}^{(i)}/d\mathrm{E}_{n+1}$ given in Eq. 5.81. For the energy-momentum consistent algorithm, the material tangent in Eq. 5.84 is multiplied by a factor of 1/2 according to the chain rule.

5.4 Material damping of high-frequency oscillations

The examples in Chapter 4 show that high-frequency oscillations arise in the axial force time history when no dissipation is considered in the formulation. While these oscillations are successfully removed by postprocessing the signal with a Savitzky-Golay filter, this section uses viscoelastic material models to reproduce the physical internal mechanisms that smooth out these oscillations. Viscous damping forces are typically not considered for this purpose because the modes of vibration for geometrically nonlinear systems change with the displacement field, and thus damping properties cannot be easily selected to target specific modes.

The following examples study representative cases from Section 4.3 to assess the material damping of the high-frequency oscillations. The reader is referred to Tables 4.6 and 4.7 for the material properties and equilibrium solution of the corresponding cables. The time integration of the governing equations is performed with the energy-momentum consistent algorithm in a pointwise approach because it preserves the Hamiltonian structure in the non-dissipative case and does not diverge when $t \to \infty$. Also, because no concentrated loads are applied in the following examples, the continuous and the discontinuous axial force implementations give results with indistinguishable differences.

The incrementally-infinitesimal and the finite viscoelastic material models are included in the proposed element with one viscous strain targeting the high-frequency waves in the axial force time history. The time-infinity stiffness of both models is set equal to the Young modulus of the cable, $k_\infty = E$, and the additional stiffness of the viscous part is taken in the proportional form

$$k = \zeta E \tag{5.85}$$

As a result, when the viscous forces dissipate completely, the cable has identical material properties to the models in Section 4.3. The relaxation time of the viscous part is taken as $\tau = 0.05$ sec in all cases so that the material damping is effective in the early time steps of the response.

5.4.1 Example 1: In-plane vibration for small sag-to-span

The first example corresponds to the in-plane free vibration of cable C1, with a sag-to-span ratio of 1/15, under an initial displacement field of the same form as in Eq. 4.13, with $\alpha_s = 15$ and $\alpha_a = 0$. The cable is discretized with a mesh of ten elements, and the time step is set to $\Delta t = 0.05$ sec. Since the cable strains are small in this case, the finite and the incrementally-infinitesimal viscoelastic material models give indistinguishable results.

Figure 5.5 presents the time histories at midspan for the normalized displacements and the 2nd PK axial forces with different values of the parameter ζ. In this case, the periodic peaks of the displacement time history in Fig. 5.5(a) are significantly reduced for increasing values of the parameter, even though the linear oscillations of the dynamic response are preserved. A slight decrease in the phase of the displacement history also appears for the largest values of ζ, and becomes more pronounced during the last cycle of the response for $\zeta = 2/5$. The time history for the 2nd PK axial force field in Fig. 5.5(b) demonstrates that small values of the parameter smooth out the high-frequency contributions effectively after a short time into the response, while having a minor impact on the amplitude of the dominant oscillations. The phase of the axial force time history decreases slightly for the largest parameter values, as is also observed in the last cycles of the response.

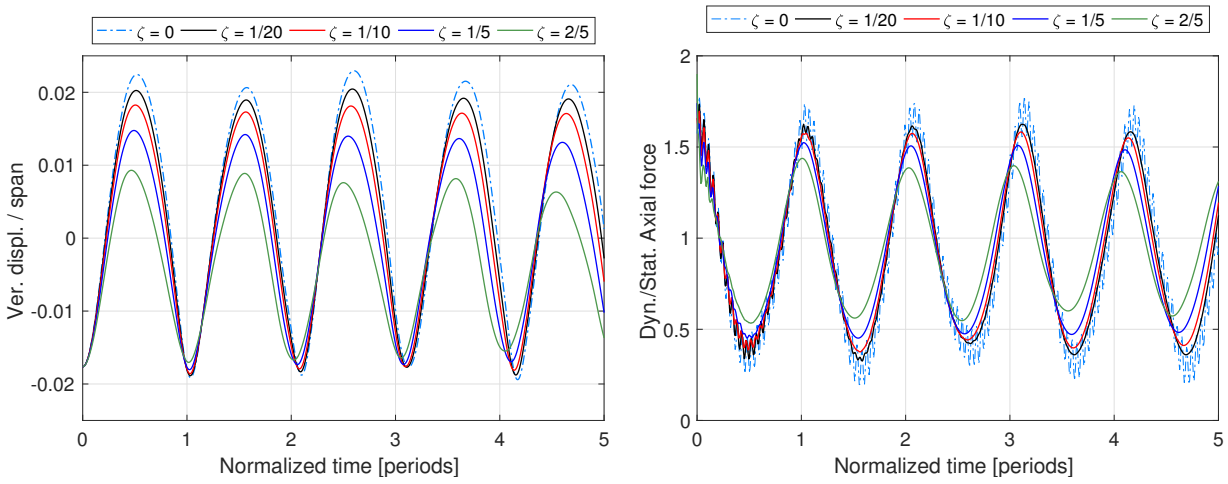

(a) Normalized midspan displacements (b) Normalized midspan axial forces

Figure 5.5: Material damping of high-frequency oscillations for in-plane vibration and small sag-to-span (Example 1).

5.4.2 Example 2: Out-of-plane vibration for large sag-to-span

This example corresponds to the out-of-plane free vibration of cable C2, with a sag-to-span ratio of 1/9.5, under an initial displacement field of the same form as in Eq. 4.14, with

$\alpha_s = 15$ and $\alpha_a = 15$. The cable is discretized with a mesh of ten elements, and the time step is set again to $\Delta t = 0.05$ sec. Since the cable strains are small in this case, the finite and the incrementally-infinitesimal viscoelastic material models give indistinguishable results.

Figure 5.6 presents the time histories for the normalized displacements at quarter span and the 2nd PK axial forces at the supports with different values of the parameter ζ. For small values of ζ, the displacement history in Fig. 5.6(a) remains practically unaffected relative to the undamped response, while large parameter values reduce slightly the displacement peaks and produce an increment of its phase, which is noteworthy in the last cycles of the response for $\zeta = 2/5$. The significant energy dissipation caused by the largest values of ζ also slows down the translation of the double peak in the displacement time history, and thus reduces the modal coupling of the response. The time history for the 2nd PK axial force field in Fig. 5.6(b) starts with significant high-frequency oscillations in all cases, but these are rapidly smoothed out by the energy dissipation of the material model. The phase of the axial force time history also increases for large values of the parameter ζ as observed in the last cycles of the response, but these have a minor effect on the axial force peaks.

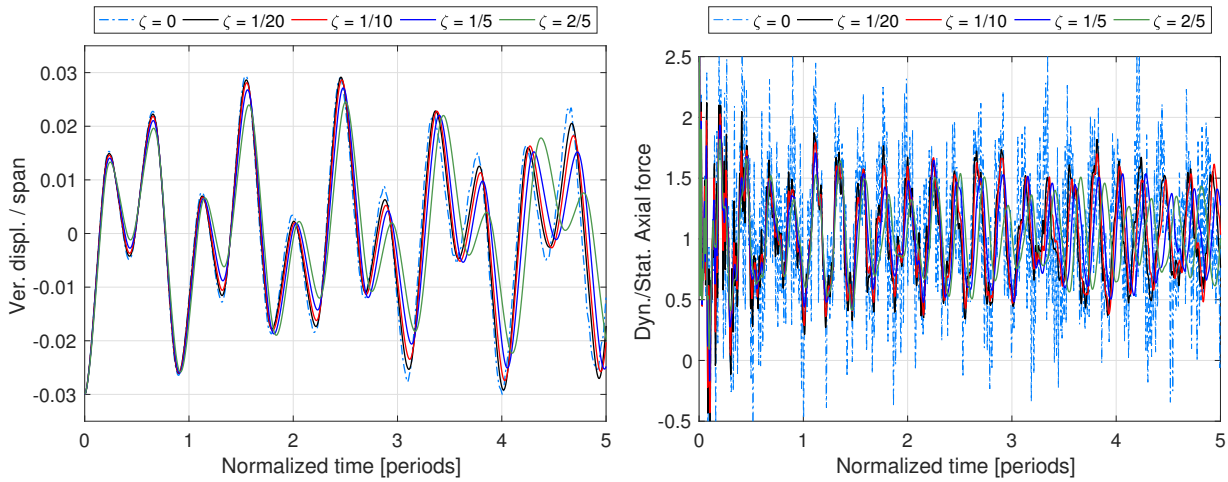

(a) Normalized displacements at quarter span (b) Normalized axial forces at supports

Figure 5.6: Material damping of high-frequency oscillations for out-of-plane vibration and large sag-to-span (Example 2).

5.4.3 Example 3: In-plane vibration for very large sag-to-span

The third example corresponds to the in-plane free vibration of cable C3, with a sag-to-span ratio of 1/5, under an initial displacement field of the same form as in Eq. 4.15, with $\alpha_s = 16.5$ and $\alpha_a = 0$. The cable is discretized with a mesh of ten elements, and the time step is set to $\Delta t = 0.05$ sec. Since the cable strains remain relatively small in this case, the

finite and the incrementally-infinitesimal viscoelastic material models give indistinguishable results.

Figure 5.7 presents the time histories at midspan for the normalized displacements and the 2nd PK axial forces with different values of the parameter ζ. While the displacement history in Fig. 5.7(a) follows the same overall behavior for all parameter values, the high modes of the response caused by the very large sag-to-span ratio of the cable are progressively dampened out as ζ increases. In contrast to Examples 1 and 2, the parameter ζ does not have a significant influence on the phase of the signal in this case. The time history for the 2nd PK axial force field in Fig. 5.7(b) demonstrates that relatively large values of ζ are required to effectively dampen out the high-frequency contributions in the response, while its phase remains unchanged for all values of the parameter. The secondary low-frequency amplitudes of the signal, in the spectral decomposition of Fig. 4.44(a), are also reduced by the largest values of ζ, even though the overall trend of the signal does not change significantly.

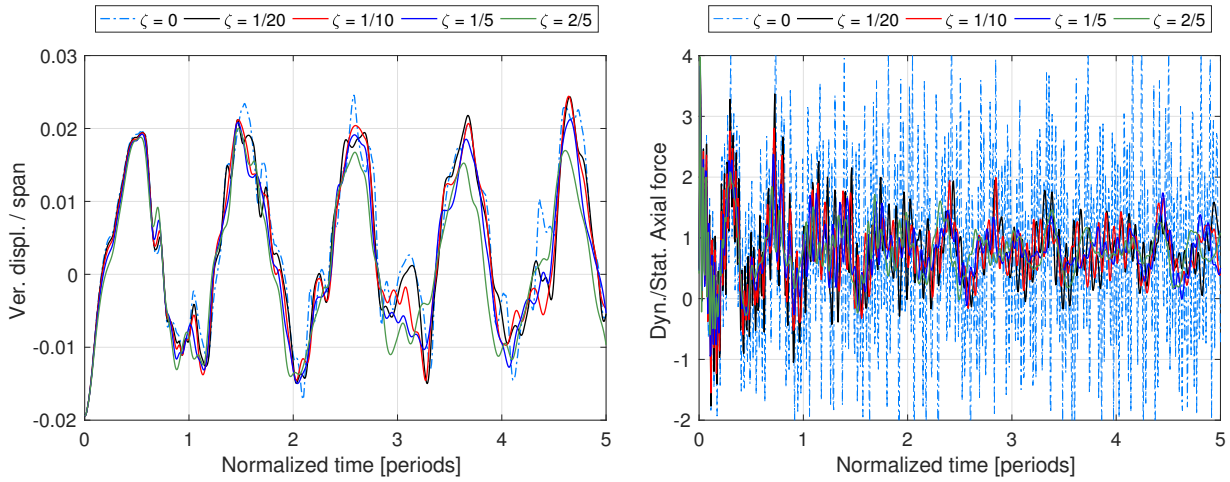

(a) Normalized midspan displacements (b) Normalized midspan axial forces

Figure 5.7: Material damping of high-frequency oscillations for in-plane vibration and very large sag-to-span (Example 3).

5.5 Decaying large-amplitude free vibration

After assessing the material damping of the high-frequency contributions, the following examples focus on the global decaying response of the cable free vibration under viscous damping forces and viscoelastic material models. Examples 4 and 5 consider the structural models for cables C1 and C3 of Section 4.3, and the reader is referred to Tables 4.6 and 4.7 for their material properties and equilibrium solution. Analogously to Section 5.4, the governing equations are integrated in time with the new energy-momentum consistent algorithm.

Because no point loads are present, the continuous and the discontinuous implementations of the proposed mixed cable element give identical results for the following examples.

5.5.1 Example 4: Viscous forces vs. viscoelastic model for small sag-to-span

The fourth example studies the decaying in-plane free vibration of cable C1, discussed in the absence of damping in Section 4.3.2.1, and compares the dynamic response for the following two models:

- **Model 1 (M1).** A combination of an incrementally-infinitesimal material model with one viscous strain for the damping of the high-frequency waves, with the viscous forces given by the isotropic damping matrix

$$\mathbf{C} = c\mathbf{I} \tag{5.86}$$

where c is the damping coefficient and $\mathbf{I}$ is the identity matrix. The material properties for the viscoelastic part are taken from Example 1 as $k_\infty = E$, $\tau = 0.05$ sec and $k = \zeta E$, with $\zeta = 1/10$ and St. Venant-Kirchhoff elastic springs. The damping coefficient c for the viscous forces is selected according to the infinitesimal approximation [12]

$$c = 2m\bar{\zeta}\omega_1 \tag{5.87}$$

where m is the contributing mass lumped at the node, $\bar{\zeta}$ is the damping ratio for small deformations and ω_1 is the angular frequency of the dominant mode of vibration. A damping ratio of $\bar{\zeta} = 0.005$, common for cables under free vibration [30], gives a damping coefficient of $c = 0.38$ kg/s.

- **Model 2 (M2).** An incrementally-infinitesimal viscoelastic material model with two viscous strains, one intended to dampen the high-frequency waves and another, to model the overall decay of the dynamic response. As in model 1 (M1), the material properties for the Maxwell element with a short relaxation time are taken from Example 1 as $\tau_1 = 0.05$ sec and $k_1 = \zeta E$, with $\zeta = 1/10$ and a St. Venant-Kirchhoff elastic spring. The time-infinity part is also considered as St. Venant-Kirchhoff elastic with $k_\infty = E$. For the Maxwell element governing the overall decay of the response, a relaxation time τ_2 given by weighting the dominant period T_1 by the damping ratio $\bar{\zeta}$ is adopted

$$\tau_2 = (1 - \bar{\zeta})\frac{2\pi}{\omega_1} = (1 - \bar{\zeta})T_1 \tag{5.88}$$

in empirical correspondence to model 1, giving the long relaxation time of $\tau_2 = 6.82$ sec, and with the same St. Venant-Kirchhoff spring with $k_2 = k_1$.

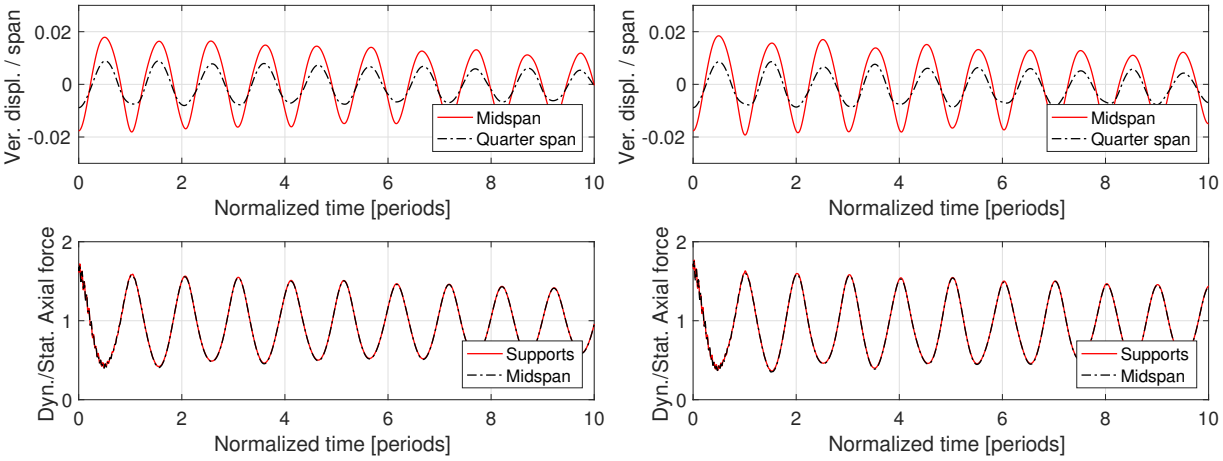

(a) Model 1 (b) Model 2

Figure 5.8: Results for decaying in-plane free vibration of cable C1 (Example 4).

The initial displacement field for the free vibration is given in the plane of the cable according to Eq. 4.13, with magnification factors $\alpha_s = 15$ and $\alpha_a = 0$. The time step is set to $\Delta t = 0.05$ sec for both models.

Figure 5.8 shows the time histories for the normalized displacements and the 2nd PK axial forces under models 1 and 2. The larger initial stiffness of model 2, equal to $k_0^{M2} = (1+2\zeta)E$, gives slightly larger 2nd PK axial forces in the beginning of the response relative to model 1, with an initial stiffness of $k_0^{M1} = (1+\zeta)E$, even though the initial displacements for the two models are almost indistinguishable. As time advances, the viscous forces of model 1 homogenize the displacement oscillations at quarter span, as observed by the peaks converging to the same decaying amplitude in Fig. 5.8(a). In contrast, model 2 conserves the relative differences between the displacement peaks of the decaying response. The same signal homogenization occurs in the axial force time history for model 1. A decrease in the phase of the displacement and the 2nd PK axial force time histories is also observed for the viscoelastic material model (M2), as demonstrated in the last cycles of the response. Because the short relaxation time is the same for both models, the high-frequency waves in the axial force time history are equally dampened out during the first half period of the dynamic response.

5.5.2 Example 5: Viscous forces vs. viscoelastic model for very large sag-to-span

The fifth example studies the decaying in-plane free vibration of cable C3, discussed in the absence of damping in Section 4.3.4.1, and compares the dynamic response with the following two models:

- **Model 1 (M1).** A combination of a finite viscoelastic material model with one viscous strain for the damping of the high-frequency waves, with the viscous forces given by the isotropic damping matrix

$$\mathbf{C} = c\mathbf{I} \tag{5.89}$$

where c is the damping coefficient and $\mathbf{I}$ is the identity matrix. The material properties for the viscoelastic part with short relaxation time are taken from Example 3 as $\tau = 0.05$ sec and $k = \zeta E$, with $\zeta = 1/5$ and a St. Venant-Kirchhoff elastic model for $\bar{S}_v^{11}$, while the time-infinity part is considered nonlinear with a compressible neo-Hookean material model according to Section 4.1.2 and a stiffness $k_\infty = E$. The damping coefficient c for the viscous forces is selected according to the infinitesimal approximation [12]

$$c = 2m\bar{\zeta}\omega_1 \tag{5.90}$$

where m is the contributing mass lumped at the node, $\bar{\zeta}$ is the damping ratio for small deformations and ω_1 is the angular frequency of the dominant mode of vibration. A damping ratio of $\bar{\zeta} = 0.005$, common for cables under free vibration [30], gives a damping coefficient of $c = 0.31$ kg/s.

- **Model 2 (M2).** A finite viscoelastic material model with two viscous strains, one targeting the high-frequency contributions and another, the overall decay of the dynamic response. As in model 1, the material properties for the viscous part that addresses the high frequencies are taken from Example 3 as $\tau_1 = 0.05$ sec and $k_1 = \zeta E$, with $\zeta = 1/5$ and a St. Venant-Kirchhoff elastic model for $\bar{S}_v^{11,1}$, while the material properties for the viscous part governing the overall decay of the response are taken as $k_2 = k_1$ with a St. Venant-Kirchhoff elastic model for $\bar{S}_v^{11,2}$ and τ_2 given by weighting the dominant period T_1 by the damping ratio $\bar{\zeta}$ in the form

$$\tau_2 = (1 - \bar{\zeta})\frac{2\pi}{\omega_1} = (1 - \bar{\zeta})T_1 \tag{5.91}$$

thus $\tau_2 = 8.36$ sec. A compressible neo-Hookean material model according to Section 4.1.2, with $k_\infty = E$, is considered for the time-infinity part of the finite viscoelastic model.

The initial displacement field for the free vibration is given in the cable plane according to Eq. 4.15, with amplification factors $\alpha_s = 16.5$ and $\alpha_a = 0$. The time step is set to $\Delta t = 0.05$ sec in all cases to capture the nonlinear oscillations of the response with accuracy.

Figure 5.9 shows the time histories for the normalized displacements and the 2nd PK axial forces under models 1 and 2. As is the case for Example 4, the larger initial stiffness of model 2, equal to $k_0^{M2} = (1+2\zeta)E$, gives slightly larger 2nd PK axial forces in the beginning of the response relative to model 1, with an initial stiffness of $k_0^{M1} = (1+\zeta)E$. However, larger initial displacements at midspan and at quarter span are observed in this case for model 2 during the first three cycles of the response. These discrepancies disappear after a

short period of time, and the displacement time histories for both models result in similar amplitudes during the second half of the response. The phase of the displacement time history remains unchanged for both material models, and the high modes in the response are conserved in time with slight differences in amplitude. While the displacement time histories in Figs. 5.9(a) and 5.9(b) show relatively similar behaviors, model 1 dampens the amplitude of the axial force time history much faster than model 2. Moreover, some high-frequency oscillations still appear in the fifth cycle of the response for model 2, while model 1 almost completely remove them after the third cycle. The phase of the axial force time history also remains unaltered for both material models.

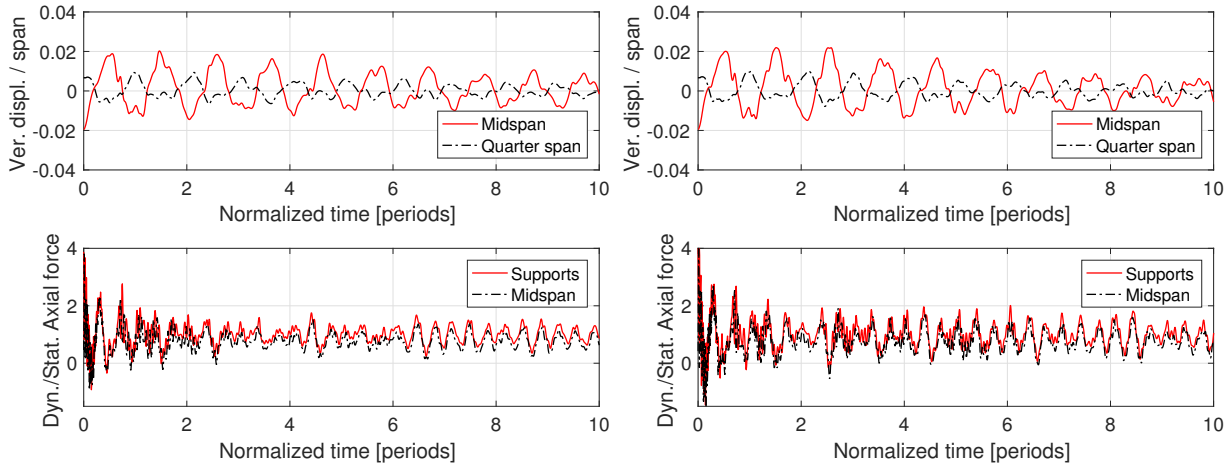

(a) Model 1 (b) Model 2

Figure 5.9: Results for decaying out-of-plane free vibration of cable C2 (Example 5).

5.6 Example 6: Earthquake response

The last example assesses the addition of damping into the earthquake response of cable C1 that was discussed in Section 4.3.5. To this end, the same two models as in Example 4 are considered for adding energy dissipation to the system: the first model (M1) includes viscous damping forces with a damping ratio of $\bar{\zeta} = 0.005$ as suggested in Ref. [30], while the second model (M2) considers viscous damping at the material level with an incrementally-infinitesimal viscoelastic model with $\tau_2 = 6.82$ sec and $k_2 = \zeta E$, and $\zeta = 1/10$. Both models also include a Maxwell element with a short relaxation time $\tau = \tau_1 = 0.05$ sec and $k = k_1 = \zeta E$, with $\zeta = 1/10$, to address any high frequency oscillations in the response. All elastic springs are considered as St. Venant-Kirchhoff elastic, and the time-infinity stiffness is given by the Young modulus of the cable, $k_\infty = E$.

The structural model is subjected to the El Centro ground acceleration with an amplification factor of 8 to induce nonlinear cable behavior under large displacements. The ground

acceleration $\mathbf{a}_g$ is imposed according to the method in Ref. [12] by defining $\mathbf{u}$, $\mathbf{v}$ and $\dot{\mathbf{v}}$ as values relative to the ground motion and considering the term $\mathbf{M}\mathbf{a}_g$ as an applied load.

The cable is discretized with a mesh of ten equal-size elements and the dynamic response is integrated in time with the proposed energy-momentum consistent algorithm. The time step is set to $\Delta t = 0.02$ sec according to the record of the ground motion in Ref. [12].

5.6.1 Two-dimensional response

In the first simulation the ground acceleration is imposed in the direction along the cable span so that the dynamic response is two-dimensional. Figure 5.10 presents the time histories for the vertical and the horizontal displacements and both models, while Fig. 5.11 shows the corresponding time histories for the 2nd PK axial forces.

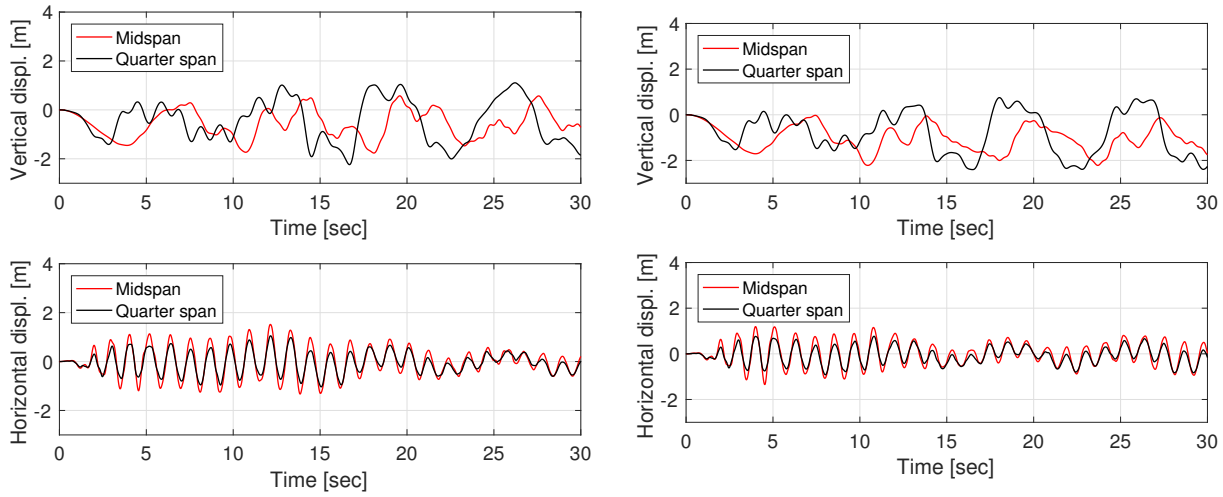

(a) Model 1

(b) Model 2

Figure 5.10: Displacement results for the 2d earthquake response with damping (Example 6).

The results show that the energy dissipation introduced by the two models in Figs. 5.10 and 5.11 smooths out the displacement and the 2nd PK axial force time histories significantly, and decreases their phase compared to the undamped response in Figs. 4.51 and 4.52. The horizontal and the vertical displacement time histories in Fig. 5.10 show similar initial amplitudes for both models, even though discrepancies appear after five seconds into the response: the viscoelastic material model (M2) gives smaller amplitudes for both components and smooths out the high modes that appear in the vertical displacements. Figure 5.11 shows that the axial force time history at midspan remains almost at the static value with minor oscillations, as observed in the undamped solution in Fig. 4.52. The same time history at the supports has no significant high frequency contributions, and shows a major decrease after 15 sec into the response that was not observed in the undamped case. Figure 5.11(b)

demonstrates that the 2nd PK axial forces at the supports experience increasing amplitudes for model 2 after 20 sec into the response, in accordance with the horizontal displacements in Fig. 5.10(b). This phenomenon shows a modal coupling for model 2 that is not observed in the response for model 1.

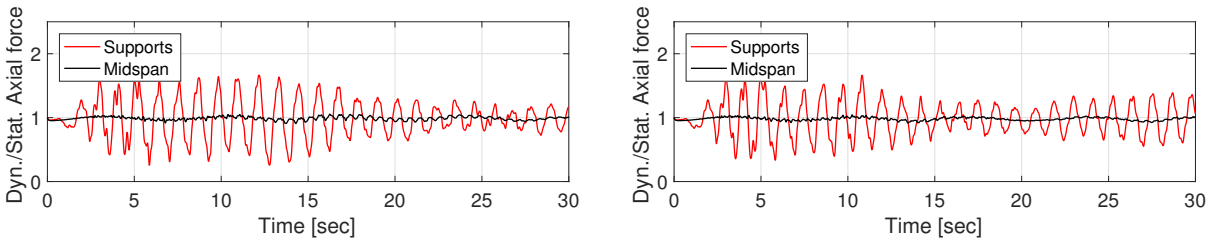

(a) Model 1 (b) Model 2

Figure 5.11: Axial force results for the 2d earthquake response with damping (Example 6).

5.6.2 Three-dimensional response

The second simulation involves the same horizontal ground acceleration with a 10-degree angle from the cable span, so that the dynamic response is three-dimensional. Figure 5.12 presents the time histories for the out-of-plane (OOP), vertical and horizontal displacements and both models, while Fig. 5.13 shows the corresponding time histories for the 2nd PK axial forces.

As was the case for the 2d response, both models smooth out the displacement and the 2nd PK axial force time histories significantly in Figs. 5.12 and 5.13 with respect to the undamped solutions in Figs. 4.53 and 4.54. The OOP displacements in Fig. 5.12 are almost identical for both models during the first 10 sec of the response. However, the same 3d coupling between the horizontal and the OOP displacements that was observed in the undamped case appears for model 1 15 sec into the response. This energy transfer is small for model 2, which conserves a small amplitude for the horizontal displacements and results in a slight increase in the OOP displacements. This coupling effect is also observed in the axial force history for model 1 in Fig. 5.13(a), while the axial force history for model 2 in Fig. 5.13(b) almost conserves the same amplitude. The 2nd PK axial forces at midspan show minor oscillations and a value almost equal to the static one for both models, as observed in the undamped solution.

5.7 Concluding remarks

Chapter 5 presents three different approaches to include viscoelastic energy dissipation into the proposed mixed cable element: viscous damping forces, incrementally-infinitesimal viscoelastic material models and finite viscoelastic material models.

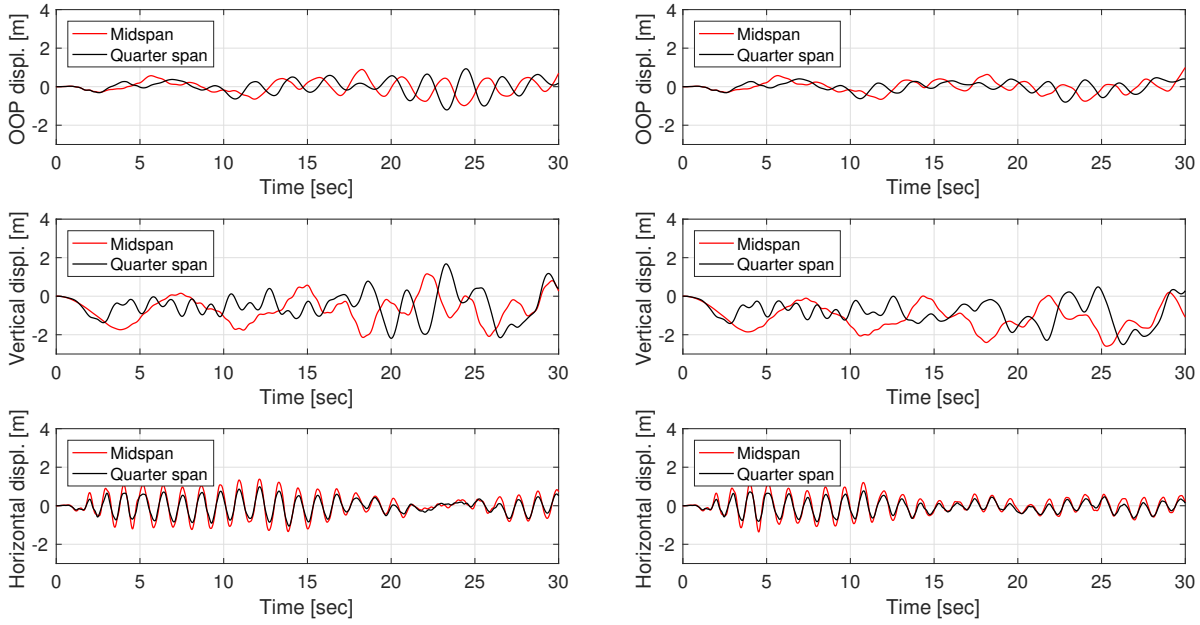

(a) Model 1 (b) Model 2

Figure 5.12: Displacement results for the 3d earthquake response with damping (Example 6).

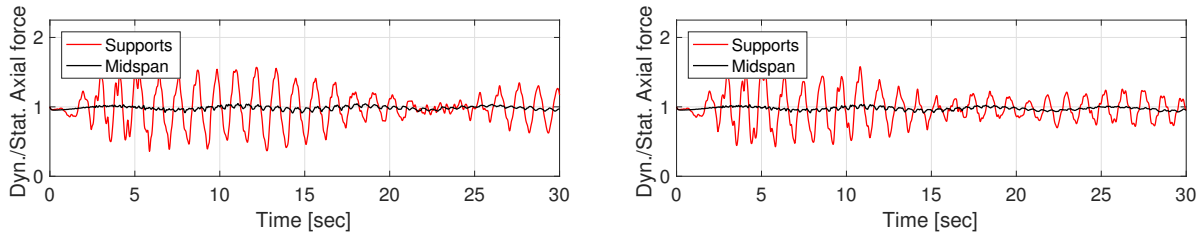

(a) Model 1 (b) Model 2

Figure 5.13: Axial force results for the 3d earthquake response with damping (Example 6).

The two viscoelastic material models are used to reproduce the internal dissipation that leads to the damping of the high-frequency waves in actual cable structures. Results show that a viscous part with a short relaxation time successfully removes the high-frequency contributions in the axial force time history, but also has some impact on the overall dynamic response of the cables. In the case of in-plane free vibration, a significant decrease in the displacement peaks and a slight decrease in the phase of the response is observed for small sag-to-span ratios and large stiffnesses of the viscous part. When the sag-to-span ratio increases, no significant change in the phase of the response is observed, with only a slight

decrease of the displacement peaks. In contrast, a slight increase in the phase of the response appears for the out-of-plane free vibration.

A damping model considering viscous forces is compared to the viscoelastic material models to account for the overall decay of the free vibration. For small sag-to-span ratios, the former model homogenizes the displacement and the axial force time histories, while the latter model preserves the relative differences of the oscillations during the response but give larger initial axial forces and decrease the phase of the response. In the case of very large sag-to-span ratios, no significant differences in the phase of the response are observed between models, even though the model with viscous forces gives smaller amplitudes for the 2nd PK axial forces than the viscoelastic ones.

When viscous forces and the incrementally-infinitesimal viscoelastic material model are considered in the 2d and the 3d earthquake response of cables with a small sag-to-span ratio, the displacement and 2nd PK axial force time histories are significantly dampened, and the phase of the response is slightly decreased with respect to the undamped solution. Moreover, the viscoelastic material model reduces the 3d coupling effect between the horizontal and the out-of-plane displacements that is observed in the undamped 3d case, and thus keeps the dynamic response mostly in the cable plane.

Chapter 6
Cable structures

The proposed mixed cable element is used in this chapter to study the response of three-dimensional cable nets.

The discussion begins with the numerical treatment of cable joints, which require special attention for the continuous implementation to satisfy equilibrium, and continues with the static analysis of three cable structures: a skyline cable system, a hyperbolic paraboloid cable dome and a saddle cable dome. The earthquake response of a planar cable system is also studied in the last example. The results for these structures are compared to other studies [1, 28, 29, 33, 50, 52, 53] and experiments [35].

6.1 Numerical treatment of cable joints

A cable joint, shown in Fig. 6.1(a), is a node where two or more cables meet. Equilibrium at the joint therefore requires that the resultant of all cable axial forces balance the external loads in the current configuration. In general, this condition generates discontinuities between the different axial force values that need to be reproduced if physical results are to be achieved. Example 2 in Section 4.2.2 demonstrated that the discontinuous implementation of the cable element is intrinsically capable of reproducing jumps in the axial force distribution with high accuracy, since the axial forces are computed at the element level. In contrast, the continuous implementation assigns a single axial force degree of freedom at each node and hence requires a very fine mesh to accurately reproduce physical jumps in the neighborhood of the node, but still gives rise to Gibbs oscillations.

To overcome this limitation in the case of a continuous axial force distribution, a numerical cable joint is designed to accommodate axial force jumps. As a matter of fact, a jump can be achieved with the continuous form of the element if several nodes are placed at the same spatial point. This multiplicity allows different axial force degrees of freedom, while the continuity in the displacement field can be guaranteed by linking the displacement

degrees of freedom of the nodes at the joint. As a result, the numerical implementation of the joint with the continuous formulation, shown in Fig. 6.1(b), consists of n different nodes with equal coordinates and degrees of freedom $\{\mathbf{u}_i, \hat{\mathrm{N}}_i\}_{i=1}^{n}$ for which

$$\mathbf{u}_1 = \mathbf{u}_2 = \cdots = \mathbf{u}_n \tag{6.1}$$

with $n \geq 2$ the number of cables connecting to the joint. The continuous formulation thus results in a continuous axial force distribution along the cable with a discontinuity at the joint.

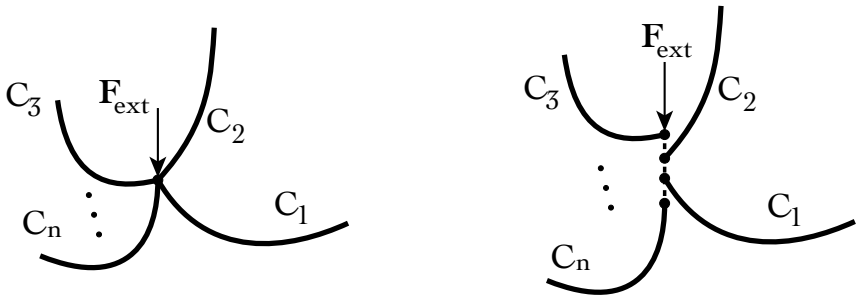

(a) Physical joint (b) Numerical joint

Figure 6.1: Numerical treatment of cable joints.

6.2 Static analysis of cable structures

First, the static behavior of three cable structures from the literature is studied in this section. These structures are three-dimensional and correspond to a triangular skyline cable system, a hyperbolic paraboloid cable roof and a saddle cable roof.

6.2.1 Triangular skyline cable system

The first application consists of a three-dimensional triangular skyline cable system that was studied by Kanzaki *et al.* [29], Such *et al.* [48], Suzuki *et al.* [50] and Thai *et al.* [53]. The structural model consists of three supports (P_1, P_2, P_3), representing the tip of three towers, at which three cables (C_1, C_2, C_3) with a common node (M) are anchored. A vertical load F=100 N is applied at the common node to simulate a weight that is hanging from the structure. Figure 6.2 and Table 6.1 summarize the geometry of the model and its material properties. A usual assumption to analyze this structure [29, 48, 50, 53] consists of neglecting the elastic deformation of the three cables because the self-weight and the applied vertical load are small. This assumption is approximated in the present model by considering a St. Venant-Kirchhoff elastic material for the cables with an elastic stiffness $EA = 100$ GN.

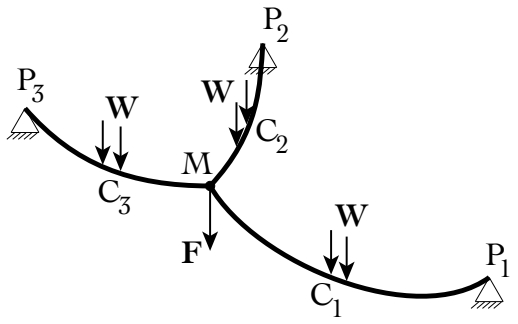

Figure 6.2: Structural model for the triangular skyline cable system.

Property	**Value**
Support location P_1	(260,210,786) m
Support location P_2	(320,685,790) m
Support location P_3	(15,680,771) m
Cable length C_1	418.00 m
Cable length C_2	193.70 m
Cable length C_3	149.23 m
Cable self-weight, W	0.1 N/m
Elastic stiffness, EA	100 GN

Table 6.1: Geometric and material properties for the triangular skyline cable system.

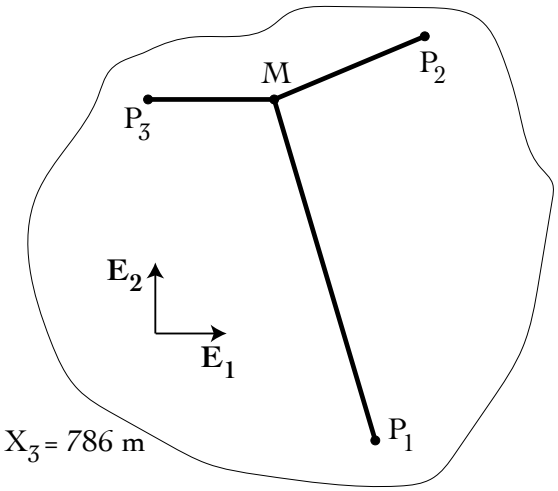

Figure 6.3: Reference configuration for the form finding of the triangular skyline cable system.

The form finding of the system is performed according to the procedure by Argyris *et al.* [5] with a reference configuration that is contained in the horizontal plane $X_3 = 786$ m, as shown in Fig. 6.3. Support P_1 starts on its final position, while support P_2 is located on the projection of its final position on the latter horizontal plane. Cable C_3 is initially placed on a straight line parallel to the X_1 axis with its corresponding unstretched length. Consequently, the initial displacements for the supports are $\Delta\mathbf{u}_{P_1} = \mathbf{0}$, $\Delta\mathbf{u}_{P_2} = (0, 0, 4)$ m and $\Delta\mathbf{u}_{P_3} = (23.1271, 69.26635, -15)$ m. To avoid the singular stiffness of the cables in the reference configuration, an initial parabolic guess with a deflection of 10 m at midspan is assigned to all cables for the first Newton-Raphson iteration.

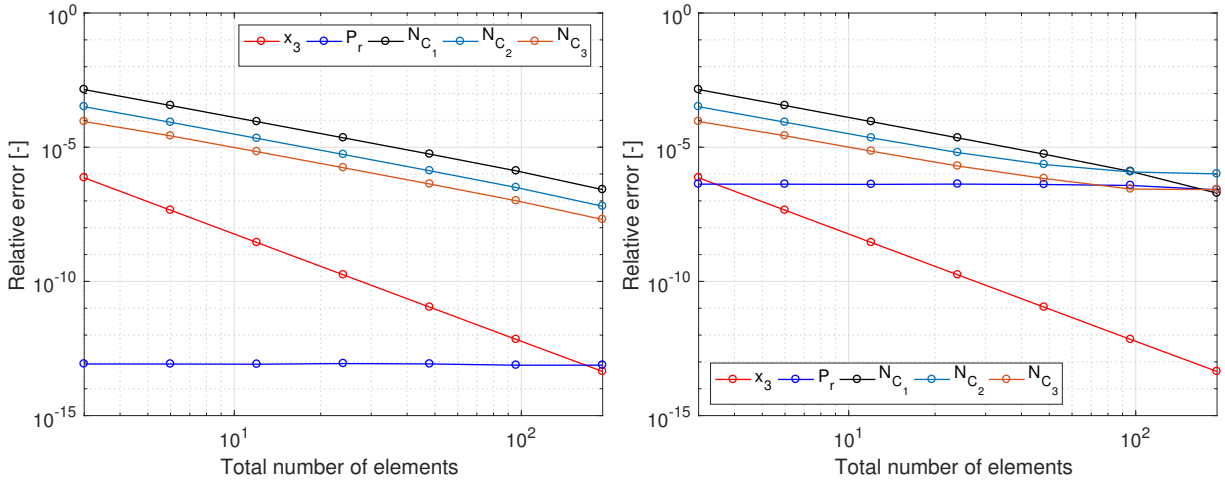

(a) Continuous implementation (b) Discontinuous implementation

Figure 6.4: Convergence study for the skyline cable system.

The two implementations of the proposed cable element, with a continuous and a discontinuous axial force distribution, are used to analyze this cable net, with the continuous formulation including the numerical joints discussed in Section 6.1. Figure 6.4 presents the convergence plots for the elevation (x_3), the vertical resisting force (P_r) and the 2nd PK axial forces of the cables (N) at the common node when all cables are discretized with the same number of elements. The relative errors are computed with respect to a mesh of 384 elements in total. While the relative errors for the displacements and the axial forces are very similar for both formulations, a significant difference exists on the accuracy of the vertical resisting force. Since the discontinuous formulation performs a static condensation to compute the axial forces, a relative error is observed corresponding to the accuracy of the axial forces when the displacement DOFs reach machine precision. In contrast, the continuous formulation considers the axial force DOFs as independent of the displacement DOFs, and therefore the latter reaching machine precision does not alter the axial force convergence rate, and the resisting force shows machine precision error regardless of the mesh size.

Table 6.2 compares the coordinates (x_1, x_2, x_3) and the axial forces N at the common node that are given by the proposed formulation with those obtained by other studies, where "o·" refers to the polynomial order of the interpolation functions and "n·", to the number of elements per cable. For the present study, the axial forces correspond to the 2nd PK representation, while the studies in Refs. [29] and [48] consider infinitesimal deformations. Reference [53] considers a decomposition of the strain into a linear and a nonlinear part, with isogeometric shape functions, but does not report axial force values. From Table 6.2, it is observed that the results for the proposed formulation agree very well with those in the literature. Moreover, the continuous implementation with numerical joints gives the same results as the discontinuous implementation. Figure 6.5 shows the deformed shape of the cable structure for a mesh of four elements per cable and compares it to the reference configuration used for the form finding procedure.

Reference	x_1 [m]	x_2 [m]	x_3 [m]	N_{C1} [N]	N_{C2} [N]	N_{C3} [N]
Kanzaki *et al.* [29]	145.50	610.30	751.60	320.0	299.4	406.9
Such *et al.* [48] (I)	145.50	610.29	751.58	320.0	299.4	406.9
Such *et al.* [48] (II)	145.50	610.30	751.58	320.0	299.4	406.9
Thai *et al.* [53] (o1n1)	142.02	610.50	807.14	-	-	-
Thai *et al.* [53] (o1n128)	145.51	610.31	751.54	-	-	-
Thai *et al.* [53] (o2n1)	145.53	610.52	750.83	-	-	-
Thai *et al.* [53] (o2n64)	145.51	610.31	751.52	-	-	-
Thai *et al.* [53] (o3n1)	145.50	610.29	751.56	-	-	-
Thai *et al.* [53] (o3n64)	145.51	610.32	751.43	-	-	-
Continuous (n1)	145.49	610.24	751.72	318.0	296.9	407.1
Continuous (n128)	145.49	610.24	751.72	318.4	297.0	407.1
Discontinuous (n1)	145.49	610.24	751.72	318.0	296.9	407.1
Discontinuous (n128)	145.49	610.24	751.72	318.4	297.0	407.1

Table 6.2: Results for triangular skyline cable system and both cable formulations.

6.2.2 Hyperbolic paraboloid cable dome

The second application refers to a pretensioned hyperbolic paraboloid cable roof, also known as *hypar net*, that was numerically and experimentally tested by Lewis *et al.* [35] and subsequently studied by Ahmad Abad *et al.* [1], Kwan [33], Sufian and Templeman [49] and Thai and Kim [52]. The complete structure is shown in Fig. 6.6, while Fig. 6.7 shows the structural model for the analysis, corresponding to one fourth of the entire structure by symmetry. All cables are assumed to be St. Venant-Kirchhoff elastic and their material properties are summarized in Table 6.3. A force F=15.7 N is applied at some nodes of the dome according to Fig. 6.7, and the structure is pretensioned with an additional axial force of 200 N before the point loads are applied.

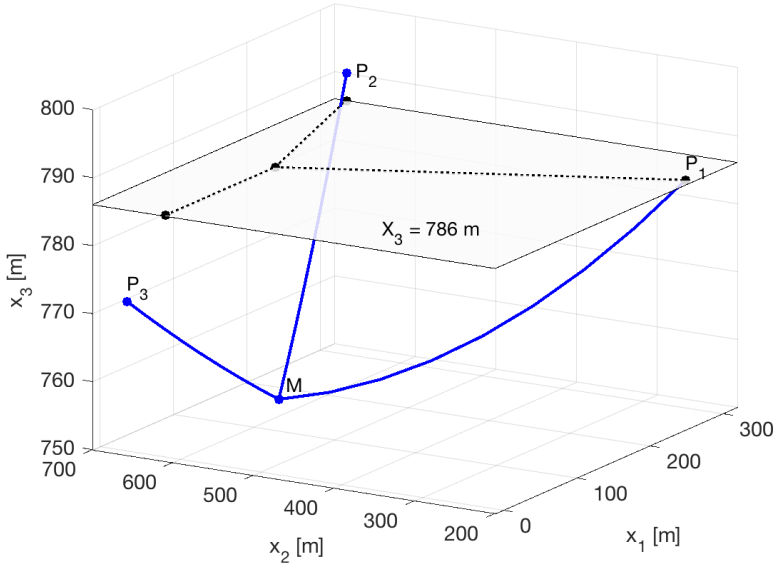

Figure 6.5: Deformed shape for the skyline cable system.

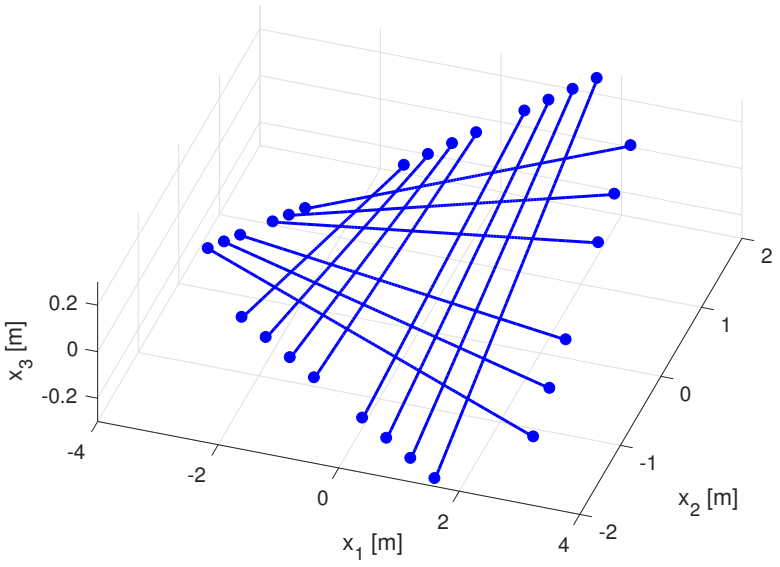

Figure 6.6: Hyperbolic paraboloid cable dome.

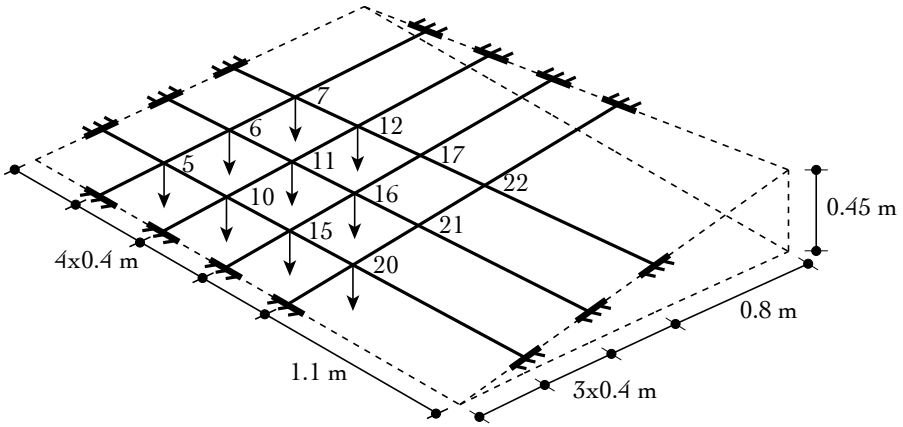

Figure 6.7: Structural model for the hyperbolic paraboloid cable dome.

Property	**Value**
Cross-sectional area	0.785 mm^2
Elastic modulus	128.3 kN/mm^2
Cable self-weight	0.195 N/m
Prestressing	200 N

Table 6.3: Material properties for the hyperbolic paraboloid cable dome.

The reference configuration for the cable roof is taken as the hyperbolic paraboloid in Fig. 6.7 in the absence of loads, with equation

$$X_3 = \frac{X_1 X_2}{12} \tag{6.2}$$

and thus no specific form finding procedure is required in this case. The average Cauchy axial force of the dome under its own weight and before pretensioning is 9 N, which increases to 209 N after the pretensioning process.

Table 6.4 presents the vertical displacements and their relative error with respect to the experimental results for the nodes in Fig. 6.7 and different studies. The results for the proposed formulation are given for a mesh of two elements per cable and are the same for both implementations. From Table 6.4, it is observed that the proposed mixed cable element reproduces the experimental results with high accuracy, showing the smallest norm of the relative error at 3.7%. The dynamic approach used in Ref. [35] to numerically find the deformed shape of the structure gives the most inaccurate results, while the minimum energy approach [49] reduces the former error to 4.7%. Elastic catenary elements in Refs. [33, 52] display intermediate relative errors in the range of 6-8%.

Results from Table 6.4 also show that, in almost all formulations, the nodes closer to the upper supports (17, 22) display the highest positive relative errors. This difference arises

Node	Experiment [35]	Dynamic relaxation [35]	Minimum energy [49]	Elastic catenary [52]	Elastic catenary [33]	Present work
5	19.5	19.3 (-1.0)	19.3 (-1.0)	19.6 (0.3)	19.5 (0.1)	19.2 (-1.8)
6	25.3	25.3 (0.0)	25.5 (0.8)	25.7 (1.6)	25.4 (0.2)	25.2 (-0.5)
7	22.8	23.0 (0.9)	23.1 (1.3)	23.4 (2.5)	23.3 (2.2)	22.9 (0.4)
10	25.4	25.9 (2.0)	25.8 (1.6)	25.9 (2.0)	25.9 (1.8)	25.4 (0.1)
11	33.6	33.8 (0.6)	34.0 (1.2)	34.2 (1.7)	34.1 (1.3)	33.5 (-0.2)
12	28.8	29.4 (2.1)	29.4 (2.1)	29.6 (2.8)	29.5 (2.4)	29.1 (1.0)
15	25.2	26.4 (4.8)	25.7 (2.0)	25.9 (2.6)	25.8 (2.3)	25.4 (0.8)
16	30.6	31.7 (3.6)	31.2 (2.0)	31.4 (2.7)	31.3 (2.3)	30.9 (1.0)
17	21.0	21.9 (4.3)	21.1 (0.5)	21.6 (2.7)	21.4 (2.0)	21.3 (1.4)
20	21.0	21.9 (4.3)	21.1 (0.5)	21.6 (2.7)	21.5 (2.3)	21.2 (0.9)
21	19.8	20.5 (3.5)	19.9 (0.5)	20.1 (1.7)	20.0 (1.0)	19.9 (0.6)
22	14.2	14.8 (4.2)	14.3 (0.7)	14.6 (2.5)	14.4 (1.4)	14.5 (2.0)
$\|\varepsilon\|$	-	10.7	4.6	7.8	6.2	3.7

Table 6.4: Vertical displacements (mm) and percentage relative errors ε for the hyperbolic paraboloid cable dome.

because no pretensioning losses are considered, and the same prestessing force is assigned to all elements in the mesh. In practice, the physical pretensioning operation, which is normally carried out at the base supports for practical reasons, produces pretensioning losses that increase towards the upper nodes of the structure.

Figure 6.8 shows the deformed shape of the structural model for a mesh of four elements per cable.

6.2.3 Saddle cable dome

The third example refers to the pretensioned saddle cable dome studied by Ahmad Abad *et al.* [1], Kwan [33] and Thai and Kim [52]. Figure 6.9 shows the structural model for the dome consisting of 142 St. Venant-Kirchhoff elastic cables with properties in Table 6.5. The structure is unsymmetrically loaded with a force of 1 kN in the x_1 and $-x_3$ directions at joints 11→15, 22→26, 33→37, 44→48, 55→59, 66→70 and 77→81 according to the projected grid of cable joints in Fig. 6.10, while the self-weight of the cables is neglected. The reference configuration for the dome is taken as the saddle ruled surface in Fig. 6.9, with the symmetric X_3 coordinates in Table 6.6, and hence no form finding procedure is required in this case.

The nodal displacements for some representative joints are summarized for different studies in Table 6.7. For the proposed formulation, a mesh of one element per cable is used, with both implementations giving the exact value in the absence of distributed loads, while the elastic catenary from Ref. [1] considers a finite difference discretization, as discussed in Sec-

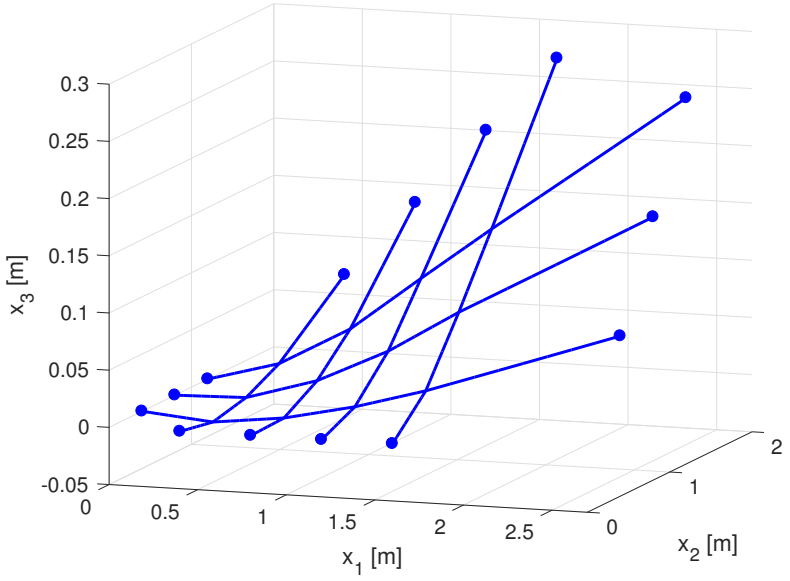

Figure 6.8: Deformed shape for the hyperbolic paraboloid cable dome.

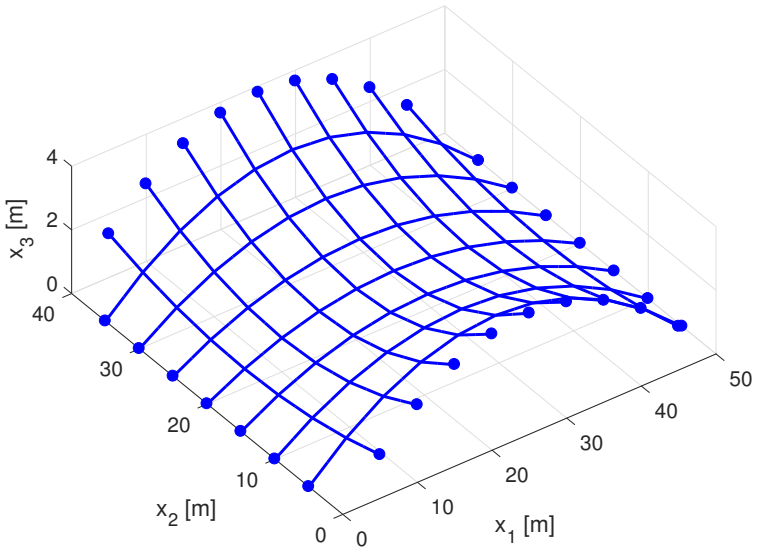

Figure 6.9: Structural model for the saddle cable dome.

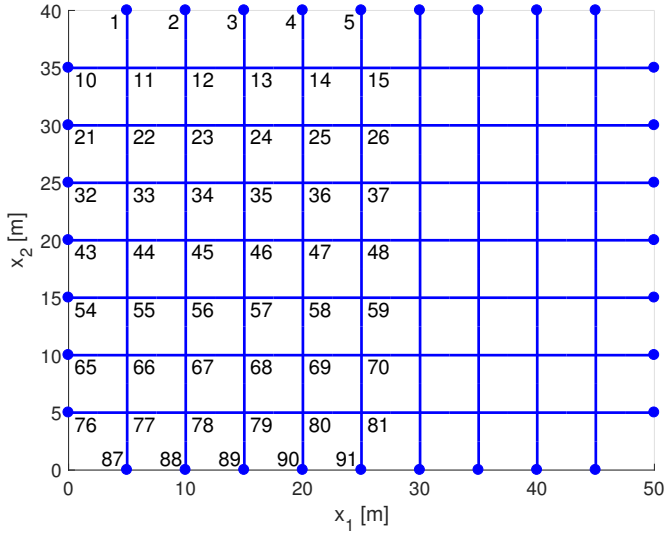

Figure 6.10: Projected grid of cable joints for the saddle cable dome.

Property	**Value**
Cross-sectional area	306 mm^2
Elastic modulus	147 kN/mm^2
Cable self-weight	0 N/m
Prestressing	60 kN

Table 6.5: Material properties for the saddle cable dome.

Node	X_3	Node	X_3	Node	X_3	Node	X_3	Node	X_3
1	1.368	11	1.032	22	0.792	33	0.648	44	0.600
2	2.432	12	1.835	23	1.408	34	1.152	45	1.067
3	3.192	13	2.408	24	1.848	35	1.512	46	1.400
4	3.648	14	2.752	25	2.118	36	1.728	47	1.600
5	3.800	15	2.867	26	2.200	37	1.800	48	1.667

Table 6.6: X_3 coordinate for the saddle cable roof in the reference configuration.

tion 2.2.2, with eight internal nodes per cable. Table 6.7 demonstrates a very good agreement between the mixed cable elements and the other models in the literature.

Table 6.8 presents the axial forces for some representative elements given by the proposed formulation, in the 2nd PK form, and by the formulation in Ref. [33], which assumes infinitesimal deformations. Since the cable self-weight is neglected, the axial force distributions for the individual cables are constant. The results in Table 6.8 confirm the good agreement

Node	Kwan [33]			Thai and Kim [52]			Abad [1]			Present work		
	u_1	u_2	u_3	u_1	u_2	u_3	u_1	u_2	u_3	u_1	u_2	u_3
11	15.6	4.5	-81.7	15.6	4.5	-81.7	15.6	4.5	-81.8	15.5	4.5	-81.7
13	7.4	4.2	-33.3	7.4	4.2	-33.3	7.4	4.2	-33.4	7.4	4.2	-33.6
15	4.1	2.8	-11.2	4.1	2.8	-11.2	4.1	2.8	-11.2	4.1	2.8	-11.3
22	14.4	3.5	-97.1	14.4	3.5	-97.1	14.4	3.5	-97.3	14.5	3.5	-97.2
24	7.3	3.0	-32.0	7.3	3.0	-31.9	7.3	3.0	-32.1	7.4	3.0	-32.4
26	4.8	0.6	11.3	4.8	0.6	11.3	4.8	0.6	11.2	4.8	0.7	10.6
33	11.7	1.7	-92.4	11.7	1.7	-92.4	11.7	1.7	-92.6	11.7	1.7	-92.5
35	6.3	1.2	-20.2	6.3	1.2	-20.2	6.3	1.2	-20.4	6.3	1.2	-20.4
37	4.7	-0.5	35.8	4.7	-0.5	35.8	4.7	-0.5	35.6	4.6	-0.5	35.3
44	10.6	0.0	-88.7	10.6	0.0	-88.7	10.6	0.0	-88.9	10.6	0.0	-88.7
46	5.8	0.0	-14.0	5.8	0.0	-14.0	5.8	0.0	-14.2	5.8	0.0	-14.4
48	4.6	0.0	45.9	4.5	0.0	45.9	4.5	0.0	45.7	4.5	0.0	45.5

Table 6.7: Nodal displacements (mm) for the saddle cable dome.

between the present study and the formulations in the literature.

Cables	Kwan [33]	Present work
11→12	53.70	53.62
23→24	57.80	58.03
47→48	62.51	62.43
1→11	75.43	75.44
24→35	69.30	69.40

Table 6.8: Axial forces (kN) for the saddle cable dome.

Figure 6.11 shows the deformed shape of the dome with a magnification factor of ten for the displacements and a mesh of one element per cable.

6.3 Earthquake response of a pretensioned cable net

The last example studies the earthquake response of a pretensioned cable net that was studied by Jayaraman and Knudson [28] and Thai and Kim [52]. The structural model consists of a central square that is hanging from eight supports as shown in Fig. 6.12, where all distances on the X_1X_2 plane are 30.48 m and the square is at an elevation of $X_3 = -9.144$ m. All cables are assumed to be St. Venant-Kirchhoff elastic and their material properties are summarized in Table 6.9. Four forces F=35.586 kN are applied at the four nodes of the central square of the structure. The reference configuration is taken as in Fig. 6.12 in the absence of loads, so that no form finding procedure is required.

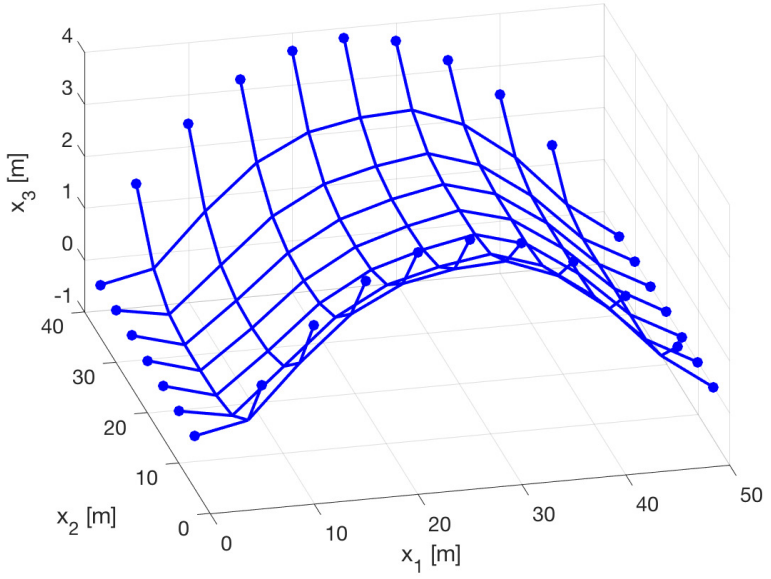

Figure 6.11: Deformed shape of the saddle cable dome.

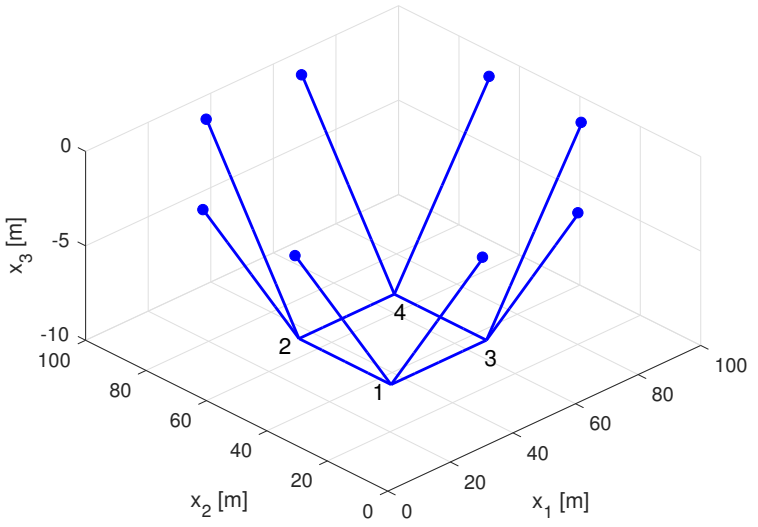

Figure 6.12: Structural model for the pretensioned cable net.

First, the static response under the applied loads is studied in Table 6.10. As in the earlier cases, the results for the continuous and the discontinuous implementations of the

Property	Value
Cross-sectional area	146.45 mm^2
Elastic modulus	82.737 kN/mm^2
Cable self-weight	1.459 N/m
Prestressing (central square)	24.283 kN
Prestressing (inclined cables)	23.687 kN
Density	140.6 kg/m

Table 6.9: Material properties for the planar cable net.

mixed cable element are identical when numerical cable joints are introduced according to Section 6.1. Table 6.10 presents the vertical displacements of node 1, and demonstrates the very good agreement between the proposed formulation, with a mesh of two elements per cable, and the models in Ref. [52].

Model	u_1	u_2	u_3
Jayaraman and Knudson [28]	-39.62	-40.20	-446.32
SAP2000 [52]	-40.28	-40.28	-448.88
Thai and Kim [52]	-40.13	-40.13	-446.50
Present work	-40.33	-40.33	-447.69

Table 6.10: Vertical displacements (mm) for node 1 of the cable net.

After the static analysis at $t = 0$, the cable net is subjected to the El Centro ground acceleration by defining $\mathbf{u}$, $\mathbf{v}$ and $\dot{\mathbf{v}}$ as values relative to the ground motion and considering the term $\mathbf{M}\mathbf{a}_g$ as an applied load [12]. The same acceleration time history is imposed to all supports in the vertical direction, and the time integration is performed with the energy-momentum consistent algorithm with a time step $\Delta t = 0.02$ s. The cable density in Table 6.9 is computed by distributing the four lumped masses in Ref. [52] along their contributing lengths, while no material damping is considered for the model.

Since the results in Ref. [52] use only four lumped masses at the four nodes of the square for the entire structure, no secondary vibration of the cables is evident in the results. In contrast, the displacement time history in Fig. 6.13 shows a primary oscillation corresponding to the dominant earthquake excitation and a secondary oscillation that is produced by the vibration of the inclined cables that is excited by the consistent mass of the structure. This secondary vibration gives rise to a compressive axial force wave in the 2nd PK axial forces of the central cables in Fig. 6.13.

6.4 Concluding remarks

Chapter 6 uses the proposed formulations to analyze the static and dynamic behavior of three-dimensional cable structures.

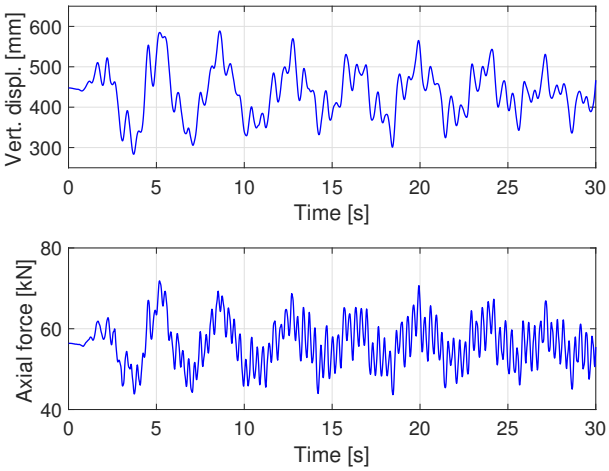

Figure 6.13: Earthquake response for the planar cable net.

The principal disadvantage of the continuous implementation of the mixed cable element, corresponding to its inability to intrinsically model jumps in the axial force distribution (Section 4.2.2), is overcome by developing numerical cable joints with different nodes and linked displacement DOFs. This numerical treatment of the joints in the continuous case produces identical results to those for the discontinuous implementation, as demonstrated in the examples.

For the hyperbolic paraboloid cable roof, the proposed cable elements reproduce the experimental results with high accuracy, and give the smallest percentage relative error at 3.5% compared to alternative models in the literature. The static analysis of the saddle cable dome and the planar cable net give almost identical results to the corresponding infinitesimal models in the literature, while the dynamic analysis of the planar cable net with mixed cable elements accounts for a consistent mass matrix, and gives accurate results with secondary oscillations in the displacement field.

Chapter 7
Summary and conclusions

7.1 Summary

This dissertation covers the development and validation of a mixed 3d cable element that accounts for nonlinear geometry effects under elastic and inelastic material behavior. The cable element is formulated for general loading conditions and is therefore capable of reproducing the continuous axial force distribution that results from distributed loads, as well as the jumps that appear in the axial forces under the application of concentrated loads.

The formulation of the proposed 3d cable element is based on a mixed variational framework under finite deformations with two independent fields: the displacement field and the axial force field. The study derives the kinematics of the problem in general curvilinear coordinates and identifies the kinematic variables and their conjugate stress measures. Subsequently, the principle of virtual work and the weak form of the strain-displacement relation are derived for general loading conditions and material models. Based on the weak statement of the nonlinear catenary problem, two numerical implementations of the cable element are possible: one with a continuous axial force distribution and one with a discontinuous axial force distribution. A new time integration scheme that preserves the discrete Hamiltonian structure of the problem is also proposed in this context, and a Savitzky-Golay filter is deployed to address the high-frequency contributions that arise in the nonlinear dynamic response of flexible cables with a large sag-to-span ratio.

The proposed 3d cable element is first validated with simple benchmark problems under two nonlinear elastic material models, a St. Venant-Kirchhoff model and a compressible neo-Hookean model. These problems show that, even for coarse meshes, the proposed element describes the displacement field and the axial force distribution with high accuracy compared to other formulations in the literature. The validation of elastic mixed cable elements also includes two continuation analyses in 2d and 3d, for which the stability points of two inclined cables are determined with accuracy. Finally, the proposed formulations are used

to investigate the nonlinear dynamic response of three simply-supported elastic cables with different sag-to-span ratios, and their results are compared with the Newmark and the HHT-α methods. These examples show that the new energy-momentum conserving algorithm is equivalent to the Newmark method for small sag-to-span ratios, and that it provides accurate results for large sag-to-span ratios in contrast to the Newmark method, which diverges in some cases. The HHT-α method includes numerical dissipation that controls the high-frequency oscillations in the axial forces but reduces the total energy appreciably in contrast to the Savitky-Golay filter.

Two incrementally-infinitesimal viscoelastic material models, the standard linear solid and the generalized Maxwell solid, are used to formulate viscoelastic mixed cable elements under small deformations. To account for large viscoelastic strains, a new viscoelastic material model is formulated under finite deformations using a rate-dependent evolution law in terms of the Lie derivative of the strains. This new material model reduces to the infinitesimal case when small deformations are considered. When these constitutive models are used in simple benchmark problems, the results show that small relaxation times model the material damping of compression axial force waves along the cable, while long relaxation times describe the overall decay of the dynamic response of actual cables.

Finally, numerical cable joints are introduced so that the continuous implementation of the element can accommodate physical jumps in the axial force field. These numerical cable joints are used to analyze the structural behavior of complex three-dimensional cable nets with the proposed cable element. In the first example, a skyline cable system with a hanging load is analyzed statically under the assumption of negligible elastic deformations, while the second and the third examples refer to a hyperbolic paraboloid and a saddle cable roof. The last example studies the earthquake response of a planar cable net suspended from eight supports.

7.2 Conclusions

The proposed 3d mixed cable element shows consistency, versatility and numerical robustness for the nonlinear static and dynamic analysis of cable structures under general loading. The following conclusions follow from the study:

- When a mixed two-field variational formulation of the catenary problem is considered, two numerical implementations are possible for the corresponding finite element: one with a continuous axial force distribution and one with a discontinuous one.

- A time integration scheme that satisfies the principle of virtual work at the midpoint between time steps, while also satisfying the weak compatibility equation for the average strain of subsequent time steps preserves the Hamiltonian structure of the mixed two-field catenary problem for any nonlinear complementary energy function.

- The static analysis of elastic cables leads to the following conclusions:

  - The continuous and the discontinuous implementations of the mixed cable element give identical results for meshes of equal-size elements and symmetric problems.
  - The discontinuous implementation gives discontinuous axial force distributions when used in meshes of unequal-size elements and symmetric problems, with the results converging to the continuous solution as the mesh is refined.
  - Under concentrated loads, the discontinuous implementation gives very accurate results for coarse meshes, while the continuous implementation requires very fine meshes to model the jump in the axial force field while giving rise to Gibbs oscillations in the axial force distribution. This shortcoming of the continuous form is eliminated by placing two nodes at the same spatial point with linked displacement degrees of freedom.
  - The accuracy of the axial force distribution for the proposed element is noteworthy compared to other models in the literature, which usually report values near the maximum of the proposed formulation.

- The dynamic analysis of elastic cables leads to the following conclusions:
  - For cables with a small sag-to-span ratio ($\sim$1/15), the energy-conserving scheme is equivalent to the Newmark method. The HHT-α method gives the same initial results but includes numerical dissipation in time.
  - For cables with a large sag-to-span ratio ($\sim$1/9.5), the Newmark method gives slight oscillations in the total energy, while the energy-conserving scheme preserves exactly the total energy of the cable. Slight high-frequency contributions are also observed in the axial force time history for these methods, but are dampened out by the numerical dissipation of the HHT-α method.
  - For cables with a very large sag-to-span ratio ($\sim$1/5), the Newmark method diverges early in the response, while the energy-conserving algorithm gives a constant total energy evolution with significant high-frequency oscillations in the axial forces. The HHT-α method shows an initial drop in the total energy that dampens out these high frequencies.
  - A Savitzky-Golay filter successfully removes the high-frequency contributions in the axial force time history with a significantly smaller reduction of total energy than the HHT-α method.
  - The earthquake response of simply-supported cables shows that small out-of-plane angles for the ground acceleration induce significant 3d coupling of in-plane and out-of-plane response that gives rise to large out-of-plane displacements even for small sag-to-span ratios.

- The analysis of viscoelastic cables leads to the following conclusions:
  - The new finite viscoelastic material model is equivalent to the common infinitesimal viscoelastic models for cables undergoing small deformations.

  - Viscoelastic material models with a short relaxation time successfully dampen out the high-frequency oscillations in the axial force time history that appear in the conservative analyses.
  - Damping forces tend to homogenize the nonlinear waves resulting from the nonlinear dynamic response of cables, in contrast to the viscoelastic material models, which preserve the relative differences between peaks.
  - Viscoelastic material models give larger initial axial forces because of the additional stiffness of the viscous part, and tend to increase the phase of the solution when the stiffness of the viscous part increases. This effect on the phase of the response is reduced as the sag-to-span ratio of the cable increases.
  - Viscoelastic material models, in contrast to damping forces, reduce the 3d coupling in the earthquake response of simply-supported cables, and thus give smaller out-of-plane displacements for the same out-of-plane angles of the ground acceleration.

- The structural analysis of three-dimensional cable nets leads to the following conclusions:
  - When numerical joints are introduced into the continuous form of the proposed element, both continuous and discontinuous axial force implementations give indistinguishable results.
  - Coarse meshes, with one or two elements per cable, suffice to give very accurate results when cable nets are studied with the proposed formulation.
  - Numerical results for the proposed cable element agree very well with those in the literature, and give the smallest relative error among all existing models when compared to experimental results.

7.3 Recommendations for further research

The results of this dissertation generate new questions about the analysis of cable structures which represent challenges for future research. In particular, the proposed 3d mixed cable elements can be extended in three areas:

- The following numerical issues deserve attention:
  - The numerical stability of high-order mixed cable elements for the proposed variational formulation.
  - The extension of the proposed energy-momentum conserving algorithm in complementary space to three-dimensional material models.

- The following issues regarding constitutive material models deserve attention:

  - Finite damage models, to permit the analysis of corrosion and other section-decreasing damage mechanisms.
  - Finite plasticity models, for determining the ultimate capacity of cable systems leading to effective repair and maintenance procedures.

- The following issues regarding application areas deserve attention:
  - Sliding cables used in modern construction techniques.
  - External forces that depend on the unknown degrees of freedom, such as hydrostatic loads in cable submarine applications.
  - Fluid-structure interaction for cables; for instance, the supersonic flows in aeronautical and military applications.

Bibliography

[1] M. S. Ahmad Abad et al. "Nonlinear analysis of cable structures under general loadings". *Finite Elem. Anal. Des.* 73 (2013), pp. 11–19.

[2] M. Ahmadizadeh. "Three-dimensional geometrically nonlinear analysis of slack cable structures". *Comp. Struct.* 128 (2013), pp. 160–169.

[3] A. Andreu, L. Gil, and P. Roca. "A new deformable catenary element for the analysis of cable net structures". *Comp. Struct.* 84 (2006), pp. 1882–1890.

[4] S. Antman. *Nonlinear Problems of Elasticity*. 2nd ed. Applied Mathematical Sciences. Springer, 2005.

[5] J. H. Argyris, T. Angelopoulos, and B. Bichat. "A general method for the shape finding of lightweight tension structures". *Comput. Methods Appl. Mech. Engrg.* 3 (1974), pp. 135–149.

[6] F. Armero and I. Romero. "On the formulation of high-frequency dissipative time-stepping algorithms for nonlinear dynamics. Part I: low-order methods for two model problems and nonlinear elastodynamics". *Comput. Methods Appl. Mech. Engrg.* 190 (2001), pp. 2603–2649.

[7] R. Bishop and S. Goldberg. *Tensor Analysis on Manifolds*. 1st ed. Dover Publications, Inc., 1980.

[8] F. Brezzi and K. Bathe. "A discourse on the stability conditions for mixed finite element formulations". *Comput. Methods Appl. Mech. Engrg.* 82 (1990), pp. 27–57.

[9] M. U. A. Bromba and H. Ziegler. "Application hints for Savitzky-Golay digital smoothing filters". *Anal. Chem.* 53 (1981), pp. 1583–1586.

[10] M. U. A. Bromba and H. Ziegler. "Efficient computation of polynomial smoothing digital filters". *Anal. Chem.* 36 (1964), pp. 1627–1639.

[11] D. Bruno and A. Leonardi. "Nonlinear structural models in cableway transport systems". *Simulat. Pract. Theory* 7.3 (1999), pp. 207–218.

[12] A. K. Chopra. *Dynamics of structures. Theory and Applications to Earthquake Engineering*. 4th ed. Prentice Hall, 2012.

[13] M. Crusells-Girona, F. C. Filippou, and R. L. Taylor. "A filtered energy-momentum conserving time integration algorithm for nonlinear dynamic analysis of cable structures". *Earthq. Eng. Struct. D.* (Submitted.).

[14] M. Crusells-Girona, F. C. Filippou, and R. L. Taylor. "A mixed formulation for nonlinear analysis of cable structures". *Comp. Struct.* 186 (2017), pp. 50–61.

[15] M. Crusells-Girona, F. C. Filippou, and R. L. Taylor. "Nonlinear static and dynamic analysis of mixed cable elements". *Proceedings of the 14th International Conference on Computational Plasticity - Fundamentals and Applications, COMPLAS 2017*. 2017.

[16] L. C. Evans. *Partial Differential Equations*. 2nd ed. American Mathematical Society, 2010.

[17] F. C. Filippou. "CE 221 course reader". University of California, Berkeley. 2014.

[18] F. C. Filippou. *FEDEASLab - Finite Elements in Design, Evaluation and Analysis of Structures*. 2007. URL: https://www.ce.berkeley.edu/people/faculty/filippou.

[19] N. Gimsing and C. Georgakis. *Cable supported bridges*. 3rd ed. John Wiley & Sons, Ltd., 2012.

[20] O. Gonzalez. "Time integration and discrete Hamiltonian systems". *J. Nonlinear Sci.* 6 (1996), pp. 449–467.

[21] M. Gurtin. *An Introduction to Continuum Mechanics*. Mathematics in Science and Engineering. Academic Press, 1982.

[22] R. B. Haber and J. F. Abel. "Initial equilibrium solution methods for cable reinforced membranes. Part I: Formulations". *Comput. Methods Appl. Mech. Engrg.* 30 (1982), pp. 263–284.

[23] R. B. Haber and J. F. Abel. "Initial equilibrium solution methods for cable reinforced membranes. Part II: Implementation". *Comput. Methods Appl. Mech. Engrg.* 30 (1982), pp. 285–306.

[24] H. M. Hilber, T. J. R. Hughes, and R. L. Taylor. "Improved numerical dissipation for time integration algorithms in structural dynamics". *Earthq. Eng. Struct. D.* 5 (1977), pp. 283–292.

[25] T. J. R. Hughes. *The Finite Element Method. Linear Static and Dynamic Finite Element Analysis*. 1st ed. Dover Publications, Inc., 2000.

[26] N. Impollonia, G. Ricciardi, and F. Saitta. "Statics of elastic cables under 3D point forces". *Int. J. Solids Struct.* 48 (2011), pp. 1268–1276.

[27] H. M. Irvine. *Cable structures*. 1st ed. MIT Press, 1981.

[28] H. B. Jayaraman and W. C. Knudson. "A curved element for the analysis of cable structures". *Comp. Struct.* 14 (1981), pp. 325–333.

[29] K. Kanzaki and T. Sakai. "Studies on the cable crane hung at three supports (I) (1) A way of calculation supposing static balanced state." *J. Jpn. For. Soc.* 54 (1972), pp. 103–112.

[30] K. Kawashima, S. Unjoh, and M. Tunomoto. "Estimation of damping ratio of cable-stayed bridges for seismic design". *J. Struct. Eng.* 119.4 (1993), pp. 1015–1031.

[31] S. Krenk. "Global format for energy-momentum based time integration in nonlinear dynamics". *Int. J. Numer. Meth. Engng.* 100 (2014), pp. 458–476.

[32] S. Krenk and J. R. HØgsberg. "Properties of time integration with first order filter damping". *Int. J. Numer. Meth. Engng.* 64 (2005), pp. 547–566.

[33] A. S. K. Kwan. "A new approach to geometric nonlinearity of cable structures". *Comp. Struct.* 67.4 (1998), pp. 243–252.

[34] W. Lacarbonara. *Nonlinear structural mechanics*. Springer, 2013.

[35] W. J. Lewis, M. S. Jones, and K. R. Rushton. "Dynamic relaxation analysis of the non-linear static response of pretensioned cable roofs". *Comp. Struct.* 18.6 (1984), pp. 989–997.

[36] J. Michalos and C. Birnstiel. "Movements of a cable due to changes in loadings". *J. Struct. Div. ASCE* 127 (1962), pp. 267–303.

[37] N. A. Newmark. "A method of computation for structural dynamics". *J. Eng. Mech. ASCE* 85 (1959), pp. 67–94.

[38] W. T. O'Brien and A. J. Francis. "Cable movements under two-dimensional loads". *J. Struct. Div. ASCE* (1964).

[39] O. O'Reilly. *Modeling Nonlinear Problems in the Mechanics of Strings and Rods*. Springer, 2017.

[40] S. Reese and S. Govindjee. "A theory of finite viscoelasticity and numerical aspects". *Int. J. Numer. Meth. Engng.* (1998), pp. 3455–3482.

[41] A. Savitzky and M. J. E. Golay. "Smoothing and differentiation of data by simplified least squares procedures". *Anal. Chem.* 36 (1964), pp. 1627–1639.

[42] J. C. Simo. "A finite strain beam formulation. The three-dimensional dynamic problem. Part I." *Comput. Methods Appl. Mech. Engrg.* 49 (1985), pp. 55–70.

[43] J. C. Simo and T. J. R. Hughes. *Computational Inelasticity*. 1st ed. Springer, 1998.

[44] J. C. Simo and N. Tarnow. "The discrete energy-momentum method. Conserving algorithms for nonlinear elastodynamics". *Z. angew. Math. Phys.* 43 (1992), pp. 757–792.

[45] J. C. Simo, N. Tarnow, and K. K. Wong. "Exact energy-momentum conserving algorithms and symplectic schemes for nonlinear dynamics". *Comput. Methods Appl. Mech. Engrg.* 100 (1992), pp. 63–116.

[46] J. C. Simo and L. Vu-Quoc. "A three-dimensional finite-strain rod model. Part II: Computational aspects." *Comput. Methods Appl. Mech. Engrg.* 58 (1986), pp. 79–116.

[47] N. Srinil, G. Rega, and S. Chucheepsakul. "Three-dimensional non-linear coupling and dynamic tension in large-amplitude free vibrations of arbitrarily sagged cables." *J. Sound Vib.* 269 (2004), pp. 823–852.

[48] M. Such et al. "An approach based on the catenary equation to deal with static analysis of three dimensional cable structures". *Eng. Struct.* 31 (2009), pp. 2162–2170.

[49] F. M. A. Sufian and A. Templeman. "On the non-linear analysis of pre-tensioned cable net structures". *Struct. Eng.* 4 (1992), pp. 147–158.

[50] Y. Suzuki, E. S. Miyata, and S. C. Iverson. "Static analyses of the triangular running skyline system: a three-dimensionally movable logging cable system". *Comp. Struct.* 60.4 (1996), pp. 579–592.

[51] R. L. Taylor. *FEAP - Finite Element Analysis Program*. 2014. URL: http://projects.ce.berkeley.edu/feap/.

[52] H. Thai and S. Kim. "Nonlinear static and dynamic analysis of cable structures". *Finite Elem. Anal. Des.* 47 (2011), pp. 237–246.

[53] S. Thai, N. Kim, and J. Lee. "Isogeometric cable elements based on B-spline curves". *Meccanica* 52 (2017), pp. 1219–1237.

[54] G. Tibert. "Numerical analysis of cable roof structures". MA thesis. KTH, 1999.

[55] D. Veenendaal and P. Block. "An overview and comparison of structural form finding methods for general networks". *Int. J. Solids Struct.* 49 (2012), pp. 3741–3753.

[56] E. L. Wilson. *Static and Dynamic Analysis of Structures. A Physical Approach with Emphasis on Earthquake Engineering.* 4th ed. Computers and Structures, Inc., 2010.

[57] Y. B. Yang and J. Y. Tsay. "Geometric nonlinear analysis of cable structures with a two-node cable element by generalized displacement control method". *Int. J. Struct. Stab. Dy.* (2007), pp. 571–588.

[58] O. C. Zienkiewicz, R. L. Taylor, and D. D. Fox. *The Finite Element Method for Solid and Structural Mechanics*. 7th ed. Elsevier, Ltd., 2014.